FACTORS INFLUENCING FLY ASH FORMATION AND SLAG DEPOSIT FORMATION (SLAGGING) ON COMBUSTING A SOUTH AFRICAN PULVERISED FUEL IN A 200 MW_e BOILER

Christopher van Alphen

A thesis submitted to the Faculty of Engineering and the Built Environment, University of the Witwatersrand, Johannesburg, in fulfilment of the requirements for the degree of Doctor of Philosophy

Johannesburg, 2005

DECLARATION

I declare that this thesis is my own, unaided work. It is being submitted for the Degree of Doctor of Philosophy to the University of the Witwatersrand, Johannesburg. It has not been submitted before for any degree or examination in any other University.

_____

_____ day of _____ 2005

ABSTRACT

In 1997, South African's major power utility, recognised the need to improve the understanding of fly ash formation and slag deposition of South African coals. This requirement is due to the predicted quality changes of power station feedstocks and the limited research into the slagging propensity of South African coals.

This research seeks to develop an analytical technique and a fly ash formation model for predicting the slagging propensity of coals. The research will establish if the models based on *Carboniferous* coals can be applied to South African *Permian* coals.

A water-cooled suction pyrometer with a custom designed slag probe was used to obtain samples of fly ash and slag from within a 200 MW_e pulverised fuel boiler. Simultaneously, samples of pulverised fuel feedstock were collected.

The mineral attributes in the pulverised fuel and the phases in fly ash and slag deposit were quantified by CCSEM. The analytical procedure, CCSEM, has been developed with a novel procedure for identifying minerals and C-bearing phases.

The new fly ash formation model assumes that the mineral attributes of the combusting pulverised fuel particle controls the size and elemental signature of the resultant fly ash particle(s).

The new model has shown that the inherent mineral attributes controls the physical and chemical characteristics of the initial fly ash phases. Thereafter, conditions (stoichiometric, temperature and turbulence) within the combustion chamber promote the physical and/or chemical interaction of the initial fly ash particles.

Slag deposits are enriched in Ca- and Fe-bearing alumino-silicates. The new slagging propensity index is based on either predicting or measuring the proportion of Ca- and Fe-bearing alumino-silicates.

The numerous fly ash formation models, based on *Carboniferous* coals are not necessarily valid for South African coals. It is not the integrity of the actual fly ash formation mechanisms that is questioned, but rather the experimental scale on which the models are based.

This research has produced an analytical technique and a fly ash formation model to predict the slagging propensity of coals. This forms a platform for further research into the role that organically bound cations, combustion conditions and boiler configuration has on the formation of Ca- and Fe-bearing alumino-silicates.

ACKNOWLEDGEMENTS

Without the advice and encouragement from many relatives, friends and colleagues this thesis would not have been possible. The following persons merit special mention and their inputs and support are gratefully acknowledged:

- To my late father, his encouragement started my quest for knowledge.
- Professor Rosemary Falcon, my supervisor, for her help, guidance and constructive suggestions.
- Eskom's Coal Combustion Technologies (CCT) research steering committee for allocating the required funds.
- Dr Mark van der Riet for his guidance and wholehearted support of the concept of this thesis.
- Mike Blenkinskop for initiating and acquiring the initial funds for the research into fly ash formation and slag development.
- The management Anglo American Research Laboratories (AARL) and Anglo American PLC for the exclusive rights to utilise the ASCAN software is thankfully acknowledged. (Without the ASCAN software, the CCSEM technique extensively used, as an analytical tool would not have been possible).
- To Dr Hanna Horsch for initiating the discussions and convincing management to grant permission to use ASCAN software.
- Konrad Hartmenn for facilitating the use of the Scanning Electron Microscope at TSI (Technology Service International, Eskom).
- Tom Keyser and his staff at Hendrina Power station for all the assistance during the slag probe test work.
- Pat Sterling and her staff at the school of Process and Mineral Engineering for sample preparation.
- The Scanning Electron Microscope unit at University of Witwatersrand for carbon coating the prepared polished sections.
- Vennessa de Boor for proof reading the original manuscipt.

To Tracey, for her devotion and commitment as a pillar of emotional and financial support during the past nine years and for enduring many lost weekends and evenings. And finally to Amber, you are my next PhD.

CONTENTS

CONTENTS **Page**

DECLARATION ..... **II**

ABSTRACT ..... **III**

ACKNOWLEDGEMENTS ..... **V**

CONTENTS ..... **VI**

LIST OF FIGURES ..... **XI**

LIST OF TABLES ..... **XVI**

LIST OF SYMBOLS ..... **XXI**

1 GENERAL INTRODUCTION **1**

1.1 Slagging in Pulverised Fuel Boilers **1**

1.2 Negative Impact of Slagging **3**

1.3 International and Current Research on Slagging **3**

1.4 Objectives of the Thesis **4**

1.5 Methodology **6**

1.6 Outline of the Thesis **7**

2 LITERATURE REVIEW: COAL AND ASH **9**

2.1 Principal Working Groups **9**

2.2 Macerals and Minerals in Coal **9**

2.3 Analysing Coal and Fly Ash **15**

2.3.1 Elemental analysis 17

2.3.2 Maceral identification 18

2.3.3 Mineral quantification - CCSEM 19

2.3.4 Mineral identification – X-ray diffraction analysis 27

2.3.5 Mineral identification – other analytical techniques 29

2.4 Predicting Fly Ash Formation and Slagging **32**

2.4.1 Bench scale investigations 32

2.4.2 Pilot scale and plant scale investigations 33

2.5 Conclusion **35**

3 LITERATURE REVIEW: FLY ASH FORMATION AND SLAGGING 37
3.1 High Temperature Mineral Matter Transformation 37
3.2 Fly Ash Formation 45
3.3 Fly Ash Transportation and Fly Ash Deposition 57
3.4 Slag Deposit Growth and Development 67
3.5 Ash Deposition Indices 76
3.6 Conclusion 77

4 METHODOLOGY 79
4.1 Sample Acquisition 80
4.1.1 Isokinetic sampling: pulverised fuel 82
4.1.2 Suction pyrometer and slag probe: fly ash and slag deposit 82
4.1.3 Suction pyrometer and slag probe operation 84
4.1.4 Boiler operational conditions 85
4.2 Sample Preparation Techniques 86
4.2.1 Pulverised fuel 88
4.2.2 Fly ash 90
4.2.3 Slag sleeves 90
4.3 Petrographic Analyses 90
4.4 Chemical Analyses 92
4.5 Particle Size Analysis 93
4.6 CCSEM 94
4.6.1 TSI-CCSEM methodology 97
4.6.2 TSI-CCSEM Mineral identification 104
4.6.3 TSI-CCSEM output 113
4.7 TSI-CCSEM Mineral Proportions Validation 115
4.8 Fly Ash Formation Model 118
4.8.1 Principals and assumption 118
4.8.2 Methodology 123
4.8.3 Validation 125
4.9 Slagging Prediction Model 127
4.10 Conclusion 128

5 RESULTS 130
5.1 Sample Description and Boiler Conditions 130
5.2 Screened Particle Size distribution 132
5.3 Petrographic Results 135
5.3.1 Maceral and microlithotypes 136
5.4 Chemical Analysis 140
5.4.1 Proximate, ultimate and XRF ash elemental 140
5.5 Mineralogy of the Pulverised Fuel 144
5.6 Maceral Inorganic Element Composition 146
5.7 CCSEM Analysis – Pulverised fuel 148
5.7.1 Mineral matter distribution 148
5.7.2 Comparative elemental analysis 149
5.7.3 Mineral grain sizes 153
5.7.4 Mineral liberation and association characteristics 155
5.8 Summary 159

6 RESULTS – FLY ASH AND SLAG DEPOSITS 161
6.1 Fly Ash 161
6.1.1 Phase distribution 161
6.1.2 Fly ash grain size 166
6.1.3 Fly ash liberation 168
6.1.4 Fly ash association 170
6.2 Slag Deposits 173
6.2.1 Slag sleeve surface temperatures 173
6.2.2 Mineral abundance 178
6.3 Summary 183

7 FLY ASH FORMATION AND SLAG DEPOSIT MODEL - RESULTS 185
7.1 Fly Ash Formation 185
7.1.1 Particle size distribution comparison 186
7.1.2 Mass percent fly ash phase proportion comparison 191
7.2 Drop Tube Furnace 194
7.2.1 DTF ash – influence of combustion conditions 194
7.2.2 DTF ash - fly ash formation model validation 199
7.3 Fly ash prediction – 200 MW_e boiler 203

7.4 Fly ash formation in 200 MW_e boiler – additional process 205
7.5 Slag Deposit Formation 211
7.6 Slagging Prediction Indices 215
7.7 Summary 216

8 SUMMARY, CONCLUSION AND FUTURE RESEARCH 220
8.1 Summary 220
8.1.1 Introduction 220
8.1.2 Analytical framework 221
8.1.3 Suction pyrometer and water cooled slag probe 221
8.1.4 CCSEM 222
8.1.5 CCSEM results – pulverised fuel 225
8.1.6 CCSEM results – fly ash 226
8.1.7 CCSEM results – slag deposits, clinkers and bottom ash 227
8.1.8 Fly ash formation model 228
8.1.9 Fly ash formation and slag deposition – 200MW_e boiler 231
8.2 Conclusion 234
8.3 Future Research 236

9 REFERENCES 238

APPENDIX A: INTERNATIONAL WORKING GROUPS 258
APPENDIX B: SLAGGING INDICES 261
APPENDIX C: SUCTION PYROMETER AND SLAG PROBE 262
APPENDIX D: DERIVING SLAG PROBE SURFACE TEMPERATURE 268
APPENDIX E: MACERAL, MICROLITHOTYPES AND MINERAL 271
APPENDIX F: CHEMICAL ANALYSES 274
APPENDIX G: CCSEM MEASUREMENT PARAMETERS 278
APPENDIX H: GLASS DENSITY CALCULATION 286
APPENDIX I: PARTICLE SIZE DISTRIBUTION 288
APPENDIX J: PETROGRAPHIC RESULTS 290
APPENDIX K: PROXIMATE, ULTIMATE AND ASH ELEMENTAL 297
APPENDIX L: PULVERISED FUEL CONSTITUENTS 299
APPENDIX M: MINERAL LIBERATION – PULVERISED FUEL 304

APPENDIX N: FLY ASH MASS-% PROPORTION 310
APPENDIX O: LIBERATION CHARACTERISTICS – FLY ASH 315
APPENDIX P: MINERAL ASSOCIATION 324
APPENDIX Q: PHASE PROPORTIONS – SLAG DEPOSITS 325
APPENDIX R: DTF FLY ASH PHASE PROPORTIONS 327
APPENDIX S: MODEL PREDICTION AND DTF FLY ASH 328

LIST OF FIGURES

Figure **Page**

Figure 1.1: Typical p.f. boiler and location of typical slag deposits..... 2
Figure 3.1: Mineral transformations in coal. (Adapted from Bryers (1986)). Mineral transformation of quartz based on data from Deer-Howie and Zussman (Deer, W. A., Howie, R. A., and Zussman, J.,1966) 37
Figure 4.1. Relative position of the four access holes. Not drawn to scale. 80
Figure 4.2a: Physical dimensions and location of the access hole. 81
Figure 4.2b: Access hole in boiler wall. Slag probe in the foreground..... 81
Figure 4.3: Depending on the orientation and position of the sectioning plane different sizes and liberation characteristics are possible. 87
Figure 4.4: A backscattered electron image of typical field of view. The epoxy resin is grey, organic fraction (macerals) varying from black to dark grey and mineral matter is white. The light grey particles are the crushed epoxy resin particles. 89
Figure 4.5: The centroidal method of positioning the electron beam at the centre of “bright” phases. The positions and corresponding reference numbers of the analytical points are superimposed in red. The box represents the image acquired at 500x magnification (Figure 4.6). Note the relatively high proportion of minerals and the organic component (black) that are not included in the analysis. Image magnification is 100X. 95
Figure 4.6: A backscattered electron image at a higher magnification (500x) level than Figure 4.5. The actual analytical points are superimposed in red. 95
Figure 4.7: CCSEM operational flow diagram 98
Figure 4.8: A processed backscatter electron image of pulverised fuel with the regular grid of analytical points superimposed. The scale bar represent 50 μm and the estimated point spacing is 11.21 μm. 102
Figure 4.9: A processed image of unscreened fly ash with the superimposed regularly-spaced analytical points (red crosses). Note that holes (black to light grey) are included. The scale bar represents 50 μm and the point spacing is 2.75 μm. 102
Figure 4.10: A backscattered electron image of slag sleeve section. The fly ash particles are light grey and the actual slag sleeve (mild steel) is white. 104

Figure 4.11. Fuzzy logic principals utilised by ASCAN for mineral identification 106
Figure 4.12: Kaolinite fuzzy logic rule and assigned truth values 106
Figure 4.13: Identified coal particles. 109
Figure 4.14: Identified fly ash particles using the developed ASCAN fly ash mineral identification libraries 112
Figure 4.15: Detailed mineralogy of slag droplets adhering onto slag sleeve (orange). 113
Figure 4.16: The fly ash forming mechanisms of fragmentation, coalescence and partial coalescence described in the included mineral fly ash formation model. 122
Figure 4.17: Principles of fly ash formation prediction 123
Figure 5.1: Generated MW_e during sampling. 131
Figure 5.2: Comparative generated MW_e versus steam load (kg/s) 132
Figure 5.3: Average screened particle size distribution of pulverised fuel and fly ash. 133
Figure 5.4: Comparison in the percent passing 75 µm 133
Figure 5.5: Average volume percent maceral abundance in the +75 and -75+38 µm size fractions. (Vit: vitrinite, Lip: liptinite, RSF: reactive semifusinite, ISF: inert semifusinite, FUS: fusinite, MIC: micrinite, RINT: reactive inertodetrinite, IINT:inert inertodetrinite) 136
Figure 5.6: The volume percent maceral variation in the combined +75 and –75+38 µm size fractions. 137
Figure 5.7: Volume percent microlithotype distribution in the +75 and -75+38 µm size fraction. (Inter: Intermediate, Semi-Fus: semifusinite/fusinite, Inertod:Inertodetrinite, CE: clarite, TE:trimacerite, DE: Durite, Carbo-min: carbominerite) 138
Figure 5.8: Variation in inherent moisture, ash percent, volatile matter, fixed carbon and carbon. 141
Figure 5.9: Variation in major ash oxides 141
Figure 5.10: The comparison between percent carbonate (ultimate analysis) and the total CaO+MgO concentration renormalized back to the ash percent. 142
Figure 5.11: Correlation between total sulphur (ultimate) and Fe_2O_3 (corrected by ash percent) 143

Figure 5.12: A backscattered electron photomicrograph illustrating sclerotinite (oval), dark liptinite and mineral rich bands flanked by vitrinite rich bands. The included minerals are white. (scale bar represents 200 µm). 146
Figure 5.13: Inorganic elements in selected macerals. 147
Figure 5.14: Grain size distribution of individual minerals and total particle size distribution (all particles). 154
Figure 5.15: The average cumulative liberation yield (CLY) plots of the major minerals in the pulverised fuel. 155
Figure 6.1: Quartz variations in suction pyrometer fly ash. 163
Figure 6.2: Kaolinite variation in suction pyrometer fly ash. 163
Figure 6.3: Pyrite/Fe-oxide variation in the suction pyrometer fly ash. 164
Figure 6.4: Ca-oxide/carbonate variation in the suction pyrometer fly ash. 164
Figure 6.5: Average cumulative mass percent grain size distributions for the major minerals/phases in fly ash samples. 167
Figure 6.6: Cumulative liberation yield for the major phases in fly ash. 168
Figure 6.7: Comparative liberation characteristics of minerals in pulverised fuel and corresponding fly ash phases. 169
Figure 6.8: Calculated variation in slag probe surface temperature based on conduction heat flux equal to convection heat flux (Appendix D) – first method. 174
Figure 6.9: Calculated variations in slag probe surface temperature based on the slope method (Appendix D). 175
Figure 6.10: Correlation between slag probe surface temperature estimates ... 175
Figure 6.11: Measured furnace temperatures (thermopyle readings from side and front wall) as opposed to calculated slag probe surface temperatures. 177
Figure 6.12: Mass% difference in proportion of slag phases in slag deposits compared to proportion in fly ash. 180
Figure 6.13: Mass% difference in the proportion of fly ash phases in the slag probe “eyebrows/clinker” deposits, bottom ash, average slag deposits compared to the average suction pyrometer fly ash distribution. 182
Figure 7.1: The modelled (coalescence, partial coalescence and fragmentation) and measured (fly ash) particle size distribution of kaolinite fly ash particles. .. 187
Figure 7.2: The modelled (coalescence, partial coalescence and fragmentation) and measured (fly ash) particle size distribution of quartz fly ash particles. 187

Figure 7.3: The modelled (coalescence, partial coalescence and fragmentation) and measured (fly ash) particle size distribution of iron oxide/pyrite fly ash particles. 188
Figure 7.4: The modelled (coalescence, partial coalescence and fragmentation) and measured (fly ash) particle size distribution of Ca-oxide/carbonates fly ash particles. 189
Figure 7.5: Modelled fly ash particle size distribution (coalescence, partial coalescence and fragmentation) compared to the measured suction pyrometer (fly ash pyrometer) and cegrit (fly ash bulk) fly ash. 190
Figure 7.6: Mass% variation of kaolinite and quartz in DTF fly ash, entering the DTF (coal (#2 0.5m)) and probe fly ash for oxidising conditions. 195
Figure 7.7: Mass-% variation of kaolinite and quartz in DTF fly ash, entering the DTF (coal (#2 0.5m)) and probe fly ash under reducing conditions. 195
Figure 7.8: Variation of Ca-oxide/Carbonate in DTF fly ash under oxidising and reducing and conditions. 196
Figure 7.9: Variation of Fe-oxide/Pyrite in DTF fly ash under oxidising and reducing conditions. 197
Figure 7.10: Variation of kaolinite (carbonate,pyrite), kaolinite (carbonate) and kaolinite (pyrite) under oxidising conditions. 198
Figure 7.11: Variation of kaolinite(carbonate,pyrite), kaolinite(carbonate) and kaolinite (pyrite) under reducing conditions. 198
Figure 7.12: Backscattered electron image of fly ash in the +75 µm size fraction. Note the quartz grain (grey) middle left with spherical molten fly ash (white) attached onto the surface of the quartz grain. 210
Figure 7.13: Small spherical molten fly ash droplets (white) attached to large quartz grain (grey). 210
Figure 7.14 Detail of slag sleeve with kaolinite(carbonate), adhering onto slag sleeve and quartz grain attached onto the kaolinite(carbonate). (refer to figure 4.16 for phase identification, #1 0.5m, length of image is 430 µm) 213
Figure 7.15: A backscattered electron image of a clinker (“eyebrow”) deposit. Note the discrete solid quartz fly ash particle (light grey) at the base of the image. 214
Figure C.1. Water-cooled suction pyrometer and slag probe. 262
Figure C.2.: Slag probe. 263
Figure C.3. Suction pyrometer at hole 4. 9-264

Figure C.4: Slag probe attached to top of the suction pyrometer. Cooling water is supplied to the front end of slag probe. Boiler wall is on the left of the photograph. 265
Figure C.5: The slag probe without the removable slag sleeve. The tapered front end is evident. The aluminium tube supplying cooling water to the slag probe is in the foreground. The boiler wall is on the lefthand side. 265
Figure C.6: The backend of the suction pyrometer illustrating the air-ejector (black) attached to the fly ash sample receiver. 266
Figure C.7: Computer screen showing the temperatures at the start of a run. The high negative temperature is indicative of a faulty thermocouple. 267
Figure D.1.: Cross section through slag probe illustrating the different radius and temperature readings required for calculating the surface temperature of the probe (Ts). (Not drawn to scale) 268
Figure D.2.: Estimate the surface temperature of the probe by assuming linear heat transfer through the slag probe. 270
Figure G.1: Terms and concepts used in automated mineral analysis. 278
Figure G.2: Aluminium X-ray counts and elemental percent 282
Figure G.3: Silicon X-ray counts and elemental percent 282
Figure G.4: Calcium X-ray counts and elemental percent 283
Figure G.5: Iron X-ray counts and elemental percent 283
Figure G.6: Cumulative liberation plot 285
Figure J.1: Vitrinite reflectance variation 296

LIST OF TABLES

Table **Page**

Table 2.1: Common minerals found in the 4L (after Bühmann, 2001)..... 13
Table 2.2: Percent clay distribution of selected collieries (after Gaigher, 1980).. 15
Table 2.3: Polymorphs of SiO_2, major Raman band and stability range (after (Etchepare et al., 1978, Sharma et al., 1983)..... 30
Table 2.4: Characteristics Raman Shifts for Iron Oxides (units cm $^{-1}$) 31
Table 3.1:Transformation of calcite and dolomite..... 42
Table 3.2: Revised limits for slagging characteristics..... 77
Table 4.1: Elemental energy window range. 100
Table 4.2. Primary mineral groups used for pulverised fuel 108
Table 4.3: Preliminary classification groups of fly ash and slag deposits..... 111
Table 5.1: Sampling details and boiler operational conditions 130
Table 5.2 Malvern particle size results 134
Table 5.3: Carbominerite/microlithotype particle distribution (volume-%) in the +75 µm size fraction. (Inter:intermediate, Inertodet: inertodetrite)..... 138
Table 5.4: Carbominerite/microlithotype particle distribution (volume-%) in the -75 + 38 µm size fraction. (Inter:intermediate, Inertodet: inertodetrite)..... 139
Table 5.5: Average proximate, ultimate and ash elemental analysis 140
Table 5.6: Average and ideal elemental compositions of selected minerals. (N.D.: not detected). 145
Table 5.7: Average mass percent mineral and coal distribution per size fraction and for total sample. (Detailed data in Appendix L)..... 149
Table 5.8: Comparative elemental distributions 150
Table 5.9: The ideal elemental composition, total sulphur, carbonates ash percent and mass percent mineral abundance. (refer to text)..... 152
Table 5.10: Particle size distribution and percent passing 75 µm of individual minerals and all particles (PSD CCSEM). The particle size distribution derived from the physical screen analysis is also included (PSD screen, Figure 5.3) ... 154
Table 5.11: Liberation characteristics of major minerals expressed in terms of the “microlithotype” classification (refer to Appendix M)..... 156
Table 5.12: Mass-% total particle, coal and mineral distribution. 157
Table 5.13: Particle association characteristics in pulverised fuel..... 158

Table 6.1: Average mass percent fly ash phase proportions in the suction pyrometer fly ash samples and in the routine cegrit fly ash sample. 162
Table 6.2: Average mass-% grain size distribution for individual phases/minerals in fly ash. 167
Table 6.3: Liberation characteristics of major minerals/phases in fly ash expressed in terms of the “microlithotype” classification. 169
Table 6.4: Average association characteristics of minerals/phases in fly ash... 171
Table 6.5: Summary of comparative association classes between pulverised fuel and corresponding association classes in fly ash (details in Appendix P)..... 172
Table 6.6: Calculate surface temperatures of the slag probe at the boiler wall (0m). 176
Table 6.7: Mass percent fly ash phase distribution in slag probe slag deposit.. 179
Table 6.8: Mass percent phase proportions in “eyebrow/clinker” deposits and bottom ash. 181
Table 7.1: Average fly ash particle compositions compared to measured fly ash particle compositions. 192
Table 7.2: Total absolute mass% difference between modelled fly ash, DTF (oxidising and reducing), suction probe and cegrit fly ash. 199
Table 7.3: Average mass-% difference of each fly ash phase between modelled and DTF fly ash combusted under oxidising conditions. 200
Table 7.4: Average fly ash phase mass-% difference of DTF fly ash combusted under reducing conditions. 200
Table 7.5a: Modelled fly ash distribution based on combining the best fly ash formation process for each fly ash phase. Input coal is coal sampled at hole 2, depth of 0.5m. Oxidising conditions. 201
Table 7.5a: Modelled fly ash distribution based on combining the best fly ash formation process for each fly ash phase. Input coal is coal sampled at hole 2, depth of 0.5m. Reducing conditions. 202
Table 7.6: Modelled mass-% fly ash particle compositions compared to measured suction pyrometer fly ash particle compositions. 204
Table 7.7: Enrichment factors (relative to average probe fly ash proportions) of individual fly ash phases. 207
Table 7.8: Comparative average slagging parameters for the pulverised fuel (bulk) and fly ash (bulk). 215

Table 7.9 : Mass-% proportion of fly ash particles in the respective slagging parameter class and by size. Slagging parameters are T250 and Fe+Ca. (limits based on Juniper, 1995b) 216
Table 8.1: Mass-% fly ash distribution 226
Table A1: United States of America working groups (circa 1996) 258
Table A2: European Working Groups (circa 1996) 259
Table A3: Australian Working Groups (circa 1996) 259
Table A4: CCSEM configurations (circa 1996) 260
Table E.1. Maceral classifications (*bold, italics*) used in this study. 271
Table E.2: Microlithotypes classifications used in this study. 272
Table E.3. Carbominerite and minerite classification scheme 273
Table G.1. Typical fields of view dimensions, analytical point spacings and field of view area for different magnification settings. 280
Table G.2: Linear algorithms used to estimate elemental proportions from CCSEM elemental count proportions. Equation is in the form y=mx+c, where y is mass-% proportion of element and x the normalised CCSEM elemental counts 281
Table H.1: Factors for calculation of Density (after Huggins and Sun), in Fundamentals of Inorganic Glass. 286
Table I.1: Particle size distribution of pulverised fuel 288
Table I.2: Particle size distribution of fly ash 289
Table J.1: Volume-% maceral distribution of the +75 µm sized fraction 290
Table J.2: Volume-% maceral distribution in the -75+38 µm sized fraction 291
Table J.3: Volume-% microlithotype distribution of the +75 µm sized fraction .. 292
Table J.4: Volume-% microlithotypes distribution of the –75+38 µm sized fractions 293
Table J.5: Percent carbominerite/microlithotype particle type distribution in the +75 µm sized fraction. (Vit: vitrite, Int: Intermediate, SF: semifusinite/fusinite, IN:inertodetrinite, Free:minerite (>60% mineral matter). 294
Table J.6: Percent carbominerite/microlithotype particle type distribution in the -75+38 µm sized fraction. (Vit: vitrite, Int: Intermediate, SF: semifusinite/fusinite, IN:inertodetrinite, Free:minerite (>60% mineral matter). 295
Table K.1: Ultimate and proximate analysis 297
Table K.2: XRF Ash elemental analysis 298
Table L.1: Description of mineral groups 299

Table L.2: Calculate mass% mineral and coal distribution of the total pulverised fuel samples analysed. (The calculation is the individual size fractions mass% distributions weighted by the mass% screened size distribution)..... 300
Table L.3: Mass-% mineral and coal distribution in the +75 µm sized fraction of pulverised fuel. 301
Table L.4: Mass-% mineral and coal distribution in the -75 + 38 µm sized fraction of pulverised fuel. 302
Table L.5: Mass-% mineral and coal distribution in the -38 µm sized fraction of pulverised fuel. 303
Table M.1: Kaolinite mass-% liberation, cumulative liberation yield and cumulative liberation class by size fraction and weighted “total” across all size fractions. .. 305
Table M.2: Quartz mass-% liberation, cumulative liberation yield and cumulative liberation class by size fraction and weighted “total” across all size fractions. .. 306
Table M.3: Carbonate mass-% liberation, cumulative liberation yield and cumulative liberation class by size fraction and weighted “total” across all size fractions. 307
Table M.4: Pyrite mass-% liberation, cumulative liberation yield and cumulative liberation class by size fraction and weighted “total” across all size fractions. .. 308
Table M.5: Coal mass-% liberation, cumulative liberation yield and cumulative liberation class by size fraction and weighted “total” across all size fractions. .. 309
Table N.1 : Fly ash phase description 310
Table N.2: Calculate Mass-% mineral of the total fly ash samples analysed. (Calculation is the individual size fractions mass-% distributions weighted by the mass-% screened size distribution)..... 311
Table N.3: Calculate Mass-% mineral distribution in the +75 µm sized fraction of the fly ash samples analysed. 312
Table N.4: Calculate Mass-% mineral distribution in the –75+38 µm sized fraction of the fly ash samples analysed. 313
Table N.5: Calculate Mass-% mineral distribution in the –38 µm sized fraction of the fly ash samples analysed. 314
Table O.1: Ca-oxide/Ca-carbonate cumulative liberation yield and cumulative liberation class by size fraction and weighted “total” across all size fractions. .. 316
Table O.2: Kaolinite cumulative liberation yield and cumulative liberation class by size fraction and weighted “total” across all size fractions..... 317

Table O.3: Kaolinite(carbonate) cumulative liberation yield and cumulative liberation class by size fraction and weighted “total” across all size fractions. .. 318
Table O.4: Fe-oxide/pyrite cumulative liberation yield and cumulative liberation class by size fraction and weighted “total” across all size fractions..... 319
Table O.5: Quartz cumulative liberation yield and cumulative liberation class by size fraction and weighted “total” across all size fractions..... 320
Table O.6: Quartz>kaolinite mix cumulative liberation yield and cumulative liberation class by size fraction and weighted “total” across all size fractions. .. 321
Table O.7: Kaolinite(pyrite) cumulative liberation yield and cumulative liberation class by size fraction and weighted “total” across all size fractions..... 322
Table O.8: Char cumulative liberation yield and cumulative liberation class by size fraction and weighted “total” across all size fractions..... 323
Table P.1: Comparative association characteristics between pulverised fuel and fly ash. 324
Table Q.1: Mass-% phase distribution in the slag deposits for holes 1 and 2 ... 325
Table Q.2: Mass-% phase abundance in the slag deposits for holes 3 and 4... 326
Table R.1: Mass-% fly ash distribution – reducing conditions 327
Table R.2: Mass-% fly ash distribution – oxidising conditions 327
Table S.1: Absolute mass-% difference between fragmentation model prediction and DTF fly ash. 329
Table S.2: Absolute mass-% difference between partial coalescence model prediction and DTF fly ash. 330
Table S.3: Absolute mass-% difference between coalescence model prediction and DTF fly ash. 331
Table S.4: Absolute mass-% difference between model fly ash distribution, probe and cegrit fly ash 332

LIST OF SYMBOLS

Description	Symbol	Units
Area of phase a	A_a	m^2
Boltzmann constant ($1.38066X10^{-23}$ JK^{-1})	k	JK^{-1}
Composition of phase i	X_i	%
Density	ρ	g/cm^3
Density, size and viscosity distribution	$f_m(\rho,x,\eta)$	
Diameter of phase a	d_a	m
Drag coefficient	C_d	
Dynamic viscosity	η	Pa.s or Ns/m^2
Element i	E_i	
Element proportion of phase i	Ep_i	%
Entropy	S	JK^{-1}
Heat transfer coefficient	h	$W/(m^2.K)$
Kinematic viscosity	ν	m^2/s
Mass-% of mineral m	M_m	%
Megawatt electrical	MW_e	W
Megawatt thermal	MW_t	W
Micron	μ	m
Net mass fraction	f	
Nusselt number	Nud	
Power	W	W
Prandtl number	Pr	
Quantity of heat	Q	J
Radius	r	m
Reynolds number	Re	
Specific heat capacity	Cp	$J.kg^{-1}K^{-1}$
Specific volume	v	m^3/kg
Sticking probability at temperature and composition	$p(T,X_i)$	
Stokes number	Stk	
Surface tension	γ	N,m^{-1}
Temperature (degree celsius or Kelvin)	T	°C or K
Thermal conductivity of water	λ_{H2O}	$W.m^{-1}K^{-1}$
Thermal diffusivity	κ	m^2s^{-1}
Time	s	seconds
Velocity	U	m/s
Weight percent	Wt%	%

1 GENERAL INTRODUCTION

1.1 Slagging in Pulverised Fuel Boilers

In 2003, South Africa's major power utility (ESKOM) combusted 104.37 million tons of coal and generated 194 046 GWh (net) of electricity in coal-fired power stations. (source ESKOM's 2003 Annual Finacial Report). The coal is pulverised (±70% passing 75 μm) and combusted in pulverised fuel boilers (p.f. boilers) ranging in capacity from 200 MW_e to 713 MW_e.

Pulverised fuel boilers are principally a combustion chamber enclosed by vertical water bearing tubes. Pulverised fuel (coal), blown into the combustion chamber through the burners, combusts and heats the water in the vertical tubes. Steam produced from heating the water powers the turbines producing electricity. Ash, a by-product of combustion either accumulates onto the boiler tubes as slag or is collected by electrostatic precipitators (ESP) or bag filters, attached to the backend of the boiler.

On entering the boiler, mineral matter in the coal undergoes complex high temperature mineral transformations to produce ash of varying elemental compositions, morphological features (size and shape) and physical characteristics (viscosity and density). Flue gas, a by-product of coal combustion will transport these ash particles (fly ash) either to the inner surfaces (waterwalls, burners and superheater tubes) of the boiler or to the dust collecting facilities (electrostatic precipitators or bag filters) at the backend of the boiler. If the combustion chamber inner surface and/or the external surface of the fly ash particles are molten, the fly ash will adhere onto the inner surface and form an ash deposit (Figure 1).

Sintered ash deposits formed on surfaces directly exposed to flame radiation (i.e. combustion chamber) are known as slag whereas fouling is the accumulation of deposits in the cooler convective heat exchange region of the boiler. Slag deposits can form on ash hopper slopes, burners (eyebrows), boiler wall tubes, superheater tubes, and on the divisional walls (Figure 1).

The principal focus of this thesis is on slagging in pulverised fuel boilers and not on fouling. Slagging is a complex process and includes the mineral matter transformations, fly ash formation process and finally the deposition of ash onto heat transfer surfaces.

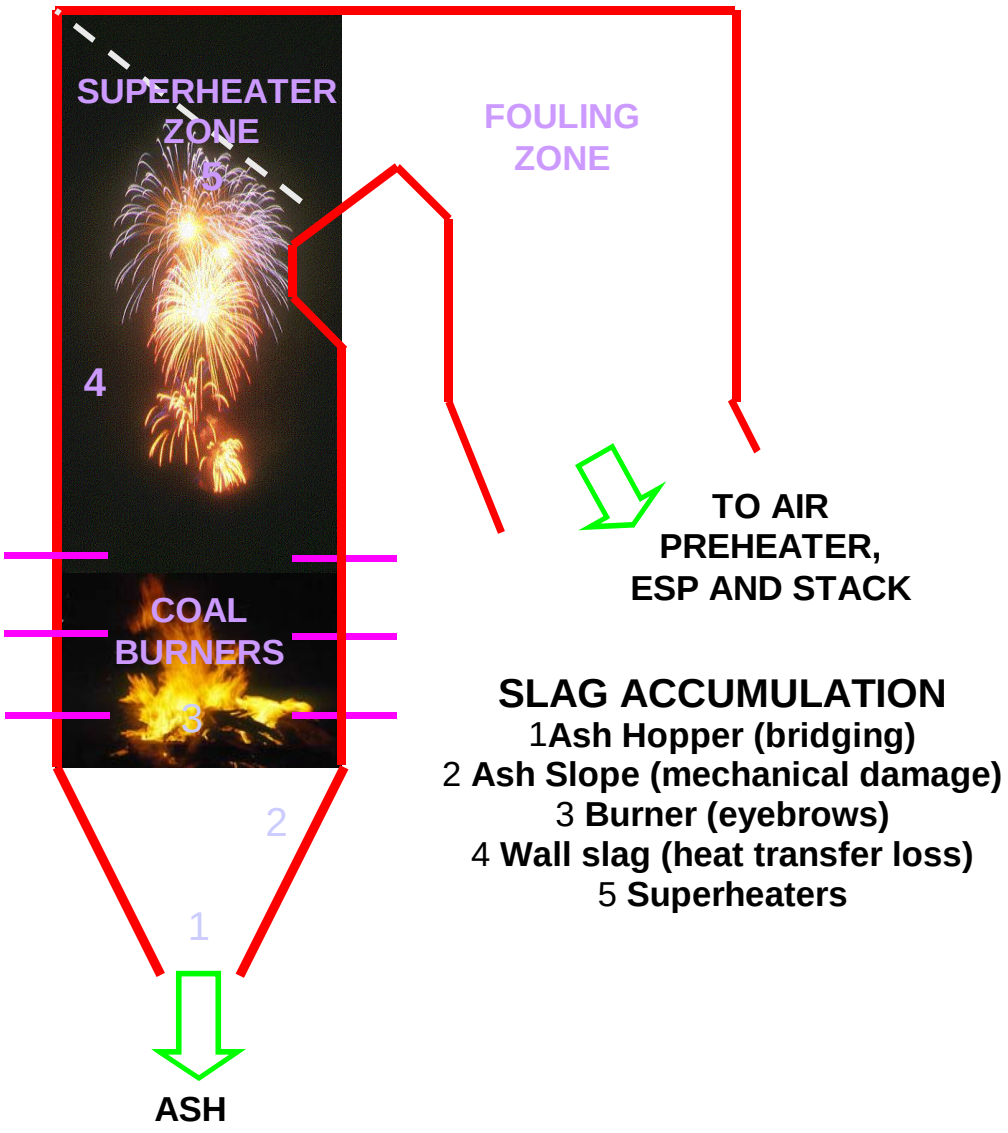

Figure 1.1: Typical p.f. boiler and location of typical slag deposits

1.2 Negative Impact of Slagging

According to Pohl (in Borio et al., 1997) ash related problems can cost the US power industry an estimated $9 billion per year. Slag deposits can detrimentally affect the thermal efficiency of the boiler and be the cause of costly unplanned outages. The negative impact of slag manifests itself in the following ways (refer to Figure 1):

- Slag absorbs heat reducing the amount of heat available for steam production. To make-up the heat shortfall, more coal is combusted.
- Slag radiates heat into the combustion chamber and increases the flue gas exit temperatures (FGET). High FGET is increase superheater deposition.
- Large ash deposits (clinkers) dislodged from the upper regions of a boiler can mechanically damage ash hopper slopes and cause bridging of the ash hoppers.
- Large clinkers can distorts boiler and superheater tubes resulting in premature tube failures and tube leaks.
- Slag deposits distort flue gas flow patterns, which can localise the erosion and attrition rate of boiler and superheater tubes.

A conservative estimate of the number of hours lost and cost due to slagging/clinkering for a five year period (1993-1997) at a ESKOM power station is 180 MWhrs at a cost R8.8 million (personal communication).

1.3 International and Current Research on Slagging

The International Energy Agency (IEA) Advisory Board has identified slagging as the most troublesome but least understood phenomenon in pulverised coal combustion (Ten Brink, 1990).

To address this universal problem extensive research on mineral matter transformations, fly ash formation and slag development using Northern Hemisphere *Carboniferous* coals has been undertaken. The models developed on these Northern Hemisphere coals have not been extensively tested using

South African *Permian* coals. Permian coal are an intimate mixture of inorganic/organic structures and have a lower proportion of reactive macerals compared to more banded Carboniferous coals (Skorupska and Couch, 1993). These differences are attributed to the colder palaeoclimatic conditions, differences in vegetation, mineral source rocks and highly varied and often turbulent and active depositional environments prevalent in the Southern Hemisphere during coal formation (Falcon, 1986) (Gibb et al., 1993). It is hypothesised that the mineral matter transformation, the fly ash formation and slag development models developed from this extensive research on Northern Hemisphere coals are not necessarily applicable to South African coals for these reasons.

Research on slagging in South Africa is limited and normally confined to resolving localised problems and does not universally examine the basic cause of slagging. Given the decreasing grades and qualities of coal predictied/estimated in future feedstocks destined for the boilers, ESKOM in 1997 identified the need to improve their fundamental understanding of mineral matter transformations; fly ash formation and slag development with South African coals. This became the principle reason for initiating the work in this thesis.

1.4 Objectives of the Thesis

Against this background the present research seeks to:

- Develop a technique to obtain samples of fly ash and slag deposits from within a fully operational boiler, while simultaneously obtaining representative samples of pulverised fuel for the purpose of establishing the relationship between these samples.
- Develop an analytical technique that automatically identifies and quantifies the mass proportion, the size and association characteristics of inorganic (minerals) and organic components (macerals) in coal, fly ash and slag deposits in order to examine the impact of one phase upon the other, and
- Develop fly ash formation and slag deposition models applicable to the *Permian* coals of South African and compare these models to published

models with which to understand, predict, diagnose anomalous slagging behaviour in power stations in the region.

Detailed quantification of the proportions, size and association characteristics of mineral matter in pulverised fuel will form the basis to which the proposed new fly ash formation model will be derived. This model assumes that each pulverised fuel particle analysed is an entity, which on combusting in a boiler, produces a fly ash particle or numerous fly ash particles of varying elemental composition and sizes. Depending on the nature of fly ash formation process (coalescence, partial coalescence and fragmentation) the fly ash particle(s) produced should have an elemental signature and size characteristics governed by the characteristics of the included mineral matter in the combusting pulverised fuel particle and of the excluded minerals. In this context a pulverised fuel particle is a particle greater than 1 μm in size and can have variable proportions of organic ("macerals") and inorganic (minerals) components. It is conceivable that the pulverised fuel particle could consist entirely of organic components or of inorganic components or of a mixture of organic and inorganic components.

Comparing the modelled based predictions of fly ash chemistry and size distributions to that encountered in actual fly ash sampled from a boiler will identify the fly ash formation process. The model will be validated by comparing these fly ash distributions to the distribution of fly ash obtained from combusting the test coal in a drop tube furnace under controlled conditions.

It is proposed that the same logical approach can be adopted for predicting slag deposition and slag development. Namely, by comparing the measured fly ash phase distribution relative to the phase distribution in slag, it should be possible to identify those characteristics of fly ash particles that are most likely to initiate and sustain slag deposition and development.

Although, in the current investigation the test coal is a South African pulverised fuel, it is anticipated that the model developed could be applied universally.

1.5 Methodology

To achieve the said objectives, a 6 m water-cooled suction pyrometer with a removable slag sleeve was used to obtain samples of fly ash and slag at different positions and depths within a 200 MW_e pulverised fuel boiler. Simultaneously, samples of pulverised fuel were obtained iso-kinetically by trained power station personnel.

Pulverised fuel was studied under an oil emulsion optical microscope to determine the variation in the organic components (macerals).

The pulverised fuel, fly ash and slag deposit samples were analysed by specifically developed analytical technique based on fuzzy logic and the recognised CCSEM (Coal Characterisation Scanning Electron Microscope) method. CCSEM data is the input data into the fly ash formation model.

The modelled fly ash elemental analysis and size distribution are compared to the measured fly ash distribution. The model simulates the combustion of individual coal particles and predicts the resultant elemental composition and size of the resultant fly ash. The elemental analysis, size and association characteristics of the minerals in the coal are used as the basis of the model. It is hypothesized that any variations or differences between the modelled fly ash distributions and the measured fly ash distributions is an indication of an alternative fly ash formation processes.

Combusting the test pulverised fuel in a drop tube furnace (DTF) under controlled stoichiometric conditions forms the control experiment. This serves to establish the impact that combusting conditions have on the elemental and size distributions of fly ash thus formed. In addition, comparison between the respective fly ashes will assist in validating the fly ash formation model and in identifying any fly ash formation mechanism that has not been previously described. The comparison provides an ideal opportunity to compare a “bench-scale” experiment to a large-scale fully functional boiler.

1.6 Outline of the Thesis

The thesis is divided into eight chapters. This chapter outlines the background, objectives and methodology of this study.

Chapter two is a literature review of the major working groups involved in slagging research, description of minerals in coal and various analytical techniques available to quantify minerals in coal and phases in fly ash and slag deposits. Some of the analytical techniques described in chapter two are used in the current research.

Chapter three is a literature review of the current research into mineral matter transformation, fly ash formation and slag development models. Included in chapter 3 is a brief outline of the slagging indices commonly used by the coal fraternity and industry.

Chapter four describes the methods applied to acquire the necessary samples, the development of the analytical technique to analyse the samples and the principals behind the ash formation and slag prediction model. The location of sampling points from within the boiler is indicated. A description of the water-cooled suction pyrometer and removable slag probe used to obtain fly ash samples and slag deposits from various positions from within unit 9 at Hendrina Power Station. Outline of the chemical analyses and reflected light oil-emulsion optical microscope methods used to characterise the coal is included in this chapter. The CCSEM technique specifically designed to automatically analyse the large number of samples, the unique sample preparation procedure and standard mineral identification libraries for coal, mineral matter in coal and phases in fly ash and slag deposits are described. Fly ash and slag deposit classification scheme is based on the elemental signature of the fly ash phases and the nomenclature of the fly ash based is based on the potential pulverised fuel mineral source. To validate the fly ash formation model, pulverised fuel obtained during the Hendrina Power Station sampling program was combusted under controlled conditions and at varying temperatures in a drop tube furnace (DTF). The physical characteristics of the drop tube furnace are described in chapter four.

Chapter five and chapter six outlines CCSEM and reflected light optical microscope results of the pulverised fuel, fly ash, slag deposits and DTF ash. For the pulverised fuel, the results include mass-% mineral matter distribution, organic-inorganic association characteristics and size distribution of mineral matter in coal. Data obtained from the pulverised fuel is used to model and predict the composition, size distribution and morphological characteristics of fly ash. For fly ash and slag deposit the CCSEM results include the mass-% distribution, association and size characteristics of minerals and amorphous glass. Boiler operation conditions and sampling details are included in this chapter.

Chapter seven outlines the modelled results and compares the predicted fly ash characteristics to the measured fly ash obtained from the power station and from the drop tube furnace. This comparison forms the basis of the thesis, as it will test the validatity of the model, identify new research areas and highlight any shortcomings or improvements to current internationally accepted fly ash formation and slag deposition models.

The conclusions and future research recommendations derived from this research are outlined in **chapter eight**.

Additional information and background details are included in the appendices.

2 LITERATURE REVIEW: COAL AND ASH

2.1 Principal Working Groups

The main working groups studying the impact of mineral matter in power stations are concentrated in Europe, United States of America and to a lesser extent Australia. A listing of these groups are summarised in Appendix A.

Although this list is not comprehensive, the Northern Hemisphere dominance is evident by the number of institutions in USA, Europe and the UK undertaking research in this matter. This highlights the importance of this topic and emphasizes the need to instigate research on Southern Hemisphere coals and more specifically on South African coals.

2.2 Macerals and Minerals in Coal

In its simplistic form, coal consists of organic (macerals) and inorganic components (mineral matter). As early as 1933, Moody and Langan recognized that the '….fusion characteristics of ash varied from one fraction to the other according to the distribution of mineral species and their juxtaposition with each other and the carbonaceous portion of coal….' (Bryers, 1991). Mineral matter in coal is heterogeneous in distribution, composition, association and habit. Pulverised coal consists of discrete coal particles (particles with no mineral matter present), mixed particles (particles with carbonaceous phases and mineral matter), and discrete mineral matter particles (Bryers,1991).

Macerals[1], the fossilised remnants of the original plant debris can be classified into the vitrinite, inertinite and liptinite groups. Rapid burial of the organic debris by sediments or through flooding by water inhibits the oxidation of the organic debris (woody tissue, bark, leaves, roots and twigs) and the formation of vitrinite. Original cellular structure of the organic debris is destroyed under these anaerobic conditions. Intertinite includes the oxidised remains of the original plant material and depending on the extent of tissue degradation the original cellular structures will still remain. Liptinite (formerly exinite) is made up of the

[1] Macerals: Microscopically recognizable organic constituents of coal analogous to the minerals of inorganic rocks, but differing from them in that macerals have no characteristic crystal form and not constant in chemical composition (defined in ISO 7404/2-1984 E)

remains of spores, cuticles, resins and polymerised waxes. Macerals are intimately associated with the mineral matter in coal

The minerals in coal occur in any of the five physical modes (Bryers, 1991):

- As fine disseminated mineral inclusion in macerals.
- In mineral-rich layers
- In nodules, including lenticular and spherical concretions
- In fissures including cleats and other fracture or void fillings; and,
- In the rock fragments derived from in-seam partings, hanging wall and footwall.

Minerals can be classified into different classes on the basis of their origin, time of emplacement and relative abundance. The terms *intrinsic* and *extrinsic* describe minerals in terms of their origin and how they were formed.

Intrinsic refers to minerals present in the original living plant tissue. These elements are trapped in the coal as discrete sub-micron mineral grains or as elements that are organically bound to the carboxyl group. Woody tissue derived from the Snuggedy Swamp in Southern Carolina, the Okefenokee Swamp on the Georgia-Florida border and from the Mississippi Delta revealed an average aluminium and silica concentration of 1.4-wt% and 7.1-wt%, respectively. XRD analysis of the low temperature ash (LTA) derived from the woody tissue indicated the presence of crystalline calcium oxalate (Renton, 1982). Bark and leaves had ash concentrations of 15-20 wt% (dry weight basis), which are significantly higher values than the 1-2 wt% of woody tissue.

Electron microprobe analyses of various telocollnite layers from a highly volatile bituminous coal (R_{max}(%) 0.68-0.99) in the Gunnedah Basin, indicate average contents of 0.05-0.45 wt% for Si, 0.04-0.22 wt% for Al and 0.01-0.02 wt% for Fe (Burba and Ward, 2000).

Extrinsic minerals are introduced into the coal either during peat accumulation or long after the coal has formed. Minerals are deposited during the accumulation of peat through fluvial action (detrital), the action of wind and through precipitation. These minerals are collectively termed *primary or syngenetic*. Once the coal has

formed, percolating waters deposit minerals into cavities, pores and fractures in the coal seams. These minerals are collectively termed *secondary or epigenetic*.

To confuse the issue further, minerals can be classified as *adventitious/excluded* or *inherent*. These terms refer to the mineral habit in a coal once it has been upgraded in a processing plant and in some case milled in a pulverised fuel power station. Liberated minerals which are not attached or included organic component are classified as *adventitious or excluded,* whereas mineral that are surrounded by or included in an organic matrix, are classified as *inherent* or *included*. Large *syngenetic* minerals deposited through fluvial action, *epigenetic* minerals found in cleats and fractures intersecting the coal seam and rock fragments derived from the floor, roof and in-seam partings rock layers are the main source of adventitious/excluded minerals.

As pulverised fuel is a processed product, the terms adventitious/excluded and included are used in this thesis to describe the association attributes of minerals in coal.

In terms of their relative abundance, minerals can be described as major, minor or trace minerals. Major minerals have concentrations levels >10 wt-%, minor concentration levels of 1-10 wt% and trace minerals occur in concentrations levels of <1 wt-%. These concentration levels are principally based on the detection levels of X-ray diffraction (XRD).

Bühmann (Bühmann, 2001), utlising X-ray diffraction has identified the minerals present in the 4L coal seam from the Witbank and Highveld Coalfields (see Table 2.1). These minerals are common coal minerals found in Southern Hemisphere and Northern Hemisphere coals.

Trace or accessory minerals, which are not listed in Table 2.1, but which occur in coal, include muscovite, glauconite, zircon, sphalerite, barite, galena, chalcopyrite, hematite, limonite/goethite, sphene and ilmenite (Finkelman, 1988) (Falcon and Snyman, 1986). Iron sulphates and hematite/limonite are typically the alteration products of pyrite.

In most coals, clay minerals (kaolinite/illite) and quartz are the dominant minerals with carbonates (calcite, dolomite), pyrite, feldspar (microcline) and apatite occurring in minor to trace levels.

Kaolinite is a common syngenetic mineral deposited in the cavities in fusinite, dispersed through vitrinite as fine included spherical and subspherical grains and filling the microfractures within the coal. In addition, kaolinite can occur as epigenetic mineral in cleats intersecting the coal seam. In contrast, illite is mainly found along bedding planes and rarely dispersed in the coal or deposited in the cavities in fusinite. Micrinite, a maceral of the inertinite group has been classified by the ICCP as a finely particulate mass with reflectance similar to fusinite and semi-fusinite. Based on SEM/EDS and TEM/EDS analyses, Faraj and Mackinnon (1993) has found that micrinite is not a maceral, but fine-grained kaolinite.

Quartz commonly occurs as syngentic sub rounded to rounded grains ranging in size from sub micron to larger sized grains. Quartz can be introduced into peat forming swamps by water and wind, and could be an intrinsic component of the plant material or is a by-product of the conversion of smectite-dominated clays into illite.

Ionic rich groundwaters percolating through already established coal seams deposit carbonates (calcite and dolomite) in stress fractures and cleats in the coal seam. This form of deposition is normally late-syngenetic or more commonly epigenetic. Precipitated carbonates can occur filling the cell cavities of fusinite.

“Raspberry” shaped pyrite framboids are spherical concretions of individual pyrite crystallites (0.1-2 μm in size) bonded in some cases by interstitial kaolinite. The pyrite framboids can reach sizes of 200 μm. Interstitial fine kaolinite is the bonding agent cementing the individual pyrite crystallites. Framboids commonly occur as clusters disseminated throughout the coal seam or they occur concentrated along bedding planes. It is thought that pyrite framboids were formed by the activity of micro-organisms (bacterial) or by colloidal deposition. Pyrite can occur as fine to coarsely dispersed euhedral pyrite grains or nodules in vitrinite and inertinite macerals. These euhedral grains or nodules can range in

size from 0.1 to hundreds of microns in size. Precipitated pyrite can occur filling the cell cavities of fusinite or in fractures, cleats and cracks in the organic matrix.

Table 2.1: Common minerals found in the 4L seam (after Bühmann, 2001)

Mineral Group	Mineral	Idealised Formula	Abundance
Clay minerals	Kaolinite	$Al_2Si_2O_5(OH)_4$	Major
	Muscovite Illite	$KAl_2(Si_3Al)O_{10}(OH)_2$ $K_{1-1.5}Al_4[Si_{7-6}Al_{1-1.5}O_{20}](OH)_4$	Trace
	Smectite	$(Na,Ca\cdot nH_2O)(Al_{2-\gamma}Mg_\gamma)(OH)_2(Si_{4x}Al_x)O_{10}$	Trace
Oxides	Quartz	SiO_2	Major
	Rutile Anatase	TiO_2	Trace
Carbonates	Calcite Aragonite	$CaCO_3$	Minor Trace
	Dolomite	$CaMg(CO_3)_2$	Minor
	Ankerite	$Ca(FeMg)CO_3$	Trace
	Siderite	$FeCO_3$	Trace
	Rhodochrosite	$MnCO_3$	Trace
Feldspars	Orthoclase Microcline	$KAlSi_3O_8$	Trace
	Plagioclase	$Na[AlSi_3O_8]$-$Ca[Al_2Si_2O_8]$	Trace
Scapolite	Analcime	$NaAlSi_2O_6\cdot H_2O$	Trace
Sulphides	Pyrite Marcasite	FeS_2	Minor Trace
Phosphates	Apatite	$Ca_5(PO_4)_3(F,Cl,OH)$	Minor
	Crandallite	$CaAl_3(PO_4)_2(OH)_5\cdot H_2O$	Trace
	Gorceixite	$BaAl_3(PO_4)_2(OH)_5.H_2O$	Trace
	Goyazite	$SrAl_3(PO_4)_2(OH)_5.H_2O$	Trace
Sulphates	Gypsum	$CaSO_4\cdot 2H_2O$	Trace
	Alunite	$KAl_3(SO_4)_2(OH)_6$	Trace
	Jarosite	$KFe_3(SO_4)_2(OH)_6$	Trace

The depositional environment can have a major influence on the type of minerals present. In an acidic fresh water depositional environment, kaolinite is the common clay mineral, whereas in an alkaline brackish or marine depositional environment, illite is the common clay mineral. The coals of the Natal coalfields, have higher illite concentrations than coals from Witbank, Highveld and Orange Free State coalfields (Snyman et al., 1983).

An acidic fresh water environment deficient in sulphate will favour the formation of siderite, whereas an alkaline, sulphate rich environment with sulphur reducing bacteria will favour the formation of pyrite and marcasite. Siderite is the common iron-bearing phase in coals from Australia, whereas pyrite is the common iron-bearing phase in South African coals.

Slaghuis et al. (1991) studied a series of 13 South African coals from the Waterberg coalfield, steam coals from the Eastern Transvaal (near Secunda) and coals from the Vereeniging/Sasolburg coalfield. Based on measurement of volatile matter, Slaghuis intimated that the volatile producing minerals are mainly associated with inertinite.

Snyman et al. (1983) pulverised (90% -75 μm) ten coals from the Witbank coalfield and washed them producing a float (<1.4 g/cm^3), and middlings (1.4 -2.0 g/cm^3) and sink (>2 g/cm^3) fractions. The proportion of macerals in the washed fractions and the distribution of inorganic element in the ash derived from the washed products were determined. Vitrinite, Al, K, Ti and P were enriched in the float fraction. Al and K enrichment can be attributed to illite associated with vitrinite, and it was found that Ti is organically bound and P is derived from apatite associated with vitrinite. Kaolinite and quartz were found to be intimately associated with inertodetrinite in the middlings fraction. The sink fraction was found to have the highest ash content and increased concentrations of iron and calcium. This suggests that extraneous pyrite and carbonates are concentrated in the sink fraction.

Gaigher (1980) used XRD to determined the mass-% mineral matter proportions, the clay distribution and the mineralogy of 35 commercial grade South African coals. Gaigher found that kaolinite is the dominant clay mineral in South African

coals. Gaigher estimated the average clay composition of South African coals to be 54.1% kaolinite, 29.2% illite and 16.7% expandable clays (mixed layered clays and smectite clays). The variation in the clay mineralogy for the different coal seams analysed by Gaigher is indicated in Table 2.2.

Table 2.2: Percent clay distribution of selected collieries (after Gaigher, 1980)

Colliery	Seam	Coalfield	Kaolinite	Illite	Expandable clays
Eikeboom	2	Witbank	87.9	3.6	8.5
Springbok	2	Springbok Flats	63.3	35.8	0.9
New Clydesdal	2	Witbank	64.2	29.1	6.1
Albion	2	Witbank	55.4	43.6	1.0
Delmas	2	Witbank	88.5	0.7	10.8
S.Witbank	4	Witbank	90.6	5.1	4.3
Anglo Power (Kriel)	4	Highveld	92.5	2.7	4.8
Blesbok	5	Witbank	52.4	22.4	25.2
Springbok	5	Springbok Flats	55.4	14.7	29.9
Greenside	5	Witbank	76.6	9.7	13.7
Navigation	5	Witbank	65.0	15.3	19.7

Gaigher noted that there was a strong association between clay minerals and inertinite and a negative association between clay minerals and vitrinite.

2.3 Analysing Coal and Fly Ash

A prerequisite for any research into fly ash formation and slag development is to analyse the pulverised fuel, fly ash and slag. Typical analyses include:

- the mass-% mineral proportion in pulverise fuel,
- the elemental composition of pulverised fuel ash and the fly ash from the boiler,

- the mineral or phase composition and distribution in pulverise fuel and fly ash,
- the morphological attributes (size, liberation and associations) of these minerals and phases in pulverised fuel and fly ash, and
- the high temperature mineral transformations that occur.

Renton (1982) described the three basic analytical methods for determining the amount of mineral matter in coal as high temperature ashing (HTA), low temperature ashing (LTA) and the optical microscope point count. The high temperature ashing (HTA) method involves heating the coal to 750 to 800 °C in an oxygen rich environment and determining the mass-% proportion of the residue ash. In low temperature ashing (LTA) the coal is slowly oxidised in oxygen plasma at temperatures of <120 °C after which the mass-% proportion of the residue ash is determined. The ash-% determined by HTA is not a true indication of the actual mass proportion of mineral matter in the coal as any mineral volatiles (H_2O in kaolinite, CO_2 in carbonates and S in pyrite) are lost to the atmosphere during the thermal decomposition of these minerals.

Since 1913, the oil emulsion reflected light optical microscope has been used to describe coal (Falcon and Snyman, 1986). Quantitative, rather than qualitative analysis of coal began to develop from the 1940's. Initial quantitative investigations were concentrated on quantifying the proportions of macerals and microlithotypes[2] and measuring the vitrinite reflectance[3]. Quantifying minerals proportions in coal by optical point count was not common practice, as it required a skilled operator, is labour intensive and is time consuming. The quantification of minerals in coal became routine with the introduction of scanning electron microscopes (SEM) and improved X-ray diffraction (XRD) techniques.

The advances made in analysing coal, fly ash and slag are described in the following section.

---

[2] **Microlithotype**: Natural occurring (see note 1) or association of one or more macerals with a minimum band width of 50 μm (as defined in ISO 7404/2-1984 (E))

[3] **Vitrinite Reflectance (RoV)**: Technique used to measure the intensity of reflected light from polished vitrinite surface. Used to determine the rank (maturity) of the coal.

2.3.1 Elemental analysis

Proximate (ash, volatiles, inherent moisture, and fixed carbon) and ultimate (carbon, hydrogen, carbonates, sulphur and oxygen) are routine analyses for coal. It is not common to determine the inorganic elements present in a coal sample, fly ash and slag. Typically, the main elements analysed are Si, Al, Fe, Ca, Mg, Na, K, P, Mn and S. These analyses are reported as oxides (SiO_2, Al_2O_3, Fe_2O_3, CaO, MgO, Na_2O, K_2O, TiO_2, P_2O_5, MnO and SO_3). These oxide analyses are extensively used to determine the slagging propensity of the coal, mineral composition and to predict the viscosity of the fly ash particles and of the slag deposits. Typical slagging prediction ratios are the acid/base ratio, slagging index, slagging factor, iron index and fouling index (refer to Appendix B). The analytical instruments used to determine the proportion of inorganic elements in ash are X-ray Fluorescence Spectroscopy (XRF), Atomic Adsorption Spectroscopy (AAS), Activation Analysis (AA), Optical Emission Spectroscopy (OES), Inductively Coupled Plasma (ICP) and Mass Spectroscopy (MS) (Vorres, 1984). AA and XRF are preferable to AAS, ICP and OES as no extensive pre-treatment of the coal is required.

Chemical fractionation is a wet chemical technique used to determine the proportion of soluble elements (NaCl), organically bound elements (to carboxyl group), acid soluble elements (carbonates) and elements associated with insoluble minerals (clays, quartz) (Zygarlicke et al., 1991). The three-stage technique involves:

1. Extracting in water to remove soluble salts (NaCl or elements associated with the groundwater).
2. Extraction in 1M-ammonium acetate (NH_4OAc) to remove elements such as Na, Ca, and Mg that may be organically bound to the carboxyl group of the organic component (macerals). A recent investigation by Matsuoka has indicated that ammonium acetate solution not only extracted ion-exchange calcium but also Ca leached from calcite (Matsuoka et al., 2002).
3. Extraction of acid soluble elements (e.g. Ca and Mg in carbonates) in 1M HCL.

The insoluble residue remaining after the three extraction processes consist of the insoluble clays, pyrite and quartz. Low-grade coals (lignites and sub-bituminous coals) generally have a higher proportion of carboxyl bounded elements than higher-grade coals (Benson et al.,1993). Baxter (1991) suggests that during the digenesis of bituminous coals, the carboxyl bound Ca and Mg form calcite and dolomite.

The valence state and the structural environment of iron in coal minerals, ash and the slag phases is an important indication of the stoichiometric combustion environment. A reducing environment may affect the oxidisation state of iron, which in turn could affect the rate that iron and aluminosilicate minerals interact (Helbe and Kang, 1993). ^{57}Fe Mossbauer spectroscopy and to a lesser extent Raman spectroscopy are considered the best methods for the quantitative analysis of the iron bearing phases in complex multiphase samples (Skorupska and Couch, 1993). Mossbauer has been extensively used to determine the iron distribution during studies of mineral matter transformations (Huffman et al., 1981 and 1993).

2.3.2 Maceral identification

The accepted technique for describing and quantifying the proportion of macerals (organic constituent) in coal is to use a reflected light optical microscope fitted with oil-immersion objectives (Falcon and Snyman,1986). A sample of coal is crushed to 100% passing 1mm and approximately 15g of the crushed material are mixed with epoxy resin and allowed to cure. The hardened epoxy resin mould is ground and polished, exposing a cross-section surface for examination. Drops of immersion oil are placed on the surface of the polished section thereby enhancing the reflectivity difference between the various macerals.

Three basic analyses are undertaken for a normal petrographic description of a coal sample. These are:

1. Maceral analysis – using an automatic point counter to advance the microscope stage by a fixed increment of 0.4 to 0.5mm the polished section is systematically scanned. The maceral intersecting the cross-hair in the objective lens is identified and recorded on the point counter. At

least 500 points are counted for each sample. At the end of the analysis the total number of points recorded for each maceral group (vitrinite, liptinite and inertinite) is divided by the total number of points counted (500) and the volume-% proportion for each maceral group is calculated.

2. Microlithotype analysis – the technique is similar to maceral analyses except that a 20-point graticule is used to define the area of interest instead of a cross hair. The magnification selected ensures that the area covered by the graticule is 50 x 50 μm. Similar to maceral analysis, the polished section is systematically scanned and the microlithotype identified and recorded. The microlithotype volume-% proportions are calculated and reported.
3. Rank/reflectance analysis – the intensity of light reflectance from the surface of vitrinite is measured and used to determine the coal rank (maturity).

2.3.3 Mineral quantification - CCSEM

A scanning electron microscope (SEM) fitted with a light element energy dispersive spectrometer (EDS) and a backscattered electron (BSE) detector can provide compositional and morphological information on individual mineral grains.

Since the early 1970s manually operated scanning electron microscopes were not extensively used in coal mineral research. This changed in the early 1970s with the combined introduction of the first commercial Noran SEM by Noran Instruments (formerly Tracor Northern) with a digital electron-beam control system and the development of the Particle and Recognition and Characterisation (PRC) software by U.S. Steel Research Laboratories (Galbreath et al., 1996). These advances enabled the unattended operation of the SEM to locate, identify and measure the morphological attributes of dispersed minerals in the coal.

The method of quantitative coal mineral analysis is referred to as SEM-based automatic image analysis (SEM-AIA) or more commonly as computer controlled or coal characterisation SEM (CCSEM). CCSEM has gained acceptance and is being used extensively in fuel science (Shah et al., 1991). It is considered to be

the single most significant commercially operated characterisation technique used to identify and quantify mineral occurrences, understand mineral transformation, fly ash formation, and slag development in boilers (Yang and Baxter, 1991).

The initial CCSEM routine developed by Lee (1978) and Huggins et al. (1982) includes two independent routines controlled by the PRC and coal mineral analysis (CMA) software. PRC software locates and measures the morphological features (area, size, perimeter and shape factors) of dispersed mineral grains in coal. The CMA software developed by U.S. Steel Research Laboratories (Nissen and Gruelich, 1987) positions the electron beam at the centre of the grain (as determined by PRC) and controls the EDS to acquire an X-ray spectrum. The elemental counts derived from the X-ray spectrum are used to identify the mineral or phase at the analytical point.

A typical CCSEM routine can be described as follows:

1. **PRC routine** – Fields of view are either randomly selected by the operator or alternatively a sequential grid is automatically generated by the CCSEM system. Under computer control, the stage positions the sample at the first field of view selected. A backscattered electron image with a typical resolution of 300 x 300 points per field of view is acquired. The backscattered electron image is a grey scale image reflecting the atomic weight variation of the minerals or phases in the field of view. For each point/pixel, the backscattered electron (BSE) intensity is compared to a pre-defined threshold value that distinguishes between the mineral and the background. For the PRC analysis, the background includes mounting medium (carnauba wax or epoxy resin) and the organic component (“macerals”). If the BSE intensity is above the threshold the image resolution is increased to 2048 x 2048 points per frame to improve the precision of the area measurements. Contiguous groups of points within a specified intensity range above the mineral/background threshold are identified. This contiguous group of points represent a mineral grain. Depending on the intensity range selected, the mineral grain could be a single mineral or a collection of minerals. The size, shape, area and position of the mineral grain are computed. The next mineral grain is

located in the field of view and the process is repeated. Analysis is terminated once a statistically significant number of mineral grains have been located and measured. To accommodate the wide size range, the same fields of view are normally measured at different magnification settings ranging from 50 to 500X.

2. **CMA routine** – Complex algorithms compute the centre of the mineral grain defined by the PRC routine. The electron beam is automatically positioned at the centre of the mineral grain and an X-ray spectrum is acquired. X-ray counts for 11 to 13 elements (Na, Mg, Al, Si, P, S, Cl, K, Ca, Ti, Fe, Ba and Cr), beam position and grain dimensions are computed and stored for off-line processing. X-ray counting times vary from two to five seconds per point. The Energy and Environment Research Centrer (EERC) at the University of North Dakota applies ZAF corrections to the elemental counts and determines the weight proportions of the elemental oxides (Steadman et al., 1991). In comparison, Imperial College uses the φ (ρz) correction procedure. A sorting routine classifies the stored X-ray spectrum into 29 composition categories. Classification is based on elemental proportions and elemental ratios. The CMA final output is the mass-% proportion of minerals in coal and the phases in fly ash or slag deposits.

The Combustion Research Facility at Sandia National Laboratories (Nissen and Gruelich, 1987, Yang and Baxter, 1991), University of Kentucky (Huffamn et al., 1991) and the Combustion Research Facility at Massachusetts Institute of Technology (Beer et al., 1991) employ CCSEM with the basic PRC and CMA routines.

Since 1970, the original CCSEM procedure has been modified and adapted by numerous laboratories and research institutions. These changes were introduced as new automated SEM, system configurations and upgrades were purchased.

EERC purchased the integrated Noran ADEM (automated digital electron microscope) system and developed the SEM point-count routine (SEMPC) and the windows based MINCLASS© mineral classification program (Folkedahl et al., 1993). The SEMPC routine does not position the electron beam at the centre of a

mineral grain but instead places a regular grid of points over the backscattered electron image. The electron beam is positioned at the first point and an X-ray spectrum is acquired for 8 seconds. If the X-ray count rate (counts per second) is below a pre-defined theshold, the electron beam is positioned at the next point. If the X-ray count rate is high, the electron beam remains in place and further X-rays are collected for a cumulative count of 25 seconds. The 25-second X-ray spectrum is processed by MINCLASS© software and classifies each point into mineral phase using a best-fit algorithm. Recent improvements to the MINCLASS software are the inclusion of carbon and oxygen and the inclusion of a preliminary classification scheme into seven broad chemical categories (oxide-rich, sulphur-rich, phosphorus-rich, carbon-rich, metal-rich, silicon-rich and "others"). The unknown X-ray spectrum is initially classified into one of the seven broad chemical categories and then classified into one of the minerals assigned to that initial chemical category. A total of 288 mineral compositions have been described.

If the sample is a fly ash or slag deposit, Imperial College acquires a backscattered electron image and locates the mineral/phase grains using image analysis routines. Only those mineral grains within a predefined size class (as defined by the magnification setting) are analysed. Instead of positioning the electron beam at the grain centre, the whole grain is scanned by the electron beam and a 20 second EDS spectrum is acquired for subsequent phase/mineral classification (Wigley and Williamson, 1991).

The University of Kentucky modified the original CCSEM procedure by lowering the "background" threshold level to include the organic ("macerals") component of a pulverised fuel. This means that the original "mineral grain" defined in the PRC routine includes the organic fraction and the inorganic minerals. An EDS spectrum was collected over a period of 15 seconds and used to classify the coal particle type (Huffman et al., 1991). A light element detector was used to classify the coal particles in terms of the proportion of C-Fe-S or C-(Fe+S)-(Al+Si). Based on this classification scheme the proportion of pyrite-maceral and clay-pyrite-maceral particles can be quantified.

The Advanced Combustion Engineering Research Center at Brigham Young University purchased the Oxford Analytical eXL-FQAI microanalysis system that includes a Quantitative Mineral Analysis (QMA) routine (Yu et al., 1993). QMA is analogous to PRC and CMA and simultaneously determines the morphological attributes and chemical composition of the minerals in coal. QMA uses images analysis routines to determine the position of mineral grains by processing backscattered electron images. An X-ray spectrum is collected for two seconds at the centre of each mineral grain. ZAF corrections are made and the background is subtracted from the X-ray spectrum. Mineral identification is based on oxide elemental composition and not on the elemental counts. Magnification settings of 100X and 400X are used.

The main components of any modern CCSEM system are a scanning electron microscope, a light element energy-dispersive X-ray detector and automated microanalysis system or image analysis software and custom written software for automatic mineral identification and data processing. The diversity of CCSEM systems is reflected in Table A4 (Appendix A), which lists the varying CCSEM configurations operated by various institutions (circa.1996).

Initial CCSEM investigations were limited to identifying and quantifying the morphological attributes of minerals in coal and not to describing inorganic-organic associations. Straszheim and Markuszewski (1990 and 1992) of Ames Laboratory employed two backscattered electron thresholds to distinguish between the organic fraction, the carnauba wax mounting medium and the minerals in coal. Particles of coal and mineral matter were described by using the LeMont Scientific "Line scan analysis" routine. Each frame was scanned at a 512 x 512 resolution (Straszheim and Markuszewski, 1991). Chords intersecting composite coal/mineral particles were identified as either coal or mineral. Specialised software "reassembled" the composite particles by combining the chords from adjacent scan lines. Minerals were identified from the X-ray spectrum acquired from each mineral in the composite particle. The X-ray counts for 21 elements were recorded and used to identify the mineral. The elements ranged from oxygen to zinc. The association characteristics of each composite particle were described by comparing the mineral identity at the end of each adjoining chord. By using this technique, the association characteristics,

morphological features and the mass-% mineral distribution in each composite particle analysed could be described (Straszheim and Markuszewski, 1990).

EERC developed the particle-by-particle scanning electron microscope programme (PBPSEM) to automatically measure the proportion of included and excluded minerals in coal (Steadman et al., 1991). The variation in backscattered electron intensity brightness between the coal, carnauba wax and the minerals can be used to distinguish between these phases. Since each phase is a collection of discrete pixels, of similar backscattered electron intensity the program is able compute the boundary, size and area proportion of each phase. Mineral associations for each phase with coal and with other minerals are computed. An X-ray spectrum is acquired and used to identify the minerals in composite particles.

The “Analysis of Mineral and Coal Associations” (AMCA) program was developed by Brigham Young University (Yu et al., 1993). AMCA uses the same principal as PBPSEM to distinguish between coal, the mounting medium and mineral matter. The area proportion of coal and/or the mineral for each particle as well as the particle size can be determined. These data are used to describe the liberation, association and morphological attributes of composite particles.

Imperial College utilises the BSE intensity to distinguish between the different phases. However, instead of identifying the minerals by acquiring an X-ray spectrum, it is assumed that all minerals have a density of 2.7 g/cm^3 and coal (macerals) has a density of 1.25 g/cm^{-3}. By multiplying the respective densities by the corresponding area-% proportion it was possible to calculate the weight-% of the organic fraction and mineral matter in each composite particle (Wigley et al., 1997). In some coals the BSE brightness of the macerals was similar to the mounting medium (iodofom-doped epoxy), which made it impossible to distinguish between the organic fraction (“macerals”) and the mounting medium in these coals.

Normally the sample is mounted in an embedding material such as carnauba wax (Straszheim et al., 1988) or iodinated epoxy resin (Gomez et al., 1984) to enhance the discrimination between coal, mineral matter and mounting material.

If carnauba wax is used, cerita wax should be added to prevent cracking (Yu et al., 1993). The University of Kentucky mounts fly ash and slag samples on 0.2 μm Nucleopore filters by filtering the sample through the Nucleopore filter. (Huffman et al., 1993).

QEM*SEM or QEMSCAN is an integrated system designed by CSIRO, Australia, and is analogous to CCSEM (Skorupska and Couch, 1993). QEM*SEM was originally designed to service the base and precious metal mining industry and not the coal industry.

Instead of determining the centroid (the typical CCSEM approach) of a bright phase and collecting a single x-ray spectrum at the centroid position, QEM*SEM places a raster of closely-spaced points over a particle and determines the mineralogy of the phase at each point (Gottlieb et al., 1991). Rapid analytical speeds are possible (16-20 micro-seconds) as the X-ray spectra from four detectors are combined.

Mineral identification is done on-line and is controlled by the species identification program (SIP). Elemental counts derived from the X-rays are compared to pre-defined mineral identification rules. Mineral identification is based on elemental proportions, elemental ratios and the type of elements present. Mineral identification rules are determined by acquiring standard X-ray spectra of the minerals in coal and the phases in fly ash. QEM*SEM has been successfully used to classify mineral matter in coal and fly ash (Creelman et al., 1993, Creelman and Ward, 1996, Gottlieb et al., 1991). Recently, the QEM*SCAN software has been modified to include the organic component of coal (Gottlieb, 2003).

A recent development has been the ASCAN system designed by Anglo American Research Laboratories in South Africa. The ASCAN system is based on the QEM*SEM method of positioning a grid of points over each particle as opposed to the classical centroid method (Van Alphen and Falcon, 2000). ASCAN, unlike QEM*SEM is not an integrated system and relies on a single energy dispersive detector. Mineral identification is done off-line and relies on the principles of fuzzy logic to identify minerals. Typical analytical times are 100 milliseconds per

point. A fully functional ASCAN system is operating at Technology Services International (TSI). The ASCAN software is able to calculate the mass-% mineral matter and the mass-% organic component in coal and the mass-% phases in fly ash and slag. ASCAN can quantify the liberation, association and morphological attributes of all components in pulverised fuel and fly ash.

The multitude of possible CCSEM configurations (Table A4), different analytical conditions and software approaches has resulted in some concern regarding the reliability and accuracy of CCSEM analyses. To address this problem an international round robin test involving six laboratories was undertaken in 1994 (Galbreath et al., 1996). The laboratories that participated were EERC (CCSEM), CSIRO (QEM*SEM), the R.J. Lee Group (CCSEM), the University of Kentucky (CCSEM), the Sandia National Labs (CCSEM) and the Netherlands Energy Research Foundation (CCSEM). Each laboratory determined the mineral abundance of calcite, kaolinite, pyrite and quartz for three North American coals. The results indicated that QEM*SEM reported the most precise results. Kaolinite showed the poorest reproducibility for all three coals. Kaolinite had the lowest BSE intensity of the minerals and typically occurs as fine disseminated grains included in a coal particle. These attributes make it difficult to accurately detect kaolinite and to quantify its morphological and association properties.

The University of Kentucky ascertained that elemental analysis from CCSEM data was within 20-40% of XRF and AA elemental analysis (Helbe et al., 1990). It was emphasised that CCSEM was generally accurate to within 20% for minerals greater than 5 mass% and that at least 1000 particles must be counted. Helbe proposed that CCSEM, being a semi-quantitative method, should be augmented with other analytical techniques. In comparison, Sandia National Laboratories (Baxter, 1990) reported a 12% coefficient of variation in compositional measurements for minerals greater than 5 mass%.

Huggins and co-workers (Huggins et al., 1980) in the recent round-robin comparative tests have reported the tendency of CCSEM to overestimate the proportion of pyrite. The over-estimation of pyrite as opposed to the underestimation of kaolinite can be attributed to the extremely high BSE intensity of pyrite relative to the other minerals in coal.

Baxter (1990) prepared a polished section with equal proportions of kaolinite and pyrite and analysed this polished section on the CCSEM. The mass-% proportions of pyrite and kaolinite were within 3% of each other. The importance of the SEM setup and sample preparation has been highlighted by Baxter (1990) and by Yang and Baxter (1991).

In a recent publication by Huggins (2002), CCSEM has been heralded as an advanced and the most promising analytical technique in coal science. In spite of CCSEM's positive aspects the main criticisms are:

- it is empirical
- it is expensive
- it requires a skilled operator and data analysis by experts
- more than one compound can be assigned to a particular classification scheme
- it does not identify organically bound alkali and alkaline-earth elements. (These elements form part of the organic structure and are normally bound to the carboxyl group).

2.3.4 Mineral identification – X-ray diffraction analysis

X-ray diffraction (XRD) is a long established technique for identifying minerals in coal (Gentzis et al., 1995) and the crystalline phases in fly ash (Oktay and Bayat, 1998) (Sakorafa et al., 1996) (Bellotto et al., 1990),in slag deposits (Koyama et al., 1996) (Unsworth et al., 1988) and in particulates in flue gas (Enders et al., 2000). Normally, minerals in coal are derived from a study of LTA or HTA ash sample obtained from the coal and not from analysing the coal directly. Owing to mineral transformation, the minerals in the ash are not necessarily representative of the minerals in the coal. Although this problem is not as prevalent in LTA, the time required to obtain a LTA sample is counter productive.

Analysing coal directly by XRD is problematical as the non-crystalline organic component produces an accentuated background, which could mask the peaks of selected minerals.

Since a high proportion of fly ash comprise of amorphous phases, XRD is unable to identify all the phases in fly ash. Traditionally, XRD is known for its limited ability to quantify the proportions of minerals in coal and the phases in fly ash (Ward et al., 2001). This is attributed to variation in mineral crystallinity, preferential crystal alignment, the differential absorption of X-rays by the minerals in a mixture and a detection level of 2-3 mass-%.

Prior to 1990, it was accepted that XRD is a semi-quantitative technique as the expected errors of determination are 10% or more (Renton, 1986). This was based on the Round Robin XRD analyses of a LTA ash submitted to 10 laboratories. Coefficients of variation for the individual minerals ranged from 24 to 36%. This is significantly higher than the CCSEM coefficient of variation of 12% for the same minerals (Baxter, 1990).

Numerous attempts have been made to improve the ability of XRD to accurately quantify the proportions of minerals in coal. These attempts have included mixing the powdered samples with a known quantity of a mineral (spiking) such as corundum (Al_2O_3) or fluorite (CaF_2). This has proven satisfactory for certain minerals such as quartz, calcite and pyrite, but not satisfactory for clay minerals (Ward and Taylor, 1996).

However, since the development of SIROQUANT software (Taylor, 1991), there has been an improvement in the ability of XRD to quantify the proportions of minerals in coal and the phases in fly ash. SIROQUANT, developed by CSIRO, Australia is a computer-based program, which uses the Rietveld technique (Rietveld, 1969) of deriving mineral abundance from the full XRD profile and not from the integrated intensities of the individual diffractogram peak.

SIROQUANT has been used to quantify the mineralogical differences between ash obtained from a power station and laboratory ash obtained from combusting a coal in a muffle furnace at 815 °C (Wall et al., 1999). Ward et al. (2001) has correlated seams in the Gloucester Basin, New South Wales using SIROQUANT to quantify the proportions of the minerals.

A comparative study of coals, fly ash and slag from four Australian power stations indicated that the QEM*SEM technique was by far the best and most extensive technique to describe the minerals in coal (Phong-Anant et al., 1992). The quantitative optical microscope examination of the coal samples tended to overestimate the proportion of the clay minerals and underestimate the proportion of quartz. This is attributed to the difficulty of resolving and identifying the mineral composition of included and fine minerals. The XRD analysis of the LTA ash was "rather disappointing" (Phong-Anant et al., 1992). The quantitative XRD analysis tended to overestimate the quartz content by a factor of two. The differences between laboratory results can be attributed to the difficulty in separating mineral diffractogram peaks and that these results are influenced by each operator's individual interpretation and calibration.

2.3.5 Mineral identification – other analytical techniques

McMillan (1984) and Bellotto et al. (1990) have used Raman spectroscopy to determine the structure of silicate glass melts and fly-ash particles, respectively. The vibration frequency of the SiO_4 tetrahedral depends on the polymerisation of the silicate network. The higher number of non-bridging oxygens (NBO) the lower the degree of polymerisation. The occurrence of aluminium, alkali and alkali-earth elements can increase the number of NBO's.

A silicate glass with a large number of NBO's is likely to be viscous (Mysen et al., 1980). The viscosity of fly-ash particles is an important parameter used in many slagging models to predict the slagging propensity of coal.

The spectrum obtained from each fly-ash particle is described in terms of four major bands occurring in the 1100-1050 cm^{-1}, 1000-950 cm^{-1}, 900 cm^{-1} and 850 cm^{-1} regions (Bellotto et al., 1990). These bands are attributed to symmetrical Si-O stretching in SiO_4 tetrahedral with respectively one, two, three and four non-bridging oxygen. As the silica content decreases so the four bands appear successfully in that order, with the 1100-1050 cm^{-1} band maximised in relative intensity for disilicates (Si_2O_5), the 1000-950 cm^{-1} for metasilicates (Si_2O_6), the 900 cm^{-1} for pyrosilicates (Si_2O_7) and the 850 cm^{-1} band for orthosilicates (SiO_4).

The occurrence of alkaline earth elements in the glass structure could influence the absolute positions of the bands in these regions.

In addition, bands can occur in the 400-700 cm^{-1} region These bands have been assigned to the motion of the oxygen atom along a line bisecting the T-O-T angle (where T = Al or Si) or are diagnostic of Si-O-Si linkages within the glass structure (Sharma et al., 1983). Depending on the structure of the glass the position of the 400-700 cm^{-1} band varies. Typically, the band is at 430 cm^{-1} for framework silicates (NBO=0), 520-600 cm^{-1} for disilicates (NBO=1), 590-650 cm^{-1} for metasilicates (NBO=2) and 700 cm^{-1} for pyrosilicates (NBO=3).

Vitreous glass (SiO_2) is characterised by weak bands at 1195 and 1060 cm^{-1} and a strong band at 430 $cm^{-1.}$ The bands at 1195 and 1060 cm^{-1} are due to an asymmetrical Si-O stretching vibration within a fully polymerised (0 NBO) 3D tetrahedral network. On the other hand the 430 cm^{-1} band is assigned to symmetric motion of the oxygen atom.

Tridymite and cristobalite are polymorphs of quartz (SiO_2) and can be found in fly ash. The stability of these polymorphs is a function of temperature. A summary of temperature stability and the position of the major Raman bands are given in Table 2.3:

Table 2.3: Polymorphs of SiO_2, major Raman band and stability range (after (Etchepare et al., 1978, Sharma et al., 1983)

Polymorph	Stability Temperature Range °C (Xie et al., 1994)	Major Band (cm^{-1}) (Huggins et al. 1981)
α - Quartz	0-573	464
β - Quartz	573-870	462
α - cristobalite	0-273	416
β - Cristobalite	1470-1713	777
α - Tridymite	0-117	407
β - Tridymite	870 - 1470	343

Bands at 358, 340 or 371 cm^{-1} are attributed to Ca-O stretching vibration, whereas the bands at 655 and 796 cm^{-1} to AlO_4 stretching vibration (Sharma et al., 1983) in glass.

Raman Spectroscopy is an alternative technique, which can determine the valency of iron in minerals. Table 2.4 indicates characteristic Raman shifts for iron oxides.

Table 2.4: Characteristics Raman Shifts for Iron Oxides (units cm^{-1})

Fe_2O_3	Fe_3O_4	$Fe(OH)_3$	α-FeOOH	γ-FeOOH
293	550	303	299	250
299	670	387	387	376
412		698	554	
613				

Source: Renishaw Raman System

Raman spectroscopy has been used to study the secondary products of pyrite oxidation. Fe-oxides, sulphate ion and partially oxidised sulphur intermediates were identified in-situ by means of Raman Spectroscopy.

Normative calculation is a theoretical method of determining the mineral distribution of a coal based on the chemical analysis. The calculated mineralogy differs from the actual mineralogy due to the many assumptions inherent in such calculations. Raask (1986) estimated the proportion of quartz, kaolinite and potassium aluminosilicates (illite and muscovite) from the SiO_2, Al_2O_3 and K_2O chemical assays.

SEDNORM is a normative method developed by Cohen and Ward (1991) estimate mineral proportions in sedimentary materials. Ward and Taylor (1996) have adapted SEDNORM to estimate the mineral proportions in coal. Mineral distribution of a selected coal based on SEDNORM is comparable to the mineral distribution based on SIROQUANT (Ward and Taylor, 1996).

In contrast to the above finding, Creelman and Ward (1996) compared the QEM*SEM derived mineral distributions, to the quantitative XRD analysis of the

corresponding LTA ash derived from the coal and the SEDNORM normative calculations of the coal. Mass-% differences between the quartz and Fe-bearing mineral proportions for the three analytical techniques were within acceptable analytical errors. In contrast, the differences in the reported mass-% proportion of clay minerals, calcite, dolomite and phosphate species was not within acceptable analytical errors.

2.4 Predicting Fly Ash Formation and Slagging

The analytical techniques used to quantify and qualify mineral matter in coal were described in the previous section. Most fly ash formation and slag deposition models are based on the analysis of samples derived from laboratory to plant scale experiments. This section reviews a number of bench scale, pilot scale and plant scale experiments and describes of the analytical techniques utilised by a number of researchers to predict slagging propensity. Bryers presented an excellent chronological review of ash deposition, mineral transformation and analytical techniques (Bryers, 1996).

2.4.1 Bench scale investigations

Short residence times (1-3 seconds), high heating rates (1000 K s^{-1}) and the impact of the organic fraction influence mineral matter transformations in a combusting coal particles. Any apparatus used to measure mineral transformations will need to simulate these conditions. Phase diagrams for many oxide and silicate systems were based on heating the respective mineral(s) in a platinum-wound vertical tube furnace and observing the phase changes. The furnace is heated slowly to the experimental temperature and maintained at that temperature for a predefined period. By dropping the molten charge into a cold-water bath preserves (quenches) minerals formed at the experimental temperatures (Mckie and Mckie, 1974). XRD and SEM/EDS are used to determine the mineralogy of these quenched charges.

Slow heating Thermogravimetric Analysers (TGA) or Differential Thermal Analysers (DTA) are used to model the mineral transformations in coal. Minerals selected from a LTA ash samples were placed on a hot stage and heated to certain temperatures (Bryers, 1991). The molten charges were quenched and analysed (Mitchell and Gluskoter, 1976). In 1976, Gluskoter obtained minerals selected from an LTA ash sample and heated these minerals on a hot stage. The

mineral transformations occurred at slow heating rates and there was some debate whether the reactions where thermodynamically or kinetically controlled. Stinestring, (in Bryers, 1991) repeated Gluskoter experiment with LTA ash in a combustor at higher heating rates. With the exception of pyrite, these two researchers agreed that the mineral reactions where thermodynamically controlled, whereas pyrite was kinetically controlled and thus pO_2 and time dependent.

Drop tube furnaces, (DTF) entrained flow reactors and particle jet smelting systems have been used to observe the decomposition of pyrite (Huffamn et al., 1989) (Srinivasachar et al., 1989, and 1990a) siderite (Mclennan et al., 2000) and illite (Srinivasachar et al., 1990b) in controlled environments. These systems are designed to simulate the residence times, range of temperatures and stoichiometric environments (oxidising or reducing) prevalent in pulverised fuel boilers (Abbott and Austin, 1986). The resultant fly ash was analysed using techniques such as CCSEM, ^{57}Fe Mossbauer (Srinivasachar and Boni, 1989) and Scanning Electron Microscopy (SEM). Thermal analysis - mass spectrometry (T.A.-m.s.) has been successfully used to study the reactions of coal and coal minerals under combustion related conditions (Burchill et al., 1990).

Zygarlicke (1990) used a laminar flow drop tube furnace to combust carefully sized coal fractions. The size distribution and nature of the resultant fly ash were characterised by CCSEM analysis and used to predict the fly ash formation process.

Unsworth (1987) used a high temperature XRD camera to obtain diffraction spectra from a sample heated in a vacuum. The LTA sample resting on a thin sheet of platinum foil wrapped around a resistively heated tantalum bar heated from 450 to 1500°C in steps of 200°C. The temperature was achieved in a few seconds and held at that level for 15 minutes before XRD analysis was started.

2.4.2 Pilot scale and plant scale investigations

Pilot scale combustion rigs have been extensively used to model and describe ash deposition (Walsh et al., 1990) (Fonesca et al., 1988) (Hanson and Abbott, 1997), fly ash erosion (Creelman et al., 1993), model fly ash composition (Baxter,

1991) and establish the impact of coal beneficiation has on slag deposition and fouling (Hurley et al.,1991). Ash deposits were collected by either inserting water-cooled slagging probes or ash deposition probes or by installing slagging panels.

The major problem with bench scale and pilot scale (0.15-1.76 MW_t) combustion rigs is whether or not the results obtained can be used to represent a full sized coal-fired boiler. Fonseca (1988) indicated that the confidence level of data obtained from bench scale (laboratory scale) tests were 40-90% representative of commercial scale, whereas for pilot scale the results are 70-98% representative. In comparison, the cost of running a bench scale is $10^{\wedge 4}$ times cheaper than tests on a full sized boiler.

Due to the prohibitive cost there have not been many full-scale sampling programs on commercial coal-fired power stations. During 1991 to 1994, extensive plant trails were undertaken at Ratcliffe Power Station (Gibb et al., 1993). This formed part of the UK research program involving seven collaborators and was instituted to investigate all aspects of slagging in pulverised fuel boilers. The collaborators included two fossil fuel utilities in the UK (PowerGen and National Power), their main coal supplier (British Coal), a major UK boiler manufacturer (Babcock Engineering), a sootblower manufacturer (Diamond Power Speciality) and two Universities (Imperial College and Bristol University). Extensive used was made of an air-cooled sampling probe to obtain samples of fly ash and slag from within the Ratcliffe boiler, a 60MW_t single burner rig to provide information on the in-flame particulate generation (Livingston and Gibb, 1993), a 150 kW ash deposition rig (Barnes et al., 1993), drop tube furnace to simulate deposition behaviour and CCSEM to quantify and qualify fly ashes, pulverised fuel and slag deposits.

Detailed ash deposition trails were undertaken on three power stations in Denmark (Laursen et al, 1998). The power stations selected were Ensted (600 MW_e), Funen (350 MW_e) and Vendsyssel (300 MW_e). Main objective of the investigation was to evaluate the influence of increasing steam temperatures; load and general operation has on the morphology and chemistry of ash deposits. An air-cooled probe was used to obtain samples in the convective regions of the boiler and a water/air-cooled probe was used to obtain samples in

the boiler. A ceramic probe was installed to simulate the deposits formed in boiler areas not influenced by cooling water in the boiler tubes.

ACIRL in collaboration with CSIRO undertook an extensive study aimed at improving the understanding of mineral matter transformation process in Australian bituminous coals in coal-fired boilers and the effects these minerals have on boiler operation and ash deposition. The study included sampling four Australian power stations and combusting a pulverised fuel at a pilot scale. The four power stations selected were Bayswater, Gladstone, Callide and Mica Creek. Samples of coal, fly ash and slag deposit were analysed using advanced analytical techniques including Fourier Transform Infrared (FTIR) microscopy, ^{27}Al and ^{29}Si Nuclear Magnetic Resonance (NMR) spectroscopy, scanning electron microscope with an electron probe for microanalysis (EPMA), X-ray diffraction (XRD) and QEM*SEM. Gladstone power station slag deposits were taken from the furnace wall region near the burner area. For the other power stations, the slags were sampled near the superheater region. Fly ash samples were supplied by the power stations.

Samples of coal were combusted in Australian Coal Technology Centre (ACTC) 0.15MW_t Boiler Simulation Furnace (BSF). Slag deposits were collected on water-cooled slag panels installed in the BSF.

Minerals in coal and phases in fly ash were quantified using XRD, QEM*SEM and optical microscopy. The ^{27}Al and ^{29}Si Nuclear Magnetic Resonance was used to determine the degree of structure disorder in fly ash.

2.5 Conclusion

Chemical compositions and morphological features of the fly ash formed during the combustion of coal is influence by the chemical and morphological characteristics of the minerals in coal. The analytical techniques used to identify and quantify the minerals in coal and their morphological features are highlighted in this chapter. These techniques are not exclusively used to describe minerals in coal, but also extended to include describing and quantifying minerals and phases in fly ash and slag deposits.

CCSEM (Coal Characterisation Scanning Electron Microscope) is probably the method used by the majority of coal scientists and engineers to quantify and identify minerals in coal and phases/minerals in fly ash and slag deposits. As will be seen from the next chapter, CCSEM data is used extensively as the principal input into slagging models and is used to verify the model predictions.

A current review of mineral matter transformations, fly ash formation, fly ash transportation, fly ash deposition and slag development are discussed in the following chapter. This is the final step in the complex process of slagging in pulverised fuel boilers.

3 LITERATURE REVIEW: FLY ASH FORMATION AND SLAGGING

In the previous section the various methods used to identify and characterise mineral matter in coal and fly ash have been described. In this chapter, the process of transforming minerals in coal and subsequent deposition of the resultant ash will be covered. **High temperature mineral transformation, fly ash formation, fly ash transportation and deposition** onto a heat transfer surface. In this context a heat transfer surface could be any surface within the boiler directly exposed to flame heat radiation.

3.1 High Temperature Mineral Matter Transformation

The individual mineral transformations have been well documented and recorded. Bryers (1986) published a schematic illustrating the mineral transformations of adventitious minerals in coal (Figure 3.1).

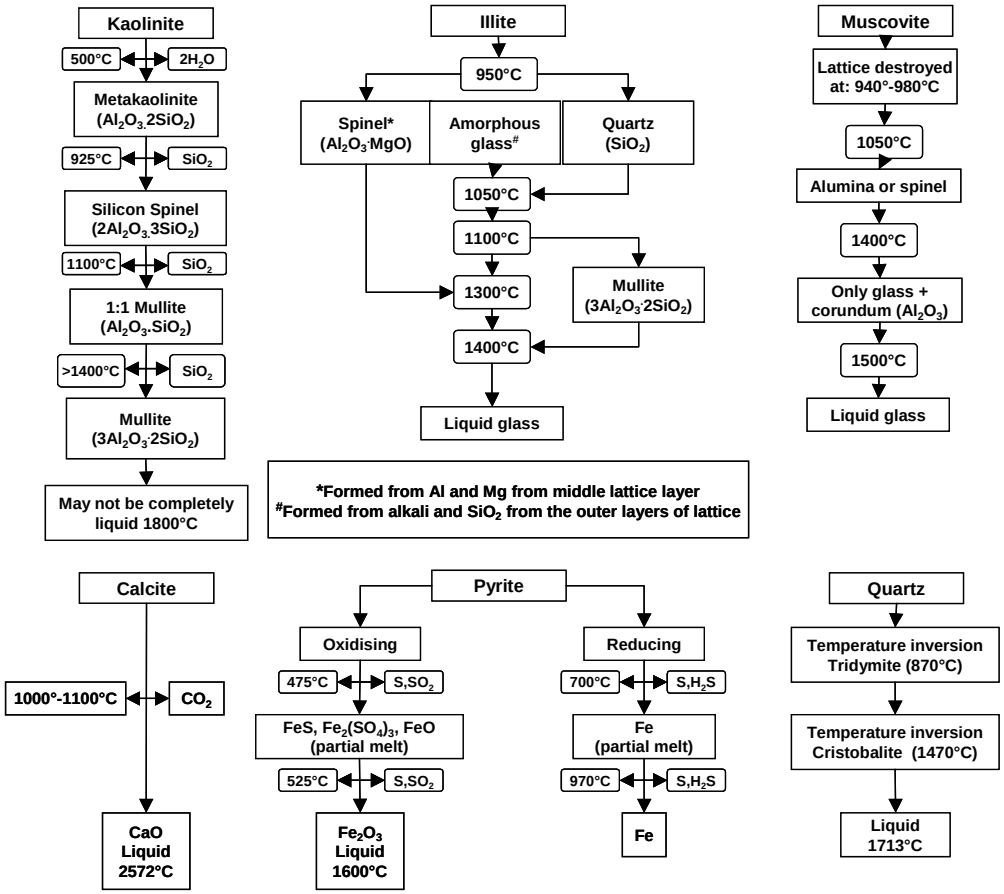

Figure 3.1: Mineral transformations in coal. (Adapted from Bryers (1986)). Mineral transformation of quartz based on data from Deer et al., (1966)

Iron bearing minerals have been known to play a significant role in initiating and sustaining the development of slag deposits (Srinivasachar and Boni, 1989). The major iron-bearing minerals found in coal are pyrite (FeS_2) and siderite ($FeCO_3$). Due to the importance of these minerals, extensive research into the transformation of pyrite (Shyu et al., 1981) (Gomesa et al., 1999) (Huffmann et al., 1989) (Enders et al., 2000) (Alekhnovich and Gladkov, 1989) (Ten Brink et al., 1991) and the transformation of siderite (Ten Brink et al., 1993) has been undertaken.

Shyu et al. (1981) heated pyrite particles of varying sizes in an oxygen environment at temperatures between 25 and 400 °C. Pyrite in the Illinois coal No.6 coal was oxidised to form iron sulphates ($FeSO_4$ and $Fe_2(SO_4)_3$) between 25-310 °C, to γ-Fe_2O_3 between 310-325 °C and to α-Fe_2O_3 between 325-400 °C. A maximum of 7% of mineral pyrite oxidised at 400°C as opposed to to 100% of pyrite in coal. Shyu et al. (1981) concluded that the oxidisation of included pyrite (in coal particles) differs from oxidation of excluded (mineral) pyrite.

In 1986, Stewart et al. (1986) simulated the decomposition of pyrite in a coal matrix by heating crushed coal containing pyrite in a tube furnace under argon. Constant temperatures of 410-645 °C were used. The chars produced were mounted and examined under the SEM and studied using ^{57}Fe Mössbauer. Results obtained indicated that the following reaction occurred:

$$FeS_2 + (1\text{-}x)H_2 = FeS_{(1-x)} + (1\text{-}x)H_2S$$

The presence of pyrrhotite, which started to form at 450 °C was confirmed by ^{57}Fe-Mössbauer. The concentration of S increased in the char matrix surrounding the decomposing pyrite. Stewart proposed that S in the coal matrix is due to the reaction of H_2S with the surrounding coal matrix and not due to the diffusion of S^{2-} through the matrix.

Srinivasachar and Boni (1989) proposed a kinetic model for the transformation of excluded pyrite. Published data (Huffman et al., 1989) on pyrite transformation was used to validate the kinetic model. The seven stage kinetic model is based on the observations of numerous researchers. These stages are:

- Stage 1 – Decomposition of excluded pyrite is between 770K (497°C) to 970K (697°C). For the model the average temperature is assumed to be 870K (597°C).
- Stage 2 – At an average temperature of 870 K (597°C) excluded pyrite transforms to pyrrhotite and gaseous sulphur (S_2). This reaction is endothermic. Any excess oxygen in the atmosphere surrounding the decomposing pyrite will react with S_2 to form SO. This reaction is exothermic and promotes the removal of S from the reacting boundary layer. Bryers proposed that SO_2 (Figure 3.1) is formed instead of SO. The decomposition rate of excluded pyrite is controlled by the rate of S removal and diffusion of oxygen through the boundary layer. Towards the end of pyrite decomposition, particle fragmentation is observed. Porous pyrrhotite particles are formed.
- Stage 3 – Porous pyrrhotite particles formed at the end of stage 2 are heated to the melting point of pyrrhotite (1356K (1083°C)). During the heating stage, oxygen can diffuse to the particle surface to form magnetite or wustite. The oxidation of pyrrhotite is exothermic and the particle temperature is expected to increase.
- Stage 4 - Pyrrhotite melts to form a liquid phase. Magnetite or wustite formed in the previous stage dissolves into the melt and forms a Fe-S-O (oxysulphide) molten droplet. The particle temperature is expected to remain constant during this stage.
- Stage 5 – Oxidation of the molten Fe-S-O droplet occurs until all the sulphur is removed. A Fe-oxide melt is the final product of this stage.
- Stage 6 – The molten Fe-oxide particle, produced in stage 5 is supercooled to 1600 K (1327°C) before onset of magnetite crystallisation. Huffman (1989), predicted that the onset of magnetite crystallisation will be at 1740K (1467°C).
- Stage 7 – The oxidation temperature of magnetite to form thermodynamically stable haematite depends on the ambient oxygen concentration. The temperature ranges from 1366K (1093°C) at 0.01% O_2 to 1597K (1324°C) at 5% O_2. The transformation of magnetite to hematite is kinetically slow.

Srinivasachar et al. (1990a) combusted pyrite in an entrained flow reactor and monitored the transformation by using ^{57}Fe Mössbauer spectroscopy and SEM/EDS to determine the composition and morphological attributes of the particles. Mössbauer and SEM/EDS identified the phases predicted in the kinetic model. The predicted transformation sequence of pyrite to pyrrhotite ($Fe_{0.877}S$), the formation of an oxysulphide (Fe-S-O) melt, the crystallisation of magnetite from the melt and the final oxidation of magnetite to form hematite were confirmed by particles analysed at different residence times. Experimental data indicate that magnetite crystallisation commences once 85% of the Fe-S-O melt becomes Fe-oxide. This is contrary to the original model assumption that magnetite crystallisation occurs once all the sulphide has been removed. Pyrite in the 53 to 63 μm fraction decomposed within 400 msec and in the 75 to 90 μm, within 575 ms.

Huffman et al. (1989) selected pyrite from Rosebud Coal and performed tests in a drop tube furnace at 1311–1727K (1083-1454°C) and residence times of 0.1-1.2 seconds. Magnetite was the dominant oxide phase present, while pyrrhotite was the dominant sulphide phase. Small amounts (<10 wt%) of hematite, wustite and remnant pyrite were common. In inert conditions and above 1460K (1187°C) Fe-S-O melt formed in the place of pyrrhotite.

Ten Brink et al. (1991) investigated the transformation of 60 μm pyrite particles in a bench scale laminar flow burner. Under reducing conditions pyrite was transformed to pyrrhotite and sulphur gas within 20 milliseconds (msec) and was molten after 30 msec. Under oxidising conditions, the transformation of pyrite to Fe-oxide occurred within 120 msec. This is significantly faster than the 400 msec measured by Srinivasachar et al. (1990a). Ten Brink attributed the difference to the higher combusting temperatures of 1450°C and the possibility of using pure pyrite instead of pyrite obtained from coal.

Ten Brink (1993) investigated the transformation of siderite ($FeCO_3$) in a laboratory burner at final temperature of 1400°C. In this study, CCSEM was used to characterise ‘siderite’ in the coal, thermogravimetric analysis (TGA) to identify mineral transformations and mass spectrometry (MS) to identify the amounts of CO and CO_2 formed. The proportion of ‘siderite’ in five coals was quantified by

CCSEM (based on the CMA method). The CMA method used in this research classifies any Fe-oxide phase as 'siderite' and is unable to distinguish between siderite, magnetite and iron hydrate. The Australian Hunter Valley coal, Belgian Behringen coal and the German Emil Mayrisch coal have, respectively 8, 60 and 60 mass-% siderite, whereas "siderite" in the Colombian El Cerrejon and the Eastern US Scotts Branch coals is actually magnetite and pyrite.

A small amount of the sample (35 mg) was heated in argon at a rate of 10 $K \cdot min^{-1}$ up to 1173K (900°C). Heating the siderite rich Emil Mayrisch coal produced a major TGA and an MS peak at 760K (487°C) and a minor peak at 970K (697°C). The peak at 760K can be attributed to the decomposition of siderite ($FeCO_3$) to form FeO and CO_2 and the peak at 970K (697°C) to the decomposition of calcite to form CaO and CO_2.

Srinivasachar (1990b) heated 53 to 75 μm illite particles mixed with char in an entrained flow reactor. The particle residence time and gas temperature of the entrained flow reactor were 2.5s and 1500K (1227°C), respectively. At 1400K (1127°C), illite loses its crystalline structure and completely melts to form a potassium aluminosilicate glass with varying proportions of ferrous and ferric iron. This reaction is endothermic and is associated with the loss of the hydroxyl groups. Under reducing conditions a higher proportion of the Fe will remain in the ferrous state. If illite is heated at slow heating rates to temperatures below its bulk melting point, surface concentrations of Fe, K, Ca and S are observed (Srinivasachar et al., 1990b). Under these conditions solid-state diffusion controls the concentration of these elements at the surface and causes the observed elemental segregation. Under combusting conditions (high temperatures and rapid heating rates), the illite particles become completely molten. This prevents solid-state diffusion and consequently homogenous compositions can be expected.

The transformation and subsequent sulphation of calcite and dolomite according to the reactions in Table 3.1 are well documented and described. The CaO formed reacts with sulphur dioxide SO_2 (g) to form calcium sulphate ($CaSO_4$).

The sulphation of CaO is an important process in the pulverised fuel boiler as it removes SO_2 from the flue gas and restricts the formation of sulphuric acid.

Table 3.1:Transformation of calcite and dolomite

Reaction
$CaCO_3 \Rightarrow CaO + CO_2(g)$
$CaMg(CO_3)_2 \Rightarrow CaO + MgO + 2CO_2(g)$
$CaO + SO_2 + 0.5O_2 \Rightarrow CaSO_4$
$CaOMgO + SO_2 + 0.5O_2 \Rightarrow CaSO_4 + MgO$

Bogwardt and Bruce (1986) calcined dispersed limestone particles in an entrained flow reactor at temperatures ranging from 516 to 1000°C. Particle size and temperature influenced the rate of calcite and dolomite transformation. At 850°C 52% of 10 μm was calcined and at 1000°C, 92% of 10 μm particle were calcined. In comparison, only 82% of a 50 μm particle was calcined at 1000°C. Calcium oxide (CaO), the by-product of calcite and dolomite transformation melts at 2572°C (Jak et al., 1998).

Figure 3.1 is a good indication of the transformations of kaolinite and quartz. Kaolinite ($Al_4Si_4O_{10}(OH)_8$) dehydration starts between 425°C and 525°C and is complete by 800°C. The final products of kaolinite transformation are mullite ($3Al_2O_3{\cdot}2SiO_2$) and cristobalite (SiO_2) with a silicon spinel ($2Al_2O_33SiO_2$) occurring as an intermediate phase (Unsworth et al., 1987b). Quartz, forms a number of polymorphs ranging from α-quartz (573°C), β-quartz (573°-870°C), β_2-tridymite (870°-1470°C) and β-cristobalite (1470 °-1713°C). β_2-tridymite melts at 1670°C, whereas β-cristobalite melts at temperatures greater than 1713°C. (Unsworth et al., 1987b). The final transformation products of kaolinite and quartz melt at temperatures exceeding the typical temperatures found in pulverised fuel boilers (1600-1650°C).

Briggs and Lindsay (1986) indicated that mineral associations affect the melting temperatures of minerals. In this study, individual minerals, pairs and triplets of clays, pyrite and calcite were mounted and heated in heating-stage crucibles. The mineral transformation of single minerals yielded the expected product, i.e.

pyrite to pyrrhotite, calcite to CaO and carbon dioxide and clay to silicate glass. In a triplet mount of either illite or montmorillonite with, pyrite and calcite, a liquid formed at the pyrite/calcite boundary at 600-650°C. When the clay mineral was kaolinite, the liquid formed at 750-760°C. Based on XRD analysis, the quenched liquid showed the presence of pyrrhotite, CaO and oldhamite (CaS). The presence of the clay mineral significantly lowered the reaction temperature between pyrite and calcite to 1140°C. Once the pyrite started to decompse the adjacent clay darkened. This is attributed to a breakdown in the clay structure to form silicate glass.

Huffman et al. (1981) selected a wide range of North American coals and heated the ash derived from them in reducing (60% CO/40% CO_2) and oxidising (air) atmospheres. The quenched ash samples obtained at different temperatures were examined by ^{57}Fe-Mossbauer, scanning electron microscope and XRD. Under reducing conditions, ash melting increased rapidly between 900-1100°C, saturating at temperatures above ≈1200°C. The presence of wustite (FeO), fayalite (Fe_2SiO_4), hercynite ($FeAl_2O_4$) and ferrous (Fe^{2+}) glass in the quenched ash point to the effect of iron has on the melting of ashes under reducing conditions. The occurrence of these Fe-bearing phases together with S in the form of Fe-sulphide and not CaS, suggests that the FeO-Al_2O_3-SiO_2 and FeO-FeS phase diagrams could be used to predict the melting characteristics of ash under reducing conditions.

It is well documented that ferrous iron (Fe^{2+}) is a fluxing element, which lowers the melting temperatures of clays and quartz (Bryers, 1991). Under oxidising conditions, the proportion of glass formed in ashes quenched from 1100° to 1200°C correlated to the mass-% proportion of illite in the original coal. Calcium and to a lesser extend iron became the important fluxing elements above 1200 °C. Calcium and iron accelerated melting between 1200-1400°C, approaching completion at 1500°C.

Compounds or elements that control thermal reactions and thus influence mineral transformations are termed mineralisers in the ceramics industry (Kuhnel and Eylands, 1991). In the review by Kühnel and Eylands (1991), mineralisers have been grouped into :

1. substances rich in volatiles such as water, fluorine, chlorine, boron and sulphur,
2. mobile elements such as lithium, magnesium, sodium, and calcium,
3. gases evolved through oxidation, e.g. carbon dioxide and sulphur dioxide,
4. organic complexes.

A boiler is an open system. Therefore it would not be possible to achieve general equilibrium for the system (i.e. boiler) as a whole. It is probable that only partial equilibrium could be achieved along the grain boundaries between two phases. Kühnel and Eylands (1991) have cautioned against the use of data obtained under ideal equilibrium condition in a closed system (eg. phase diagrams) to infer mineral transformations and reactions in an open system, such as a boiler.

Mineral transformation studies in the Northern States of America have been focused on the combustion of lignites and brown coals (Srinivasachar et al., 1990c) (Zygarlicke et al., 1990a). Apart from the normal variations in moisture, volatile matter (VM) and calorific value (CV), lignites and brown coals are characterised by carboxyl bounded alkali elements, namely potassium, sodium, calcium and magnesium. During combustion, these carboxyl bounded elements react with quartz and kaolinite to form Ca-silicates and Ca-aluminosilicate fly ash phases. Alternatively, a portion of these organically bound elements can vaporise and condense out in the cooler convective regions of the boiler or on the surfaces of glassy silicates (Srinivasachar et al., 1990c). Kühnel and Eylands (1991) have proposed that after combustion of the organic matter, the liberated organically bound elements are extremely reactive. In bituminous coal, K is mainly associated with illite, Ca with calcite, dolomite and feldspar, Na with feldspar and Mg with chlorites, micas and dolomite. In these forms, the elements are inert to vaporisation (Srinivasachar et al., 1990c).

Numerous mineral matter transformation models have been included in the commercially available software (Erickson et al., 1991). The following are a list:

- ATRAN - Ash transformation model
- MMT - Mineral Matter Transformation
- MIT - Mineral Transformation Code

- LEADER - Low-temperature algorithm for deposition risk
- FPI, ADLVIC - slagging advisor and fuel performance index
- PHOEBE - phase ordering and equilibrium evaluation.

ATRAN predicts the particle-size and composition distribution (PSCD) of mainly sub-bituminous and lignite combusted in tangentially fired pulverised fuel boilers and cyclone-fired boilers. The input into ATRAN is CCSEM data, ultimate, proximate and XRF ash elemental analysis. LEADER predicts the deposition of ash in the lower temperature convective pass region of the boiler.

3.2 Fly Ash Formation

The particle size distribution (psd), density and the elemental composition of fly ash particles are three of the many parameters controlling the slagging propensity of a coal feedstock. Particle size and density determine whether the fly ash particle will reach a heat transfer surface to initiate or sustain the development of a slag deposit. On the other hand the elemental composition and temperature directly influence the viscosity (“stickiness”) of the fly ash particle. If the impacting fly ash particle has a low viscosity it will readily adhere to the surface. Conversely, if the impacting fly ash particle has a high viscosity it will rebound off the surface and not play any role in slag development. If the receptive surface of the slag deposit is molten (low viscosity) then any fly ash particle irrespective of its viscosity will probably adhere onto the outer surface of the slag deposit. Other controlling parameters not related to the physical characteristics of the fly ash particle are temperature, localised combusting atmosphere (reducing or oxidising) and carrying capacity of the flue gas. Higher temperatures and a reducing atmosphere readily reduce the viscosity of the fly ash particle and indirectly promote subsequently slagging.

Owing to the influence that fly ash particle size, density and composition have on slagging, numerous phenomenological (Baxter, 1990 and 1991) (Straszheim and Markuszewski, 1992) (Mclennan et al., 2000a) (Liu et al., 2000) (Yan et al., 2001) and stochastic (Charon et al., 1990) (Loehden et al., 1989) (Zygarlicke et al., 1991) (Wilemski et al., 1992) (Barta et al., 1993) (Wilemski and Srinivasachar, 1993) (Seggiani et al., 2000) fly ash formation models have been developed to

predict these ash characteristics from the mineral size distributions, the mineral compositional variations and coal particle size distributions in a variety of coalfeed stocks. A number of these models use CCSEM and AIA to determine the compositional and size distributions of mineral inclusions in coal.

Field et al. (1967) predicted fly-ash particle size distributions (PSD) by assuming that as the char burns the outer surface shrinks and all the ash coalesces to form a single ash particle per char particle. Based on this assumption the size of the ash particle (d_a) was calculated by multiplying the char size (d_c) by the cubed root of the coal:ash density ratio, ρ_a/ρ_c and the ash mass (Ma):

$$d_a = d_c \left[\frac{\rho_a}{\rho_b} \right]^{1/3} Ma \qquad \textbf{3.1}$$

As part of the Fly Ash Generation Model (FLYASH.PAS, Loehden et al., (1989)) developed ‘coarse limit’, the ‘fine limit’ and the ‘partial coalescence’ models to predict fly ash particle size distribution. The ‘coarse limit’ model is based on the assumption proposed by Field that each char particle produces one fly ash particle (complete coalescence of all included minerals in a char particle). In contrast the ‘fine limit’ model assumes that for each mineral inclusion (ash) one fly ash particle is formed. The ‘partial coalescence’ model assumes that extensive char fragmentation occurs during the late stages of combustion (90% of burnout) releasing char fragments and restricting the degree of coalescence. The resultant fly ash particle size distribution (psd) probably lies somewhere between the particle size distribution of the ‘coarse’ and ‘fine’ limits. The concept of char fragmentation was initially used by Flagan (1977) to estimate particle size distributions of fly ash based on the particle size distribution of coal (Mollaha et al., 1999).

The degree of coalescence or lack thereof is partially controlled by the extent of char fragmentation and the proportion of high melting point mineral inclusions. Extensive char fragmentation and/or a high proportion of high melting point mineral inclusions that do not coalesce will favour the ‘fine limit’ (no coalescence) (Wilemski et al., 1992). Factors favouring char fragmentation are low ash content, high char porosity, large particle size and high particle temperature (Wilemski et

al., 1992) (Helbe et al., 1990) (Canadas et al., 1990). In contrast a high proportion of low melting point mineral inclusions and the absence of char fragmentation will favour the ‘coarse’ limit (full coalescence) model.

In their respective fly ash formation models Barta et al. (1993) and Willemski et al. (1992) have proposed different coalescence and char fragmentation mechanisms. Barta et al. (1993) assumes that as the char particle combusts mineral matter is transformed into molten spherical droplets on the receding surface of the char. Coalescence occurs when these molten particles migrate to the centre of the char (“volumetric coalescence”), or as a results of the reduction of the inter particle distance on the continually reducing outer surface of the burning char (“surface coalescence’’). Barta assumes that coalescence will cease once combustion reverts from surface burning to internal burning. When the oxygen diffusion into the centre is significant and the resistance to external diffusion and surface reaction is equal internal combustion will commence. It is assumed that the char particle size remains constant and that the minerals do not move. This will effectively stop the further coalescence of included minerals. At a critical porosity level the char particle will disintegrate and the size and chemical composition of the ash particle derived during the surface combustion stage will prevail. In contrast, Wilemski et al. (1993) assumes that char fragmentation is dependent on the formation of cenospheric chars. Wilemski postulates that during the pyrolysis and devolatilisation of coal particles many coal particles become plastic and form thin walled cenospheres on account of the high internal gas pressures. Wilemski assumed that most of the initial mineral matter is concentrated in or retained on the surface of the cenosphere. As combustion progresses, the cenosphere wall becomes thin and eventually ruptures producing localised areas of cenosphere shell separated by large pores. The development of these pores will promote lateral burning and the char matrix shrinks. If the mineral inclusions in the localised shell fragments are molten they will coalesce. Eventually the cenosphere shell will burn out completely or fragment releasing a number of fragments with either coalesced mineral inclusions or ash the size and composition of which are similar to the mineral inclusions in the original localised fragment. In a recent combustion trail of an Australian bituminous coal, Liu found that up to 40% of the char was cenospheres with a highly varied porous structure and a large central void (Liu et al., 2000). In the char fragmentation model

proposed by Baxter (Baxter, 1992), fragmentation is defined as the process, which produces more than a one-ash particle from a char particle.

In developing the fly ash formation models numerous researchers have used the CCSEM derived mineral association characteristics, mineral composition and mineral size distribution in coal as major inputs in the stochastic models. These models artificially construct coal particles by using statistical algorithms to randomly distribute the measured mineral matter compositions and sizes between different coal densities and size classes. This method is analogous to randomly placing balls of various sizes (mineral inclusions) into different sized buckets (artificial coal particles). Generating artificial coal particles is deemed necessary, as the traditional CCSEM data are only routinely available for a small number of particles and not for the large number of particles required. By applying the different fly ash formation processes (as described above) the artificial coal particles are mathematically transformed to produce a modelled fly ash size and composition distributions.

Charon et al. (1990) used the Monte Carlo methods to randomly distribute mineral inclusions into coal particles varying in size from 10 to 170 µm. Coal particles are classified into steps of 10 µm and the mineral inclusions are classified into six size classes ranging from 1 to 60 µm. These models include the five mineral classes defined by CCSEM. The modelled mineral proportion is equivalent to the mineral content of the coal and the modelled coal particle size distribution is equivalent to distribution determined by Malvern.

Barta et al. (1993) developed a probabilistic method (”urn model”) based on Poisson statistics to develop a joint size and chemical composition distribution model for mineral inclusions based on CCSEM data. The mass of each mineral class found in the narrow mineral particle size range is subdivided into equal sized small fractions and distributed randomly among coal particles of a narrow size range. Barta then used a “random coalescence model” to predict the fly ash size and composition distributions.

Willemski et al. (1992) adopted a composite approach using Poisson statistics to distribute mineral inclusions in the smaller coal particles range (<10 µm) and the

Monte Carlo method to distribute minerals in the larger coal particles. To save on computational time the smallest inclusions (<2 μm) were distributed in the larger coal particles on an average basis. Ash distributions were predicted assuming full coalescence, no coalescence or char fragmentation mode applicable to cenospheric chars (Wilemski and Srinivasachar, 1993).

In validating these models, moderate success was achieved in predicting the actual fly ash distributions and the compositional variations in the fly ash. Loehden et al. (1989) combusted a sub-bituminous Eagle Butte coal, which has a moderately high proportion of organically bound calcium. The computed fly ash particle and the composition distribution, assuming 'partial coalescence', were in good agreement with the measured fly ash distribution. Loehden attributes the lack of any coalescence to significant char fragmentation. Loehden concluded that the fly ash distribution is independent of the coal particle size distribution, but dependent on the mineral matter (inclusion) size distribution.

Barta (1993) obtained a good correlation between the predicted and measured SiO_2 content and size distribution of the fly ash for Wyoming lignite.

Wilemski et al. (1992, 1993) combusted Illinois (No.6), a washed Illinois (No.6), Kentucky (No.11), Upper Freeport, San Miguel Lignite and a Pocahontas bituminous coal in the PSIT drop tube furnace and compared the experimental fly ash distribution to the modelled distribution assuming full coalescence, no coalescence and char fragmentation model (based on cenospheric chars). Generally the full coalescence model gave acceptable results for Illinois (No.6), Kentucky (No.11) and Upper Freeport whereas the no coalescence limit predicted a finer ash distribution and failed to identify certain ash classes. The full coalescence model consistently over predicted the proportion of iron aluminosilicate in the Kentucky (No.11), Illinois (No.6) and Upper Freeport bituminous coals, indicating incomplete coalescence between pyrite and the aluminosilicate minerals (clay) forming non-homogenous fly ash particles. The proportion of calcium aluminosilicate was incorrectly predicted. Calcium aluminosilicates are formed as a result of the interaction of organically bound calcium with aluminosilicate minerals and not by the interaction of calcite (excluding fine calcite inclusions) within aluminosilicates. The full coalescence

model assumes homogeneous fly ash particles and since calcium is concentrated at the surface of the ash particles, the model is unable to predict the surface concentrations as measured by CCSEM. The full coalescence model showed good predictive capabilities for particles smaller than 15 microns, whereas limited coalescence is applicable for particles greater than 15 microns for the Kentucky (No.11), Illinois (No.6) and Upper Freeport bituminous coals.

An independent investigation by Helbe (1990) on Kentucky (No.11) and Illinois (No.6) bituminous coals confirmed that coalescence and mineral agglomeration were the dominant mechanisms of ash formation. In comparison, the char fragmentation model adequately predicted the ash particle size distribution obtained from the washed Illinois (No.6). Neither the full coalescence model nor the char fragmentation model adequately predicted the ash size distribution of the Pocahontas coal. The full coalescence model over predicted the proportion of fly ash in the two finest size classes and under predicted its proportion in the coarser size classes. For the Pocahontas coal the model was rerun assuming char fragmentation of cenospheric chars with a thick shell (as opposed to a thin shell). The agreement for the two finest size fractions and the coarser size fractions was acceptable. However, for the intermediate size ranges were either under- or over predicted. Discrepancies in the model can be attributed to the model assumptions, which do not necessarily reflect the conditions that actually prevail. These assumptions include the non-random distribution of mineral inclusions, the different macerals produce either cenospheres or solid char particles, the production of non-homogeneous fly ash particles through incomplete coalescence and more importantly the inability of the stochastic redistribution models to include the small (< 10 μm) particles as liberated mineral particles and not only as included mineral particles.

A CCSEM analysis of two eastern U.S. bituminous coals indicates that the mineral matter in the coal is not necessarily distributed randomly (Yu et al., 1993). Pyrite and calcite predominate as excluded minerals and are not associated with other minerals. This non-randomness of mineral matter affects the ability of the random distribution model to predict the size and compositional distributions of fly ash.

The shortcomings of the Wilemski model are considered in the recent model developed by Yan et al. (2002). Included and excluded minerals are treated separately and the influence that the char structure has on the fly ash size and compositional distributions is considered in the Yan Model. CCSEM derived included mineral size distributions and measured coal size distributions are used to randomly disperse the included minerals between the coal particles. The model assumes partial coalescence for included minerals and simulates fragmentation for excluded minerals. The partial coalescence of included minerals is related to the char structure and Poisson statistics are used to simulate the fragmentation of the included minerals. Model predictions compare favourably with the fly ash particle and size compositions of an Australian bituminous coal combusted in a drop tube furnace.

Alternative approaches to predict fly ash size and composition distributions are based on experimental observations and not on the statistical manipulation of the data. Numerous experiments have been undertaken on different coal feedstocks. Zygarlicke et al. (1991) of EERC has combined stochastic modelling and experimental observations in developing two fly ash formation models. The first model is a stochastic approach similar in concept to the random redistribution models, but includes a CCSEM analysis of the fly ash and uses mineral transformation knowledge obtained from previous investigations. To accommodate the influence of pyrite fragmentation, an iron-free stochastic model (excluding pyrite and any Fe-bearing phases) and a bulk mineral stochastic model were developed. The iron-free stochastic model assumed that liberated minerals do not interact and that included minerals coalesce randomly. The second model is a first order expert system (ASHPERT) comprising an empirical knowledge base (data base) and an interference engine based, on accumulated plant experience. The ASHPERT software essentially compares the measured coal with the large database and uses the comparison to predict fly ash composition and size. To validate the model, Kentucky (No.9) coal was combusted in a laminar drop tube furnace at gas temperatures of 1500°C, residence times of 3 seconds and an oxygen atmosphere of 21%. Deviations from the model can be attributed to fragmentation of large (>20 μm) pyrite grains, the coalescence of smaller iron oxide fly ash particles and the extensive coalescence of calcium and sodium-rich fly ash particles.

Numerous researchers have experimentally ascertained whether coalescence or fragmentation have occurred during the combustion of coal particles. This has been achieved by comparing the particles size distributions of mineral inclusion and/or coal particles with fly ash and by comparing the compositional variation of the fly ash to the minerals in coal. In a combustion study of four bituminous coals the distributions of potassium and iron in ash particles were determined by CCSEM (Helble et al., 1991a). The four coals analysed were Upper Freeport, Western Kentucky (No.9), Western Kentucky (No.11) and Illinois (No.6). Potassium is predominatly in the mineral illite, with 2300 ppm to 3500 ppm occurring as carboxyl bonded potassium. CCSEM analyses of the ash particles indicate that coalescence is the dominant ash forming process. The rapid melting of illite and its full coalescence with other inclusions within the carbon matrix was evident. By varying the combustion temperature (1500K and 1650 K) and oxygen concentration (7% and 21%) it was shown that there was no effect on the composition of quartz, illite and pyrite-derived fly ash particles. At higher temperatures, kaolinite showed an increased propensity to react with other minerals. The absence of a fluxing element in kaolinite, such as potassium (as in illite), means that the viscosity of the kaolinite will remain relatively high while the coalescence of kaolinite at lower temperatures will be less likely as opposed to illite. ^{57}Fe-Mössbauer indicates that the proportion of Fe in a glass phase varies from 16 to 35%, suggesting that some reactions do occur between pyrite and aluminosilicates (clays). CCSEM and Fe-Mossbauer data indicate that the majority of the iron occurs as discrete iron-oxide and not as included Fe-oxide (magnetite, hematite) in the glass. This was confirmed by a transmission electron microscopic (TEM) examination of the Illinois (No.6) ash that did not observe any discrete Fe-oxide particles in a silicate glass matrix. Further examination of the ash by SEM/EDX suggests that there is only as partial mixing/dissolution of the phases, which will also contribute to the low levels of iron-rich glass.

Srinivasachar and Boni (1989) indicated that included pyrite tends to coalesce with clay/silica minerals to produce an iron potassium aluminosilicate glass, whereas single excluded pyrite grains tend to fragment to form smaller hematite or magnetite particles.

Comparing the CCSEM derived mineral matter size distribution with the size distribution of the corresponding fly ash is a good technique for determining whether extensive fragmentation or coalescence has occurred.

Samples of Upper Freeport ash combusted in the EERC entrained flow reactor were obtained at regular residence time intervals (0.1s to 0.8s) (Zygarlicke et al., 1990b). Initially (after 0.1 s) there was a higher proportion of fine ash compared to the proportion of fine minerals in the coal. After 0.8 s, fly ash particles coarser than 3 μm followed the size distribution of the mineral matter in coal. The similarity between the mineral size distribution and the resultant ash is attributed to the combustion of the coal matrix liberating ash particles of the same size as the included minerals. This is analgous to the 'fine limit' model described by Loehden, with the exception that the small particles are not necessarily formed by extensive char fragmentation. These results contradict the results obtained by Wilemski et al. (1992) suggested that full coalescence is the major fly ash formation process in Upper Freeport coal.

The impact of calcium on the evolution of ash from low rank coals was examined (Helble et al., 1991b). The coals selected were Beulah lignite, Eagle Butte and Loy Yang. The Beulah lignite and Eagle Butte sub-bituminous coals are characterised by a high proportion of organically bound calcium. The reaction and coalescence of calcium with aluminosilicates is rapid. Ash samples are characterised by calcium oxide in the coarse fraction, and a high proportion of fine calcium-aluminosilicate particles in the finer sized fractions. Calcium oxide occurring in the coarse-sized fractions is unexpected as there is no evidence of calcium-bearing mineral (calcite) in these samples. The tendency for calcium-aluminosilicate to concentrate in the fine fractions and not in the coarse fractions suggests that the reaction between calcium and aluminosilicates is size-dependent.

Four Fe-rich coals were combusted in a drop tube furnace at set temperatures and under reducing and oxidising conditions (Mclennan et al., 2000b). The coal samples and the resultant ash produced were analysed by CCSEM, electron microprobe analyses of iron containing ash particles and Mossbauer analysis of the ash. The excluded kaolinite, quartz, and calcite were not affected by the

changes in combustion stoichiometries or the changes in temperature. Excluded pyrite decomposed to pyrrhotite and oxidised to form hematite under oxidising conditions but remained as iron oxysulphide melt under reducing conditions. Included pyrite underwent the same transformation as excluded pyrite, except that the rate of transformation was retarded by the combustion of coal particles. If the pyrite had been in contact with aluminosilicate then a composite iron sulphide/iron-glass ash particle is formed with Fe incorporated into the glass phases as the iron sulphide oxidises. Initially, the Fe will be Fe^{2+} and will eventually change to Fe^{3+}. Excluded siderite decomposes to form wustite and oxidises to form magnetite under oxidising condition. It remains as wustite under reducing conditions. Included siderite will follow the sample decomposition trend as excluded siderite, but like pyrite will be retarded by the combustion of the char. If siderite is in contact with aluminosilicate a iron-aluminosilicate glass will form.

Coalescence, partial coalescence and char fragmentation are the main fly ash formation mechanisms described above. The additional fly ash formation mechanisms described by Baxter (1992) are:

1. the vaporisation and recondensation of volatile inorganic elements such as potassium, sodium and the refractory elements calcium, magnesium, silicon and aluminium. Volatile aerosol fumes can recondense to form submicron (<0.6 μm) particles or condense onto fly ash particles or heat transfer surfaces.
2. the fragmentation of included minerals and excluded minerals on account of inorganic reactions.
3. the convective heat transfer of ash on account of rapid organic reactions
4. the shedding of ash particles from char particle surfaces.

The submicron aerosol particles could have an average size of 0.1 μm (Canadas et al., 1990). Typically, they account for less than 2 mass% of the inorganic fraction in bituminous coal (Quann et al., 1990) and less than 10 mass% in sub-bituminous coal and lignites. In contrast, Seapan and Van Lo (1990) estimates that up to 50-65% of the oxides common in coal will be a vaporous phase at the estimated flame temperature of 2000 K (1727 °C). This assumption is based on the vapour pressures of the common oxides found in coal. The fine (<1 μm) ash derived from Polish bituminous coals (Joutsensaari et al., 1993) had a distinct bi-

modal distribution with modes centred around 0.07 and 0.4 µm, respectively. Particles below 0.1 µm appeared to be agglomerations of ultrafine primary particles, whereas particles between 0.1-1 µm were spherical and probably formed by the nucleation of vaporised ash species. It is estimated that only 0.3 mass% of the total ash occurred in the sub-micron fractions and represented 5% of the total elements. In low-grade lignites and brown coals the sub-micron particles are derived from the carboxyl bounded sodium, potassium and calcium, which when released during combustion, react with sulphur dioxide to form sodium sulphate (Na_2SO_4), potassium sulphate (K_2SO_4) and calcium sulphate ($CaSO_4$). In bituminous coals, carboxyl bound sodium, calcium, and potassium is uncommon.

To quantify the composition and nature of sub-micron fumes eleven selected coals from lignites to bituminous coals were burned in a laboratory furnace (Quann et al., 1990). The percentage of fumes generated from the bituminous coals ranged from 0.6-1.7% and mainly consisted of SiO_2 (23-49%), FeO (21-45%) and Na_2O (7-21%). The reduction of included silicate (quartz and clays) minerals by carbon and carbon monoxide forms unstable silicon oxide (SiO) on cooling. The unstable silicon oxide (SiO) will oxidise to form silicon dioxide (SiO_2) and could condense on the surface of ash particles or boiler surfaces. Raask (1984) estimates that 0.01% of silica is volatilised in pulverised-coal fired boilers. The localised reducing conditions and higher temperatures favour the formation of silicon fume. It is for this reason that included silicates are more likely to produce silicon fume than extraneous quartz. Iron oxide in the fumes can be attributed to the fragmentation of extraneous pyrite, siderite and ankerite producing fume particles of 0.1 to 0.5 microns (Raask, 1984). Included pyrite associated with finely disseminated illite grains in a char matrix can promote the vaporisation of iron (Quann et al., 1990).

Raask has suggested that the sub-micron iron oxide particles formed from pyrite and iron carbonates can dissolve into silicate ash forming a reactive fluxing material. This will lower the viscosity of the resultant slag. The majority of the K in bituminous coals occurs as illite. Thermodynamic calculations indicate that potassium in this form is unlikely to vaporise (Helble et al., 1991a). To verify this,

a synthetic coal doped with illite crystals was burnt in a drop tube furnace at a gas temperature of 1650 K and with oxygen concentrations ranging from 20 to 80%. The particle combustion temperature was increased with an increase in oxygen concentration. Higher temperatures favour potassium fumes. At the practical combustion levels of 2% oxygen only 2% or less of the potassium vaporised. In experiments conducted on the four bituminous coals only three percent of potassium was present in the fume. It has been proposed that mobile sodium (carboxyl bounded) may displace potassium in the aluminosilicate matrix, thus providing a path for vaporisation.

Not only char, but also included and excluded minerals can fragment producing fly ash particles smaller than the original size of the mineral matter. Mineral fragmentation can be attributed to the release of sulphur dioxide during the dissociation of pyrite and carbon dioxide during the dissociation of calcite. Baxter (1990) concluded that included pyrite fragments into two to three fragments per original pyrite grain. The pyrrhotite/Fe-oxide fragments were 4-5 times smaller than the original pyrite grains. In the same study, included quartz was also observed to fragment. This can be attributed to incipient cleavage in quartz, microfractures and recrystallised quartz (chalcedony). In contrast, excluded quartz is known to pass through a boiler without fragmenting (Levendis et al., 1993) (Helble et al., 1990) (Mclennan et al., 2000b) (Yan et al., 2002).

Canadas et al. (1990) argued that the final particle temperature plays an important role in determining the final ash distribution. If the final particle combustion temperature is greater than the ash fusion temperature of included mineral matter, then it can be expected that the included minerals will coalescence. If the final combustion particle temperature is lower than the ash fusion temperature of the included minerals then coalescence of include minerals incomplete, and a considerable number of ash particles will be produced (partial coalescence). This could be extended to the nature of the macerals. Unsworth et al. (1987) suggested that mineral rich inertinite particles would burn at lower particle temperatures and would inhibit coalescence of the mineral matter in coal. In contrast, vitrinite rich coals would probably produce thin wall chars that would favour char fragmentation.

In addition to the formation of solid spherical ash droplets, ash envelopes may be created. They take the form of cenospheres or plerospheres (spherical particles within a cenosphere). Cenospheres are hollow spherical particles with an ash wall of variable thickness. Raask (1984) proposed that the formation of cenospheres is due to carbon monoxide gas formed within a slag particle. This gas is formed owing to the reaction of coke carbon with the slag. In ash with ferric oxide content less than 8% the production of cenospheres is negligible (Mollaha et al., 1999).

3.3 Fly Ash Transportation and Fly Ash Deposition

For a slag deposit to form, the ash produced from mineral matter transformation in the flame region must firstly be carried by the flue gases to a heat transfer surface and secondly have the appropriate physical properties to adhere to the heat transfer surface or be assimilated into the already existing slag deposit. In the context of this discussion, ash particles that are transported by flue gases are referred to as fly ash.

The crucial controlling parameters for slag deposition are fly ash particle size, fly ash density, ambient temperatures, carrying capacity of the flue gas, localised velocity variations of the flue gas and the surface viscosity of the ash particle and of the existing slag layer on the heat transfer surface.

In the previous sections the mineral matter transformations, ash forming mechanisms and physical characteristics (size, density, elemental composition and viscosity) of the ash were discussed. In this section, the mechanisms that control the **transportation** of the ash to a heat transfer surface and its subsequent **deposition** (if any) onto heat transfer surfaces will be outlined.

The main fly ash transport mechanisms are as follows (Loehden et al., 1989):

1. Inertial impaction – drag and inertial forces are the main forces acting on a particle approaching a heat transfer surface (e.g. a boiler tube). The inertial forces are proportional to the particle mass, whereas the drag forces are proportional to the projected surface area of the

particle (Beer et al., 1991). Small particles will follow the streamline around obstacles, whereas larger particles will transgress the streamlines and collide with the obstacle. The particle mass is a function of the particle density and the particle size, whereas the surface area is a function of the particle size. Inertial impaction is normally applicable for fly ash particles greater than 10 µm. In the majority of coals, the bulk of the ash deposits is due to inertial impaction.

2. Thermophoresis - this is a process of particle transport in a gas as a result of local temperature gradients (Baxter et al., 1991) (Baxter, 1997). The deposition of particles in the 0.001 to 10 micron size range is controlled by thermophoresis. These forces may be generated either by temperature gradients in the gas or within the particle itself. Thermophoretic deposition is a major deposition mechanism for submicron ash particles.
3. Condensation – condensation occurs when vapours in the flue gas are deposited on surfaces cooler than the local gas. Low rank subbituminous coals and lignite have a greater propensity for producing condensate than bituminous coals.
4. Chemical reaction – reactions occur between the gas and materials within the deposit and sometimes the surface on which the deposit has formed.
5. Eddy impaction – particles are more likely to be deposited on a surface by turbulent eddies than as a result of to inertia (inertial impaction).

Inertial impaction, thermophoresis and eddy impaction are the main mechanisms for the deposition of particulate material, whereas condensation and chemical reactions are the main mechanisms for vapour deposition.

Any model describing initial slag deposition through inertial impaction and subsequent growth must first consider the proportion of particles that will reach and impact with a surface, and secondly, the proportion of impacting particles which will adhere to the surface.

To ensure deposition of a fly ash particle on reaching a surface, the particle must first decelerate and then adhere to the surface (Wagoner and Yan, 1991). Factors that control the adhesion of the particle to a surface are particle viscosity, surface tension, velocity and the angle of impact. In addition, the chemical composition and the physical state of the surface upon which the deposition is occurring are important factors.

The viscosity of the particles was found to be a reasonable measure of the particles propensity to adhere to a surface. The viscosity of a fly ash particle is controlled by particle elemental composition, particle temperature history and localised combustion conditions. Being able to predict the viscosity of a particle at different temperatures is important for understanding and modelling the slagging propensity of a coal. The final step in the slagging process is the growth and development of the deposit.

Numerous models have been developed to predict the proportion of fly ash particles likely to collide with a surface, and the probability that the impacting particles will adhere the surface (Beer et al., 1991) (Baxter et al., 1991) (Walsh et al., 1990).

Walsh et al. (1990) developed a model for slag deposition through inertial impaction and growth based on the following premise of ash deposition. Fly ash particles colliding with a surface can vary from molten “sticky” particles to dry (highly viscous) particles. Initially, only the molten “sticky” particles will adhere to a clean boiler tube surface and depending on the surface temperature of the tube will solidify to form a slag deposit. It is conceivable that dry particles colliding with the surface will erode the slag deposit. This process is known as shedding. As the slag deposit grows, so the poor thermal properties of the slag deposit will result in an increase in the surface temperature. Higher temperatures will reduce the probability of the sticky particles from solidifying. These particles will remain molten on the surface. At this stage the growth rate will increase exponentially as dry ash particles will adhere to the “sticky” surface. Shedding at this stage of growth will not be through the erosion by incoming dry ash particles, but due to the weight of the slag deposit. Under favourable conditions, a state of equilibrium

will prevail whereby the rate of slag growth will be equal to the rate of mass loss on account of shedding.

The sticking probability of a particle is considered to be inversely proportional to the viscosity of a given particle mass and velocity (Walsh et al., 1990) (Nowok et al., 1991b). In defining the sticking probability of an ash particle, Walsh et al. (1990) compared the viscosity of the incoming ash particle to a reference viscosity (η_{ref}). The sticking probability [*p*(T,Xi)] of a given particle at temperature (T) and composition (X_i) is defined as:

$$p(T, X_i) = \left(\frac{\eta_{ref}}{\eta} \right) \quad \eta > \eta_{ref} \quad \text{or} \quad p(T, X_i) = 1 \quad \eta \leq \eta_{ref} \qquad \textbf{3.2}$$

In this model Walsh assumes that a particle with a viscosity of 80 poise is perfectly sticky and will be the reference viscosity (η_{ref}). Any particle with a viscosity less or equivalent to 80 poise will adhere to a surface and any particle with a viscosity greater than 80 poise will have a variable probability of either adhering to the surface or bouncing off the surface.

Walsh argues that the mass fraction of impacting particles that will adhere to a surface is a function of three scenarios:

1. An incoming sticky particle collides with a sticky particle on a “dry” slag deposit surface. The rate of mass accumulation is a function of the impacting particle flux and the mass fraction of the “sticky” particles
2. Incoming particles collide with a sticky slag deposit surface. The rate of mass accumulation is proportional to particle flux and the surface area proportion of the slag deposit which is “sticky”
3. Non-sticky dry particles collide with a dry surface and remove portions of the slag deposit by erosion. The rate of mass removal (shedding) is proportional to the incoming particle flux, the proportion of dry colliding particles and the surface proportion of dry slag.

The resultant quadratic equation includes the probability of particles sticking to a surface either as a result of the first or second scenario described above. The

equation makes provision for the mass-loss due to erosion (scenario 3). The basic form of the equation is as follows:

$$f_{dep} = p(T_g) + [1 - p(T_g)\,p_{sur}(T_s) - k_e[1 - p(T_g)][1 - p_{sur}(T_s)] \qquad \textbf{3.3}$$

Beer et al. (1991) derived the impaction efficiency as the proportion of particles colliding with a cylindrical tube. This function is based on the Stokes number (Stk), Reynolds number (Re), and drag coefficient (C_d). The non-Stokesian behaviour of larger particles is corrected for by applying the Israel and Rosner correction factor (ψ). The impaction efficiency model is based on a computer program written by Loehden (in Beer et al., 1991). The derivation of this model is summarised as follows:

Impact Efficiency (ξ_{imp}):

$$\xi_{imp} = \left[1 - \frac{1.25}{Stk_{eft} - 0.125} - \frac{0.014}{(Stk_{eft} - 0.125)^2} - \frac{0.508 * 10^{-4}}{(Stk_{eft} - 0.125)^3}\right]^{-1}$$

$$where:\ Stk_{eft} = \psi Stk \quad and \quad \psi = \frac{24}{\mathrm{Re}_p} \int_0^{\mathrm{Re}_p} \frac{d\,\mathrm{Re}_p}{C_d(\mathrm{Re}_p)\mathrm{Re}_p} \quad and\ C_d = \frac{24}{\mathrm{Re}_p}\left(1 + \frac{1}{6}\mathrm{Re}^{2/3}\right)$$

where Stokes (Stk):

$$Stk = \frac{\rho d_p U}{9 \mu_g d_t}$$

*where Reynolds Number (*Re*):*

$$\mathrm{Re} = \frac{U d_t \rho_g}{\mu_g}$$

where drag coefficint (C_d): **3.4**

$$C_d = 24/\mathrm{Re}(1 + 1/6\,\mathrm{Re}^{2/3})$$

Beer included the 'sticking coefficient' in the deposition model to describe the proportion of impacting particles that will adhere to the surface. A critical viscosity is defined. Ash particles with a viscosity lower than the critical viscosity will adhere to the surface and above the critical viscosity will bounce off the surface.

The ‘sticking coefficient’ is an integral function of the mean impaction efficiency and the critical viscosity value:

$$E(S) = \int_{0}^{\eta_{crit}} \int_{0}^{\infty} \int_{0}^{\infty} \xi_{IMP}(\rho, x) x f_{m(\rho,x,\eta)} dx d\rho d\eta \qquad \textbf{3.5}$$

In Baxters model (Baxter et al., 1991), the rate of inertial impact is defined as the product of the total mass flux of the particles (q_i) in the flow, and the proportion of these particles (impaction efficiency, η_i), which actually strike the surface. The general form of the equation is as follows:

$$Ii(Stk) = q_i \eta_i (Stk) \qquad \textbf{3.6}$$

Baxter has included a modification to the above equation for particles striking a flat wall. Capture efficiency is defined as the ratio of the number of particles adhering to the surface to the number of particles colliding with the surface. This is similar to the sticking efficiency as defined by Beer. The relation is empirically derived and is a function of the particle residence time in a boiler and of time since the last sootblowing cycle.

Kalmanovitch (1991a, 1991b, 1993) and Ten Brink et al. (1991) have extended the use of the CaO-FeO-Al_2O_3-SiO_2 phase diagrams, combining with chemical data obtained from CCSEM and SEMPC analyses to predict the composition of the phase (CCSEM data) and its viscosity changes with temperature (phase diagrams). The eutectic point temperature for each fly ash particle is determined by using the SEMPC elemental distribution and the CaO-FeO-Al_2O_3-SiO_2 phase diagrams (Kalmanovitch, 1993). The particle-by-particle eutectic point temperature distribution can be used to predict the proportion of low viscosity (‘sticky’) fly ash particles at different temperatures. This can be used to establish the slagging propensity of a coal at different temperatures.

In all the models described above, fly ash particle viscosity is a crucial component for defining the sticking probability of an impacting fly ash particle. Estimating the viscosity of slag could be based on configurational entropy

models, Arrhenian models or by formulating relationships based on experimental data (Nowok et al., 1991b).

Adams and Gibbs (in Nowok, 1991a, 1991b and Richet, 1984) determined viscosity based on configurational entropy (S_{conf}). The basic form of the equation is:

$$\eta_{conf} = A\exp\left(\frac{B}{TS_{conf}}\right) \quad (T \text{ in } K) \qquad \textbf{3.7}$$

where A is a pre-exponential factor and B is a constant accommodating the free energy barrier. The equation is similar to one by Arrhenius. In the Arrhenius equation B is replaced by activation energy E and S_{conf} by the Boltzmann constant k.

The commonly used phenomenological equations are the Urbain model (Urbain et al., 1982), the Watt and Fereday model (Watt and Fereday, 1969) and the Hoy, Roberts and Wilkins model (Hoy et al., 1965).

The Urbain model is:

$$\ln(\eta) = \ln(A) + \ln(T) + \left(\frac{B}{kT}\right) \qquad \textbf{3.8}$$

where A and B are a function of ash elemental compositions.

The Watt and Fereday equation is:

$$\log\ \eta\ = \frac{10^{\,7}\,B}{(T\ -150\ )^{2}} + F \qquad \textbf{3.9}$$

where B and F are based on the composition of the particles. The Hoy Roberts and Wilkins method is:

$$\log_{10}\eta = 4.468\left(\frac{SP}{100}\right)^2 + 1.265\left(\frac{10^4}{T}\right) - 7.44$$

$$SP = \left(\frac{100xSiO_2}{SiO_2 + Fe_2O_3 + CaO + MgO}\right) \qquad \textbf{3.10}$$

At higher temperatures molten slag is a Newtonian liquid and the predicted viscosities using the Urbain and Watt/Fereday model can be calculated. At these high temperatures the log viscosity temperature plot displays a linear trend. At a certain temperature during cooling the liquid becomes non-Newtonian and the predicted viscosities are invariable lower than experimentally measured viscosity. This results in a deviation from the linear trend. The temperature at which there is a deviation is often referred to as the temperature of critical viscosity (Nowok and Benson, 1991a). The deviation can be attributed to changes in the structure of the molten slag induced by crystallisation and the formation of a multiphase system.

Vorres et al. (1984) prepared 21 synthetic ash slags from reagent chemicals. The viscosities of these slags were measured at regular intervals at temperatures ranging from 1300°C to 1550°C. For the majority of the ashes the deviation from the linear trend occurred between 1300-1400°C. This temperature range also coincides with the eutectic temperatures of the major equilibrium phase diagrams describing these compositions.

The crystallisation of a solid from an homogeneous melt will alter the composition of the residual liquid, which will change the viscosity of the liquid (Kalmanovitch and Williamson, 1986). As a phase is crystallised from a homogeneous melt, either from within a deposit or from within the fly ash particle itself, the residual melt will be depleted in the elements that comprise the crystallising phase. The degree of crystallisation, which is measured in terms of the proportion of crystallised phases, has an impact on the viscosity of the liquid phase. In general, if mullite and anorthite start crystallising, then there will be a relative increase in the silica content of the residual melt, which will result in an increase in the viscosity of the residual melt. Alternatively, if gehlenite crystallises, the viscosity

of the liquid will initially decreases, but as crystallisation progresses, the viscosity will increase again (Ten Brink et al., 1991).

To accommodate the observed effect of viscosity changes, Nowok et al. (1991b) developed a correction factor for both the Arrhenius and configurational entropy models. The base/acid ratio is extensively used in these correction factors. Hurst et al. (1999a, 199b) and Kondratiev and Jak (2001) used a modified Urbain model to predict the viscosity of slag in the Al_2O_3-CaO-'FeO'-SiO_2 system. These modifications accommodate the impact that crystallisation has on the viscosity of slags.

Stanmore and Budd (1996) suggested that a fly ash particle in the viscosity range 10^5 to 10^7 Pa s (0.1-10 Mpa s) would probably adhere to a surface. Any particle with a viscosity greater than 10^7 Pa s would probably bounce off the surface. If the particle viscosity were less than 10^5 Pa s would have sufficient liquidity to adhere and flow across the surface. In the glass industry the working range is between the working point of 10^3 Pa s and the softening point of $10^{6.65}$ Pa s. This is similar to the viscosity range proposed by Stanmore and Budd.

Richards et al. (1991) studied the effect of composition; variations in the size and physical properties of fly ash particles on the deposition and development of slag deposits. Two western coals (Dietz and Utah Blind Canyon) were used as test coals. The results indicate that for small particles the capture efficiency reached 1 at 1000K for the Dietz fly ash, but only reached 1 at 1050K for Utah Blind Canyon. For the coarser particles, the capture efficiency did not reach 1 even with the gradual increase in temperature. This has been attributed to coarse quartz particles, which are crystalline and non-sticky. The difference in capture efficiency between coal types can be attributed to the lower average viscosity of the Dietz ash. It was also noted that both the impaction efficiency and the sticking efficiency increased as the deposit thickness increased over time. This is in accordance with Wibberley and Wall (Wibberley and Wall, 1982), who suggested that quartz particle capture is enhanced by the reaction of sodium with quartz to form a thin molten layer (0.1 micron) on the surface of the quartz grains. This molten layer is sufficient to promote the capture of a quartz grain on the deposit surface.

The composition and morphology of the slag deposit surface layer is important for the adhesion of fly ash particles. A ‘sticky’ fly ash particle can adhere to a solid slag deposit surface and a solid fly ash particle can adhere to a sticky slag deposit surface. Ten Brink et al. (1991) noted that under reducing conditions, molten pyrrhotite particles arriving at the surface of the probe did not adhere as expected. Ten Brink attributed this to the unburnt carbon on the surface of the deposit, which will effectively reduce the ‘stickiness’ of the deposit, hence restricting capture. In the same experiment, steel plates were used as deposit probes. On cooling these steel plates to 800°C, no deposits adhered to the steel plates.

The temperature of the impacting particle can have an influence on the potential to adhere to a surface. Richards et al. (1991) have proposed that a particle has to pass through a thermal boundary layer before colliding with a surface. Retarding the particle will decrease the particle temperature. Richards has determined that particles greater than 25 microns will have sufficient inertia to pass through the boundary layer, whereas particles smaller than 12 microns are cooled to the temperature of the surface. In addition, dense iron oxide particles will have a higher temperature than silicates. This is attributed to the expected higher particle inertia of iron-oxide particles of same size as a silicate particle.

Raask (1986) proposed that the initial particles adhered to the surface by Van der Waal forces. The combination of these forces and surface roughness is sufficient for sub-micron particles to adhere to the initial surface. This layer then forms the surface for subsequent liquid phase adhesion through chemical and mechanical bond formation. The purpose of the liquid layer is to promote the initial adhesion of solid particles as a result of surface tension. Raask proposed that in a reducing environment, sulphides are reduced and the S reacts with K and Na to form K_2SO_4 and Na_2SO_4 on any surfaces. It is estimated that only a thin layer (hundred molecules thick) is sufficient to promote the adhesion of sub-micron particles. Mechanical and chemical bonds then promote the further growth of the slag deposit.

3.4 Slag Deposit Growth and Development

Fly ash particles of variable size and shape characteristics are deposited on a heat transfer surface. The processes whereby these fly ash particles arrived and were deposited on a surface were described in the previous section. To form a slag deposit from these ash particles, the individual fly ash particles need to fuse (sintering). The processes and conditions required to form a slag deposit on a heat transfer will be outlined in this section.

Viscous flow sintering is recognised as the dominant mechanism for the formation and consolidation of loosely deposited ash particles on internal furnace chamber surfaces and heat exchange surfaces (Gibson and Livingston, 1991). The degree of sintering and hence the strength of the deposit is dependent on the chemical and mineralogical composition of the fly ash particles, the particle temperature, the surface temperature of the deposit and the gas temperature (Gibson and Livingston, 1991). Viscous sintering of coal ashes involves three main processes (Nowok, 1996) (Nowok et al., 1990) (Gibson and Livingston, 1991). These processes are:

1. The formation of closed pores through the rearrangement of the ash particles. The meniscus of a thin liquid layer between two ash particles ('neck') will tend to pull the particles together. Nowok (1996) estimates that the viscosity of the thin molten layer is greater than 10^5 Ns/m^2 (10^6 poise). The deposit is characterised by large refractory ash particles, which are surrounded and linked by molten phase. There is a network of large irregularly shaped inter-particle pores and mainly spherical intra-particle pores. The deposit will be friable and can be broken by hand.
2. The shrinkage of inter-particular large pores. With an increase in temperature more molten material is formed. Molten material will flow into the open pore structure of the deposit, thus forming closed pores. Shrinkage may arise from inward-acting stress within the pores. This is caused by surface and grain boundary tensions (Nowok et al., 1990). At this stage the deposit has no recognisable refractory ash particles and spherical inter-particular pores.
3. Pore-filling. This final stage will only occur if there is an excess of molten phase able to fill the smaller inter-particular pores through plastic flow (Nowok et al., 1990). This will occur at higher temperatures and when the

viscosity of the molten liquid is $<10^5$ Ns/m^2 (10^6 poise) (Nowok, 1996). A fused deposit is formed.

An increase in the degree of sintering results in a corresponding increase in the density and strength of the deposit. The density of the slag deposit is expected to gradually decrease during closed pore formation (1 above), reaching a minimum point at a temperature equivalent to the temperature of critical viscosity. During the shrinkage of the closed pores the density gradually increases to a density of the original deposit. With an increase in temperature, the density will gradually increase if there is excess liquid to infill the pore (Nowok, 1996) (Nowok et al., 1990).

The rate of deposit growth and subsequent strength is given by (Kalmanovitch and Williamson, 1986) (Nowok and Benson,1991a):

$$\frac{ds}{dt} = \left(\frac{3\gamma q}{2\eta r} \right) \qquad \textbf{3.11}$$

where γ is the surface tension and q a constant dependent on the composition of the fly ash particle. The viscosity of the liquid phase is η while r is the radius of the initial particle. For a given coal ash, q and surface tension are effectively constant. Therefore the strength of a deposit is inversely proportional to the viscosity of the liquid phase and the radius of the particle. This implies that the smallest ash particles would enhance the initial sintering and densification rate.

Nowok and Benson (1991a) attempted to compare the viscosity and surface tension to the base/acid ratio and the number of nonbridging oxygen per tetrahedrally co-ordinated cations (NBO/T). Generally, it is accepted that the viscosity of highly polymerised silicate melts is dependent on the strongest bonds such as Si-O, Al-O and the enhanced abundance of three dimensional network units. Alkali and alkali-earth elements decrease the viscosity in the order of K>Na>Li and Ba>Sr>Ca>Mg. If iron occurs as Fe^{2+} it acts as a network modifier, decreasing the viscosity. If iron occurs as Fe^{3+}, it acts as a network former and increases the viscosity. Nowok found that under reducing conditions the surface

tension/viscosity ratio increased with an increase in the base acid ratio. Under reducing conditions the slag is less polymerised than under oxidising conditions. This can be attributed to a change of the iron oxidation state from Fe^{3+} to Fe^{2+}. Generally, the number of NBO/T decreases with a decrease in the proportion of Fe^{3+}. Compressional strength increases with the surface tension/viscosity ratio. The findings by Nowok, indicate that the deposit strength and growth is likely to be higher under reducing conditions than under oxidising conditions. Experiments on the slagging behaviour of Drax fly ash, indicated that the initiation of sintering occurs at temperatures 50 to 100°C lower under reducing conditions than under oxidising conditions (Gibson and Livingston 1991).

According to Gibson and Livingston (1991) the process of slag development can be described in three major stages:

1. Initial Stage - At this stage the boiler surfaces are relatively clean and the adhesion of fly ash particles is minimal. The deposit surface is dry and the degree of sintering is low. The metal surface temperature of the heat transfer surface controls deposition. The composition of the initial layers is significantly different from the overall fly ash compositions. This initial slag surface is generally enriched in the low fusion temperature components such as Fe_2O_3 and the alkali metal compounds. The temperature is normally low, not exceeding 1000°C. A magnetite rich layer up to 1mm thick was observed to develop on the surface of a slag probe prior to the development of an aluminosilicate slag deposit (Cunningham et al., 1991). Based on extensive combustion trails of three UK coals, Wigley and Williamson (1991) reported an enrichment of ferric iron (Fe_2O_3) and calcium oxide in the initial layer. Decomposition of pyrite will account for the iron enrichment, whereas CaO is derived from the decomposition of the carbonate mineral ankerite and/or calcite. Unsworth et al. (1987a) suggests that aerodynamic classification occurs within a boiler that favours the deposition of Fe-rich particles. Allen and Hallam (1993) analysed the surfaces of fly ash particles using XPS and determined

the presence of a sulphate layer less than 15nm deep. The sulphate layer was identified as $Fe_2(SO_4)_3$, $FeSO_4$ and Na_2SO_4.

2. Intermediate Growth - As the deposit grows by a few millimeters, the fireside slag surface temperature increases to above 1000°C. The degree of sintering increases accordingly. The rate of sintering is dependent on the temperature and the composition of the slag. The deposit begins to develop a more receptive surface and the fly ash capture rate increases accordingly. The composition of the outer deposit surface approximates the overall ash composition.
3. Mature Deposit - As the deposit grows, the fused surface becomes receptive to even solid slag particles. The capture rate is at a maximum. All fly ash particles colliding with this surface will adhere, adding to the deposit.

The thickness of and the distribution of the deposits in a boiler are controlled by the temperature distribution within the boiler, the position of sootblowers and on-load cleaning equipment. Secondary ash deposits can occur on surfaces on account of the detachment of primary ash deposits. This is particularly prevalent in the lower regions of the boiler.

The chemical, morphological and physical characteristics of the initial slag deposit have been studied in detail. At the initial stages, the surface is clean and the adhesion of incoming fly ash particles to a clean surface would be difficult. Wagoner and Yan (1991) proposed that thermophoresis (thermal forces) controls the adhesion of an impacting particle to a clean surface. It is proposed that a thermal force can be larger than gravitational force and that it can hold a small, stationary particle against a heat exchange surface or a deposit surface. A thermal gradient of 171°K/mm would produce a thermal force equal to the gravitational force of a 5-micron Al_2O_3 particle. Gradients of 7 K/mm and 2 K/mm are required for a 1μm and a 0.5 μm Al_2O_3 particle respectively. The thermal forces will slow an elastic impacting particle to zero velocity after a number of successive rebounds. It is estimated that zero velocity can be achieved within 1.25 seconds for a 1 μm Al_2O_3 particle and 1.45 seconds for a 5μm particle.

Decelerating the impacting particle to zero velocity and retaining this particle on the surface through thermopheric forces can initiate deposit growth.

Abbot et al. (1986) combusted a variety of coals in a drop tube furnace and obtained a slag deposit on a water-cooled boiler steel substrate. The same depositional sequence described by Gibson and Livingston (1991) was evident in the slag deposits formed. In summary, the initial slag layer consisted of iron-rich particles strongly bounded to the steel substrate oxide layer. In addition, there was a layer of very fine (<3 μm) particles, which covered the entire substrate surface. A loosely bounded predominately aluminosilicate rich deposit accumulated on the initial iron-rich bonded layer. With time the sintering of the loosely bound particles occurred. An increase in the thickness of the deposit resulted in a corresponding increase in the deposit surface temperature relative to the initial steel surface and the fusion of ash particles occurred. In some cases, a fluid outer surface was formed. When the steel surface temperature would increased from 310°C to 340°C the rate of slag development would increase by a factor of 10. Slag development is promoted by higher flame temperatures and char fragmentation, which produce a higher proportion of smaller particles.

Extensive research by Abbott, Austin and Moza and colleagues on the interaction of slag droplets with relatively cold substrates of varying composition has resulted in the development of the Moza-Austin sticking test (Moza and Austin, 1981) (Abbott and Austin, 1985). The main fundamental findings of this research are as follows:

1. For adhesion to occur it is necessary that the interfacial region between the slag droplet and the substrate surface should be a liquid. Slag droplets will not adhere if the temperature of the substrate is below a defined sticking temperature.
2. Increasing the temperature of the substrate increases the adhesion strength of the deposit. Long contact times favour the formation of strong bonds as compounds can interchange between the slag droplets and the oxidised steel substrate.
3. The oxide layer of the substrate plays a crucial role in deposition. Ash droplets will adhere to the oxide layer. If the ash droplets are removed, part of the oxide layer will form part or the slag layer. Slag droplets can

adhere to one of three localities. These include the outer oxide layer (Fe_2O_3/Fe_3O_4 layer) and slag boundary, within the oxide layer itself at the FeO- Fe_2O_3/Fe_3O_4 boundary, and finally along the Fe-FeO boundary. The adhesion strength increases accordingly from being the weakest at the slag- Fe_2O_3/Fe_3O_4 layer to being the strongest at the Fe-FeO boundary. At higher temperatures (570°C) the outer Fe_2O_3/Fe_3O_4 layer is thin allowing for the penetration of the slag into the FeO layer.

4. Compounds (NaCl and FeS_2), which lower the liquidus temperature of the droplet, will increase the adherence strength. These alkali salts have a greater influence on adhesion strength than do the fluxing elements (K, Na and Ca) found in clays montmorillonite and illite.
5. Pyrite adheres strongly to the oxidised surface in the form of pyrrhotite ($Fe_{0.995}S$). It is proposed that sulphur in these droplets not only lowers the liquidus temperatures but also lowers the surface tension between the slag droplet and the substrate
6. The chemical composition of the slag droplet has an effect on its adhesion strength. This can be attributed to the influence that composition has on the diffusion of iron, variations in viscosity and surface tension. On cooling, the coefficient of thermal expansion could increase the stress between the droplet and substrate. Adhesion strength was ranked in the order pyrite/quartz, pyrite/kaolinite and pyrite/illite.

In extensive ash deposition trails at three power stations in Denmark, Laursen et al. (1998) was able to conclude the following:

1. Based on the textural characteristics of the slag deposits, five distinctive slag deposit types were described. These include a porous deposit, powder deposit, iron-rich deposit, a semi-fused slag and a fused slag deposit.
2. The porous deposits formed on the upstream side of the deposition probe principally consist of Fe-rich particles. These deposits are formed through inertial impaction. These molten particles deform when they collide with the surface. The viscosities of these iron-rich particles are controlled by the oxidation state of the iron. It is possible that the iron-rich deposits in the cooler regions of the boiler are formed through the diffusion of iron from the boiler tube into the deposit. Local

eddies formed result in the deposition of fine Al-silicate particles. An increase in deposit thickness reduces the thermal conductivity of the slag layer. This in turn increases the surface temperature resulting in the formation of a semi-fused and eventually, a fused slag deposit. At this stage, any impacting particle will adhere to the surface and elemental composition of the slag deposit is similar to the composition of the fly ash. The above is analogous to the results described by Gibson and Livingston (1991) and Abbott and Austin (1986). The crystallisation of minerals from the molten slag does occur.

3. Powdery deposit is probably formed as a result of eddy deposition behind the tubes. These particles are considerably finer than the iron-rich deposits. Indications are that $CaSO_4$ contributes to the bonding of these fine particles.

Anorthite ($CaAl_2Si_2O_6$) is a mineral commonly found in Ca-rich bituminous coal slag deposits (Unsworth et al., 1988) (Wain et al., 1991). However, anorthite is not a common mineral in bituminous coals. Owing to this discrepancy, Unsworth speculated that by understanding the formation of anorthite in a slag deposit would clarify the mechanisms controlling slag formation. Unsworth et al. (1988) fired seven bituminous coals in a 160kW pilot scale combustor and studied the deposits formed. The main combustor parameters were peak temperatures of 1500-1600°C and residence time's 2 to 2.5s. The calcium in these coals occurs in dolomite, calcite, ankerite and fluorapatite. Anorthite occurred in all the deposits, mullite occurred in some and gehlenite ($Ca_2Al_2SiO_7$) in deposits from the cooler regions of the furnace. Haematite and magnetite were also present. Two processes have been proposed to account for the formation of anorthite in slag deposits:

1. Crystallisation from a homogeneous melt - Based on the average bulk ash compositions of these coals and the CaO-Al_2O_3-SiO_2 phase diagrams, it is predicted that the mullite will crystallise at 1600°C followed by the co-crystallisation of anorthite and mullite from 1500°C to 1350°C. Finally, quartz will start crystallising at 1345°C

2. Solid State reactions between minerals – Solid-state reactions take place at lower temperatures (900-1300°C) between the high temperature form of the calcium-bearing minerals (calcite and dolomite) and kaolinite or illite to form anorthite (Unsworth et al., 1988). The rate-determining step is the diffusion rate of calcium into the aluminosilicate (kaolinite or illite). This is a function of temperature and the proportion of Ca-bearing minerals intimately associated with aluminosilicates.

Absence of anorthite in fly ash suggests that anorthite is formed within the slag deposit. Deposit characteristics are influenced by the boiler wall and tube surface temperatures, the degree and duration of contact between aluminosilicates and calcium-bearing ash particles, and by any impurities, which could act as fluxing agents.

Phase diagrams can be used to determine the nature of the surface and hence the potential for slag growth. It has been argued that phase diagrams are not applicable as equilibrium is not reached on account of the short residence times of one to two seconds in a boiler (Unsworth et al., 1988).

Weisbecker et al. (1991) has defined an index to determine the behaviour of certain coals in a boiler. This index is based on the effect that certain elements and minerals have on the strength and characteristics of the deposit. The influences are as follows:

1. Sodium content - Organically bound sodium vaporises as a hydroxide or sulphate and reacts with aluminosilicates to form hard deposits. Na_2SO_4, can be deposited on the surfaces of fly ash particles, which alter the viscosity of the surface, and promote sintering.
2. Calcium content - Calcium reacts with aluminosilicates and quartz to produce lower melting point phases that will enhance deposit formation.
3. Quartz content - Fine excluded quartz grains less than 4.6 microns in size are more likely to be carried to the back end of a boiler. Small quartz grains have a larger surface area per unit volume. Large surface area increases the potential of sodium reacting with quartz.

Included quartz grains are more likely to react with organically bounded cations to produce low melting point phases than excluded quartz grains.

4. Calcite content - discrete calcite grains can increase the viscosity of liquid phase, which in turn increases the deposit strength.

It is apparent from the application of this index that it is case-specific and cannot be used generically for all coals with great success.

Cunningham et al. (1991) studied the influence of calcite, pyrite, kaolinite and illite on slag formation. In the main, calcite and pyrite slightly lowered the temperature at which deposition commenced. In comparison, kaolinite and illite, tended to raise the temperature at which fly ash deposition occurred. In a reducing environment, slag growth and strength were enhanced in contrast to an oxidising environment. Increasing particle size reduced the temperature of deposition (Cunningham et al., 1991). Barnes et al. (1993) in the investigation of three UK coals, showed that sintering strength was higher at lower oxygen levels.

Experiments undertaken by Barnes et al. (1993), indicated that beneficiated coals produced thinner slag deposits than the parent coal, but were more difficult to remove (Hurley et al., 1991). Barnes attributed the increase in the deposit strength to the relative increase in the iron to silicate ratio, which produces a lower viscosity fly ash. Decreasing fly ash viscosity increases deposit strength.

3.5 Ash Deposition Indices

Many researchers have developed slag prediction factors based on ash elemental analysis and ash fusion temperatures. Details of slagging indices commonly used are summarised in Appendix B (Bott, 1991) (Juniper, 1995a, 1995b) (Skorupska and Couch,1993).

The characteristics of the ash deposits formed on combusting 30 coals in the Boiler Simulation Furnace (BSF) at the Australian Combustion Technology Centre (ACTC) were examined and compared with typical ash deposition indices (Juniper, 1995a). Deposit characteristics include:

- Non-troublesome powdery deposits
- Varying degrees of sintered deposits which may cause troublesome deposits
- Molten deposits which are difficult to remove and will cause troublesome deposits.

Reasonable correlations for predicting slagging characteristics were obtained using the $CV_{1426°C}$, iron index and the Fe+Ca index. The T250 index and any index based on the initial deformation temperatures (IDT) did not seem to work for the Australian coals. Based on this evaluation the best indices listed in order of preference were:

1. Iron Index
2. Fe+Ca in ash
3. Multi-Viscosity Index
4. Calculated viscosity , $CV_{1426°C}$

Investigations by Phong-anant et al. (1992a, 1992b) favoured the Fe+Ca index as the most reliable index, although they found that the majority of the existing indices were not considered reliable.

The limits used in the Australian industry are summarised in Table 3.2 (Juniper, 1995b).

Table 3.2: Revised limits for slagging characteristics

Coal Index	Unit	Low Slagging	High Slagging
Calculated Viscosity, $CV_{1426°C}$	poise	>2000	<350
Silica Ratio		>90	<75
T_{250}	°C	>1370	<1200
Base/Acid Ratio		<0.09	>0.3
Slagging Factor, R_s		<0.6	>2.6
Iron Index	%	<0.6	>2.0
Multi-Viscosity Index		<0.6	>1.2
Slagging Temperature	°C	>1350	<1150
Fe_2O_3/CaO		<0.3	>3.0
Fe_2O_3+CaO	%	<7.0	>12.0

The total iron-bearing (pyrite and siderite) and calcium-bearing minerals (calcite, gypsum and dolomite) have been used by Phong-anant to define the slagging propensity (Phong-Anant et al., 1992b). An approximate limit of <16% for low slagging coals is defined. In addition, simple ternary phase diagrams of CaO-FeO-Al_2O_3-SiO_2 can be used to predict the primary phase and the liquidus temperature based on the ash elemental analysis of the slag deposit.

3.6 Conclusion

The initiation and development of slag deposits is a complex process involving the physical characteristics of the fly ash, combustion environment and the surface characteristics of the surface onto which the slag deposit is forming. From a fly ash perspective, fly ash size, density and viscosity characteristics are fundamental. Important operational parameters that control deposition are temperature, flue gas velocity and the localised combustion environment.

After the complex high temperature mineral transformations in the char particle a cloud of ash particles are formed from the mineral matter in the coal. Fly ash is transported to a heat transfer surface by the gases generated by the combustion of coal. If the fly ash particle is within a specific size and density range the fly ash particle will reach the heat transfer surface. Flue gas velocity will also have an impact.

The viscosity of the fly ash particle and of the receptive surface determines whether the impacting fly ash particle will adhere to the surface. If the fly ash particle is molten or semi-molten then the probability of a fly ash particle adhering to the surface is high. If the receptive surface is molten, then fly ash particles will adhere to the surface irrespective of the viscosity of the fly ash particle.

4 METHODOLOGY

Modelling fly ash formation from the mineral matter associations in coal and predicting slag deposition in a pulverised fuel boiler requires a detailed knowledge of the mineral matter characteristics of pulverised fuel, fly ash and slag deposits. The samples could be obtained at a laboratory scale designed to simulate a fully operational boiler, or *in-situ*, from a fully operational boiler.

Laboratory scale or bench scale sampling is logistically easier and cheaper than obtaining samples from a fully operational boiler. Unfortunately, laboratory or bench scale samples are not necessary representative of a fully operational boiler. Due to the inherent scale up problems from bench scale to operational scale the experimental platform chosen for this thesis is a fully operational boiler, while the laboratory scale (a drop tube furnace) was used to verify the fly ash formation model based on the data obtained from the boiler.

To achieve the said objectives of this thesis, a number of new and unique sampling and analytical techniques were developed by the author. These techniques include:

1. Slag probe: a new slag probe was designed to simulate slag deposition in a boiler and to monitor temperatures of the steel surface. The slag probe was attached to a “water cooled” suction pyrometer. The suction pyrometer was used to convey the slag probe into the boiler and enabled fly ash to be sucked out of the boiler.
2. Sample preparation method: a new method by which to distinguish coal/char particles from embedding resin was devised because analysing coal using a scanning electron microscope presents problems as it is difficult to distinguish the coal from the traditional epoxy resin mounting medium.
3. Automated analytical technique: A new analytical technique was configured to obtain statistically unbiased viable data on mineral composition and mineral association characteristics in coal and correspondingly in fly ash and slag deposits.
4. Fly ash formation and slag deposition model: A new model was developed with the ultimate objective of devising a functional software

model which can used to predict fly ash characteristics from mineral matter data in coal and from this predict the slagging propensity of the coal.

The methodology and concepts behind the analytical techniques designed and utilised are discussed in this chapter.

4.1 Sample Acquisition

The 200MW_e unit 9 pulverised fuel boiler at Hendrina Power station was selected for the detailed sampling campaign. Samples of pulverised fuel, fly ash and slag deposit are required in order to understand mineral matter transformations, fly ash formation and slag deposition in a pulverised fuel boiler. Samples were acquired over a period from September 1998 to May 2000.

To obtain samples of fly ash and slag four access holes were constructed on the left-hand side of the boiler (if standing facing the front of the boiler) of unit 9. Hole 1 and hole 2 are positioned 1.5 m from the backwall in line with burners E4/3 (bottom row) and A4/3 (middle row), respectively (Figure 4.1). Hole 3 and 4 are positioned near the centre of the boiler with hole 3 above the thermopiles and hole 4 on 124 ft level, beneath the super heaters. The access holes are 350x250mm with a covering hatch secured to boiler wall by four bolts (Figure 4.2a and b).

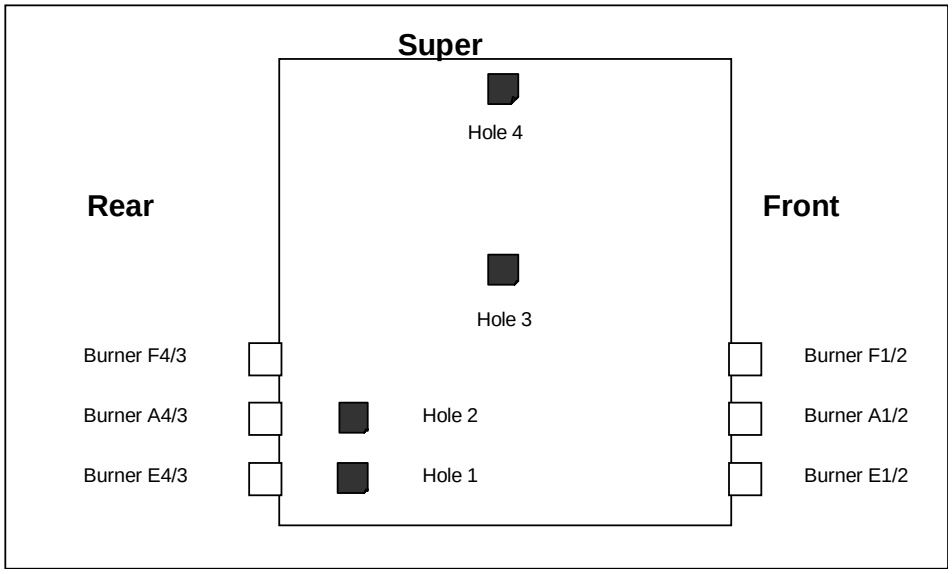

Figure 4.1. Relative position of the four access holes. Not drawn to scale.

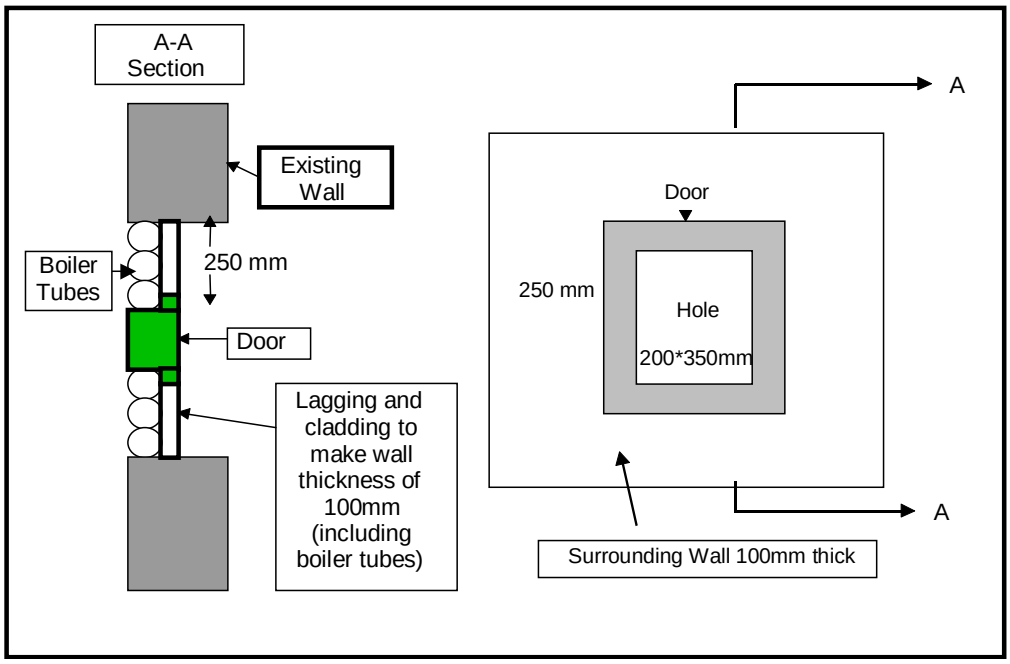

Figure 4.2a: Physical dimensions and location of the access hole.

Figure 4.2b: Access hole in boiler wall. Slag probe in the foreground

During the analytical phase two cegrit (bulk) samples of fly ash were obtained from between the superheaters and economiser. The cegrit samples are routinely used to determine the proportion of unburnt carbon that is indicative of combustion performance. It is commonly accepted that cegrit samples are not as

representative as those samples that have been acquired isokinetically. Sample details are discussed in chaper 5, section 5.1.

4.1.1 Isokinetic sampling: pulverised fuel

Obtaining samples of pulverised fuel is routinely done at power stations. Pulverised fuel is isokinetically obtained from specified sampling points between the mills and the burners. Sampling is achieved by inserting a sampling probe at predefined depths within the pipe feeding the burner. Compressed air is used to create suction at the tip of the sampling probe. The probe is kept in position for a specified time at each depth and the sample is sucked through the sampling probe into a glass-receiving jar. Sampling the pipe at different depth ensures that any particle segregation introduced as a result of particle size and density differences is negated. Isokinetic sampling ensures that a representative sample of the pulverised fuel entering the boiler is obtained. Pulverised fuel was iso-kinetically sampled at the same time as the fly ash and slag deposits were collected.

4.1.2 Suction pyrometer and slag probe: fly ash and slag deposit

A prerequisite of this research was to obtain *in-situ* samples of fly ash and slag deposits during normal boiler operation. To achieve this a ”water cooled” suction pyrometer and a custom designed slag probe was used (Figures C.1 and C.3).

The suction pyrometer consists of two six-metre hollow stainless steel tubes (64 mm diameter) connected by regularly spaced hollow plates. Cooling is achieved by flowing water from the top tube through the connecting hollow plates and out the bottom tube into a drain (Figure C6). ESKOM personnel designed the original suction pyrometer.

An air-ejector is connected to the backend of the bottom tube while the slag probe is attached to the front end of the suction pyrometer top tube (Figures C.1 and C.6). The compressed air passed through the air-ejector creates a suction enabling fly ash to be sucked from within the boiler along the length of the bottom tube into a receiving container.

The 230 mm long slag probe is designed to collect slag deposits on a removable steel sleeve (see Figures C.2, C.4 and C.5). The slag probe is a hollow cylindrical

tube, with a 60mm outer diameter, a 40 mm inner diameter and a 10mm thick wall. The outer surface of the slag probe has a 5° taper from the middle to the front of the probe. The back-end of the slag probe fits into the top tube of the suction pyrometer. A one-metre long stainless steel pipe (8mm outer diameter) was welded onto the back-end of the slag probe to allow for the return water to flow out at the back of the suction pyrometer. A steel plate with a threaded hollow tube (8 mm diameter) in the centre closed the front end of the slag probe. A removable cylindrical slag sleeve with a 5° tapered inner surface fits onto the front end of the slag probe. The tapering ensures good contact between the slag probe and the removable slag sleeve. It also facilitated the efficient cooling of the removable slag sleeve and the removal of the slag sleeve on completion of the analyses.

An aluminium tube (6mx8mm) was fixed along the length of the suction pyrometer and connected by stainless steel couplings to the threaded tube in front of the slag probe (see Figures C.5 and C.6). The slag probe is cooled by regulating the flow of water through this 6m long aluminium tube into the front end of the slag probe and out the back through the 1m tube extension and finally along the suction pyrometer. A manually operated lever valve controls water flow rate. All the components of the slag probe and the removable sleeve are made of boiler tube steel.

A hole (4 mm in diameter) was drilled at an angle into the solid wall of the slag probe (see Figure C.2). The end of this hole is 5mm from the outer surface of the slag probe. A second 4mm hole is drilled horizontally to a depth of 1mm from the inner wall of the slag probe. Type K thermocouples with a 446 stainless steel sheath are placed into these holes and used to measure the surface temperature of the slag probe (TC1) and inner wall temperature (TC2). A third thermocouple (TC3) is placed in the centre of the slag probe cavity to measure the temperature of the water in the slag probe. Thermocouple leads were threaded from the slag probe along the length of the suction pyrometer and connected to a data logger (see Figure C.6). Data logging software (visual designer) converts the analogue thermocouple signal and constantly displays the temperature on a monitor (see Figure C.7.). Temperatures are written to an ASCII file every 60 seconds. By regulating the water flow rate to the slag probe during the operation, the water

temperature (TC3) in the slag probe could be maintained at ±100 °C (boiling/steam point of water).

The surface temperature of the slag probe is an important parameter for slag deposition. To estimate the surface temperature of the slag probe it was assumed that the heat required to heat the water in the slag probe was equal to the heat conducted through the wall of the slag probe. The assumption made was that no heat could be lost between the slag probe and the removable slag sleeve. Details of the formulae used to calculate the slag probe surface temperature is summarised in Appendix D.

4.1.3 Suction pyrometer and slag probe operation

The suction pyrometer is supported by two variable height stands. Scaffolding was used for holes 1, 2 and 3 to support the suction pyrometer at the correct height. Power station water was used to cool the suction pyrometer. A 100 litre plastic tank with a 0.75kW external water pump was used to supply water to cool the slag probe.

Samples were obtained by manually sliding the suction pyrometer through the access holes into the boiler. Samples at depths of 0m, 0.5m, 1m, 1.5m and 2m were collected for holes 1 to 3. Poor water pressure restricted the collection of slag from hole 4 at depth of 2m. Pulverised fuel from burner E4 and burner A4 were collected during the sampling of hole's 1 and 2 respectively, and from burners B1, B2, C1, C2, D1 and D2 for holes 3 and 4.

Prior to inserting the suction pyrometer into the boiler a new slag sleeve was slipped onto the slag probe. A plastic sample bag is placed in the air-ejector sample holder. Connections between the compressed air and the air-ejector were sealed using plastic electric tape. The cooling water supplying the suction pyrometer and slag probe was switched on and the data logger program activated. At start-up, the initial temperature readings should be the expected ambient temperatures of 25 to 30 °C.

The probe was slowly inserted into the boiler up to the required depth. The water flow rate to the slag probe was slowly increased until the temperature (TC3) of

the water in the slag probe cavity was between 95 and 105 °C. The compressed air supplying the air-ejector was switched on to commence the sampling of fly ash. The suction pyrometer was kept at this position until sufficient slag had accumulated on the slag probe. Depending on the position and height within the boiler, the sampling duration varied from 30 minutes to maximum of three hours. On completion, the suction pyrometer was removed from the boiler and the removable sleeve was allowed to cool.

The slag sleeve was removed by screwing in the grub screw at the front of the slag sleeve (see Figure C.1). The slag sleeve with accumulated slag deposits and any other loose slag deposits, were placed in a plastic sample bag.

The compressed air hose was connected to the front end of the suction pyrometer and used to purge any remnant fly ash accumulated in the bottom tube of the suction pyrometer into the fly ash sample bag. The fly ash sample bag was removed and the air-ejector was cleaned, using compressed air.

4.1.4 Boiler operational conditions

Power stations routinely acquire operational data for controlling and monitoring the performance of the boiler. The data are continuously acquired on-line at fixed time intervals. The data includes:

1. Generated MW_e – this indicative of the boiler load (capacity $200MW_e$)
2. Flue gas temperatures at the superheaters, economiser and before it has exited the boiler.
3. Thermopile temperature readings from the front wall and side wall of the boiler
4. Steam flow in kg/s
5. Total, primary and secondary air flow (kg/s).

To minimise the effect that boiler operations could have on the fly ash formation processes, sampling was undertaken whilst the boiler was operating at full load. The operational data served to monitor the operational status of the boiler at the time of sampling. With the operational data of the boiler at hand, it was possible to link any sample abnormalities to the performance of the boiler.

The surface temperature of the slag probe was calculated in terms of basic heat transfer principles (Appendix D). By comparing the calculated slag probe surface temperatures with the measured surface temperatures of the front and sidewalls of the boiler, it was possible to validate the surface temperature estimates on this basis.

4.2 Sample Preparation Techniques

For an accurate CCSEM and petrographic analysis, the quality of the prepared sample is crucial. Firstly, it is imperative that the prepared sample should be as representative as possible, and secondly, that the prepared sample should satisfy the stereological assumptions (Appendix G) made for the type of analysis required. Representative samples were achieved by splitting samples using a suitable splitter.

An accurate quantitative CCSEM analysis is dependent on the sample preparation techniques in accordance with the assumptions made for the first law of stereology. Stereology is a branch of mathematics that transposes any one-dimensional (point) or two-dimensional (area) measurement into a three-dimensional value (volume). Stereology is important as the CCSEM measurements are made on a one- and a two-dimensional plane and the reported results (e.g. volume %) are three-dimensional values.

An analytical point is a one-dimensional measurement, whereas the two-dimensional plane is the prepared polished surface, which is scanned and analysed by the CCSEM. The conversion of an one/two- dimensional value to a three-dimensional value such as volume percent is based on the first law of stereology (refer to Appendix G)

In essence, this law states that proportion of phase/mineral analysis points (P_p) is equivalent to the volume percent of that phase or mineral in a sample. Similarly, the law can be extended to include the linear intercepts (L_L) and area (A_a) proportions. However, to apply this rule in this study, the following conditions and assumptions were made:

- Analytical points are spaced at regular intervals (i.e. grid of points).

- The distribution and orientation of the particles must be random (i.e. no preferred orientation or density and size segregation).
- The sectioning of sample is random (an analytical surface).

The sample preparation technique must ensure that these assumptions are met. If not, then it would be erroneous to apply the first law of stereology (Appendix G) and the results obtained would be misleading.

It must be noted that the plane of sectioning also influences the average sizes and the association and liberation characteristics. In general, the size of a mineral can be underestimated and the degree of mineral liberation overestimated (see Figure 4.3). This is a limitation of the CCSEM method.

In preparing any sample for a typical CCSEM analysis, it is imperative that the potential errors introduced by sampling preparation should be minimal.

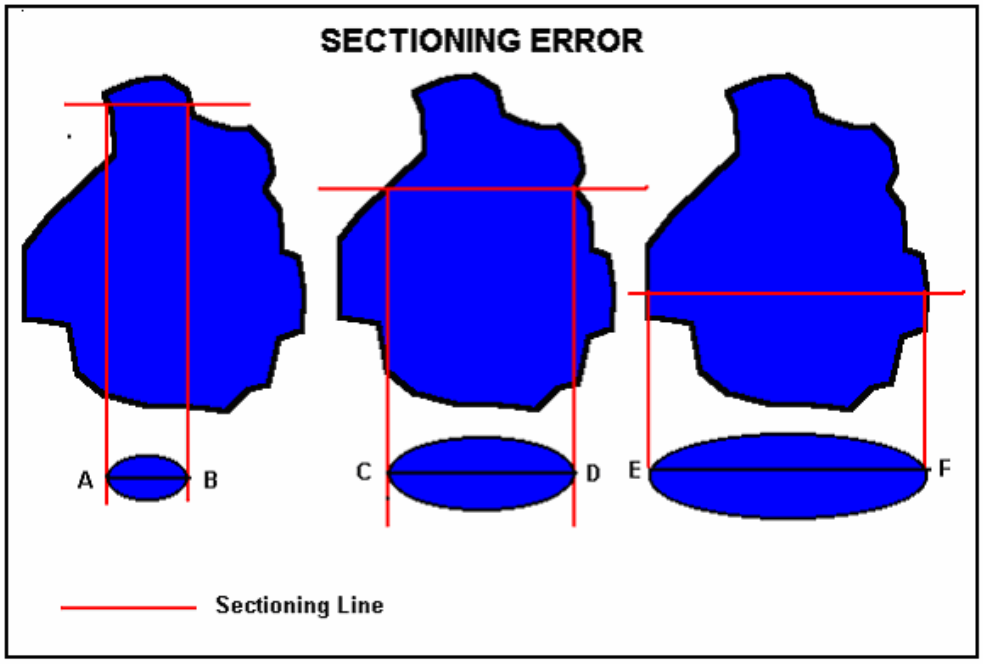

Figure 4.3: The orientation and position of the sectioning plane influence size and liberation.

By screening the sample into specified size fractions, the negative impact that sectioning has on particle sizes (Figure 4.3) was reduced.

4.2.1 Pulverised fuel

Samples of pulverised fuel were split into ±50 gram aliquots using a rotary splitter. Three randomly-selected 50 gram aliquots were individually wet-screened into +75μm, -75+38μm and -38 μm sized fractions. The total sample mass and sample mass of each size fraction were recorded. Samples were screened into separate size fractions in order to reduce the sectioning bias introduced (Figure 4.3). One 50 gram aliquot of screened sized fractions was submitted for ultimate, proximate and ash elemental analysis, the second set for petrographic analysis and the final set for CCSEM analysis.

For the petrographic analysis, the screened size fractions of pulverised fuel were mounted in epoxy resin, cured in 30mm moulds and polished to a final finish of 0.25 and 0.01 μm using diamond paste. Analysing screened sized fractions at sizes as small as 75 μm is not the normal approach. The acceptable method is to crush a representative bulk sample of coal sample to 100-% passing 1mm and to prepare a polished section of the crushed bulk sample. However, for the purpose of this thesis, it was necessary to describe the organic and inorganic mineral matter associations of the pulverised fuel and not those of the crushed material. The prepared polished sections were examined using a reflected light optical microscope fitted with oil immersion objectives.

Prior to preparing the samples for CCSEM analysis, the screened fraction of the coal was mixed with similar sized crushed iodinated epoxy resin in a ratio of 1g:2g. The inclusion of crushed epoxy resin was necessary for the following reasons:

1. Crushed iodinated resin acts as a framework to restrict sample segregation, ensuring that the cross-section analysed is a representative fraction.
2. To satisfy the stereological assumptions that particles must be randomly distributed and orientated
3. To restrict the number of touching particles. (This is particularly important for quantifying the association and size characteristics of minerals in coal and fly ash phases).

For CCSEM analysis, the pulverised fuel/crushed iodinated mixture was mixed with iodoform(CHI_3) doped epoxy resin. Using iodinated epoxy resin ensures that the organic constituent of the coal can be distinguished from the epoxy resin (see Figure 4.4). To prepare the iodinated epoxy resin, seven gram of iodoform were slowly dissolved in 50 grams of epoxy resin. This was heated in a water bath at a maximum temperature of 60 to 80 °C. The epoxy resin was cooled and stored until required. The epoxy resin/sample mixture was poured into 30mm plastic moulds and allowed to cure at ambient temperatures over a 12 to 14 hour period. The cured moulds were ground and polished to a final finish of 0.01 μm. A thin veneer of conductive carbon was sputter-coated onto the surface of the polished section. Carbon minimises the image artefacts caused by charging of specimen by removing the excess electrons from the analytical surface.

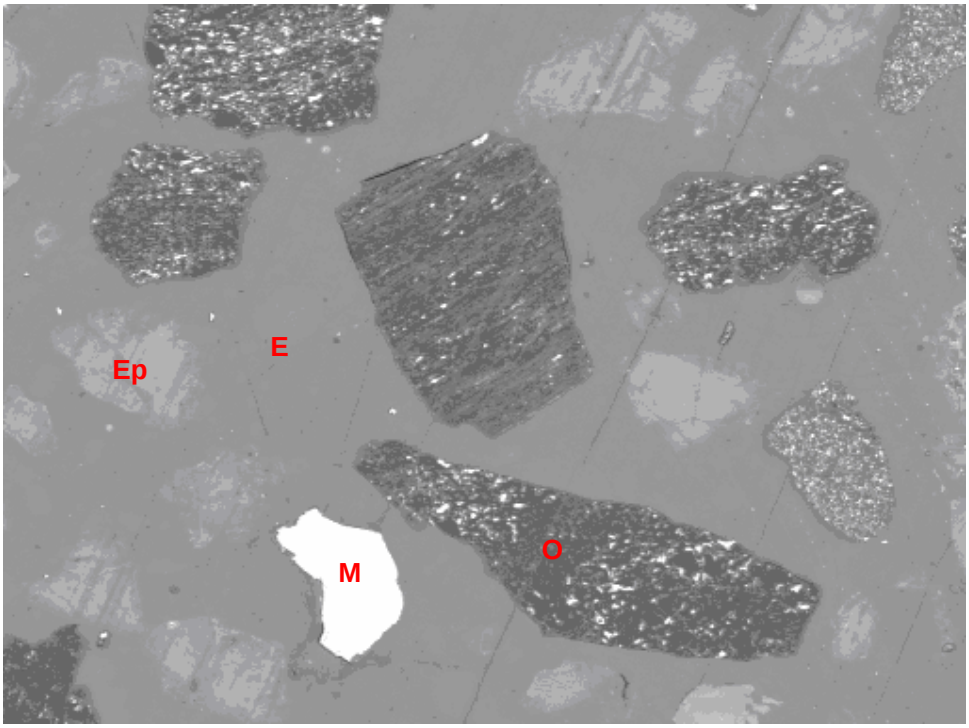

Figure 4.4: A backscattered electron image of typical field of view. The epoxy resin is grey (E), organic fraction (macerals) vary from black to dark grey (O) and mineral matter is white (M). The light grey particles are the crushed epoxy resin particles (Ep).

4.2.2 Fly ash

Representative ±50g aliquots of fly ash were wet screened into +75μm, -75+38μm and -38 μm sized fractions. The mass of each fraction and total mass screened were recorded and used to calculate the particle size distributions (PSD). Samples were mixed with crushed iodinated epoxy resin, the same ratio as used for the preparation of pulverised fuel. The fly ash/crushed iodinated epoxy resin mixture was mixed with iodinated epoxy resin and polished sections were prepared using the same technique as the one applied to the pulverised fuel. Iodinated epoxy resin was used instead of normal epoxy resin as it was necessary to identify any char or unburnt carbon in the fly ash.

4.2.3 Slag sleeves

On completion of the sampling, the removable slag sleeves were carefully removed and covered in plastic to ensure that slag deposit remained intact. At the laboratory, the plastic covering was removed and the slag sleeve with the slag deposit still intact was placed into a 500ml plastic container. Epoxy resin was poured into the plastic container containing the slag sleeve and allowed to cure. Areas of interest were marked and the slag sleeve was cut into circular sections. These cross-sections were ground, polished and coated with carbon. By preparing the slag sleeves in this manner (cross section) it was possible to ensure that the physical characteristics of the initial fly ash particles and subsequent slag deposit could be ascertained.

4.3 Petrographic Analyses

Petrographic analysis in this study is used to determine the maceral and microlithotype compositions and rank (by virtrinite reflectance) and, more importantly, to describe the association characteristics of mineral matter with macerals. As discussed previously, the screened size fractions and not the ISO (ISO 7404/2-1985 E) accepted crushed product (100-% passing 1mm) were analysed. The sample mounting, grinding and polishing techniques that are outlined in ISO standard (ISO 7404/2-1985 E) to prepare a particulate block[4] were adhered to.

---

[4] **Particulate block**: Solid block consisting of particles of crushed coal representative of the sample, bound in resin, cast in a mould and with one face ground and polished (ISO 7404/2-1984(E))

For the maceral, microlithotype and mineral group analyses, the particulate blocks were microscopically examined using a Zeiss incident light microscope with a vertical illuminator and oil immersion objectives. A mechanical 10-point counter was attached to the microscope stage to numerically record the number of points per defined maceral and microlithotype categories (maximum of 10 categories), respectively. A “point” is the identity of the maceral or microlithotype at the reference position. It is defined either by the cross-hair (maceral analysis) or the 50 µm graticular (microlithotype analysis) in the microscope eye-piece. On recording the identity of the maceral or microlithotype the microscope stage is moved at a fixed increment to the next reference point. The particulate block is systematically scanned until a total of 500 points have been counted. The magnification setting is 400X. (This is in accordance with the accepted ISO standards for maceral analysis (ISO 7404/3-1984(E) and microlithotypes (ISO 7404-4 1988-E)), and described by Falcon and Snyman (1986)). The maceral types, microlithotypes and mineral groups and categories used are described in Appendix G. The volume percent proportion is calculated from the total number of recorded points per category. The proportions of macerals are recorded as volume-percent mineral-free basis and microlithotype and mineral group on a volume percent mineral-containing basis. This is in accordance with the ASTM D2799 standard. Any deviations from this standard have been developed in-house by Falcon Research and Laboratory (South Africa).

Included in the petrographic analyses, is a unique “particle” type analysis, which was developed for this study. It is an additional method for classifying the carbominerite and minerite[5] microlithotypes[6]. The purpose of this analysis is to describe the mineral association with specific macerals. The maceral component (40-80 volume percent) was classified as vitrite, intermediate, semi-fusinite and inertodetrinite. An additional category, “Free” refers to excluded minerals and particles with >60 volume percent mineral matter (details in Appendix E).

The -38 µm sized fraction was not analysed petrographically as it was difficult to conclusively distinguish between the macerals and subsequently the

[5] **Carbominerite**: Microlithotype classification of coal + 20-60 Vol-% minerals or 5-20 vol-% pyrite (Falcon and Snyman, 1986)

[6] **Minerite**: Particle with >60-vol-% mineral matter.

microlithotypes. Technically speaking, undertaking a microlithotype analysis of the -75+38 µm sized fraction is not appropriate as, by definition, the term microlithotype describes the association of macerals in a band of 50x50 µm. However, for the purpose of this study, the principal focus was the association between the minerals and the organic component and not a description of microlithotypes as is traditionally undertaken. For this reason, the microlithotypes definition was extended to include 38x38 µm particles.

The rank of the coal was determined by measuring the percentage incident light reflected (%RoV) from a polished vitrinite surface in accordance with ISO standard ISO 7404/1-1984(E). Rank positions the coal in the coalification series, ranging from brown coal (very low rank) to meta-anthracites (very high rank). The mean random reflectance defined by UN-ECE and not the maximum random reflectance (ISO) is the preferred method adopted in this study.

A Zeiss polarising microscope with oil objectives and fitted with a photomultiplier tube was used to determine the reflectance of light from selected vitrinite particles. The photomultiplier tube provides an incident monochromatic green light of 546 nm. The light reflected from the polished vitrinite surface is compared to light reflected from a number of glass standards of known reflectance readings (0.41-0.42, 0.91-0.92, 1.71-1.74 and 3.15-3.19 %RoV). The system is standardised using these glass standards every half hour.

Reflectance readings were taken from randomly selected vitrinite particles in selected +75 µm sized samples. Vitrinite particles devoid of surface blemishes and polishing artefacts were preferentially selected over poorly polished vitrinite particles. Approximately 100 readings were taken per sample analysed. The mean random reflectance and estimated standard deviations were calculated.

4.4 Chemical Analyses

Chemical analyses of coal are routinely undertaken and extensively used to classify and predict the combustion and slagging performance of coal. The chemical analyses that were undertaken on each size fraction in this study included:

- Proximate analyses – to determine the moisture content, ash content, volatile matter and fixed carbon content
- Ultimate analyses – to determine the proportions of carbon, hydrogen, nitrogen, total sulphur and oxygen (by difference). Included in the ultimate analysis is the proportion of carbonates (measured CO_2)
- Ash elemental analysis – to determine the oxide proportions of the major elements (Al, Si, Ti, Fe, Ca, Mg, K, Na and Mn).
- Gross calorific value (MJ/kg) –the energy content of the coal.
- Particle size distribution

All chemical analyses were undertaken by Technology Service International (TSI) laboratory. TSI is a SANAS and ISO (guide 25/SABS 0259 and EN45001) accredited laboratory. Details of the chemical analysis methods used are included in Appendix F.

Chemical analyses were undertaken on the bulk sample and on the screened fractions of pulverised fuel sampled from hole 2 at a depth of 0.5m. The objective of undertaking the chemical analyses include the following:

1. To ascertain the overall characteristics of the test coal and identify any other test coals, which deviate from the norm.
2. To compute selected slagging indices through ash elemental analysis (see Appendix B).
3. To ascertain the proportion of ash (ash-%), carbonates (reported as CO_2), total sulphur and ash elemental composition (reported as oxides) which are used to validate the CCSEM derived mineral proportions. (CCSEM technique is discussed in detailed in section 4.6).

4.5 Particle Size Analysis

A representative ±50-gram split of pulverised fuel and fly ash was wet-screened through a 75 µm and 38 µm steel screen. The mass of the fraction prior to screening, the mass retained on each screen and the mass of sample passing

the 38 µm screen were recorded. These masses were used to calculate the percent size distribution (alternatively particle size distribution (PSD)).

As part of the model validation a single test coal (hole 2, 0.5m) was selected and each screened size fraction was individually combusted in the drop tube furnace (DTF, see section 4.8). A Malvern particle size analyser measured the particle size distribution for each screened size fraction combusted in the drop tube furnace.

4.6 CCSEM

Crucial to modelling the fly ash formation process and subsequent ash deposition is a good understanding of the morphological attributes and mass percent abundance of minerals in the pulverised fuel, as well as the phase/minerals in the fly ash and slag deposits. In order to compare results, a quantitative - not a semi-quantitative- analysis is required. The literature review in chapter two clearly indicates that the CCSEM technique is the preferred method of analysis (see section 2.3.3).

There are different CCSEM approaches adopted by the numerous institutions around the world. For the purpose of this thesis, it is imperative that the association between the mineral matter in coal and the organic association should be quantified. Furthermore, it is imperative that any mineral variations within a particle should be identified and quantified.

As mentioned previously (chapter 2), the traditional CCSEM approach is to position the electron beam at the centre of a “bright” phase as illustrated in Figures 4.5 and 4.6. (the centroidal or PRC method). To accommodate the variation in size, the same field of view is scanned at different magnification settings (see Figures 4.5 and 4.6).

It is evident from Figures 4.7 and 4.8 that the centroidal method is selective as not all the mineral matter inclusions are analysed in a field of view. Furthermore the organic component is not analysed. This is not acceptable for a detailed description of association characteristics of inorganic and organic components, which are, as previously stated, a prerequisite for this thesis.

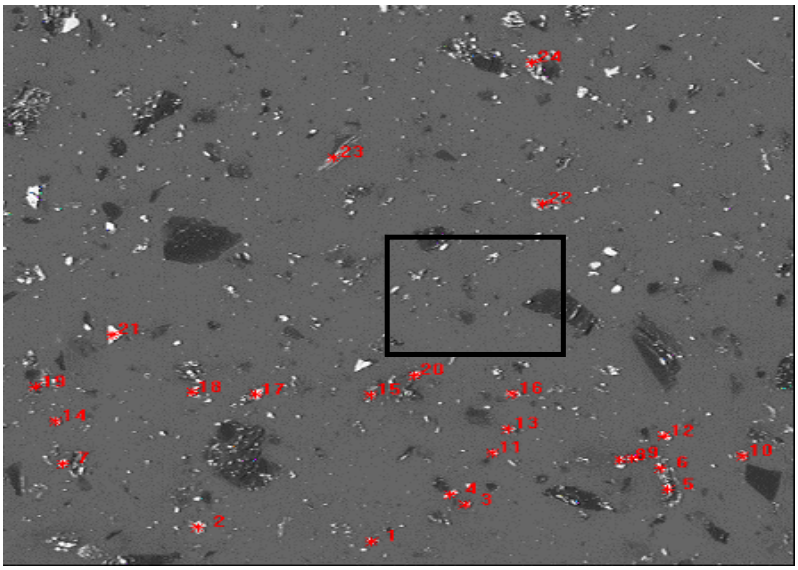

Figure 4.5: The centroidal method of positioning the electron beam at the centre of "bright" phases. The positions and corresponding reference numbers of the analytical points are superimposed in red. The box represents the image acquired at 500x magnification (Figure 4.6). Note the relatively high proportion of minerals and the organic component (black) that are not included in the analysis. Image magnification is 100X.

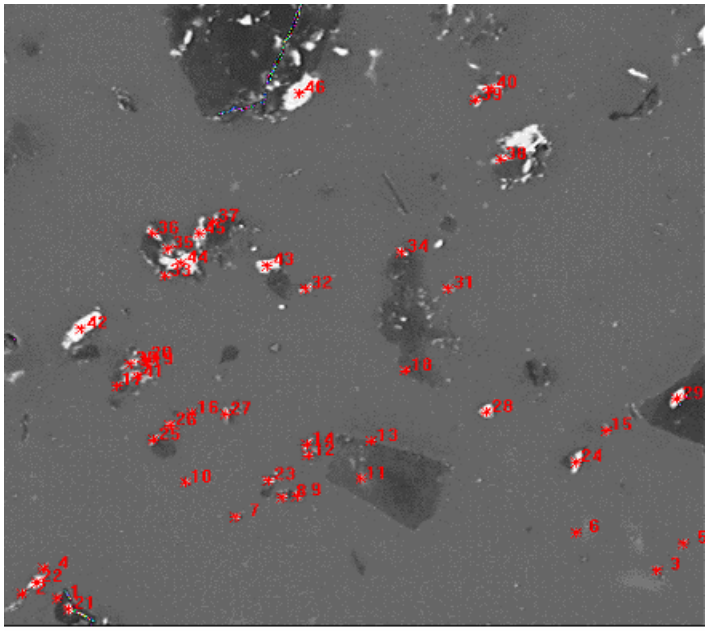

Figure 4.6: A backscattered electron image at a higher magnification (500x) level than Figure 4.5. The actual analytical points are superimposed in red.

It is for this reason that to position the beam at the centre of a pre-defined mineral grain is not acceptable.

Instead, the method adopted by CSIRO (QEM*SEM) in positioning a raster of equally spaced points across an included or excluded mineral grains is preferable. The QEM*SEM technique could not be used in its current form at the time of this research as the technique is unable to distinguish between the organic fraction and the mounting epoxy resin. This is a prerequisite for this research as it is crucial to identify and quantify the association characteristics between mineral matter and the organic fraction.

To overcome the shortcomings of the PRC techniques available, a new methodology was designed. Based on the strengths of the QEM*SEM method and of image analysis algorithms, this method was able to separate the organic fraction from the mounting medium (epoxy resin).

A further feature of any CCSEM analysis is the automatic identification and classification of minerals from the X-ray elemental counts. To achieve this, a unique classification scheme for the mineral matter in coal, and for the minerals or phases in fly ash, had to be developed.

The CCSEM analytical method and mineral identification scheme developed for this thesis will be described in the following section.

4.6.1 TSI-CCSEM methodology

The Technology Service International (TSI) CCSEM system is used to analyse pulverised fuel, fly ash and slag deposits. The TSI CCSEM system comprises a CAMSCAN CS44 scanning electron microscope (SEM), an Oxford ISIS microanalyser, a windowless light element energy dispersive X-Ray detector, a backscattered and secondary electron detector and the standalone ASCAN automated mineral identification and processing software. For a detailed review of scanning electron microscope and the different components refer to Postek et al (1980).

The ISIS system automatically controls the scanning electron microscope. During a routine analysis the ISIS software controls all stage movements and the positioning of the electron beam during image acquisition (scanning) and X-ray acquisition. Since the backscattered electron image (BSI) is an atomic weight contrast image it is preferable to a secondary electron image (SEI) as the atomic weight variation is used to distinguish between the minerals and the organic fraction. IMQUANT-AUTO is the image analysis module within ISIS. Image analysis routines using standard image analysis algorithms are used to threshold the BSI, define the particles and to establish the regularly-spaced grid of analytical points.

Anglo American Research Laboratories (AARL) developed the ASCAN software for the automated analysis of base metals, beach sands and a variety of metallurgical samples. ASCAN software provides the method of automatically classifying and identifying inorganic and organic components in coal, fly ash and slag deposits. The data is written to a comma separated ASCII file generated by the ISIS system. The data comprise electron beam positions, stage coordinates, raw X-ray counts of predefined elements and total X-ray counts for each analytical point. ASCAN software is written in a 4GL language called PV-WAVE (designed by Visual Numerics International, VNI).

The TSI-CCSEM operational flow diagram is summarised in Figure 4.7.

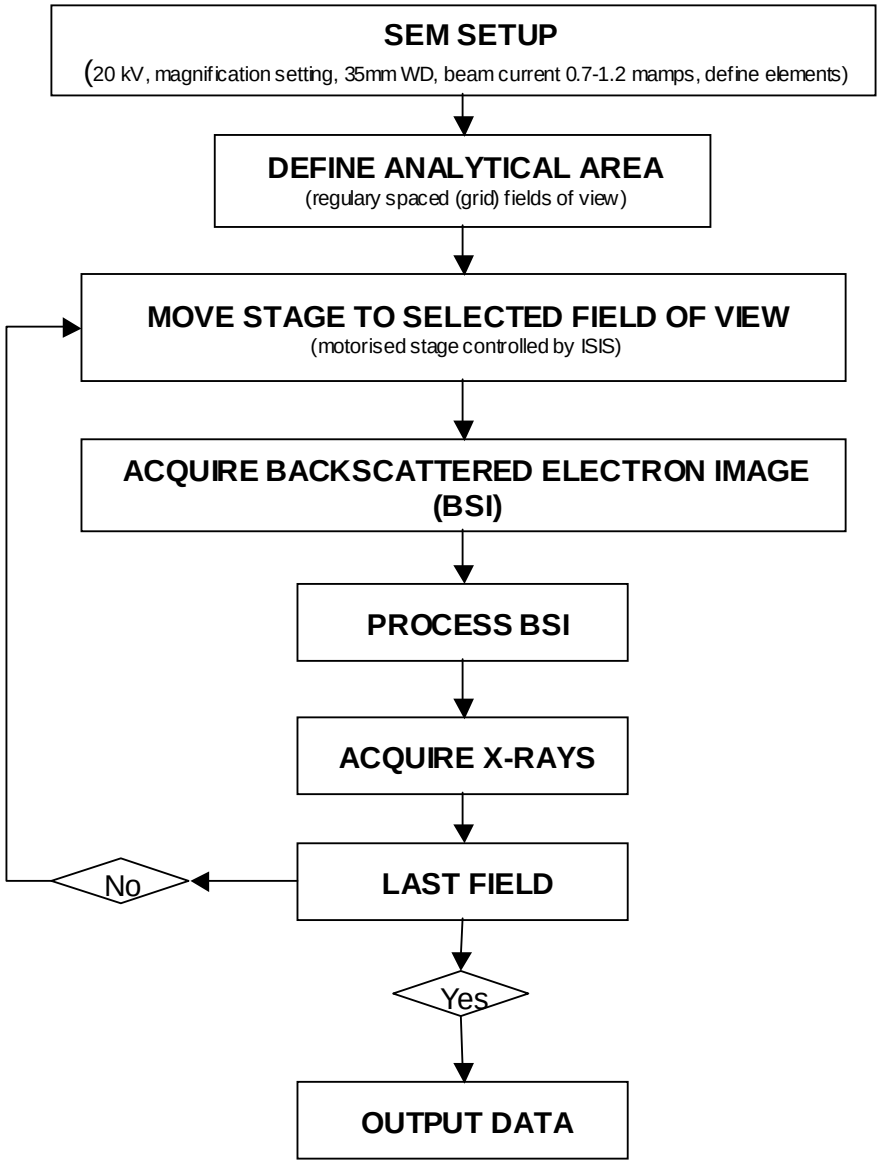

Figure 4.7: CCSEM operational flow diagram

4.6.1.1 TSI-CCSEM analytical conditions

To ensure consistency, the TSI-CCSEM is set up using the same analytical conditions. These are an acceleration voltage of 20 kV, a specimen beam current of 0.7 to 1.2 mA and a working distance (WD) of 35 mm. The magnification setting is dependent on the size fraction analysed. Typical magnification settings

are 100X for the +75 μm sized fraction, 300X for the -75+38 μm sized fraction and 500X for the -38 μm sized fraction.

In the context of this thesis, the field of view is defined as the visual surface area scanned and analysed (see Figure 4.8). The size of the field of view (image) depends on the magnification setting selected (refer to Table E.1). The image sizes vary from 1076x841 μm at 100X, 359x280 μm at 300X and 215x168 μm at 500X. Prior to any analysis, a regular grid of fields of view are defined and analysed. The number of fields of view analysed in this study varied from 100 to 150 per polished section. The X- and Y-coordinates of the upper left-hand corner of the field of view were recorded and used by ISIS to position the sample during the automated CCSEM analysis.

Once the motorised stage under instruction from ISIS has moved to the current field of view, a backscattered electron image (BSI) is acquired. Coal is black and mineral matter is white in a backscattered electron image. Each BSI image has a pixel resolution of 512x400. The backscattered electron intensity is scaled between dimensional less values of 0 (black) to maximum of 255 (white).

The X-ray counting time for each analytical point is set for 100 milliseconds. This is significantly faster than traditional CCSEM technique/procedure that have analytical times varying from 1 to 25 seconds. The processing time is set to ensure that a maximum count rate is achieved. The X-ray spectrum is subdivided into predefined ”elemental windows”, and the total counts for each ”elemental window” are recorded (see Table 4.1).

Table 4.1: Elemental energy window range.

Element	Spectra Line	Energy Range (eV)	
		Min	Max
Carbon - C	Kα	0.1975	0.3675
Nirtrogen - N	Kα	0.368	0.428
Oxygen - O	Kα	0.44	0.610
Fluorine - F	Kα	0.62	0.7525
Sodium - Na	Kα	0.9625	1.1325
Magnesium - Mg	Kα	1.1675	1.3475
Aluminium - Al	Kα	1.4075	1.5675
Silicon - Si	Kα	1.6475	1.8275
Phosphorous - P	Kα	1.9275	2.1075
Sulphur - S	Kα	2.2075	2.4075
Chlorine - Cl	Kα	2.5175	2.7375
Potassium - K	Kα	3.2075	3.4275
Calcium - Ca	Kα	3.5875	3.8075
Iodine - I	$L\alpha_1$	3.828	4.068
Titanium - Ti	Kα	4.3875	4.6275
Chrominium - Cr	Kα	5.2875	5.475
Manganese - Mn	Kα	5.7675	6.0275
Iron - Fe	Kα	6.2675	6.5275

4.6.1.2 TSI-CCSEM - image analysis routine

A backscattered electron image is a grey image comprising of 512x400 pixels with varying backscattered electron intensity values ranging from 0 to 255. The developed TSI-CCSEM image analysis processing steps are listed below:

1. Threshold the backscattered electron image into three discrete grey level groups. These groups include the “white” mineral matter, the “grey” iodinated epoxy resin and the “black to dark grey” organic fraction (coal in pulverised fuel and char in fly ash).
2. Remove any particles touching the frame boundary. This ensures that a complete particle is analysed and not a particle bisected by the frame boundary.

3. Removed particles that are smaller than the lowest size of the sized fraction. Small particles in the field of view could be attribute to poor screening and/or due to the size bias introduced by sectioning a particle (see Figure 4.3).
4. Combine the “white” mineral matter with the “black to dark grey” organic fraction to produce a composite binary image that defines the individual particles in the selected field of view.
5. Define the boundary of the composite particle and fill in any artificial holes produced through incomplete thresholding. This will occur when the grey level of a pixel within the boundary of a particle is within the threshold range of the “grey” iodinated epoxy resin. This typically occurs along a boundary between “bright” mineral matter and “black” coal and is also due to polishing imperfection introduced through poor sample preparation.
6. Superimpose the regular grid of points over the processed binary image of the composite particles. The analytical point is where the superimposed grid and the composite binary particles intersect.
7. Record the coordinates of each analytical point relative to the top left hand corner of the field of view. The coordinates are used to position the electron beam during X-ray acquisition.

On completion of the image analysis routine, the electron beam is positioned at each analytical point (Figure 4.8) and a 100 msec X-ray spectrum is acquired. Elemental counts for the pre-defined elements (Table 4.1) minus the predefined background level are recorded and written to an ASCII file. This elemental data is written to an ASCII file for further processing by the ASCAN software. Elemental count data constitute the input for the unique automated mineral identification routine.

The final output on the completion of the TSI-CCSEM image analysis routine is illustrated in Figure 4.8 (for pulverised fuel) and Figure 4.9 (for fly ash). The analytical points are depicted as black dots (Figure 4.8) or as a red crosses (Figure 4.9).

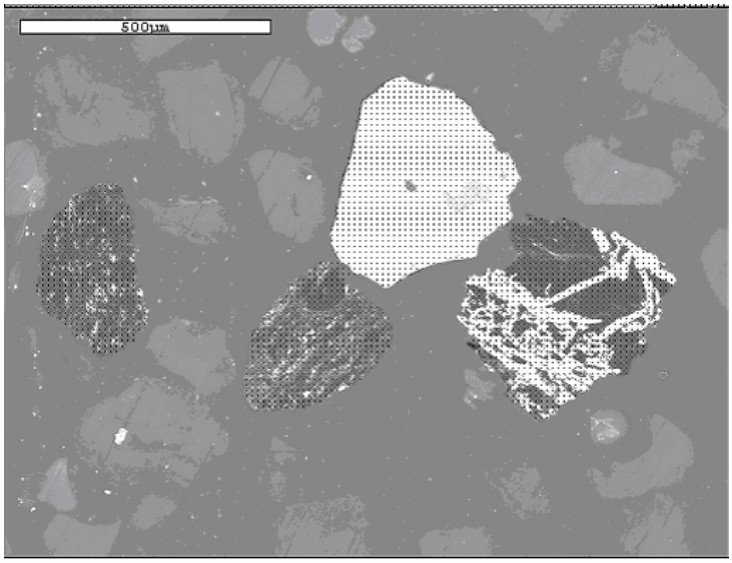

Figure 4.8: A processed backscatter electron image of pulverised fuel with the regular grid of analytical points superimposed. The scale bar represent 50 μm and the estimated point spacing is 11.21 μm.

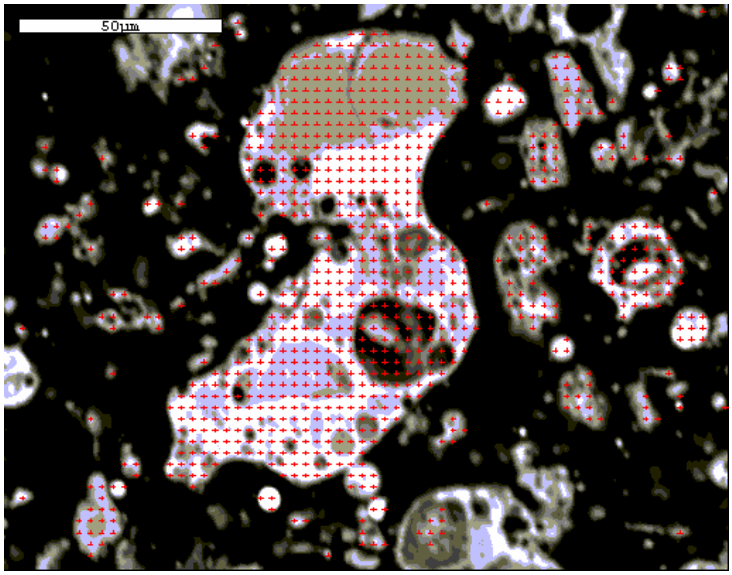

Figure 4.9: A processed image of unscreened fly ash with the superimposed regularly-spaced analytical points (red crosses). Note that holes (black to light grey) are included. The scale bar represents 50 μm and the point spacing is 2.75 μm.

4.6.1.3 TSI-CCSEM analysis of slag deposits

Slag deposits on the removable slag sleeves are not discrete particles but particles fused onto the removable mild steel sleeve. The CCSEM method described to measure mineral distribution in pulverised fuel and fly ash had to be modified to make provision for variations in the slag deposits (see section 4.6.1.2).

The analytical procedure developed to analyse the sectioned slag sleeves is as follows:

- Fields of view with visual evidence of slag deposits were manually selected for analysis.
- Backscattered electron images were acquired and saved to disk for off-line image processing.
- A single threshold value is used to separate the epoxy resin from the slag deposit and the removable sleeve.
- A grid of points is superimposed upon the threshold image and analytical points defined. This is analogous to Figure 4.8 and Figure 4.9.
- An electron beam is positioned at each analytical point and a 100 msec X-ray spectrum is acquired. Elemental counts for pre-defined elements are computed and stored to an ASCII file.

The image analysis routine used to overlay the grid on the threshold image did not distinguish between the removable steel sleeve and the ash deposited on the surface (Figure 4.10). In order to distinguish the slag sleeve from the slag deposit, the saved images were processed off-line and the analytical points superimposed on the slag sleeve were identified and separated from the analytical points covering the slag deposit. A new results file with only accepted X-ray elemental counts for the slag deposit was written. The adoption of this approach ensured that only the slag deposits and not the slag sleeve would be quantified.

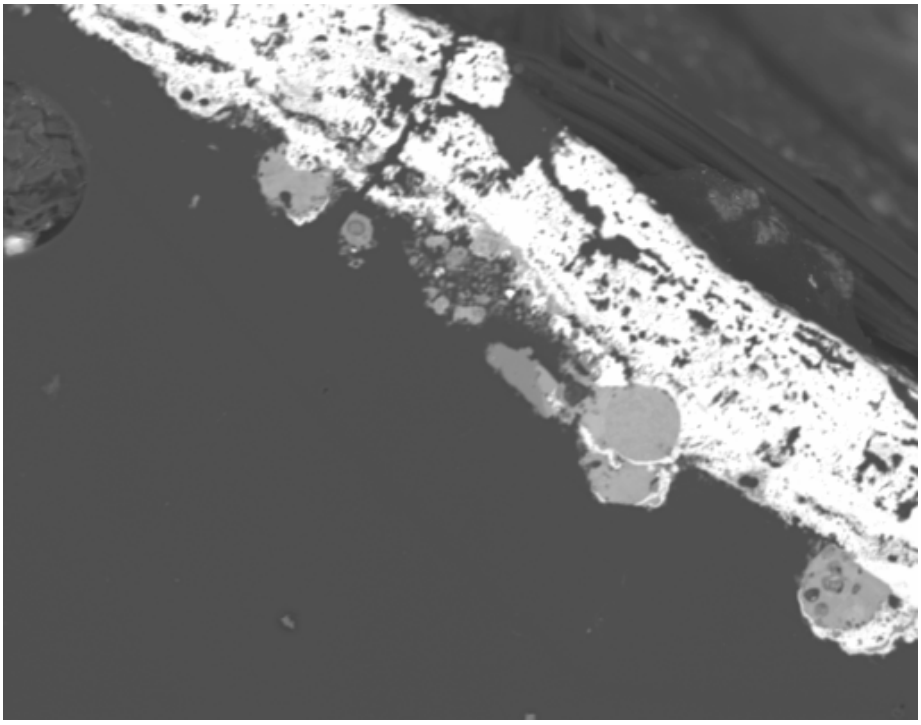

Figure 4.10: A backscattered electron image of a slag sleeve section. The fly ash particles are light grey and the actual slag sleeve (mild steel) is white. The width of large fly ash particles are 30-40 μm.

4.6.2 TSI-CCSEM Mineral identification

Elemental data derived from the TSI-CCSEM formed the principal data input into the ASCAN software. The ASCII file consists of stage coordinates of each field of view, field of view number, the analytical point number, the X-ray counts for each predefined elemental window, total X-ray counts, beam coordinates and the backscattered electron intensity of the each analytical point. The effect of the X-spectrum background is taken into account and the X-ray counts for each elemental energy window are corrected accordingly.

The ASCAN software reads in the ASCII file and stores the data in data structures. X-ray counts are normalised and the relative elemental proportions are computed. The ASCAN mineral identification is based on normalised elemental counts and not on normalised oxide proportions as used by a few CCSEM systems.

Typical CCSEM methods, such as the QEM*SEM species identification program (SIP), adopted a sequential search approach, where the unknown elemental data are compared to a database of pre-defined rules. Mineral identification by QEM*SEM is based on elements which must be present, elements that can be present and elements which must not be present. To refine the rule further, QEM*SEM includes elemental ratios and backscattered electron intensity as further methods of classifying the unknown X-ray data. In a sequential search, the following criteria can be checked:

$$A = B \text{ or } A \geq B \text{ or } A \leq B \text{ or } A > B \text{ or } A < B$$

In this context A could be an unknown elemental count and B the rule criterion specified in the database. The answer to the above question in a sequential search would be either YES or NO, analogous to the binary code of 1 or 0. In contrast, the ASCAN mineral identification is based on the principles of fuzzy logic. In fuzzy logic the question asked is:

Is component X equal to fuzzy number A.

Once again, X could be an unknown elemental count and B the fuzzy number specified in a database. Instead of a YES or NO, fuzzy logic will assign a truth-value or the probability (α-value) that A is equal to B. The outcome of fuzzy logic is the probability factor varying from 0-1 that A is equal to B (Figure 4.11).

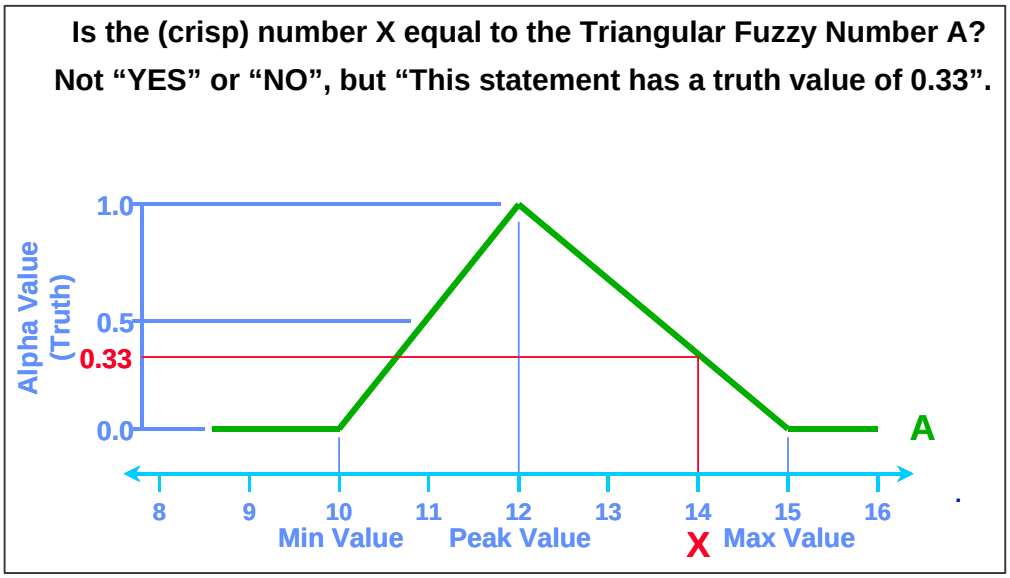

Figure 4.11. Fuzzy logic principles utilised by ASCAN for mineral identification

In the context of mineral identification, the kaolinite fuzzy logic rule in the mineral identification database is described in Figure 4.12.

Rule : Kaolinite : O=(0.15, 0.21, 0.32) & Al=(0.29, 0.35, 0.45) & Si=(0.23, 0.31, 0.42)

Normalised Counts: Oxygen : 0.23 Aluminium : 0.42 Silicon : 0.34

Truth Value : Oxygen : 0.82 Aluminium : 0.60 Silicon : 0.28

Figure 4.12: Kaolinite fuzzy logic rule and assigned truth values

A truth-value is returned for each of the elements. ASCAN software will return the minimum value of 0.28 for silicon. There is a 28% probability that the mineral is kaolinite. The normalised counts are compared with all the rules in the database and the truth-value is computed for each rule. The five top truth-values and the corresponding mineral identification are stored and the mineral with the highest truth-value is assigned to that analytical point.

The development of the fuzzy logic rules for each mineral in pulverised fuel or phase in fly ash and slag deposits is necessary prior to undertaking any mineral

identification. Randomly selected drill cores samples of the coal seams, floor rock, in-seam partings and roof rock were selected. These drill core samples were sampled from Optimum colliery, the main supplier to Hendrina power station. Polished sections were prepared and different minerals were located under the scanning electron microscope and used as reference minerals. The identities of the minerals were confirmed quantitatively by energy dispersive (EDS) X-ray analysis. For EDS analysis, a X-ray spectrum is acquired for minimum counting time of 50 seconds at a dead-time of between 20 to 60%. To simulate, the 100 millisecond-counting time used during the CCSEM analysis, the 50-second standard X-ray spectrum is randomly divided up into a 50 to 100 100 millisecond spectrum using Poisson statistics. The normalised element counts for each 100 millisecond spectrum are computed and used to establish the minimum, peak and maximum value of the fuzzy logic number (Figure 4.11). Alternatively, a regular grid of points can be superimposed over a large pure mineral grain and 100 millisecond X-ray spectrum acquired at each point. Using these two techniques, a comprehensive mineral identification library can be developed.

A major shortcoming of any automated mineral identification system is the effect of mineral boundaries, image artifacts and particle edges. If the electron beam were to intersect a boundary between two minerals, the resultant X-ray spectrum would be a combination of the two phases. To counteract the problem, representative spectra are obtained from these boundaries and incorporated into the mineral identification library. Unique mineral names such as “kaolinite>coal”, were assigned to describe these boundary artefacts. These artifacts could be assigned at a later stage to a particular mineral group or assigned as “other”. The strength of the mineral identification procedure lies in its flexibility. It is limited only by the operators’ imagination and attention to detail.

To speed up the mineral identification, the minerals in pulverised fuel were grouped into seven groups. These groups are summarised in Table 4.2.

Table 4.2. Primary mineral groups used for pulverised fuel

Mineral Group Name	Main Minerals
Sulphide/sulphate	Pyrite, gypsum, anhydrite, baryte
MgFeSilicate	Quartz
AlSilicate	Kaolinite, illite, orthoclase, muscovite, montmorillonite
Oxide	Hematite, magnetite, rutile
Carbonates	Calcite, dolomite, ankerite,siderite
Phosphate	Apatite, zircon, monazite
EpoxyCoal	Coal (organic component), epoxy resin (mounting medium)
Boundary	Boundary artefacts, unclassified or other

Developing a mineral library for minerals in pulverised fuel is easier than establishing a suitable mineral/phase library for fly ash and slag deposits. Minerals in pulverised fuel are described in literature and by definition must have fixed elements present within prescribed elemental ranges. For instance, kaolinite ($Al_2Si_2O_5(OH)_4$), must have Al, Si and O, but can have trace proportions of Fe and possibly Mg. The exception is the organic component (macerals), which in the context of this study is referred to as “coal”. Coal is not classified as a mineral as it has neither a regular crystalline structure nor a fixed elemental proportion. The organic (C, O, N and H) elemental proportion of the macerals is a function of the rank of the coal. Coal classification is based on the minor inorganic elements present in the coal and not on the different macerals (vitrinite, liptinite and inertinite). Although macerals have different O, C, H and N compositions, it is difficult for the CCSEM to distinguish between the macerals. This difficulty can be attributed to the inability of CCSEM to detect the light elements, H and N, and to the rapid acquisition rate of 100 millisecond per point. It was apparent in this study that the levels of S and C can vary appreciably and thus could be used to classify the “coal”.

The mineral composition of coal particles in Figure 4.8 is illustrated in Figure 4.13.

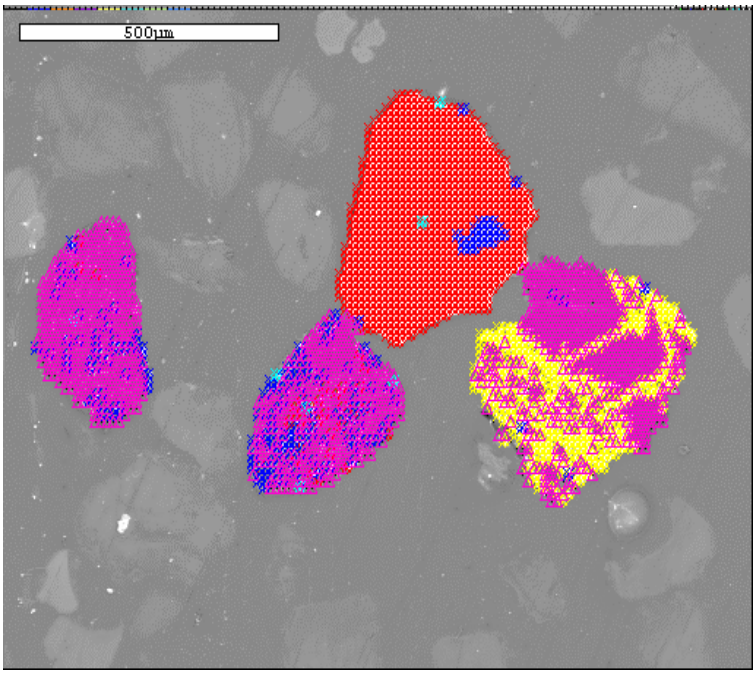

Figure 4.13: Identified coal particles.

The large quartz grain in Figure 4.13, has small kaolinite and illite inclusions which would not have being detected if the centroid method of beam positioning had been adopted. Positioning the beam at regular intervals across each particle ensures that the mineral composition, mineral grain size and mineral associations are adequately described.

In contrast, fly ash and slag deposits consist of minerals, amorphous glass phases of variable elemental compositions and unburnt carbon (char). A unique fly ash classification scheme was developed to accommodate the elemental forms of fly ash present. As was the case with the pulverised fuel, fly ash samples were examined in detail, and the variation in the elemental chemistry for different fly ash particles was obtained. Based on the chemistry, and a good understanding of the products resulting form mineral transformation of “coal” minerals, the fly ash classification scheme was developed. The fly ash names were derived from the perceived mineral source of the fly ash particle. For instance a fly ash with aluminium, silica, calcium and oxygen as its major elements must have been derived from kaolinite (source of aluminium (Al) and silica (Si)), quartz (source of silica (Si)) and carbonates (source of calcium). The assigned name is “kaolinite(carbonate)”. If there was iron present, the fly ash

name is “kaolinite(carbonate,pyrite)” as pyrite is the principal source of iron in the coal that was researched. These two fly ash types could only be derived from kaolinite, carbonates and pyrite, as there is no mineral in appreciable quantities in this coal source, which contain aluminium, silica and calcium.

Fly ash particles with only aluminium, silica and oxygen represent the transformation products of kaolinite (metakaolinite, silicon spinel and mullite (see Figure 3.1). Since the fly ash phase nomenclature scheme refers to the original source mineral in coal, all Al-Si-O bearing fly ash is termed “kaolinite”.

The major and minor fly ash phases defined for this study are summarised in Table 4.3.

Table 4.3: Preliminary classification groups of fly ash and slag deposits

Fly Ash Group Name	Origin
Ca-Carbonate	Prediminately Ca-oxide, Ca-Mg-oxide or Mg-oxide with varying proportions of C. Represents the incomplete carbonate transformation products.
Ca-Oxide	Ca-carbonate, excluding C. Represents the complete transformation of carbonates (calcite and dolimite).
Kaolinite	Predominately Al-Si-O representing the mineral transformation of kaolinite. Includes metakaolinite, silicon spinel and mullite
Kaolinite(pyrite,carbonate)	Predominately Al-Si-O with minor to trace proportions of Fe, Ca and Mg. Represents the interaction of kaolinite, pyrite and the carbonates, calcite and dolomite.
Kaolinite(carbonate)	Al-Si-O with minor to trace proportions of Ca and Mg representing the interaction of kaolinite with calcite and dolomite.
Kaolinite(pyrite)	Al-Si-O with minor to trace proportions for Fe representing the interaction of pyrite with kaolinite. Can have trace concentrations of S.
Kaolinite(K,Ti)	Al-Si-O with minor to trace concentrations of K and Ti. K is probably derived from illite/muscovite and Ti from mica and possibly Ti-oxide.
Orthoclase	Al-Si-K-O in similar proportions to orthoclase felsdspar found in pulverised fuel (see Table 5.5).
Quartz60Kaol40	Si-Al-O with Si concentrations greater than the expected Si concentration of metakaolinite. Represents mixture of quartz and kaolinite in an estimated proportion of ±60:40.
Quartz80Kaol20	Si-Al-O with elevated Si concentrations analogous to mixture of quartz and kaolinite in an estimated proportion of ±80:20.
Quartz	Si-O with trace concentrations of Al and possibly Ca,Mg,Fe and K. Represents the mineral transformation product of quartz
Iron-oxide/pyrite	Capture products of pyrite transformations. Includes pyrrhotite, pyrite (not transformed), Fe-S-O phases and Fe-oxide (hematite and magnetite). Represent fly ash particles with varying proportions of Fe, S and O. Trace concentrations of Ca,Mg,Al,Si and K are possible
Ti-oxide	Ti-oxide. Final transformation product of Ti-oxide (rutile?)
Char	Uncombusted remains of “coal”. Predominately C and O
Unmatched	Describes unclassified fly ash particles, which cannot be allocated into a specific class. Varying proportions of Al,Si,Ca,Mg,K,Fe,Ti, O, Cand S

The preliminary list of fly ash groups is complex and is designed to represent the potential products of mineral matter transformations in the pulverised fuel boiler.

Fly ash particles can be complex and contain more than one fly ash phase (Figure 4.14).

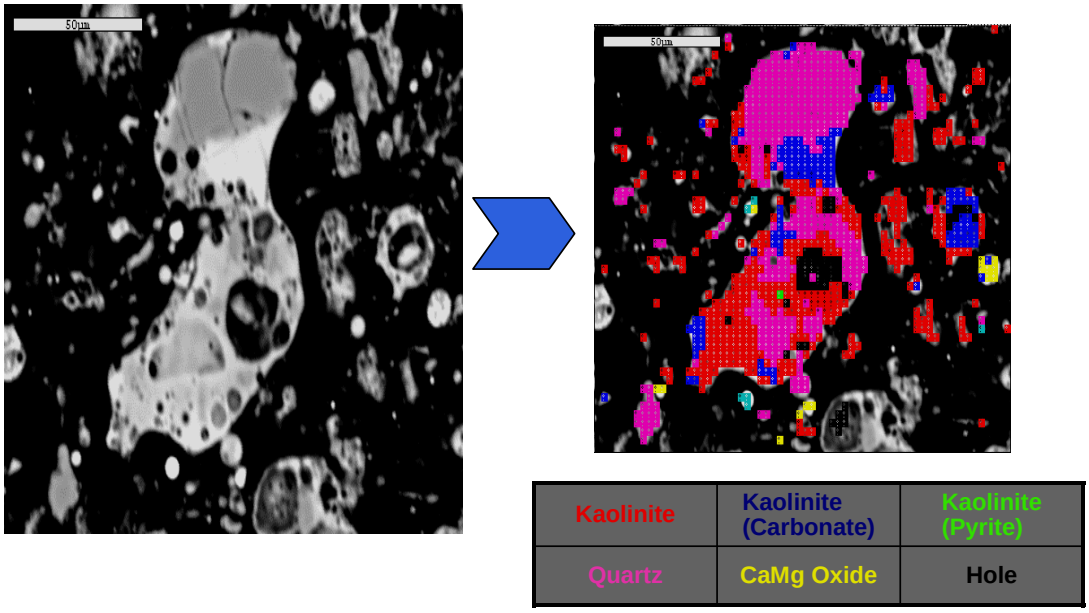

Figure 4.14: Identified fly ash particles using the developed ASCAN fly ash mineral identification libraries

A large fly ash particle (Figure 4.14) consists of unaltered quartz grains associated with the fly ash phases kaolinite and kaolinite (carbonate).

The fly ash mineral identification scheme is used to classify minerals and phases in slag deposits (Figure 4.15).

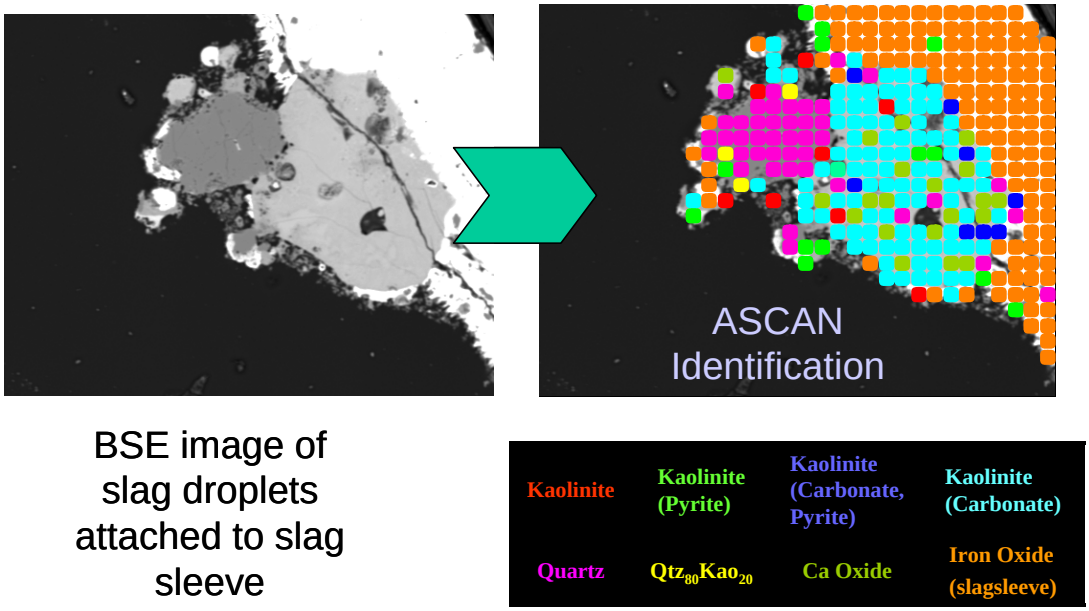

Figure 4.15: Detailed mineralogy of slag droplets adhering onto slag sleeve (orange).

In summary, the developed ASCAN mineral identification libraries and analytical methodology allow for the detailed description of coal, fly ash and slag deposits.

4.6.3 TSI-CCSEM output

The mass-percent mineral and coal distribution in pulverised fuel, the mass-percent phase distribution in fly ash and slag deposits, the mineral grain sizes, particle sizes, particle association characteristics, elemental composition and average particle density are the major outputs from ASCAN. Each of these parameters is important in describing the particle characteristics and form-required data for the fly ash formation model. The different parameters required for measuring the typical ASCAN output are described in detail in Appendix G.

The mass percent mineral distribution is derived from the volume percent mineral distribution of the particular phase in the sample. As stated in the introduction to this chapter volume percent is determined by applying the first law of stereology. In simple terms, the volume percent is the proportion of points intersecting a particular phase divided by the total number of points analysed. This technique is analogous to the manual “point count” method adopted by most petrographers to describe the maceral and microlithotypes volume percent.

The density of the mineral is used to compute the mass percent mineral distribution. The formula used is:

$$Mass\%_x = \left(\frac{volume\%_x * \rho_x}{\sum_0 volume\% * \rho} \right) * 100.0 \qquad \textbf{4.1}$$

The density of minerals in pulverised fuels is well documented and can be found in authoritative mineralogical references such as Deer et al. (1966) and on the webpage www.webmineral.com. The density of the coal is based on the maceral distribution and documented densities of macerals (Faclon et al., 1986).

Unfortunately, a large proportion of the phases in fly ash and slag deposits are amorphous. As such, the densities are not documented. Exceptions are the recognised fly ash phases such as quartz, metakaolinite, mullite and iron oxide (hematite and magnetite). Fortunately, the glass manufacturing industry has developed a technique for computing glass densities from the elemental composition of glass. The Huggins and Sun method described in Appendix H is used to calculate the respective densities of fly ash phases.

The average **particle density** is simply a weighted average density of all the constituents (minerals and macerals) in a coal particle.

Determining the **particle and mineral grain sizes** from a cross section is not a true reflection of the actual grain sizes. Even if it were possible to measure the three-dimensional grain or particle size it would be difficult to define which aspect (long axis, short axis) of the particle should be measured. The orientation of the sectioned plane (Figure 4.3) has a crucial influence on the measured size, representing the actual size of the particle. It was for this reason that the sample was screened into closely-spaced size classes. This reduced the possibility of underestimating the mineral and particle grain sizes. In the context of this study, the three size parameters used are the equivalent circle diameter (ECD), the maximum and minimum intercept length, and the average intercept length bisecting a mineral grain or particle.

The average **elemental composition** of the pulverised fuel is based on the mass percent mineral or phase distribution and the average elemental compositions of the minerals as determined by quantitative energy dispersive analysis and from the literature. The CCSEM-derived elemental composition of pulverised fuel can be compared with the XRF ash elemental analysis (see section 4.4). In the context of this research, this comparison is one methods used to validate the CCSEM technique.

To determine the average composition of fly ash particles, it was necessary to derive algorithms for converting the total X-ray counts obtained from ASCAN into mass percent elemental proportions. This was achieved by analysing a suite of minerals that had variable concentrations of the common elements. The mass percent elemental concentration was determined through energy dispersive X-ray analysis. The ASCAN counts were derived by randomly breaking down the 50 second EDS spectrum into 50 100-millisecond X-ray spectra, and computing the average count for the element. The algorithms for the major elements are described in Appendix G.

The association and liberation characteristics of individual particles are based on computing the area of the total particle and the area percent proportion of the inorganic and organic components which make-up that particle. In the context of this study a particle is defined as an entity that consists of different mineral grains (Figure E.1)

4.7 TSI-CCSEM Mineral Proportions Validation

The four possible techniques, which could be used to validate the mineral proportions as determined by TSI-CCSEM are:

1. Other CCSEM systems
2. Quantitative XRD (SIROQUANT)
3. Quantitative optical microscope
4. Chemical analysis (ash-%, XRF ash elemental composition, carbonate content (inferred from CO_2 concentration) and total sulphur content).

Using other CCSEM systems proved to be problematical as the numerous round robin tests and comparative results indicate large discrepancies between the different CCSEM systems (see section 2.3.4). Two independent round robin investigation indicated that QEM*SEM is the more precise technique to describe the minerals in coal (Galbreath et al., 1996) (Phong-Anant et al.,1992). At the time of this research (1998), QEM*SEM was configured to only determine the characteristics of the minerals in coal and not the organic fraction (“coal”).

Quantitative XRD and optical microscope were also not conclusive as XRD tended to overestimate quartz and the optical microscope tended to under estimate the proportion of quartz and overestimate the proportion of clay minerals (Phong-Anant et al.,1992).

The XRF ash elemental analysis, ash percent proportion of carbonates and total sulphur content are indirect indicators of the mineral proportions and could be used to validate the proportion of minerals as determined by TSI-CCSEM.

Each technique described above is not without its particular faults and not necessarily ideally suited for validating the TSI-CCEM mineral abundance. Owing to the uncertainty of the CCSEM comparative results, the inability of QEM*SEM at the time to determine the mass percent coal proportion, problems associated with quantitative XRD and the optical microscope these systems were not considered.

Chemical analysis, although not ideal was selected over the other techniques purely because these analyses were undertaken on each sample. In addition, these analyses are routine and the laboratories follow audited analytical procedures (Appendix F).

A direct comparison between an XRF-derived ash elemental analysis and CCSEM deribved elemental analysis is not feasible as the XRF ash elemental analysis are reported as the oxide composition of the ash derived from the coal, whereas the calculated CCSEM elemental proportions are based on the absolute mass percent proportions of the minerals in coal. To accommodate these differences the following calculations were undertaken:

1. A XRF elemental analysis is the elemental composition of the ash derived from a coal. CCSEM elemental analysis is the calculated elemental proportions based on the mass percent mineral abundance and the standard elemental composition of the mineral (Appendix G). Simplistically, XRF elemental analysis is an indirect measure of the elemental composition of the coal, whereas CCSEM elemental analysis is absolute indication of the mineral elemental compositions. In order to compare the two elemental compositions it is necessary to normalise the XRF ash elemental proportions to the total mass percent mineral proportion in the sample as determined by CCSEM.
2. Iron (Fe) is reported as Fe_2O_3 in XRF ash elemental analysis, which assumes that all Fe is ferric (Fe^{3+}) and not ferrous (Fe^{2+}). To correct the discrepancy, the proportion of iron is calculated from the XRF Fe_2O_3.
3. During the process of ashing, the sulphur derived from pyrite transformation and organic sulphur in coal reacts with carbonates to form calcium sulphates. The reported SO_3 in the ash elemental analysis is therefore not a true reflection of the absolute sulphur concentration in the sample, but an indication of the proportion of sulphur that has reacted with carbonates. The comparison excluded the proportion of sulphur tri-oxide (SO_3).

The reported ash percent is not a direct measure of the mass percent mineral matter proportion as, during the process of ashing, some of the volatiles associated with minerals (H_2O from clays, CO_2 from carbonates and SO_3 from pyrite) are emitted. It is possible to calculate the mass percent of mineral volatiles from the CCSEM mass percent mineral distributions and to subtract this value from the total mineral matter proportion as derived from the CCSEM results. This calculated ash percent could be compared to chemically derived ash percent.

The proportion of carbonates could be inferred by measuring the mass percent proportion of carbon dioxide (CO_2) gas evolved on mixing the coal with hydrochloric acid (HCl). Similarly, the proportion of CO_2) associated with the carbonates could be calculated directly from the measured CCSEM carbonate mineral proportions.

Chemically determined total sulphur content is the total sulphur associated with pyrite and organically bound sulphur. These proportions could be calculated from the CCSEM derived mass percent pyrite and the proportion of organically bound sulphur from the mass percent coal.

The ash percent, the XRF ash elemental analysis, the proportion of carbonates inferred from carbon dioxide (CO_2) concentration and the total sulphur content were used to validate the CCSEM mineral distribution in the coal.

4.8 Fly Ash Formation Model

4.8.1 Principals and assumption

The output of many of the fly ash formation models described in chapter 3 serve to predict the fly ash particle size distribution and elemental composition of these modelled fly ash particles. Modelled fly ash characteristics are based on measurements (CCSEM) or statistical predictions. Model input is typically the mineral attributes (mass percent abundance, size, minerals compositions and associations) in coal.

Models by Field (1967) Loehden et al. (1989), Barta et al. (1993) and Willemski et al. (1992) have proposed coalescence and char fragmentation mechanisms that control the size and elemental characteristics of the resultant fly ash. All the models listed above are based on included minerals and do not consider extraneous mineral particles. The Yan model (Yan et al. (2002)) assumes partial coalescence for included minerals and simulates fragmentation for excluded minerals. Another shortcoming of many stochastic models (Charon et al. (1990), Barta et al. (1993) and Willemski et al. (1992)) is the assumption that minerals are randomly distributed in the coal matrix.

The fly ash formation model developed for this research is based on the observed particle characteristics and the aspects of the numerous fly ash formation models described above and in Chapter 3. Cognisance was taken of the importance attached to the concept prevalent in all of these models, namely

the fly ash-forming mechanisms of coalescence, partial coalescence (random coalescence) and non-coalescence (fragmentation).

Simplistically the three fly ash forming mechanisms commonly used in many models can be explained as follows:

1. Coalescence – All the included mineral matter in coal coalesces to form a single fly ash particle per coal particle combusted. The elemental signature and size are controlled by the properties of the included minerals.
2. Non-coalescence (fragmentation) – Each included mineral grain forms a single fly ash particle. The size and chemical properties of the fly ash are controlled by the subsequent mineral transformations undergone by the released included mineral grain.
3. Partial coalescence or random coalescence (RC) – The molten mineral matter on the surface of a combusting char particle coalesce to form fly ash particles. Coalescence of the surface particles is stopped when the combustion is reverted from surface to internal combustion. The number of fly ash particles, their size and their chemical composition is a function of the spatial distribution of the included minerals in coal particles.

Typical particle types in a pulverised fuel are "ash free" organic rich coal particles, coal particles with varying proportions of included minerals and organic component and extraneous mineral-rich particles. Three sub-models were developed to accommodate these three particle types, the fly ash formation mechanisms described above and the mineral transformation processes described in Chapter 3. An explanation of the concepts and assumptions on which these three sub-models were based follows:

1. **The included mineral fly ash formation sub-model** is based on the principals of coalescence, partial coalescence or fragmentation described above. With the detailed CCSEM description of each coal particle it is possible to simulate coalescence, partial coalescence and fragmentation. For coalescence the model assumes that all included minerals will coalesce and the resultant elemental composition is a weighted average of the elemental compositions of the included minerals. To simulate partial coalescence it is hypothesized that each

touching included mineral grain will coalesce to form a single fly ash particle, whereas each included mineral grain completely surrounded by organic fraction will not coalesce and will form a single fly ash particle per included mineral grain (Figure 4.16). For fragmentation each discrete included mineral is a separate entity and the mineral grain will undergo the expected mineral transformations and form a fly ash particle for each included mineral grain. Only those coal particles with a mineral matter content of less than 60 area percent is considered as a coal particle with included minerals.

2. **Ash free coal particle fly ash formation sub-model -** During the preliminary mineralogical investigations X-ray spectra were acquired from coal particles that visually appeared to have no included minerals. Trace and minor concentrations of inorganic elements S, Al, Si, Ca, Fe and Mg were identified in these “mineral free” coal particles. It is likely that the S was organically bound and the other inorganic elements were either organically bound or associated with sub-micron mineral grains smaller than the CCSEM electron beam resolution of 2-3 μm (see section 5.6). The “**ash free**“ **coal particle fly ash formation sub-model** was devised to accommodate these “ash-free” coal particles. The model computed the average inorganic element composition of the particles and assumes that one-micron (1 μm) fly ash particle will form.
3. **Extraneous fly ash formation sub model -** In the context of the ash formation model, an extraneous particle is defined as a particle with a mineral matter content exceeding 60 area percent and the coal fraction is less than 40 area percent. This is analogous to microlithotype, minerite (appendix E). In the **extraneous fly ash formation sub model,** it is assumed that irrespective of size all minerals in the extraneous particle will undergo normal mineral transformations and produce one ash particle for each extraneous coal particle. The extraneous fly ash formation sub model did not provide for fragmentation of extraneous particles. This could be common in the case of pyrite, carbonates and possibly kaolinite rich extraneous particles.

The outputs of these sub-models are fly ash size distribution and mass percent fly ash phase abundance based on the fly ash phase classification scheme described in section 4.6.2 and Table 4.3.

By comparing the model outputs to the measured fly ash size distribution and mass percent fly ash phase abundance it was possible to hypothesise which fly ash formation process can be used to predict the properties of the fly ash.

In terms of size distribution comparisons, the principle was based on the assumption that coalescence would produce a coarser particle size distribution than the measured coal mineral grain size distribution and fragmentation, a finer size distribution than the measured coal mineral grain size distribution (Figure 4.17).

In terms of comparing mass percent fly ash phase abundance, coalescence will be indicated by fly ash phases, which have a combination of elements that are not present in the minerals in coal. For example, if included kaolinite were to coalesce with included calcite, then the resultant fly ash phase would be a combination of Al-Si-Ca-O in variable proportions, depending on the original proportion of kaolinite and calcite in the coal particle. In the context of the fly ash classification scheme, a Al-Si-Ca-oxide particle is termed kaolinite(carbonate). If fragmentation were to be the dominant fly ash formation process, then the modelled fly ash mass percent phase will be equivalent to mass percent proportion of the transformation products of the individual minerals. The proportion of these phases will be directly proportional to the mass-% distribution of the source minerals in the coal (Figure 4.17).

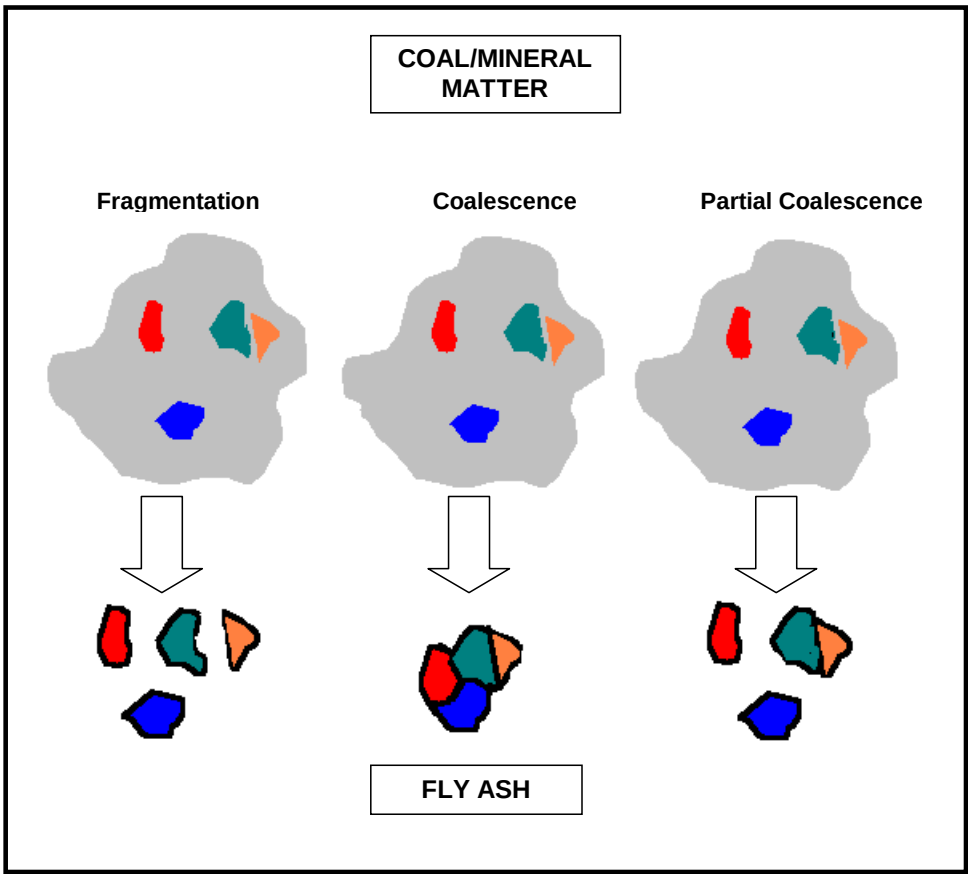

Figure 4.16: The fly ash forming mechanisms of fragmentation, coalescence and partial coalescence described in the included mineral fly ash formation model.

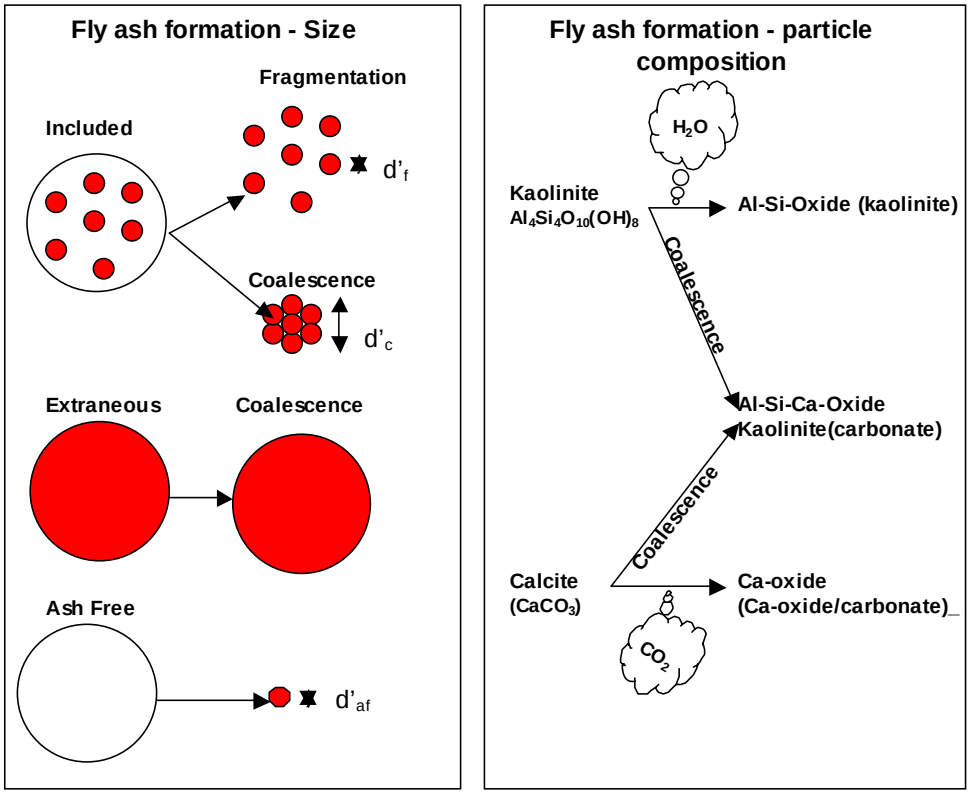

Figure 4.17: Principles of fly ash formation prediction

4.8.2 Methodology

The model is written in a 4GL language called PV-WAVE and the output processed using EXCEL macros. The fly ash formation model comprises of 172 individual PVWAVE routines and 20 Excel macros were written by the author.

Each coal particle analysed is classified based on the area proportion of mineral matter into either “ash free”, “included” or “extraneous/excluded” coal particles. Depending on the particle type, the applicable sub-model is applied. In the **included mineral fly ash formation sub-model** “included” particles are processed for each of the three fly ash formation mechanisms, namely coalescence, partial coalescence and fragmentation, based on the principals illustrated in Figure 4.16 and Figure 4.17 described above.

In obtaining the size distributions and mass percent fly ash phase abundance, the following assumptions are made for each sub-model:

1. **Included mineral fly ash formation sub-model** - The size of the modelled fly ash particle is the individual size of the included mineral grains (fragmentation) or the total size of the coalescing included minerals (coalescence or partial coalescence). The average elemental concentration of the coalesced fly ash particles (coalescence or partial coalescence) is the weighted average of the elemental proportions of the original included minerals. The weighting factor is the area proportion of the respective included minerals in the coal particle. The proportions of C, O, S and H associated with the volatile components, CO_2 (carbonates), S (pyrite) and H_2O (clay minerals) are not included and are deemed to have escaped from the system. In contrast, the elemental proportions of the fragmented fly ash particles are based on the original elemental proportions of the source mineral minus the volatile components and the expected transformed product of the original source mineral. For pyrite, the expected transformed product is iron-oxide and for carbonates it is Ca-oxide or Ca-Mg-oxide depending on the original carbonate.
2. **Extraneous fly ash formation sub-model** - The size of the fly ash particle is the same size as the original extraneous mineral particle. Elemental composition is the weighted average (by area-proportion) of the minerals in the extraneous particle.
3. **“Ash-free” coal particle fly ash formation sub-model** – Any ash free particle is made up of a number of analytical points (Figure 4.8). For each analytical point, the X-ray counts for the predefined elements (Table 4.1) are recorded. If the X-ray count for the inorganic elements (Mg, Al, Si, Ca, K, S and Fe) exceeds a minimum “background” value the elemental concentration would be calculated using the algorithms described in Appendix G. If the X-ray count of the element were lower than the “background” value then it would be assumed that the element is not present and the elemental concentration is set to zero. The inorganic elemental composition of the “ash-free” coal particle is the average of the inorganic elements of each analytical point within the “ash-free” coal particle. The modelled fly ash composition from the “ash-free” particle is

the normalised inorganic elemental composition of the “ash-free” coal particle. The size of the modelled fly ash is assumed to be 1 μm.

The measured boiler fly ash mineral identification is based on the elemental proportions of each analytical point (see Appendix G, **point analysis**), whereas the modelled fly ash phase identification is based on the weighted average elemental composition of the entire modelled fly ash particle (**particle analysis**). The particle analysis is analogous to scanning an entire particle, deriving the average elemental composition and using the average elemental composition to classify the particle based on the fly ash classification scheme (Table 4.3). In order to compare the fly ash phase abundance of the boiler fly ash to the modelled fly ash, it is imperative that the boiler fly ash identification should be based on whole fly ash particles and not on the individual analytical points, which make up the fly ash particle. To correct this impasse, the measured boiler fly ash is re-processed and the fly ash phase identification is based on the average elemental composition of the boiler fly ash particle. By adopting this process it is possible to compare the modelled fly ash phase abundance to the reprocessed fly ash particle-based phase abundance. This comparison is an important model validation step.

In deriving the final output, the modelled fly ash size distribution and mass percent phase abundance modelled from the extraneous and “ash-free” sub-model are combined with the outputs of the included mineral sub-model, assuming coalescence, partial coalescence or fragmentation.

4.8.3 Validation

The fly ash formation model simulates the combustion of single pulverised fuel particles and the formation of fly ash particles from the minerals in these coal particles. To validate this model, it is necessary to combust single coal particles under boiler conditions and to collect and analyse the ash particles formed from these coal particles.

The drop tube furnace (described in the following section) is ideally suited for generating ash particles from combusting individual coal particles under boiler combustion conditions.

A comparison of the measured drop tube furnace ash with the modelled ash distribution was used to validate the fly ash formation model. The impact of the boiler size and configuration (scale factor) had on fly ash formation could be inferred by comparing the modelled to the measured (obtained from within the boiler) fly ash mass-% phase proportions.

4.8.3.1 Drop tube furnace

The TSI (Technology Service International) drop tube furnace (DTF) is a laboratory scale combustor used to evaluate the ignition and combustion characteristics of current and future coals. Under normal conditions, the test coal is sized to 100 percent passing 106 μm and heated in pure nitrogen (N_2) to a temperature of 1400°C. The pre-charred material is screened into -75+38 and -38 μm sized fractions and combusted in an oxidising environment (3% O_2, 97% N_2) at temperatures varying from 1000 to 1450°C. The normal feed rate is 0.1g/min and typical residence times vary from one to four seconds.

The DTF comprises a vertical, electronically heated two-metre long aluminium tube (70mm diameter) with a ceramic outer-layer. A water-cooled injection probe feeds the sample through the vertical tube. On entry the particles are immediately exposed to a heating rate of 10000°C/s, which is similar to the particle heating rates in a boiler.

In the context of this research, the drop tube furnace is not used to evaluate the ignition and combustion characteristics of the coal, but instead is used to validate the fly ash formation model and to establish the impact of temperature and the combustion environment (reducing or oxidising) has on ash formation. Since the DTF is considered a single particle combustor it is ideally suited to validate the fly ash formation model (see previous section). The oxidising environment could be simulated by combusting the coal in 3% oxygen and the reducing environment by combusting the coal in 1% oxygen.

Based on the ultimate, proximate and screened size analysis, the pulverised fuel from hole 2 at a depth of 0.5m was selected for the DTF tests. Each size fraction was combusted at 1000°, 1100°, 1200°, 1300° and 1400°C under oxidising and

reducing conditions. After each test, the ash was collected and analysed by CCSEM to determine the phase and size characteristics of the DTF fly ash. To simulate combustions conditions in the 200MW_e boiler, the sample was not pre-charred but heated to approximately 100 °C prior to its injection into the DTF. The DTF particle residence time of 2.8s is equivalent to the average particle residence time in a 200MW_e boiler.

4.9 Slagging Prediction Model

Two fly ash characteristics, which are important for initiating and sustaining the development of slag deposits, are the size and the “stickiness” of the fly ash particle. The “stickiness” is a function of the average fly ash particle viscosity. Viscosity is an important criterion controlling the ability of the fly ash to adhere to a surface. In principal, a low viscosity particle will have a higher degree of “stickiness” and will in all probability adhere to a surface, whereas a solid particle will probably bounce off the surface.

Since the major outcome of the fly ash formation model is the elemental distribution of fly ash particles, it is possible to calculate the viscosity of the individual particles and the corresponding slagging indices for each particle. The Watt and Fereday and Urbain viscosity models (see section 3.5) were included in the fly ash formation code to derive an estimate of the “stickiness” potential of each modelled fly ash particle. The input into these viscosity prediction algorithms was the calculated elemental oxide proportions for each measured and modelled fly ash particle. The average density of the modelled fly ash particles was calculated using Sun and Huggins method (Appendix H).

The elemental signature and physical characteristics (size) of the fly ash particles, which are likely to initiate and sustain, slag development could be derived by comparing the characteristics of the slag developed on the removable slag sleeve to the characteristics of the fly ash in the vicinity of the slag sleeve. The chemical signature of those fly ash phases enriched in the slag deposits can be derived. The mass percent abundance of these enriched ash phases constituted an important slagging prediction parameter in the slag prediction model.

The output of the slagging prediction model was the average slagging potential of coal and fly ash based on the temperatures at viscosities of 250 (T_{250}), 2000(T_{2000}) and 10000 (T_{10000}) poise and total Fe+Ca content. The total Fe+Ca content and T_{250} are calculated for each modelled fly ash particle and each measured fly ash particle. Each particle is then classified into a low, medium or high slagging category, based on the accepted ranges for Fe+Ca and T_{250} outlined in Table 3.5.

The ultimate slagging potential factor is the proportion of fly ash particles in the high slagging class for the different size fractions. It is perceived that high slagging particles in the -38 µm size fraction will exit the boiler via the flue gas and will not form a slag deposit. On the other hand those particles in the +38 µm size fraction, being coarser and denser, would be carried by the flue gas to the heat transfer surfaces, where if the conditions are suitable, they would actively promote and sustain the development of slag.

4.10 Conclusion

This chapter discussed the new techniques developed and the methodology used to achieve the principal objective of modelling fly ash formation from mineral matter attributes in coal. The model assumes that each combusting particle is a single entity which would produce (a) fly ash particle(s) with its own elemental signature, size and degree of “stickiness”, the latter being governed by the mineral attributes associated with or included in the combusting coal particle.

These new techniques and methodologies include the following:

1. developing a new suction pyrometer slag probe and removable sleeve to facilitate the simultaneous acquisition of fly ash samples and slag deposits from a fully operational 200MW_e boiler,
2. developing a new sampling preparation technique to separate coal from epoxy resin and to restrict the impact of sample segregation,
3. developing a new CCSEM-based analytical technique to qualify and quantify the morphological properties of mineral matter in coal, of fly ash phases and of slag deposits,
4. developing a unique fly ash classification scheme,

5. developing a fly ash formation model based on the inherent properties of the minerals in the pulverised fuel. The fly ash formation model was based on simulating the combustion of individual coal particles in a boiler and exploring the interactions of included mineral particles. Detailed data on the mineral/organic associations, mineral grain sizes and the spatial distribution of minerals in the individual coal particle are the input in the fly ash formation model., and finally
6. a slagging propensity prediction method.

Standard chemical analysis, petrographic description, particle sizing and combusting a test coal in a drop tube furnace support the new techniques that were developed.

The analytical results obtained for the coals, fly ash and slag deposits, the validation of the fly ash formation model, and the development of a new slagging indicator are outlined in the following three chapters.

5 RESULTS

5.1 Sample Description and Boiler Conditions

Samples were acquired over a period of two years starting in April 1999 and finishing in May 2000 (Table 5.1). The details of the suction pyrometer and slag probe used to acquire the samples are discussed in section 4.1 and in Appendix C.

Table 5.1: Sampling details and boiler operational conditions

Date	Hole	Depth (m)	Sampling duration (minutes)	Boiler Load (MW_e)	Steamflow (kg/s)
06-Apr-99	1	0	120	190.3	90.95
07-Apr-99	1	0.5	95	186.5	91.22
08-Apr-99	1	1	105	187.9	90.72
20-Apr-99	1	1.5	60	197.0	98.3
09-Apr-99	1	2	60	187.6	92.46
18-May-99	2	0	151	189.8	89.89
20-May-99	2	0.5	110	194.2	94.34
27-May-99	2	1	105	196.2	96.21
27-May-99	2	1.5	90	197.4	96.5
01-Jun-99	2	2	50	198.9	97.42
24-Sep-99	3	0	80	195.4	94.5
19-Aug-99	3	0.5	60	198.1	96.2
03-Feb-00	3	1	100	194.9	95.36
17-Feb-00	3	1.5	100	195.3	95.75
17-Feb-00	3	2	60	194.5	95.01
18-Apr-00	4	0	70	198.8	96.61
20-Apr-00	4	0.5	100	195.4	94.27
20-Apr-00	4	1	90	196.5	95.69
2-May-00	4	1.5	25	193.2	96.2
2-May-00	4	2	See text	193.2	96.2

The flow rate of the water through the suction pyrometer was too low to ensure adequate cooling for hole 4 at a depth. The weak flow rate was attributed to the height of the probe above the water source and the resultant low water pressure. For fear of melting the suction pyrometer and the slag probe, no samples were acquired for hole 4 at a depth of 2m.

A single sample of pulverised fuel was obtained for hole 3 ,at depths of 1.5 and 2m, and for hole 4, at depths of 0.5m and 1m.

To ensure that the slag probe could be extracted from within the boiler without loosing the slag deposit, it was imperative that the size of the slag deposit should

not exceed the height of the access hole. This controlled the duration of sampling. On the whole, the sample duration was generally shorter at a 2m depth, and longer closer to the boiler wall.

The variation in the boiler load during the sampling period is depicted in Table 5.1 and Figures 5.1 and 5.2.

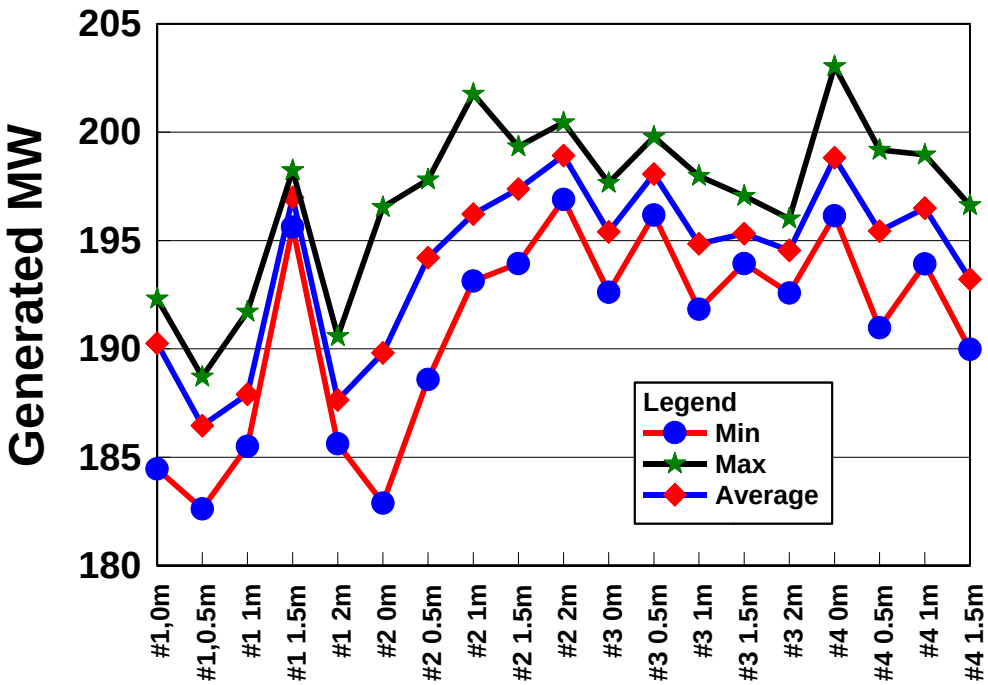

Figure 5.1: Generated MW_e during sampling.

On average hole 1 (excluding #1, 1.5m) was sampled at moderately lower load (186-191 MW_e) than the remaining holes (Figure 5.2).

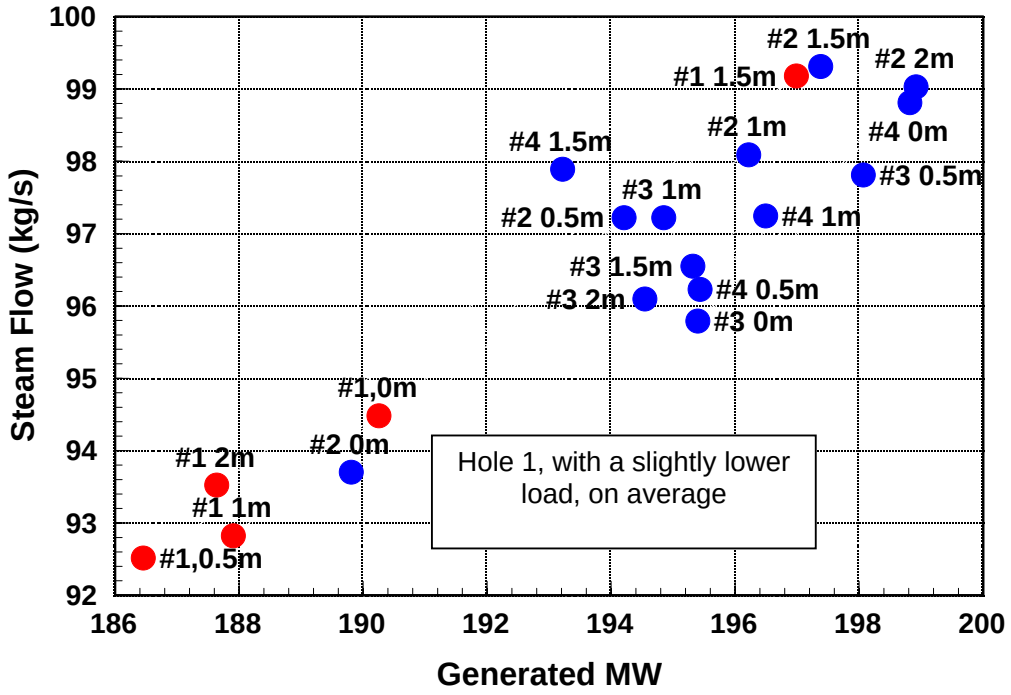

Figure 5.2: Comparative generated MW_e versus steam load (kg/s)

5.2 Screened Particle Size distribution

The particle size distribution technique is discussed in section 4.5. The expected grind for the mills is between 65 and 75% passing 75 µm. The detailed particle size distributions for the pulverised fuel and fly ash are summarised in Appendix I.

On average, the fly ash is significantly finer than the corresponding pulverised fuel burnt (Figure 5.3). This is expected, as the size of the included mineral grains is finer than that of the pulverised fuel particles and the extraneous (excluded) mineral rich particles are similar in size to the carbon rich pulverised fuel particles.

If coalescence were to be the dominant fly ash formation process, then the resultant fly ash particle size distribution would be coarser than the mineral grain size distribution in the pulverised fuel. If fragmentation is the dominant fly ash formation process, then the resultant fly ash particle size distribution will be finer or equivalent to the mineral grain size distribution in the pulverised fuel. If the dominent fly ash formation process is to be predicted from the fly ash particle size

distribution then the mineral grain size distribution (included and extraneous) and not the pulverised fuel particle size distribution should be used as the reference.

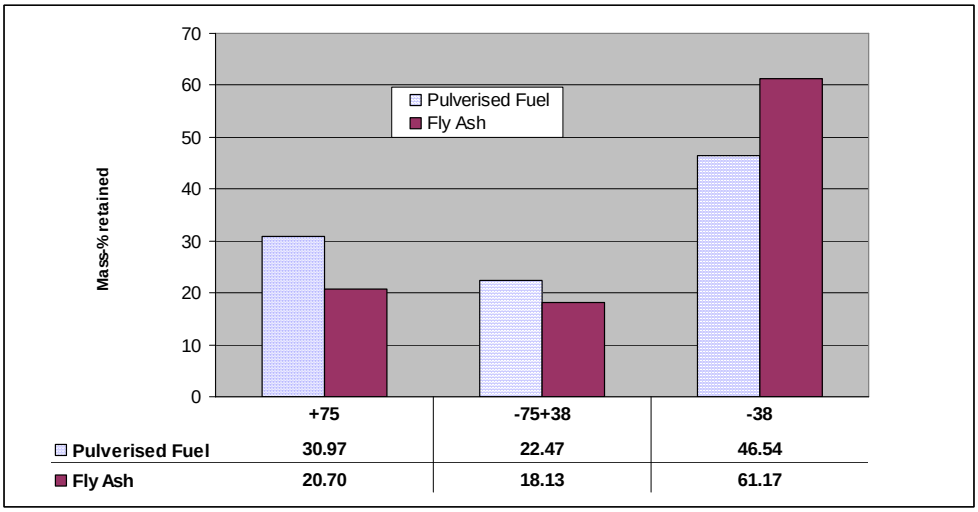

Figure 5.3: Average screened particle size distribution of pulverised fuel and fly ash.

Based on Figure 5.4, the fly ash varies in size from the boiler wall (0m) to the centre (2m) of the boiler and with height.

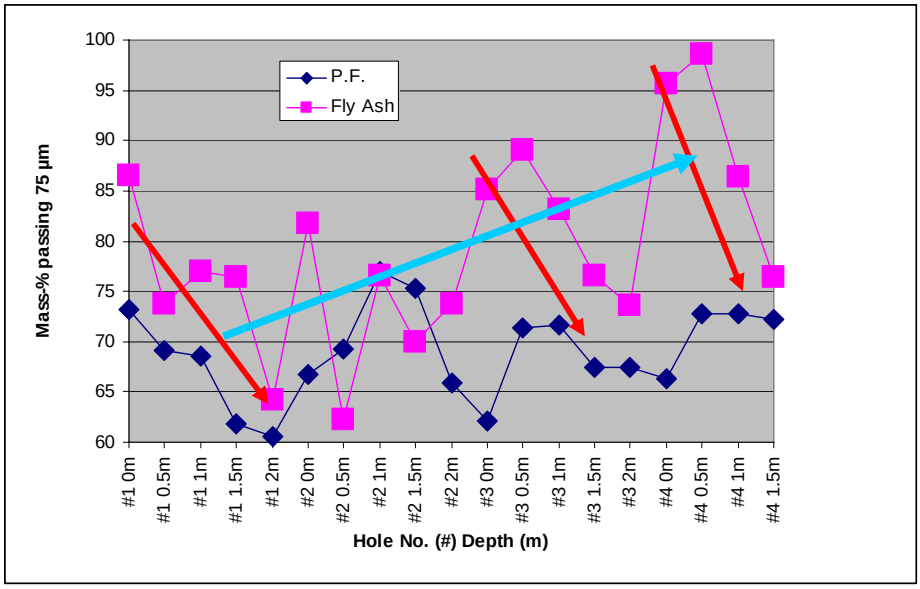

Figure 5.4: Variation in the percent passing 75 µm

Apart from hole 2, the fly ash particle size proved to be finer at the boiler wall and comparatively coarser towards the centre of the boiler (highlighted by the orange arrow in Figure 5.4). The variable particle size distribution of the fly ash sampled from hole 2 could probably be attributed to the effects of the burners five metres below and five metres above hole 2. On average, the fly ash was finer in the upper regions of the boiler (hole 4) than in the lower regions (hole 1 and 2)(highlighted by the red arrows in Figure 5.4).

Based on the percent passing 75 µm, the average fly ash particle size distribution sucked from within the boiler by the suction pyrometer was moderately finer (79.3% -75 µm) than the bulk cegrit sample (73.7% -75 µm) obtained in April 2000 (Table I.2, appendix I). This was expected as, unlike the isokenitic samples, the cegrit samples are generally influenced by size segregation. As such, the cegrit sample does not necessarily represent a good cross section of particle sizes.

The Malvern particle size analyser results for the pulverised fuel sample's screened +75, -75+38 and -38 µm-sized fractions at a depth of 0.5m at hole 2, are summarised in Table 5.2.

Table 5.2 Malvern particle size results

Screened size fraction (µm)	Malvern particle size results				
	$d_{0.1}$	$d_{0.5}$	$d_{0.9}$	Mode	Density
+75	74.58	138.62	277.1	126.35	1.55
-75+38	43.16	65.04	100.37	63.91	1.59
-38	4.94	17.9	40.77	22.23	1.77

$d_{0.1}$: screen size (µm) at which 10-mass-% passes (i.e. finer)

$d_{0.5}$: screen size (µm) at which 50-mass-% passes

$d_{0.9}$: screen size (µm) at which 90-mass-% passes

The Malvern particle size distribution, described by d(0.1), d(0.5) and d(0.9), indicated that the physically screened fractions are moderately clean with an insignificantly low proportion of undersized or oversized particles for each screened size fraction. The pulverised fuel particle size ranged from 0.5 to 600 µm, with less than two mass percent of the total sample finer than the CCSEM electron beam resolution of 2 to 3 µm.

5.3 Petrographic Results

The petrographic sample preparation technique was discussed in section 4.2.1, its principals and methodology in sections 2.2 and 4.3, and in Appendix E.

Maceral analysis describes the volume percent proportion of the individual organic components (analogous to minerals) in a pulverised fuel, whereas microlithotype analysis describes the relationship (association) between the macerals themselves and the minerals.

An important aspect of this research is to describe the relationship (association) between the individual macerals and the included minerals. As CCSEM is unable to distinguish between the different macerals, the petrographic results are important in complimenting the CCSEM results. The rationale behind this approach is that an understanding of the association between the macerals and the mineral matter would lead to a greater understanding of the fly ash formation process and ultimately of the development of slag deposits. It is for this reason that the unique microlithotype/carbominerite particle classification scheme was developed (Appendix E).

The maceral and microlithotypes for the +75 and -75+38 µm screened size fractions are described. The -38 µm fraction was not described, however, as it was difficult to distinguish between the macerals and by definition a microlithotype describes the attributes of a particle under a 50x50 µm graticle, which is larger than the average particles in the -38 µm size fraction.

Rank determination is based on the average vitrinite reflection and is used to classify the maturity of the coal.

5.3.1 Maceral and microlithotypes

Vitrinite, inert semifusinite and reactive intertodetrinite are the major macerals in the +75 and -75+38 size fractions (Figure 5.5). There is no significant difference in the relative maceral abundance (expressed as volume percent) between the two size fractions analysed.

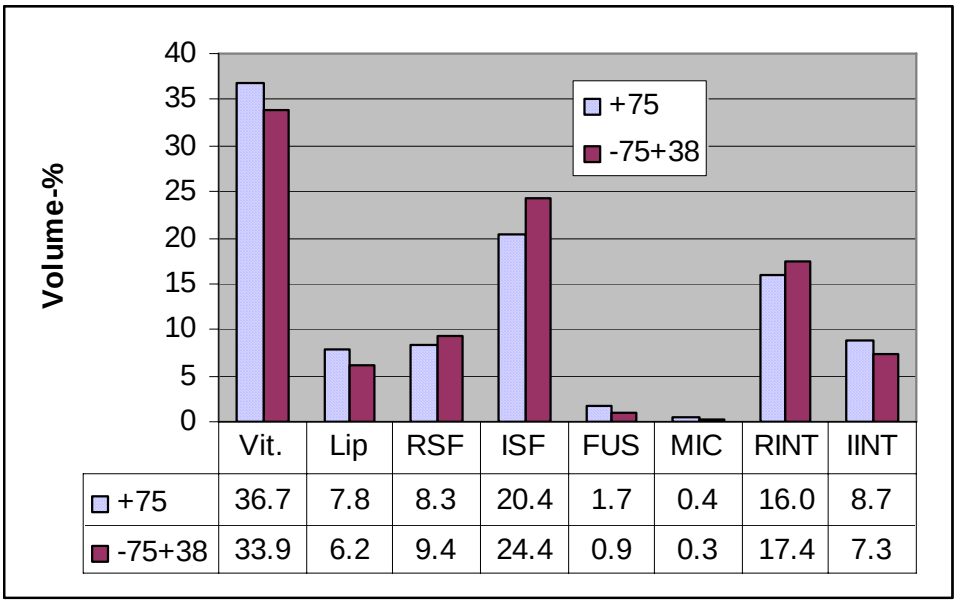

	Vit.	Lip	RSF	ISF	FUS	MIC	RINT	IINT
+75	36.7	7.8	8.3	20.4	1.7	0.4	16.0	8.7
-75+38	33.9	6.2	9.4	24.4	0.9	0.3	17.4	7.3

Figure 5.5: Average volume percent maceral abundance in the +75 and -75+38 µm size fractions. (Vit: vitrinite, Lip: liptinite, RSF: reactive semifusinite, ISF: inert semifusinite, FUS: fusinite, MIC: micrinite, RINT: reactive inertodetrinite, IINT:inert inertodetrinite)

The detailed variation in the volume percent maceral abundance for the respective holes and sampling depths is summarised in Tables J.1 and J.2 (Appendix J).

An estimate of the total volume percent abundance for the +75 and -75+38 µm size fraction combined (weighted by PSD) is illustrated in Figure 5.6. For clarification of this diagram, the reactive semifusinite, inert semifusinite and fusinite are combined as semifusinite/fusinite and reactive and inert inertodetrinite as inertodetrinite. The proportions of semifusinite/fusinite and liptinite are fairly consistent. The proportion of vitrinite appears to be inversely proportional to the

proportion of inertodetrinite. The correlation coefficient for this relationship is r=-0.77.

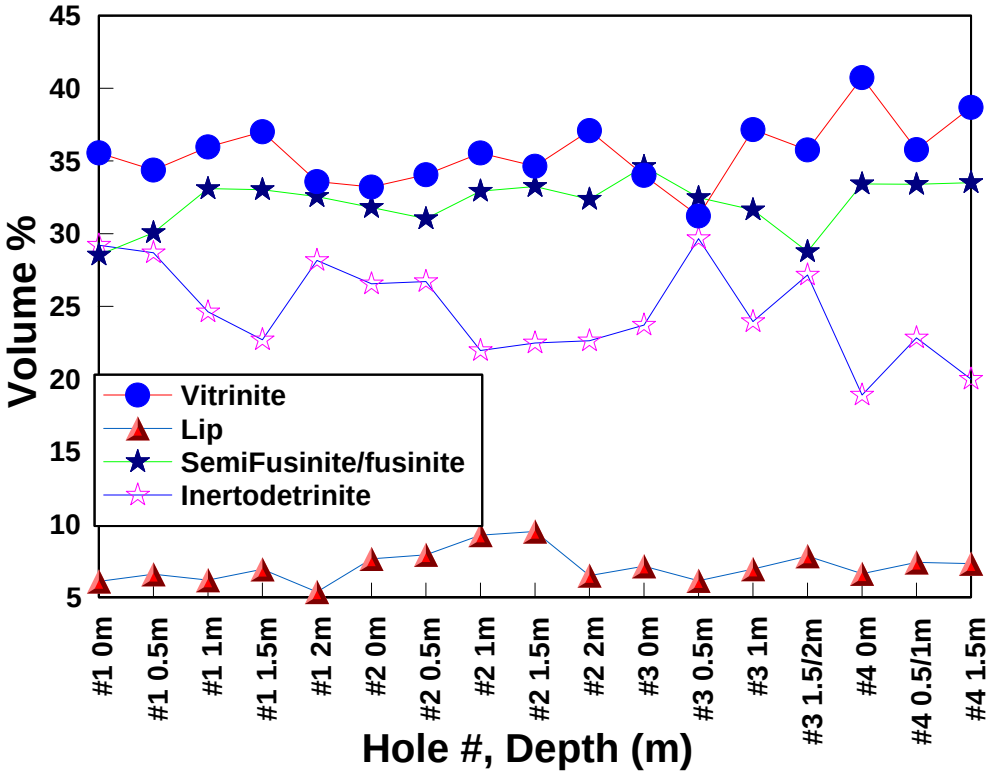

Figure 5.6: The volume percent maceral variation in the combined +75 and –75+38 µm size fractions.

Vitrite, intermediate, semifusite/fusiite and inertodetrite are the prominent microlithotypes (Figure 5.7).

The notable difference in the semifusinite/fusinite and intermediate mircolithotype distribution for the respective size fractions might be the artefact of size and not necessarily reflect a genuine difference. Since microlithotype classification is based on the relative proportions of individual macerals in a 50x50 µm band it is conceivable that a mircolithotype defined in the -75+38 µm will not be the same as in the +75 µm fraction. For instance, a semifusinite/fusinite microlithotype in the -75+38 µm fraction could have being a fragment of intermediate

mircolithotype. The detailed microlithotype analysis for the individual coal samples is summarised in Tables J.3 and J.4 (Appendix J).

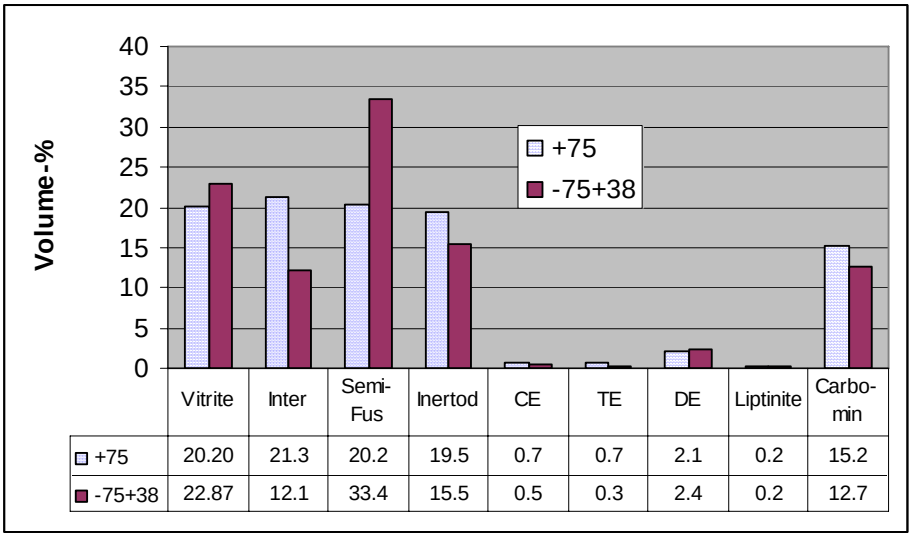

	Vitrite	Inter	Semi-Fus	Inertod	CE	TE	DE	Liptinite	Carbo-min
+75	20.20	21.3	20.2	19.5	0.7	0.7	2.1	0.2	15.2
-75+38	22.87	12.1	33.4	15.5	0.5	0.3	2.4	0.2	12.7

Figure 5.7: Volume percent microlithotype distribution in the +75 and -75+38 µm size fraction. (Inter: Intermediate, Semi-Fus: semifusite/fusite, Inertod:Inertodetrite, CE: clarite, TE:trimacerite, DE: Durite, Carbo-min: carbominerite)

The average relative proportions of microlithotype/carbominerite particle types in the +75 and -75+38 µm size fractions are summarised in Table 5.3 and Table 5.4, respectively. The detailed microlithotype/carbominerite particle types for the individual coal samples are summarised in Tables J.5 and J.6 (Appendix J).

Table 5.3: Carbominerite/microlithotype particle distribution (volume-%) in the +75 µm size fraction. (Inter:intermediate, Inertodet: inertodetrite)

Carbominerite	Organic component (microlithotype)				
	Vitrite	Inter.	Semi-Fus Fusite	Inertodet.	Minerite
CarboArgillite	5.8	5.0	1.5	47.7	5.5
Carbosilicate	0.0	0.1	0.1	0.2	12.8
Carboankerite	0.2	0.3	1.3	2.7	6.3
Carbopyrite	3.0	0.1	0.1	0.0	4.7
Carbopolyminerite	0.4	0.4	0.3	0.9	0.5
Total	**9.4**	**5.8**	**3.2**	**51.6**	**29.9**

Table 5.4: Carbominerite/microlithotype particle distribution (volume-%) in the -75 + 38 µm size fraction. (Inter:intermediate, Inertodet: inertodetrite)

Carbominerite	Organic component (microlithotype)				
	Vitrite	Inter.	Semi-Fus Fusite	Inertodet.	Minerite
Carboargillite	4.7	2.4	2.5	47.3	7.7
Carbosilicate	0.0	0.0	0.1	0.5	7.0
Carboankerite	0.5	0.6	1.8	3.0	9.7
Carbopyrite	3.4	0.0	0.0	0.0	7.8
Carbopolyminerite	0.1	0.0	0.0	0.1	1.0
Total	8.6	2.9	4.4	51.0	33.0

The following trends were noted from Tables 5.3 and 5.4:

- The majority of the clay minerals (carboargillite) are associated with “inertodetrinite” and occur to a lesser extent as “free” particles. The correlation coefficient between inertodetrinite maceral and carbominerite is 0.74
- The majority of the quartz (carbosilicate) is “free”
- The majority of the carbonates (carboankerite) are “free” and associated to a lesser extent with “inertodetrinite”
- Pyrite is largely “free” or associated with vitrite.

The average rank (RoV-% random) is 0.642 $\pm$ 0.066 (Figure J.1, Appendix J). This coal is classified as a High-Volatile Bituminous (Falcon, 1998) or a Medium-Rank C (Pinheiro et al., 1998). [7]

[7] International Classification of In-seam Coals of the Economic Commission for Europe – United Nations. Based on standard (Energy/1998/19)

5.4 Chemical Analysis

The methodology is described and discussed in detail in section 2.3.1, 4.4 and in Appendix F.

5.4.1 Proximate, ultimate and XRF ash elemental

The average proximate and ultimate analysis for the suite of samples sampled from the boiler is summarised in Table 5.5 with the detailed data appended in Appendix K.

Table 5.5: Average proximate, ultimate and ash elemental analysis

	Proximate Analysis			
	Average	**Min**	**Max**	**Std. Dev.**
Inherent Moisture (%)	2.66	1.70	3.10	0.39
Ash (%)	24.91	23.80	27.50	0.96
Volatile Matter (%)	23.66	22.40	24.80	0.58
Fixed Carbon (%)	48.78	47.40	49.50	0.56
	Ultimate Analysis			
	Average	**Min**	**Max**	**Std. Dev.**
Carbon (%)	58.84	57.44	60.48	0.86
Hydrogen (%)	2.86	2.69	3.10	0.11
Nitrogen (%)	1.29	1.25	1.35	0.03
Total Sulphur (%)	0.77	0.64	0.92	0.08
Carbonate (as CO_2, %)	0.95	0.57	1.75	0.26
Oxygen (%)	7.72	6.84	8.29	0.37
CV (MJ/Kg)	23.02	22.28	23.90	0.45
Element (%)	**Ash Elemental**			
	Average	**Min**	**Max**	**Std. Dev.**
SiO_2	60.64	57.60	64.00	1.55
Al_2O_3	24.68	22.30	27.20	1.18
Fe_2O_3	3.55	3.00	4.83	0.45
TiO_2	1.50	1.06	1.86	0.20
P_2O_5	0.63	0.31	1.17	0.25
CaO	3.82	2.87	4.40	0.40
MgO	0.98	0.68	1.29	0.17
Na_2O	0.19	0.13	0.28	0.05
K_2O	0.61	0.49	0.82	0.10
SO_3	2.42	1.72	3.01	0.31

There is no significant variation in the quality of the pulverised fuel (Figure 5.8) or in the variation in the inorganic ash elemental distribution (Figure 5.9).

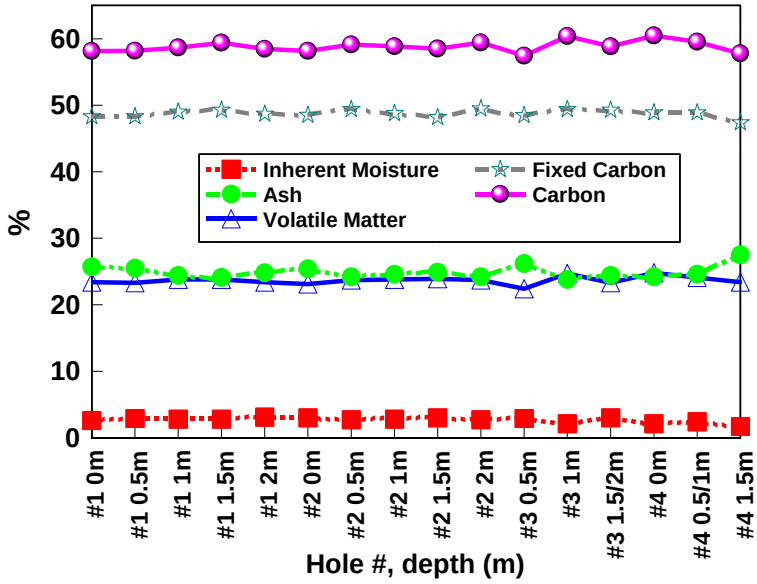

Figure 5.8: Variation in inherent moisture, ash percent, volatile matter, fixed carbon and carbon.

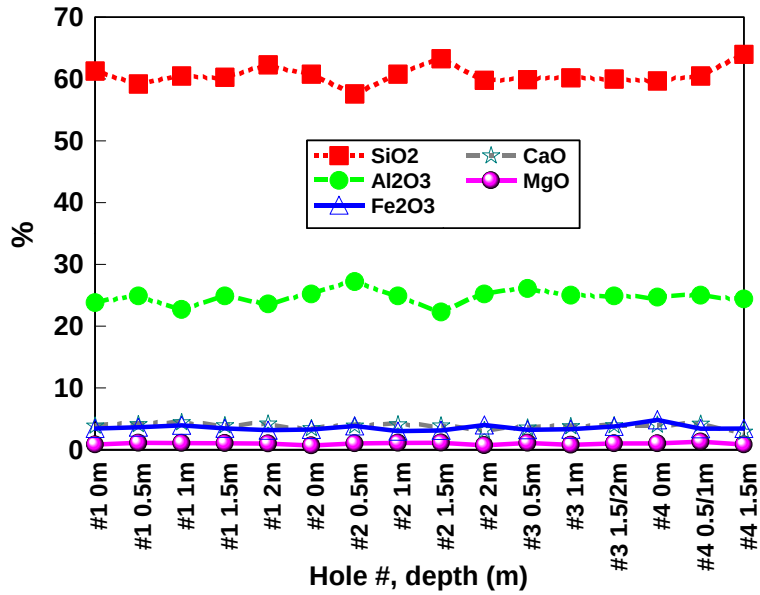

Figure 5.9: Variation in major ash oxides

The high proportion of SiO_2 and Al_2O_3 is consistent with the high proportion of carboargillite (clay) and carbosilicate particles in the +75 µm (see Table 5.3) and -75+38 µm (Table 5.4) size fractions. The principal mineral in carboargillite is kaolinite ($Al_2Si_2O_5(OH)_4$) clay and carbosilicate is quartz (SiO_2).

The major carbonate minerals, calcite ($CaCO_3$) and dolomite ($CaMg(CO_3)_2$) are the principal sources of calcium and magnesium in coal. There is a poor correlation of r=0.45 between the total calcium oxide (CaO) and magnesium oxide (MgO) content in the pulverised fuel ash and the ultimate carbonate content (Figure 5.10). The ash elemental analysis is the elemental distribution of the ash and the total is approximately 100, whereas ultimate carbonate is an indirect measure of the total mass percent carbonate content in the pulverised fuel sample. To compare the two, CaO and MgO content of the ash were renormalised relative to the ash percent (Table J.1).

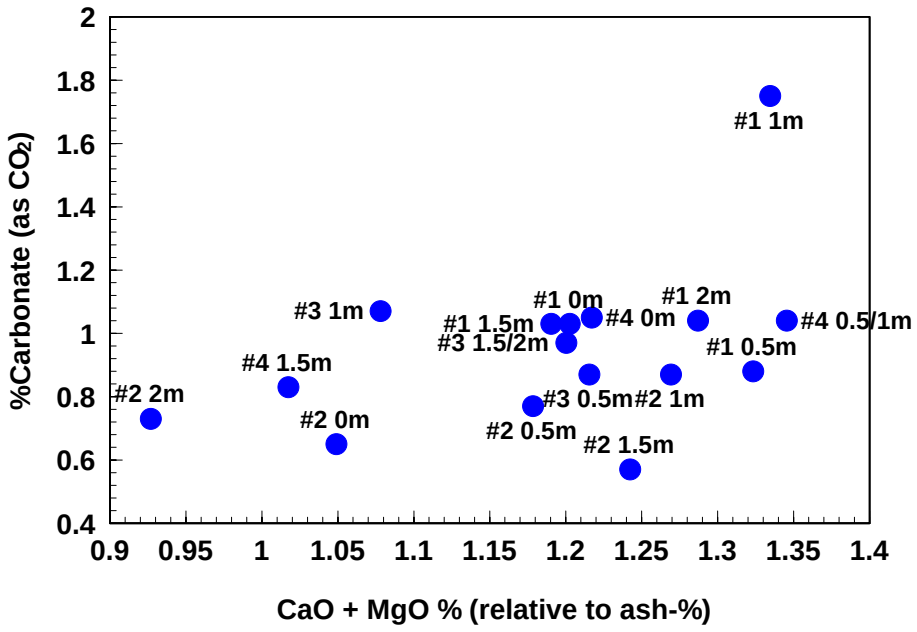

Figure 5.10: The comparison between percent carbonate (ultimate analysis) and the total CaO+MgO concentration renormalized back to the ash percent.

This weak correlation suggests that either there is an alternative non-carbonate mineral source of calcium and magnesium, or the ultimate carbonate analysis is not a true reflection of the true carbonate mineral content. It is notable that hole one's 1m sample seems to have an appreciably higher proportion of carbonates.

Pyrite is the major source of iron and sulphur in the majority of South African coals. There is a better comparison (correlation coefficient of 0.79) between the total Fe_2O_3 concentration (corrected by ash percent) and total sulphur content (ultimate analysis, Figure 5.11).

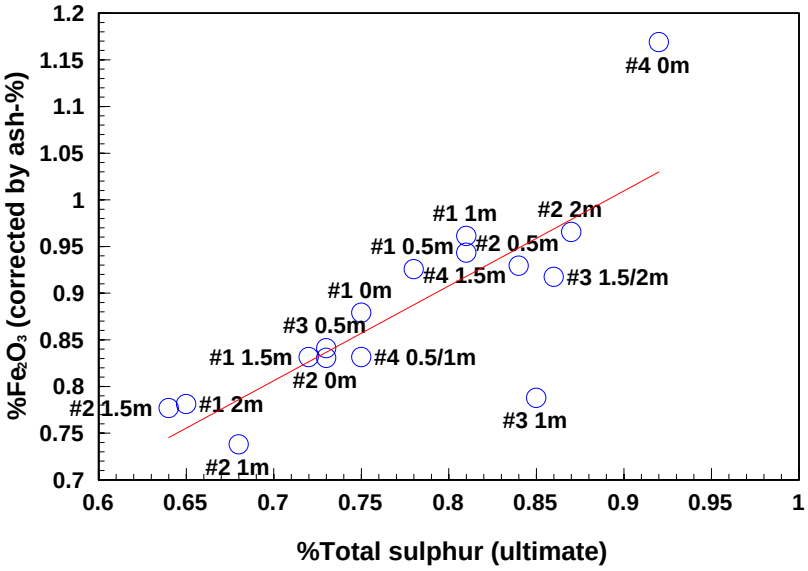

Figure 5.11: Correlation between total sulphur (ultimate) and Fe_2O_3 (corrected by ash percent)

This strong correlation between S and Fe, confirms that the majority of iron and sulphur are predominantly associated with pyrite. A comparison between the SO_3 concentrations (corrected by ash-%) in the ash to total sulphur is weak (correlation coefficient of -0.3). It is common knowledge that during ashing, pyrite transforms to iron-oxide and releases sulphur. This sulphur can combine with calcium oxide (CaO) to form anhydrite ($CaSO_4$). It is perceived that the SO_3 in the ash is predominantly sulphur associated with sulphates and is not a true representation of actual sulphur concentrations. This is confirmed by the good correlation of r=0.62 between the total calcium oxide and magnesium oxide (CaO+MgO) and the SO_3 of the ash.

5.5 Mineralogy of the pulverised Fuel

A prerequisite for the CCSEM analytical technique is the development of a unique mineral identification library based on the principles of fuzzy logic (see section 4.6.2). The minerals in the drill cores and from the pulverised fuel were identified through semi-quantitative energy dispersive X-ray analysis (EDS), visual observations (optical) and based on CCSEM elemental results.

The major and minor minerals identified were kaolinite ($Al_2Si_2O_5(OH)_4$), quartz (SiO_2), calcite ($CaCO_3$), dolomite ($CaMg(CO_3)_2$), pyrite (FeS_2), orthoclase ($(K,Na)[AlSi_3O_8]$), muscovite ($K_2Al_4[Si_6Al_2O_{20}](OH)_4$), apatite ($Ca_5(PO_4)_3(OH,F,Cl)$), rutile/anatase ($TiO_2$), Fe-oxide (hematite or magnetite). Trace minerals were zircon ($ZrSiO_4$), Cr-spinel (chromite($FeCr_2O_4$)), magnesite ($MgCO_3$), ankerite ($Ca(Mg,Fe)CO_3)_2$), and siderite ($FeCO_3$).

Illite ($(K_{1-1.5})Al_4[Si_{7-6.5}Al_{1-1.5}O_{20}](OH)_4$) is a common clay mineral in sediments (shale and siltstones) that are associated with coal seams and with coal itself. Illite is a weathering/degradation product of feldspars (orthoclase) and muscovite. During diagenesis, illite is an alteration product of clays. During the routine mineralogical investigation, illite was neither identified positively by EDS nor confirmed visually. Mineral identification rules were developed to identify phases, which are similar to muscovite, but have a lower potassium (K) and higher silicon (Si) content than muscovite. This phase was called “illite” and could describe the minerals illite and/or hydromuscovite. However in reporting the mineral abundance results (Tables 5.7 and Tables L2-L5), muscovite and “illite” are grouped and reported as “Illite/mica”. The justification for grouping “illite” together with muscovite can be understood in terms of the following:

1. Since the CCSEM mineral identification is based on elemental proportions derived from a rapidly acquired X-ray spectrum (100 msec), the technique is not sensitive enough to distinguish between elementally similar “illite” and muscovite at these counting rates.
2. Since illite is principally an alteration product, it is likely that the grain size of illite is smaller than the CCSEM electron beam resolution of 2-3 µm. Any “illite” spectrum could be a complex mixed spectrum of illite and the surrounding host minerals such as muscovite, orthoclase or kaolinite.

3. The proportions of “illite” and muscovite are less than 0.5 mass percent and are comparatively insignificant (Tables 5.7 and Tables L2-L5).

The average elemental proportions determined by the semi-quantitative energy dispersive X-ray analysis (EDS) of selected minerals are summarised in Table 5.6. The ideal mineral compositions calculated from the stoichiometric mineral formula is also included in Table 5.6.

Table 5.6: Average and ideal elemental compositions of selected minerals. (N.D.: not detected).

	Kaolinite		Orthoclase		Illite/mica		
	Semi-Quant EDS	Ideal	Semi-Quant EDS	Ideal	Semi-Quant EDS	Ideal Muscovite	Ideal Illite
SiO_2	46.2	46.55	63.7	64.76	46.5	45.26	52.84
TiO_2	0.03	0.00	0.04	N.D.	0.2		
Al_2O_3	39.0	39.48	18.4	18.31	34.0	38.39	34.82
FeO	0.3	0.00	N.D.	N.D.	4.4		
MgO	0.02	0.00	N.D.	N.D.	1.1		
CaO	0.2	0.00	N.D.	N.D.	0.00		
Na_2O	0.02	0.00	0.7	N.D.	0.00		
K_2O	0.1	0.00	17.2	16.92	8.4	11.82	7.64
SO_3	0.3	0.00	N.D.		N.D.		
H_2O	13.97	13.97	N.D.		5.3	4.53	4.69
Total	100.0	100.00	100.0	100.00	99.9	100.00	100.0

The kaolinite in this coal has trace concentrations of the impurities, iron (Fe), magnesium (Mg), calcium (Ca), sodium (Na), potassium (K) and sulphur (S). Owing to the fine-grained nature of kaolinite, it was difficult to ascertain whether these impurities are structural substitutions or sub-micron discrete mineral grains (anatase) or impurities on the surface of the kaolinite.

Titanium (Ti), iron (Fe) and magnesium (Mg) are associated in minor to trace concentrations in “illite/mica”. In muscovite, titanium (Ti), iron (Fe) and magnesium (Mg) commonly substitutes aluminium (Al) in the octahedral site, while magnesium (Mg) and iron (Fe) can substitute aluminium (Al) in the illite group mineral, phengite.

A semi-quantitative analysis of calcite, pyrite and quartz was not undertaken as, by definition, these minerals do not vary extensively in elemental composition.

Dolomite could have minor concentrations of iron (Fe) (< 2 mass-%) and calcite could have minor concentrations of Mn.

5.6 Maceral Inorganic Element Composition

Included in the drill core samples used as mineral references, were sections of the 2A and 4 coal seams from the colliery supplying Hendrina power station. Polished sections of the coal seam were prepared and analysed optically and by means of the scanning electron microscope (SEM). Macerals were identified optically and their respective positions marked. These marked positions were located under the scanning electron microscope and X-ray spectra were acquired for each maceral group identified. The position of the electron beam was carefully chosen, ensuring that there was no visible evidence of mineral matter in the proximity of the electron beam.

An example of a vitrinite, sclerotinite and exinite association as well as the approximate positions of the X-ray spectra acquired is illustrated in Figure 5.12.

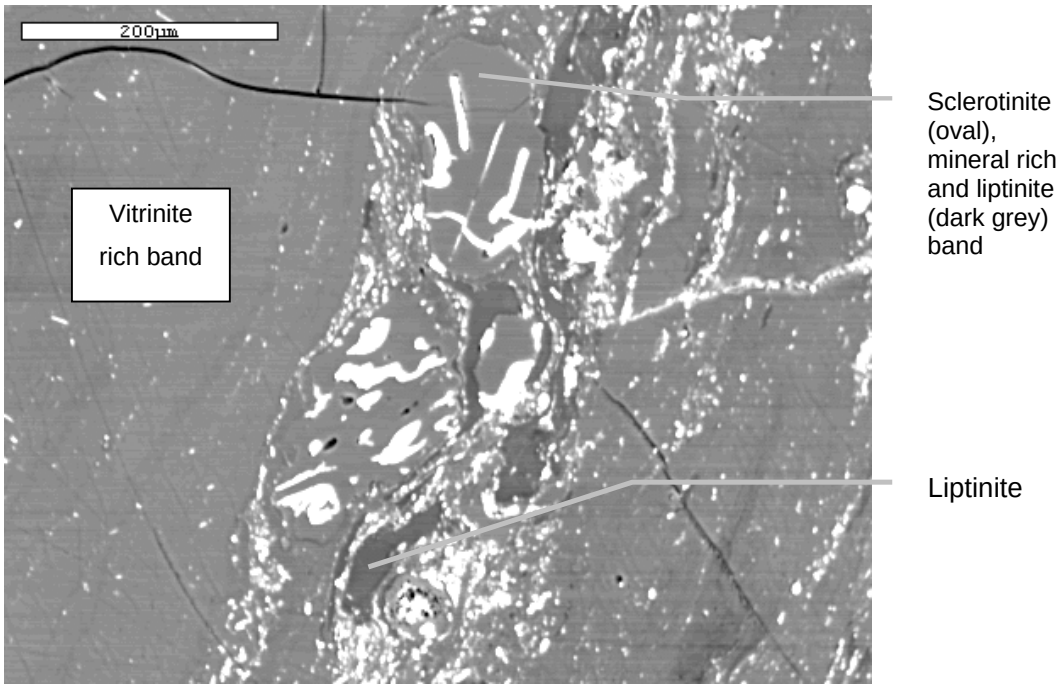

Figure 5.12: A backscattered electron photomicrograph illustrating sclerotinite (oval), dark liptinite and mineral rich bands flanked by vitrinite rich bands. The included minerals are white. (scale bar represents 200 µm).

The average X-ray spectra of these respective macerals did in fact indicate minor to trace concentrations of inorganic elements (Figure 5.13).

The following trends, based on Figure 5.13, were noted:

- Sulphur and titanium are elevated in vitrinite and pseudovitrinite
- Aluminium, silicon, sulphur, and to a lesser extent, calcium and magnesium are elevated in reactive and inert semifusinite
- Calcium and sulphur elevated in sclerotinite
- Aluminium, silicon, sulphur elevated in liptinite

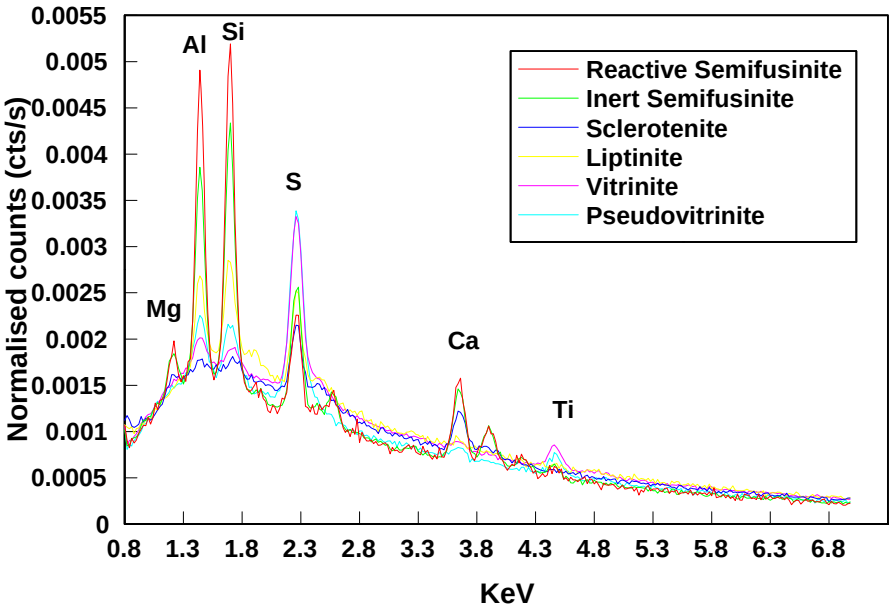

Figure 5.13: Inorganic elements in selected macerals.

The inorganic elements associated with the supposedly mineral-free macerals could be from three main sources:

- Sub-micron included mineral grains smaller than the electron beam resolution of 2 to 3 µm (Baxter, 1991).
- Mineral grains beneath the sectioned surface. The electron beam penetration depth in vitrinite at 20KeV is approximately 4 to 5 µm.
- Organically-bound elements forming part of the organic structure of the maceral. It is common knowledge that organically-bound sulphur, aluminium, silicon and calcium are prevalent in lignites and

sub-bituminous coals (Barta et al., 2000, Benson et al., 1993). Organically-bound calcium is plausible as the test coal is a high-volatile bituminous coal (RoV-% = 0.642) which is one classification rank higher than a sub-bituminous coal (RoV-% between 0.4 and 0.5). Organically-bound sulphur is common in bituminous coals with reported values varying from trace levels to up to 6% (Wagoner and Yan,1993).

- A combination of all of the above.

5.7 CCSEM Analysis – Pulverised fuel

The CCSEM technique is described in detail in section 2.3.3 and the methodology used in this research in section 4.5. CCSEM is an ideal technique to quantify and qualify the proportions of mineral matter, the degree of mineral and coal liberation, and the mineral matter associations in pulverised fuel. The CCSEM analysis is extended to include mass-percent phase/mineral distributions in fly ash and slag deposits, their particle sizes and associations.

This section presents the results of the CCSEM analysis of pulverised fuel. The CCSEM results obtained for fly ash and slag deposits are discussed in chapter 6.

5.7.1 Mineral matter distribution

Tabulated in Table 5.7 are the combined average mass percent mineral distributions for the respective size fractions and the total sample for all pulverised fuel samples analysed. The detailed mass percent mineral distributions for the samples from the individual holes are listed in Appendix L (Tables L1 to L4). Included in the mineral analysis, is “coal’, which in the context of this research is a generic term used to describe the “organic component (macerals)” of coal. Under the current analytical conditions, CCSEM is unable to effectively distinguish between the different maceral groups (vitrinite, inertinite and liptinite). This is due to the rapid acquisition rate (100 msec), similarities in the maceral elemental counts, changes in the macerals compositions with rank, and the inability of the EDS system to detect nitrogen (N) and hydrogen (H).

On average, the major and minor minerals in the test coal are 72.2 mass percent “coal”, 13.2 mass percent kaolinite, 8.3 mass percent quartz, 2.5 mass percent

pyrite, 1.2 mass percent dolomite and 1.1 mass percent calcite. Trace concentrations (<0.5 mass-%) of feldspar, illite/mica, Ti-oxide, apatite, siderite, ankerite and iron-oxide also occur.

Apart from quartz and “coal”, there is no marked variation in the proportion of minerals across the size fractions. The concentration of quartz across the size fractions is variable, with the highest concentration being in the +75 µm fraction.

Table 5.7: Average mass percent mineral and coal distribution per size fraction and for total sample. (Detailed data in Appendix L).

Mineral	Mass-%			
	+75	-75+38	-38	Total*
Pyrite	2.7	2.3	2.5	2.5
Quartz	9.6	6.9	8.1	8.3
Feldspar	0.3	0.2	0.2	0.3
Illite/Mica	0.2	0.3	0.3	0.3
Kaolinite	13.4	13.3	13.0	13.2
Fe-oxide	0.4	0.2	0.5	0.4
Calcite	0.9	1.2	1.3	1.1
Dolomite	0.8	1.4	1.4	1.2
Other Carbonates	0.1	0.2	0.2	0.2
Apatite	0.1	0.1	0.1	0.1
Ti-oxide	0.1	0.1	0.1	0.1
Other	0.1	0.2	0.2	0.2
Coal	71.1	73.6	72.2	72.2
Total	100.0	100.0	100.0	100.0
Mineral Matter	28.9	26.4	27.8	27.8

Feldspar : predominately orthoclase

Illite/mica : see text

Fe-oxide : magnetite, hematite and Fe-hydorxides

Other carbonates : ankerite, siderite

Ti-oxide : Rutile/anatase

Other : phases which could not be positively identified

5.7.2 Comparative elemental analysis

The CCSEM elemental distribution is calculated from the mass percent mineral distributions (Table 5.7) and the average elemental compositions of the minerals. The average elemental compositions are based on the semi-quantitative EDS analysis of minerals, the ideal mineral compositions derived from literature (Deer et al., 1966)

The comparison between the calculated CCSEM and XRF elemental distributions based on the method described in section 4.7, is summarised in Table 5.8.

Table 5.8: Comparative elemental distributions

	Average XRF (coal ash)	CCSEM Minerals	% Difference
Si	7.75	7.67	-1.0
Al	3.57	3.13	-12.5
Fe	0.68	1.38	103.6
Ti	0.25	0.09	-61.7
P	0.08	0.02	-71.2
Ca	0.75	0.81	8.5
Mg	0.16	0.19	17.2
Na	0.04	0.03	-25.7
K	0.14	0.09	-37.1

Aluminium and silicon are associated with the major minerals, quartz (Si) and kaolinite (Al and Si). For these elements, the percentage difference between the CCSEM elemental compositions and the ash elemental proportions is within 13%.

The notable discrepancy in the case of iron can be attributed to pyrite segregation during sample preparation, which will artificially increases the concentration of pyrite. If the XRF iron content is accurate, and all the iron is associated with pyrite then the estimated average pyrite content based on the XRF iron is 1.41 mass percent. Similarly, if the all the total sulphur content is assigned to pyrite, the estimated pyrite content is 1.49 mass percent.

The lower proportion of CCSEM aluminium can be attributed to a combination of the following factors:

1. kaolinite commonly occurs as fine inclusions (<2 μm) in these coals. The probability of not detecting these fine inclusions is increased when the CCSEM beam resolution is 2 to 3 μm and the beam spacing varies between 3 and 16 μm (see Appendix G).

2. No account is made for the “organically-bound” Al associated with the various macerals (Figure 5.13).
3. The backscattered electron intensity of kaolinite is low, but slightly higher than the iodinated epoxy-mounting medium. It is conceivable that kaolinite could be erroneously assigned to epoxy resin by the image analysis routines.
4. A combination of all the above factors.

The combination of these factors will account for the lower kaolinite concentrations and corresponding lower aluminium concentration.

In addition, the EDS analysis of individual macerals indicated the presence of inorganic elements magnesium, aluminium, silicon, calcium, sulphur and titanium associated with the macerals (Figure 5.13). It is possible that these elements were derived from minerals that are either below analytical surface or that they were sub-micron mineral grains smaller than 2 to 3 µm beam resolution.

The proportion of carbonates could be inferred from the ultimate analysis by measuring the proportion of carbon dioxide (CO_2) involved on contact with hydrochloric acid. Similarly, the proportion of carbonates as CO_2, could be deduced from the CCSEM mass percent distribution of the carbonates. The average ultimate CO_2 concentration for all coal samples analysed is 0.97% CO_2 (dry) as opposed to the CCSEM derived CO_2 of 1.16-% CO_2. The agreement between calcium and magnesium elemental proportions (Table 5.8) and CO_2 concentrations suggests that the CCSEM estimate of calcite and dolomite concentrations (Table 5.7) was acceptable.

The third possible method of validating the viability of the CCSEM results was comparing the proximate ash-percent with the mass percent of the mineral matter proportion derived from the CCSEM analysis. The estimated total mass percent mineral matter content is 27.8 mass-% (see Table 5.7), which is, as expected, higher than the average proximate ash-% of 24.91 (see Table 5.5). It is possible to estimate ash percent from the CCSEM results by accounting for the mass percent volatiles associated with minerals (H_2O from kaolinite, SO_2 from pyrite

and CO_2 from carbonates) likely to be lost during the process of ashing. The estimated CCSEM ash percent is 23.5 mass percent.

The correction factor for estimating the mass percent mineral matter (MM%) for the test coal is:

MM% = 1.15*Ash percent (dry basis)

The 1.15 factor is comparable to the 1.08 used in the Parr formula, the 1.10 proposed by Snyman et al. (1983) and the 1.08-1.25 range proposed by Gaigher (1980).

If it were to be assumed that the discrepancies in the proportion of aluminium, phosphorus, titanium and potassium could be attributed to sub-micron mineral grains not detected by CCSEM (Table 5.8) it would be possible to calculate the mineral proportions based on the XRF ash elemental analysis. The ideal mineral proportions based on the XRF ash elemental, the total sulphur content, the total carbonate and the ash percent (on a dry basis) are summarised in Table 5.9.

Table 5.9: The ideal elemental composition, total sulphur, carbonates ash percent and mass percent mineral abundance. (refer to text).

Elemental analysis	XRF Ash Element analysis %	CCSEM elemental (original) %	CCSEM elemental (ideal) %	Minerals	CCSEM (original) mass-%	CCSEM (ideal) mass-%
SiO_2	62.77	62.90	62.78	Pyrite	2.5	1.1
Al_2O_3	25.54	22.64	25.55	Quartz	8.3	7.9
Fe_2O_3	3.67	7.57	3.67	Feldspar	0.3	0.6
TiO_2	1.56	0.60	1.55	Illite/Mica	0.3	0.6
P_2O_5	0.65	0.19	0.65	Kaolinite	13.2	15.9
CaO	3.95	4.34	3.96	Fe-oxide	0.4	0.2
MgO	1.02	1.21	1.02	Calcite	1.1	0.7
Na_2O	0.20	0.15	0.17	Dolomite	1.2	1.1
K_2O	0.63	0.40	0.63	Other Carbonates	0.2	0.3
	Based on dry basis			Apatite	0.1	0.4
Total sulphur	0.8	1.32	0.61	Ti-oxide	0.1	0.35
Carbonates (CO_2)	0.97	1.16	0.93	Other	0.2	0.25
Ash	25.59	23.48	25.59	Coal	72.2	70.6

A comparison between the ideal mineral composition and the CCSEM derived mineral composition indicated that an estimated 2.7 mass percent of the kaolinite, 0.25 mass percent rutile/anatase and 0.3 mass percent apatite were unaccounted for and probably occur as fine sub-micron inclusions in coal. As expected the mass percent pyrite content of the ideal coal was significantly lower than measured.

The total carbonate content (based on CO_2) and total sulphur content based on the ideal composition suggests that the ideal pyrite, calcite and dolomite mass percent abundance are lower than expected.

The discrepancies in the ash elemental comparisons, carbon dioxide (CO_2) and ash variations are noted. However, considering the magnitude of the discrepancies, and the analytical and sampling errors that are introduced, it is perceived that the discrepancies are not significant in the context of this research.

By increasing the number of fields of view analysed, and by decreasing the beam/point spacing, the number of points analysed could be increased, thus reducing the analytical errors attributed to poor sampling statistics. Such improvements would unfortunately increase the analytical time, and the associated analytical costs, however, which might negate the benefits of improved statistics. The advent of faster computers and improved software will ensure that the increase in the number of analytical points need not result in a corresponding increase in analytical time and costs associated with better statistics. This is the next essential step to be taken in the development of the CCSEM.

5.7.3 Mineral grain sizes

Section 4.6.3 and Appendix G detail the CCSEM method of determining the grain size of the minerals in a pulverised fuel. The cumulative mass percent grain size distribution of the main minerals, namely quartz, carbonates (calcite and dolomite), pyrite and kaolinite is presented in Figure 5.14 and summarised in

Table 5.10. Included in Figure 5.14 is the total particle size distribution, which should be comparable to the screened particle size distribution (Figure 5.3).

Table 5.10: Particle size distribution and percent passing 75 µm of individual minerals and all particles (PSD CCSEM). The particle size distribution derived from the physical screen analysis is also included (PSD screen, Figure 5.3)

Size Class (mass-% retained)	Quartz	Kaolinite	Carbonates	Pyrite	PSD CCSEM	PSD SCREEN
+75	22.8	6.6	8.0	26.1	31.2	31.0
-75+38	14.3	17.9	16.2	18.7	21.7	22.5
-38	62.9	75.5	75.8	55.2	47.1	46.5
%passing 75µm	77.2	93.4	92.0	73.9	68.8	69.0

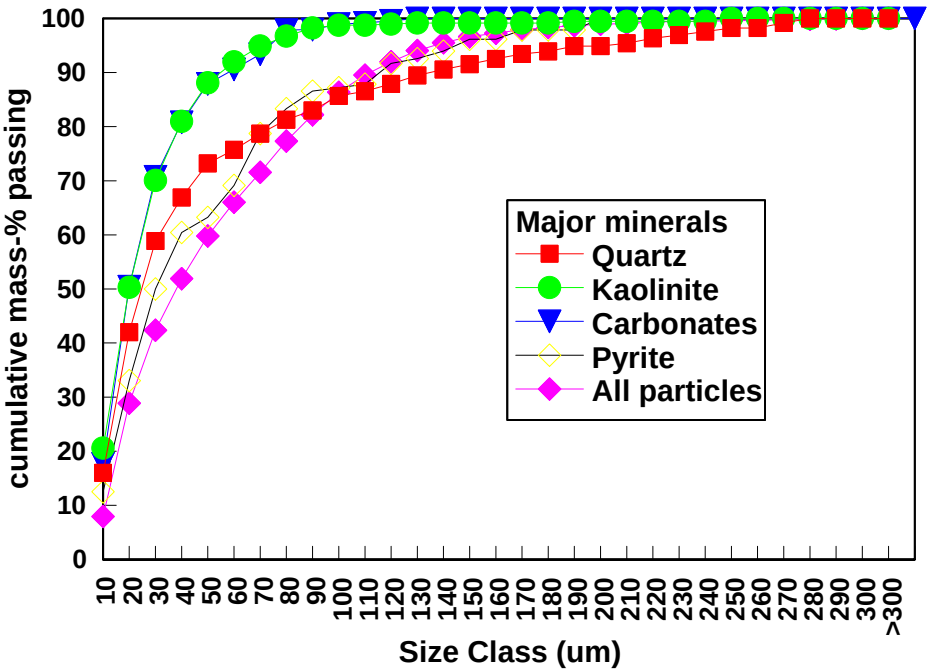

Figure 5.14: Grain size distribution of individual minerals and total particle size distribution (all particles).

Kaolinite and carbonates are significantly finer than quartz and pyrite. A large proportion of the individual minerals are finer than 38 µm. The maximum measured particle size on the other hand is greater than 300 µm. The CCSEM

measured size distribution of all particles is comparable to the screened size distribution (Table 5.10 and Figure 5.3).

5.7.4 Mineral liberation and association characteristics

The methodology used to quantify the liberation and association characteristics of minerals and of the organic component in pulverised fuel is described in Appendix G

The average cumulative liberation yield plots for the main minerals in the pulverised fuel sample are illustrated in Figure 5.15 and summarised in Table 5.11. This average is calculated by combining the liberation characteristics of each size fraction for each hole. The particle size distribution for the respective holes is used as the weighting factor. The detailed liberation data are summarised in Appendix M.

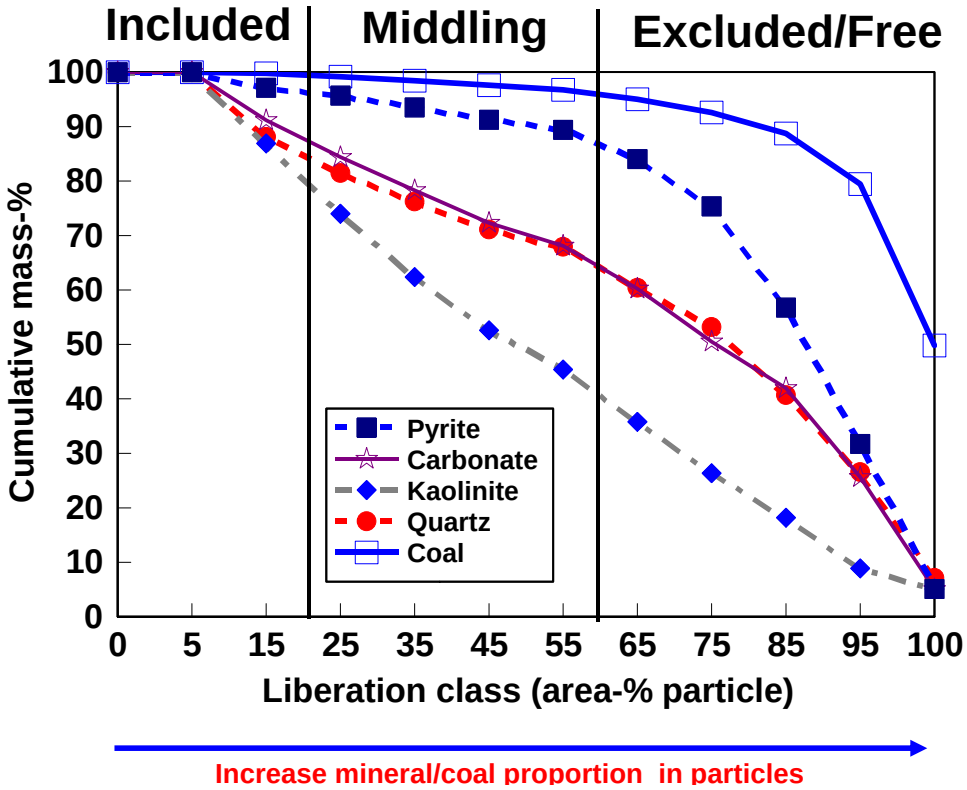

Figure 5.15: The average cumulative liberation yield (CLY) plots of the major minerals in the pulverised fuel.

The “coal” mineral phase describes the liberation of the organic fraction.

Table 5.11: Liberation characteristics of major minerals expressed in terms of the "microlithotype" classification (refer to Appendix M).

Liberation class	Area proportion	Pyrite	Carbonate	Kaolinite	Quartz	Coal
Included	0-20	4.3	15.6	26.0	18.5	0.8
Middling	20-60	11.7	24.1	38.2	21.1	4.2
Excluded	60-100	84.0	60.3	35.8	60.4	95.0
Total		100.0	100.0	100.0	100.0	100.0

The following major trends are noted from Figure 5.15 and Table 5.11:

- "Coal", the organic component of the pulverised fuel, is liberated with 95 mass percent of the coal in the excluded category. Up to 50 mass percent of the "coal" is mineral free (100% liberation class, see Table 5.13).
- In terms of the major minerals, the degree of mineral liberation increases in the following order: kaolinite, quartz/carbonate, pyrite.
- A large proportion of the kaolinite is included or occurs as middlings (20 to 60 liberation class).
- Quartz and the carbonates have similar liberation trends, with 60 mass percent occurring as excluded particles.
- Pyrite is predominantly excluded (84 mass precent).

The CCSEM liberation trends are similar to the mineral liberation characteristics described optically (refer to section 5.3.1 (macerals), Tables 5.3 and 5.4).

Alternatively, pulverised fuel particles can be characterised by the proportion of coal and mineral matter in the particle and classified into the three broad groups based on the area percent mineral matter proportions. These classification classes are differentiated into the following: "included" (0 to 20% mineral matter), carbominerite (20 to 60% mineral matter) and minerite (>60% mineral matter). These classes are analogous to the optical microscope "microlithotype" liberation classes defined in Appendix J.

The total mass percent proportion of particles, the total mass percent of coal and the total mass percent of mineral matter in these particle classes defined above are summarised in Table 5.12.

Table 5.12: Mass-% total particle, coal and mineral distribution.

"Microlithotype" Liberation class (MM – mineral matter)	Total (mass-%)	Mass-% (Coal (%))	Mass-% (Mineral (%))
Included (0-20 %MM, 80-100% Coal)	**69.8**	64.1 (88.8%)	5.7 (20.5%)
Carbominerite (20-60% MM, 40-80 %Coal)	14.5	6.4 (8.8%)	8.1 (29.1%)
Minerite (60-100 MM, 0-40% coal)	15.7	1.7 (2.4%)	**14.0 (50.4%)**
Total	100.0	72.2	27.8

The following trends are noted from Table 5.11:

- 69.8 mass percent of the total sample consists predominantly of particles rich in coal (80 to 100 area-% coal) with minor included mineral matter (0 to 20 area-%). 20.5% of the total mineral matter is associated with these predominantly coal rich particles.
- 50.4% of the total mineral matter occurs as minerite particles (≈ adventitious or excluded particles). Only 2.4% of the total "coal" is associated with this group.
- 29.1% of the total mineral matter occurs as carbominerite particles.

It is difficult to accurately reconcile the optical characterisation of the "microlithotypes" in Tables 5.3 and 5.4. The "microlithotypes" defined in Tables 5.3 and 5.4 are based on volume percent distribution and not on mass percent distribution as described above.

The average individual liberation characteristics of the major minerals per size fraction are summarised in Appendix M. Without exception, the degree of liberation increases with a reduction in size fraction.

The overall association characteristics of the particles in the pulverised fuel are summarised in Table 5.13. The projected elemental compositions of the resultant fly ash particles assuming full coalescence are also included in Table 5.13.

Table 5.13: Particle association characteristics in pulverised fuel.

Association	Mass-%	Projected Fly ash elemental composition
Coal	49.8	Al(?),Si(?),Ca(?),Mg(?),Ti(?), S(?) (Organically bound elements)
Kaolinite+Coal	16.0	Al-Si-O (mullite, metakaolinite, silicon spinel)
Kaolinite+quartz+coal	15.8	Al-Si-O (variable Al/Si ratio dependent on proportion of quartz)
Carbonate+coal	3.2	Ca-O, Ca-Mg-O, Mg-O (Ca-oxide, Mg-oxide)
Quartz+coal	2.5	Si-O
Quartz+kaolinite	1.8	Al-Si-O (variable Al/Si ratio dependent on proportion of quartz)
Pyrite+coal	1.6	S-Fe-O, Fe-oxide
Kaolinite+quartz+mica+coal	1.0	K-Al-Si-O (variable Al/Si ratio dependent on proportion of quartz)
Kaolinite+mica+coal	1.0	Al-Si-K-O
Carbonate+kaolinite+quartz+coal	0.9	Ca-Mg-Al-Si-O (variable Al/Si ratio dependent on proportion of quartz)
Quartz+carbonate+coal	0.8	Si-Ca-Mg-O
Carbonate+kaolinite+coal	0.8	Al-Si-Ca-Mg-O
Quartz	0.4	Si-O
Pyrite	0.4	S-Fe-oxide, Fe-oxide
Kaolinite+quartz+mica	0.4	K-Al-Si-O (variable Al/Si ratio dependent on proportion of quartz)
Kaolinite+quartz+oxide+coal	0.3	Al-Si-Fe-Ti-O
Kaolinite	0.3	Al-Si-O (mullite, metakaolinite, silicon spinel)
Pyrite+carbonate+gypsum+coal	0.2	S(?)-Fe-Ca-O, Fe-Ca-Mg-O
Kaolinite+quartz+feldspar+mica	0.2	K-Al-Si-O (variable Al/Si ratio dependent on proportion of quartz)
Other	2.5	Variable composition

The following trends are noted from Table 5.13:

- "Ash-free" coal particles are the main particle type (49.8 mass-%). Inorganic ash-forming elements, which might arise from these ash-free particles, are derived either from organically-bound elements or sub-micron mineral grains (see Figure 5.13) not detected by CCSEM (smaller than the CCSEM resolution).
- Kaolinite+coal (16 mass-%) and kaolinite+quartz+coal (15.8 mass-%) are the second and third most common associations. They are comparable to the large proportions of carboargillite and carbosilicate microlithotypes described in the +75 µm and -75+38 µm size fractions (Tables 5.3 and 5.4).

- The proportion of coal particles with complex mineral associations is comparatively low (8.1 mass-%). This is analogous to the low proportion of carbopolyminerite in the +75 µm and -75+38 µm size fractions (Tables 5.2 and 5.3).
- 12.6 mass-% of the coal particles have included minerals with fluxing elements, potassium, calcium, magnesium and iron. The presence of these fluxing elements will probably lower the melting points of the included minerals and produce “sticky” slag-forming fly ash particles.

5.8 Summary

There is no appreciable variation in the chemical characteristics of the pulverised fuel and, to a lesser extent, in the boiler operational conditions during the sampling period.

The size of the fly ash within the boiler tended to increase from the wall to the centre of the boiler. The fly ash particles were comparatively finer in the upper reaches of the boiler. This size stratification could possibly be attributed to the flue gas carrying capacity and the flow characteristics within the boiler.

Kaolinite and quartz are the major minerals in the pulverised fuel sample. Pyrite, calcite and dolomite are minor minerals. There are also trace concentrations of feldspar, illite/mica, Ti-oxide, apatite, siderite, ankerite and iron oxide.

The chemically derived ash elemental compositions, the carbonate content and ash percent of the pulverised fuel compared favourably to the CCSEM derived ash elemental composition, carbonate proportion and ash percent. The only discrepancies were an overestimation of the mass percent pyrite proportion and an underestimation of kaolinite proportion by CCSEM. These could be attributed to pyrite segregation during the preparation of samples and the presence of sub-micron included kaolinite grains, which were smaller than the scanning electron beam resolution (2 to 3 µm).

The pulverised fuel burnt in Hendrina power station’s unit 9 for the duration of sampling period was characterised by a large proportion (~50 mass percent) of

mineral free particles and, to a lesser extent, inertinite-rich coal particles containing either fine included kaolinite and/or kaolinite and quartz. It was perceived from the standardless energy dispersive analysis (EDS) that the “ash free” particles might contain sub-micron mineral grains or organically-bound inorganic elements (e.g. aluminium, silicon, calcium, magnesium, titanium and sulphur).

Minerals (calcite, dolomite, pyrite, illite/mica and orthoclase) with typical fluxing elements such as calcium, magnesium, potassium and ferrous iron were predominantly excluded/adventitous particles. A small proportion of these minerals is associated with other minerals or occurs as included minerals in coal.

On the basis of the mineral associations and liberation attributes of the coal particles in the pulverised fuel studied, it is perceived that Al-Si-O (with variable Al/Si ratios) and Si-oxide will be the dominant fly ash particle types. Extraneous pyrite will produce iron oxide fly ash particles, while the extraneous carbonates produce calcium oxide, magnesium oxide and Ca-Mg-oxide rich fly ash particles.

Since a high proportion of calcium, magnesium and iron is associated with extraneous carbonates and pyrite and not as included carbonates and pyrite associated with included kaolinite and quartz, the proportion of Al-silicate and Si-oxide fly ash particles with low concentrations of the fluxing elements (calcium, magnesium, potassium and iron) is expected to be comparatively low. It is predicted that the majority of the calcium and magnesium would occur as Ca-oxide/Mg-oxide/Ca-Mg-oxide fly ash particles and the iron as iron oxide fly ash particles. From a slagging perspective, aluminium-silicate particles with low concentrations of the fluxing elements (Ca, Mg, K and Fe^{2+}) were expected to have a high probability of initiating and sustaining the development of slag.

The characteristics of the fly ash sampled from within the boiler and the slag deposits formed on removable slag sleeves are described in the following chapter.

6 RESULTS – FLY ASH AND SLAG DEPOSITS

6.1 Fly Ash

6.1.1 Phase distribution

The phase classification of fly ash is described in section 4.6.2 and Table 4.3. Fly ash phase classification is based on the elemental composition of fly ash particles. The nomenclature used is based on the original minerals in the coal particles, which would have being the source of the elements. For instance, the fly ash phase, kaolinite(carbonate), is a Ca-bearing alumino-silicate fly ash phase, probably formed as a result of the interaction of kaolinite (source of Al-Si) with calcite and/or dolomite (the source of calcium).

The average mass percent mineral distribution of the fly ash sampled from within the boiler by the suction pyrometer, and a single cegrit sample is summarised in Table 6.1. Detailed fly ash distributions across size fractions and for the individual holes are tabulated in Appendix N. Cegrit samples are routinely taken by power station personnel for determining the proportion of unburnt carbon (“char”) in the fly ash.

Kaolinite, the predominantly fly ash phase (58.3 mass-%) is an Al-Si-O fly ash phase representing the transformation products of kaolinite. It includes metakaolinite, silicon spinel and mullite (see Figure 3.1). “Quartz” (13.5 mass%), the second most abundant fly ash phase. Kaolinite(carbonate), kaolinite(pyrite,carbonate), koalinite(pyrite), kaolinite(illite, mica), quartz60kaol40 and quartz80kaol20 occur in minor to trace proportions. These phases, which, in the context of this research, are collectively termed “mixed” phases, do not occur as minerals in coal, but are formed as a result of the interaction of minerals, or elements derived from the minerals, during the ash formation process. The total proportion of “mix” is 12.4 mass percent. Kaolinite(carbonate), is formed when calcium and magnesium interacts with the Al-Si derived from kaolinite. This kaolinite(carbonate) accounts for an average 5.1 mass percent of the fly ash phases. Iron oxide/pyrite is the transformation product of pyrite. Iron oxide/pyrite includes iron oxide and iron-sulphur-oxide phase which has minor concentrations of S. Phase abundance of iron oxide/pyrite is 2.3 mass percent.

The mass percent phase abundance of the cegrit sample is similar to the average suction pyrometer fly ash. The only noted difference is the proportion of char. This could be expected as the suction pyrometer sampled raw coal for holes 1 and 2 at a depth of 2m. Including raw coal will artificially inflate the proportion of char.

Table 6.1: Average mass percent fly ash phase proportions in the suction pyrometer fly ash samples and in the routine cegrit fly ash sample.

	Average suction pyrometer fly ash				Cegrit Fly Ash
Fly ash phase	**+75**	**-75+38**	**-38**	**Calc.Total**	
Ca-carbonate	1.0	1.3	0.8	0.9	1.7
Ca-oxide	0.8	1.1	0.9	1.0	1.0
Kaolinite	39.8	51.6	67.0	59.2	58.3
Kaolinite(pyrite, carbonate)	0.6	0.5	0.3	0.4	0.4
Kaolinite(carbonate)	7.9	7.9	4.1	5.1	6.0
Kaolinite(pyrite)	1.5	1.5	0.8	1.0	2.0
Kaolinite(illite, mica)	1.1	1.7	2.2	1.9	2.0
Orthoclase	0.6	0.6	0.2	0.3	1.0
Quartz60Kaol40	2.7	3.4	3.5	3.3	3.7
Quartz80Kaol20	0.8	1.0	0.7	0.8	1.3
Quartz	22.4	12.3	12.2	13.5	15.7
Iron_Oxide/pyrite	4.8	2.9	1.8	2.3	3.0
Ti-oxide	0.3	0.2	0.2	0.2	0.1
Char	15.2	13.6	4.8	9.8	3.5
Unmatched	0.5	0.4	0.4	0.4	0.1
Total	100.0	100.0	100.0	100.0	100.0

The fly ash phase variation of the major fly ash phases (kaolinite, quartz, iron oxide and Ca-oxide/carbonate) from the boiler wall to the boiler centre, and with height, indicates a distinct variation in the fly ash composition (Figures 6.1 to 6.4). These major phases represent the transformation products from the coal minerals kaolinite, quartz, pyrite and carbonates, respectively.

The straight line in Figures 6.1 to 6.4 depicts the projected mass percent proportion of these major coal minerals as they enter the boiler. The mass percent mineral proportion entering the boiler is calculated by assuming that all the coal is burnt and that the mineral proportion in the remaining ash is equivalent to the absolute proportion of the mineral entering the boiler. The mass percent

proportion of the individual minerals entering the boiler is a baseline to which the fly ash phase distribution can be compared.

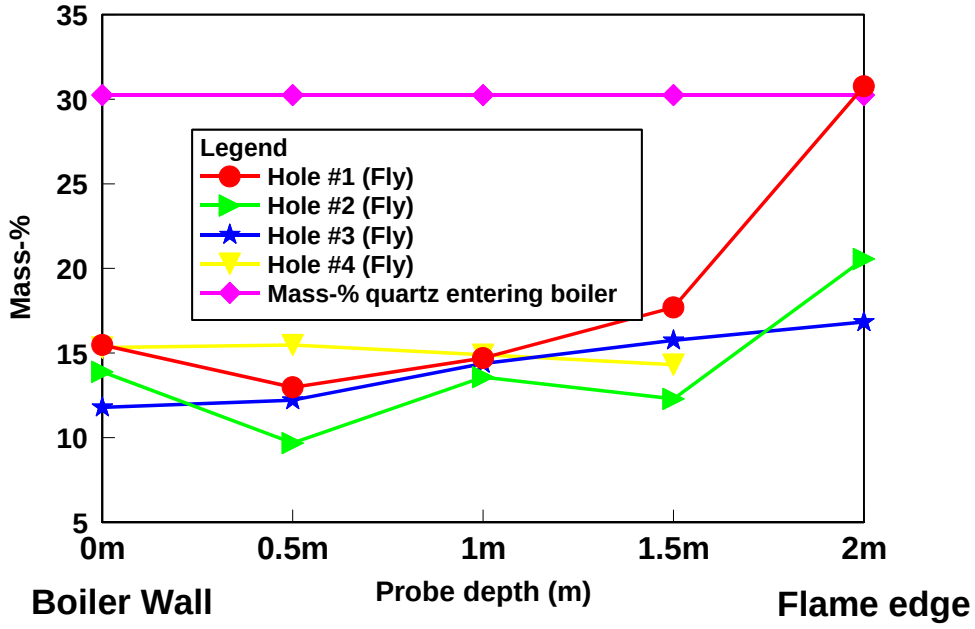

Figure 6.1: Quartz variations in suction pyrometer fly ash.

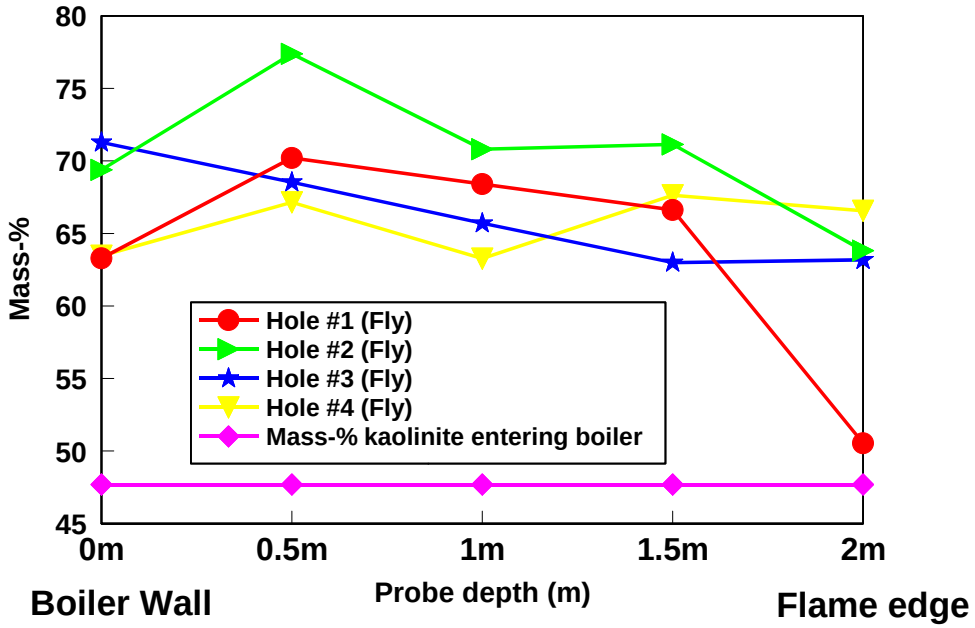

Figure 6.2: Kaolinite variation in suction pyrometer fly ash.

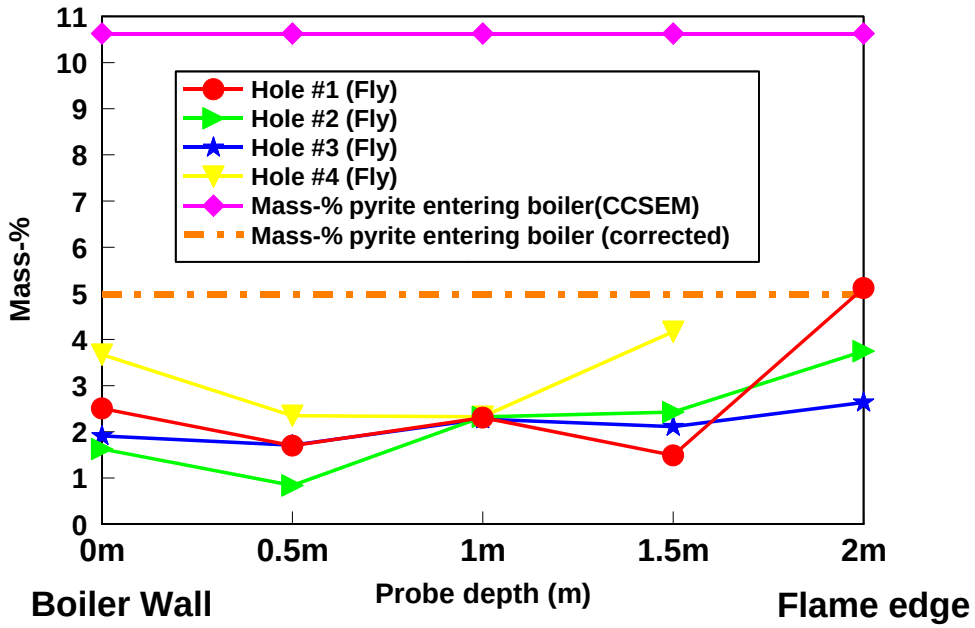

Figure 6.3: Pyrite/Fe-oxide variation in the suction pyrometer fly ash.

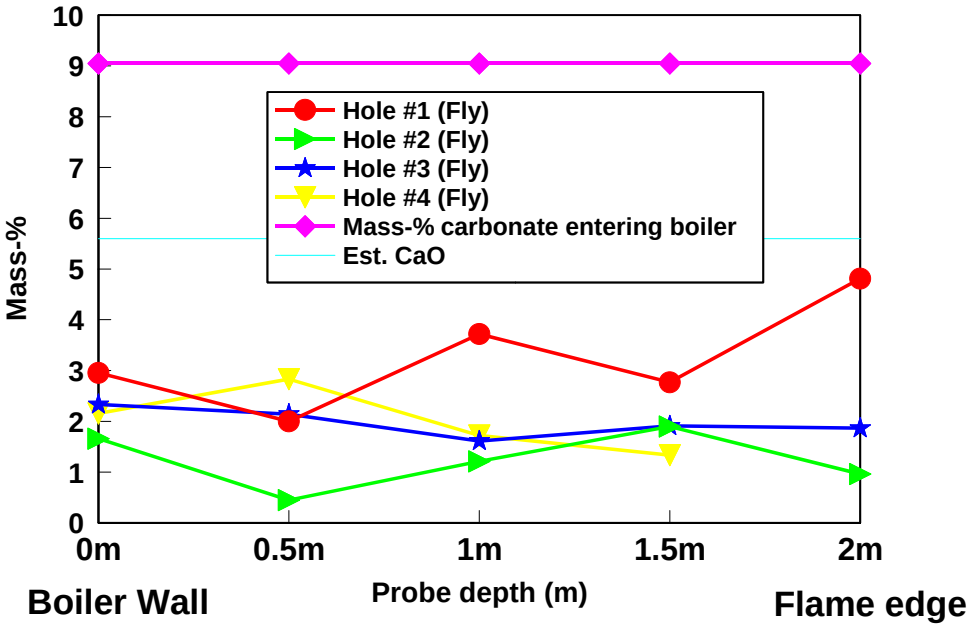

Figure 6.4: Ca-oxide/carbonate variation in the suction pyrometer fly ash.

The following can be concluded from figures 6.1 to 6.4:

1. Apart from the fly ash from hole 1 at a depth of 2m, there is significantly more kaolinite in the fly ash than the average mass percent proportion of kaolinite entering the boiler (normalised, excluding “coal”).
2. In contrast, the mass percent proportion of quartz, iron oxide/pyrite and Ca-oxide/carbonates are lower in fly ash than proportions of these minerals (quartz, pyrite and carbonates (dolomite, calcite) entering the boiler.
3. For quartz, iron oxide/pyrite and carbonate there is a general increase in the proportions of these fly ash phases from the boiler wall (0m) to the centre of the boiler (2m). Towards the upper regions of the boiler (holes 3 and 4), the mass% variation with depth is not as pronounced.
4. The mass% quartz and kaolinite in the fly ash sampled at a depth of 2m for hole #1, is similar to the average mass% quartz and kaolinite in the pulverised fuel (normalised excluding the coal). This is to be expected, as the centre of the burner is 2.5m from the sidewall. This implies that the suction pyrometer is sampling the peripheral of the pulverised fuel injected into the boiler.
5. The mass% proportions of pyrite and carbonate in the pulverised fuel entering the boiler in Figures 6.3 and 6.4 are significantly higher than the average mass% proportion of the fly ash phase’s iron oxide/pyrite and Ca-oxide/carbonates in the suction pyrometer fly ash. The corrected pyrite content based on the XRF ash elemental Fe_2O_3 content is similar to the proportion of Fe-oxide/pyrite in hole #1, at a depth two metres.

The influence of the mineral attributes (size and association) in pulverised fuel and the boiler configuration has on the concentration of the mineral transformation products in the fly ash is illustrated in the trends described above. The following points are noted:

1. Kaolinite – kaolinite in pulverised fuel predominantly occurs as fine included minerals surrounded by an organic matrix (Figures 5.14 and 5.15). The increase proportion of “kaolinite” in the suction pyrometer fly ash compared to the average proportion of kaolinite entering the boiler, suggests that kaolinite is preferentially concentrated in specifically the upper regions of the boiler. This could occur, if the included kaolinite is

released on combustion to form fine excluded kaolinite fly ash particles. These fine excluded kaolinite fly ash particles, are readily transported by flue gas to the upper regions of the boiler. The ability of the flue gas to transport a fly ash particle is a function of the flue gas velocity and the fly ash particle size and density.

2. The relative decrease in the proportion of quartz, Fe-oxide/pyrite and to a lesser extent Ca-oxide/carbonates in the suction pyrometer fly ash compared to the proportion of the corresponding minerals (quartz, pyrite and carbonates (calcite and dolomite)) entering the boiler suggests that these fly ash phases must be concentrated in the bottom ash. This is feasible as quartz, pyrite and to a lesser extent carbonates occur predominately as extraneous particles in the pulverised fuel (Figures 5.14 and 5.15). The ability of the flue gas to transport these coarse, dense fly ash particles will be severely reduced. This trend is still apparent, even taking into account the expected mass loss attributed to the transformation of pyrite to Fe-oxide and the transformation of carbonates to Ca-oxide, releasing volatile SO_3 and CO_2 gas.

The following observations will be confirmed in the following sections.

6.1.2 Fly ash grain size

Section 4.6.3 and Appendix G detail the CCSEM method of determining the grain size of minerals in pulverised fuel and fly ash. The cumulative mass% grain size distribution of the main fly ash phases/minerals, namely quartz, calcium-oxide/carbonates (remnants of carbonate transformation) and pyrite/Fe-oxide (remnants of pyrite transformation), kaolinite and kaolinite(carbonate) is presented in Figure 6.5 and summarised in Table 6.2. Included in Figure 6.5 is the total particle size distribution.

The summarised average size distributions of the major minerals/phases in the fly ash are tabulated in Table 6.2. The comparative percent passing 75 µm for the corresponding minerals in coal are included in Table 6.2.

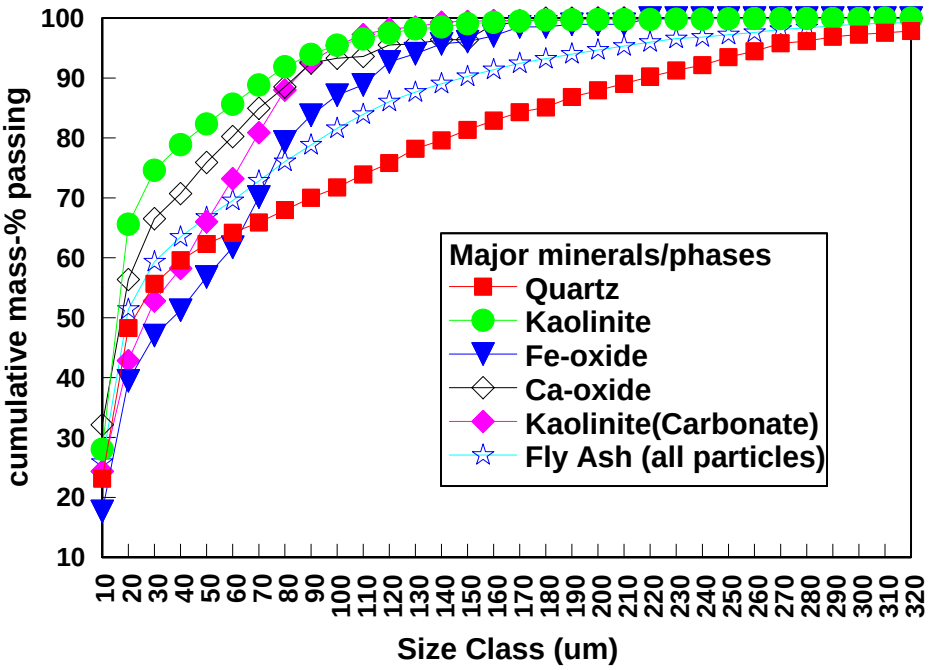

Figure 6.5: Average cumulative mass percent grain size distributions for the major minerals/phases in fly ash samples.

A notable trend in the pulverised fuel is the similarity in the carbonate/kaolinite and pyrite/quartz particle size distributions (Figure 5.14). This similarity manifests itself in the Ca-oxide/kaolinite and the Fe-oxide/quartz size distributions in the fly ash (Table 6.2).

Table 6.2: Average mass-% grain size distribution for individual phases/minerals in fly ash.

Size fraction (mass-% retained)	Quartz	Kaolinite	Fe-oxide	Ca-oxide	Kaolinite (Carbonate)	Fly Ash
+75	35.0	12.8	34.1	17.4	22.9	28.8
-75+38	7.4	10.5	16.8	14.0	21.5	9.8
-38	57.6	76.7	49.1	68.6	55.5	61.4
-75% fly ash	65.0	87.2	65.9	82.6	77.1	71.2
-75% coal minerals	77.2	93.4	73.9	92.0	N/A	N/A

The minerals/phases in fly ash are marginally coarser than the corresponding minerals in pulverised fuel. The increase in kaolinite, pyrite and carbonate size could be attributed to the release of water, SO_3 and CO_2 during the transformation of the minerals. These volatile gases would contribute to the

swelling of the particles and consequently to an increase in the overall particle size. Alternatively, the increase in size could be attributed to the coalescence of minerals grains in the combusting coal particle and also to the formation of spherical cenospheres. The fly ash formation process will be discussed in more detail in chapter 7.

6.1.3 Fly ash liberation

The methodology used to quantify the liberation and association attributes of minerals/phases in fly ash is described in Appendix G.

The average cumulative liberation yield plots for the main minerals/phases in fly ash are illustrated in Figure 6.6 and summarised in Table 6.3. This average is calculated by combining the liberation characteristics for each size fraction and for each hole, using the particle size distribution for the respective holes as the weighting factor. The detailed liberation data across size fractions and for the difference holes are summarised in Appendix O.

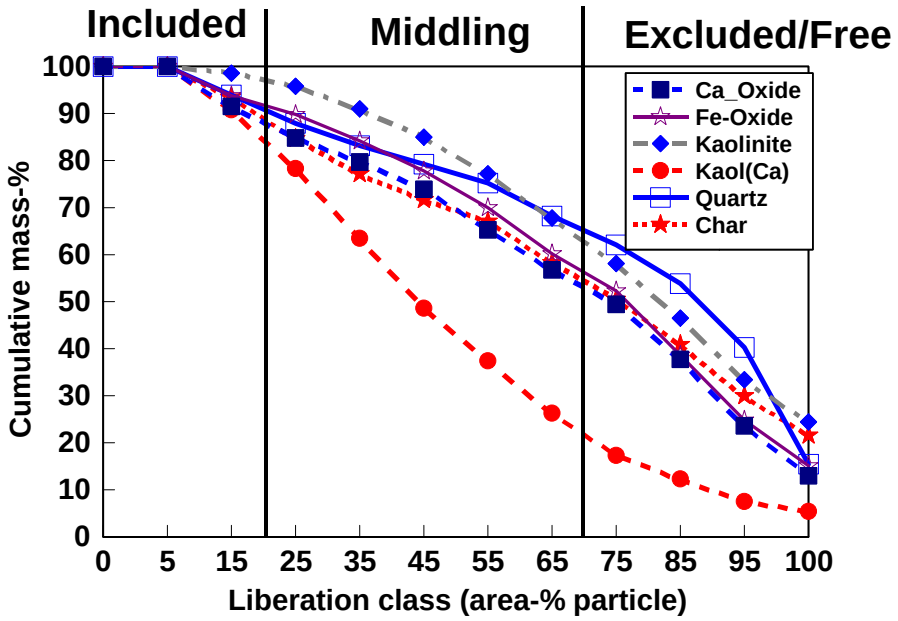

Figure 6.6: Cumulative liberation yield for the major phases in fly ash.

Table 6.3: Liberation characteristics of major minerals/phases in fly ash expressed in terms of the "microlithotype" classification.

Liberation class	Area proportion	Ca-Oxide	Fe-Oxide	Kaolinite	Kaol(Ca)	Quartz	Char
Included	0-20	15.2	10.2	4.2	21.7	12.1	15.3
Middling	20-60	28.0	29.6	27.9	52.0	19.7	26.4
Excluded	60-100	56.8	60.2	67.8	26.3	68.2	58.3
Total		100.0	100.0	100.0	100.0	100.0	100.0

Apart from kaolinite(carbonate), a high proportion of the main minerals/phases in fly ash occur as "excluded" particles. Calcium oxide and quartz have similar liberation characteristics to carbonates and quartz in pulverised fuel (Figure 6.7). In contrast, iron oxide has a higher proportion of included and middling particles and a correspondingly lower proportion of excluded particles in fly ash than is the case with pyrite in pulverised fuel. Kaolinite, initially occurring as fine included/middlings in pulverised fuel, is liberated to form predominately "excluded" kaolinite particles in fly ash.

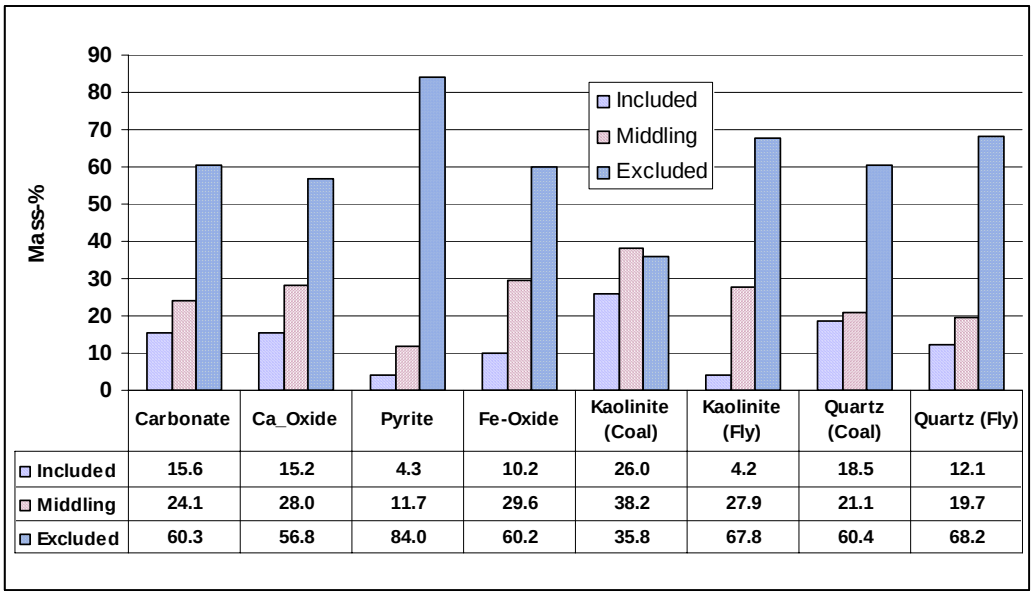

	Carbonate	Ca_Oxide	Pyrite	Fe-Oxide	Kaolinite (Coal)	Kaolinite (Fly)	Quartz (Coal)	Quartz (Fly)
Included	15.6	15.2	4.3	10.2	26.0	4.2	18.5	12.1
Middling	24.1	28.0	11.7	29.6	38.2	27.9	21.1	19.7
Excluded	60.3	56.8	84.0	60.2	35.8	67.8	60.4	68.2

Figure 6.7: Comparative liberation characteristics of minerals in pulverised fuel and corresponding fly ash phases.

The following conclusions can be made on the basis of the comparisons in Figure 6.7:

- The excluded quartz and carbonates in pulverised fuel sample remain excluded in the fly ash.
- The increase in the proportions of middling and included Fe-oxide particles in the fly ash suggests that there is a significantly larger degree of interaction (coalescence?) of Fe-oxide and the other fly ash phases.
- Included kaolinite in pulverised fuel is liberated during the combustion of the coal particle and forms fine excluded fly ash particles.

These general trends compliment the reasons proposed to explain the observed differences between the proportions of minerals entering the boiler and the proportions of the transformed products in the fly ash (Figures 6.1 to 6.4).

6.1.4 Fly ash association

Fly ash particles are classified in terms of the fly ash phases present in each particle. For instance, a “kaolinite” particle describes a fly ash particle comprising only the fly ash phase, kaolinite, whereas the association class quartz+kaolinite describes a fly ash particles comprising only kaolinite and quartz in varying proportions.

The association characteristic of the fly ash phases (Table 6.4) describe the mineral/phase associations of the particles.

The numerous association classes defined (Table 6.4) highlight the complexity of fly ash mineral/phase associations. The majority of the complex associations are invariably lower than 1 mass percent.

Kaolinite constitutes the dominant association class in fly ash. This is symptomatic of the liberation of fine included kaolinite particles in the pulverised fuel to form excluded fine “kaolinite” fly ash particles (Figure 6.7).

Table 6.4: Average association characteristics of minerals/phases in fly ash

Fly ash mineral/phase association	Mass-%
Kaolinite	41.3
Char	7.8
Quartz>Kaolinite Mix+Kaolinite+Quartz	6.4
Quartz>Kaolinite Mix+Kaolinite+Kaolinite(Ca)+Quartz	6.2
Quartz	5.4
Quartz+Kaolinite	4.7
Kaolinite+Kaolinite(Ca)	2.8
Quartz>Kaolinite Mix+Kaolinite+Quartz+Kaolinite(Fe)+Kaolinite(Ca)	2.3
Quartz>Kaolinite Mix+Kaolinite	2.2
Kaolinite+Quartz+Kaolinite(Ca)	1.6
Kaolinite(Ca)	1.4
Quartz>Kaolinite Mix+Kaolinite+Kaolinite(Ca)	1.2
Quartz>Kaolinite Mix	1.0
Quart>Kaolinite Mix+Quartz+Kaolinite(Ca)+Kaolinite+ Ca-Oxide	0.9
Quartz>Kaolinite Mix+Quartz+Kaolinite(Fe)+Kaolinite	0.9
Quartz>Kaolinite Mix+Quartz+Kaolinite(Ca)+Kaolinite(Fe) +Kaolinite+Fe-Oxide+Ca-Oxide	0.9
Quartz>Kaolinite Mix+Quartz	0.8
Kaolinite(Ca)+Kaolinite+Ca-Oxide	0.8
Ca-Oxide	0.7
Fe-Oxide	0.6
Quartz+Kaolinite(Ca)+Kaolinite(Fe)+Kaolinite+Fe-Oxide	0.5
Kaolinite+Ca-Oxide	0.5
Quartz>Kaolinite Mix + Quartz + Kaolinite(Ca) + Kaolinite(Fe) + Fe-Oxide	0.5
Quartz+Kaolinite(Ca)+Kaolinite+Ca-Oxide	0.4
Kaolinite(Ca)+Kaolinite(Fe)+Kaolinite	0.4
Quartz>Kaolinite Mix+Kaolinite(Ca)+Kaolinite(Fe)Kaolinite	0.4
Quartz>Kaolinite Mix+Quartz+Kaolinite(Ca)+Kaolinite(Fe)+Fe-Oxide	0.4
Kaolinite(Fe)	0.3
Quart>Kaolinite Mix Quartz+Orthoclase+Kaolinite(Ca)+Kaolinite(Fe)+Kaolinite	0.3
Kaolinite+Kaolinite(Fe)	0.3
Quartz+Kaolinite(Ca)+Kaolinite(Fe)+Kaolinite	0.3
Quartz>Kaolinite Mix+Quartz+Orthoclase+Kaolinite	0.3
Quartz>Kaolinite Mix+Quartz+Orthoclase+Kaolinite+Ca-Oxide	0.3
Other	5.2

Quartz>Kaolinite Mix is collective description for Quartz60Kaol40 and Quartz80Kaol40 fly ash phases
Kaolinite(Ca) – Kaolinite(carbonate) and Kaolinite(carbonate,pyrite)
Kaolinite(Fe) – Kaolinite(pyrite)

A comparison between the major associations in pulverised fuel and the major associations in fly ash, is summarised in Table 6.5 and in Appendix P. (Please note that this table excludes coal and char as a phase).

Table 6.5: Summary of comparative association classes between pulverised fuel and corresponding association classes in fly ash (details in Appendix P)

Coal Association	Coal	Fly
Kaolinite+Quartz	37.8	16.4
Kaolinite	34.4	44.8
Quartz	5.8	5.8
Pyrite	3.3	0.7
Carbonate	7.2	0.8
Kaolinite+Quartz+Carbonate	1.9	10.2
Kaolinite+Carbonate	1.6	5.9
Kaolinite+Quartz+Pyrite	0.2	1.0
Kaolinite+Pyrite	0.2	0.7
Gypsum+Kaolinite+Quartz+Carbonate	0.3	1.0
Quartz+Kaolinite+Carbonate+pyrite	0.0	6.2
Orthoclase+Kaolinite+Quartz	0.3	0.3
Mica_Illite+Kaolinite+Quartz+Carbonate	0.2	0.3
Quartz+Pyrite	1.6	0.1
Other	5.2	5.9
Total	100.0	100.0

The following trends, based on the comparative association characteristics, are noted:

- Kaolinite and quartz are commonly associated with each other in pulverised fuel but their association is not as pronounced in fly ash. The corresponding increase in the fly ash “kaolinite” proportions suggests that the kaolinite in kaolinite+quartz+coal particles is liberated and reporting in the fly ash “kaolinite” association class.
- Extraneous quartz particles in the pulverised fuel are unaffected during the process of combustion and fly ash formation.
- The decrease in the proportions of pyrite and carbonate and the corresponding increase in the fly ash association classes, namely kaolinite+quartz+carbonate, kaolinite+carbonate, kaolinite+pyrite, quartz+kaolinite+carbonate+pyrite, kaolinite+quartz+pyrite and gypsum+kaolinite+quartz+carbonate, suggests that there is a degree of interaction (coalescence) between carbonates, pyrite, quartz and kaolinite.
- The relative decrease in quartz+pyrite fly ash association class indicates a limited interaction between pyrite and quartz during fly ash formation.

The variations in the association and liberation trends of fly ash phases as opposed to those corresponding minerals in pulverised fuel suggests that the process of fly ash formation is not simplistic and that it and involves more than one process. The alternative fly ash formation processes are discussed in detail in chapter 7.

The slag deposit on the removable slag sleeves has elemental and fly ash characteristics that can be compared with the overall mass percent fly ash phase abundance. This comparison highlights any fly ash phase, which both initiates and subsequently sustains the development of slag deposits. The results obtained from the slag deposition trails are summarised in the following section.

6.2 Slag Deposits

Removable slag sleeves with a thin veneer of slag deposits were obtained for each hole that was analysed. In certain cases, a substantial clinker deposit, analogous to “eyebrows” formed on the burners developed on the slag sleeve. A bottom ash sample was also collected from the ash hoppers for analysis. The slag sleeves and the clinker samples were prepared and analysed by CCSEM. The surface temperatures of the slag sleeves were estimated using the equations described in Appendix D.

The variations in the slag sleeve surface temperatures and mass percent phase abundance in the slag deposits and clinkers are discussed in the following sections.

6.2.1 Slag sleeve surface temperatures

Two methods were developed to estimate the surface temperatures of the removable slag sleeves (Appendix D).

The first method is based on the assumption the heat conducted through the slag probe is equal to the convection heat required to heat the water in the slag probe to 100 °C (Figure 6.8).

The second method is based on the assumption that there is a linear temperature relationship between the slag probe surface and the inner surface of the slag probe.

The variation in the slag probe surface temperature, based on the first assumption (convection=conduction), is summarised in Figure 6.8. This same variation, based on the second method (slope) is summarised in Figure 6.9. The average slag probe surface temperatures are included.

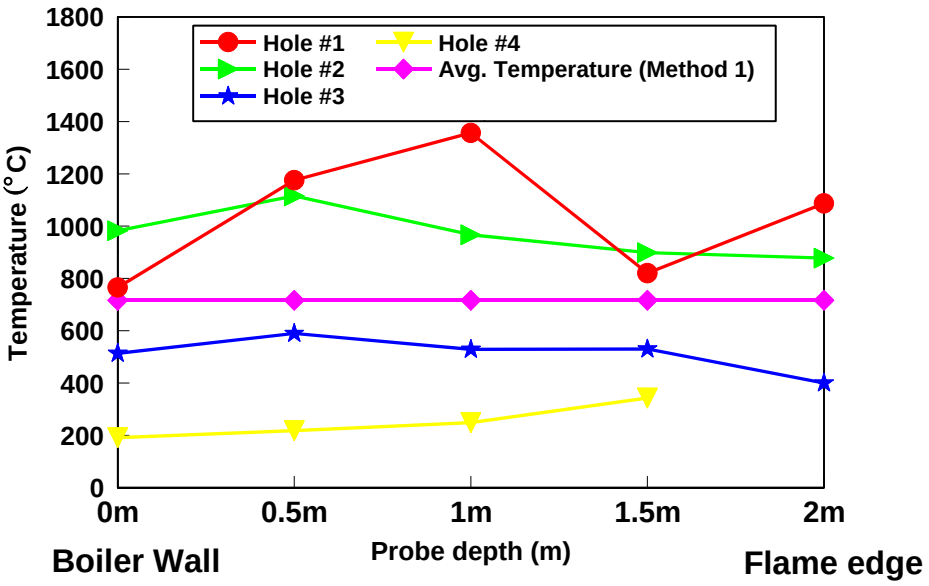

Figure 6.8: Calculated variation in slag probe surface temperature based on conduction heat flux equal to convection heat flux (Appendix D) – first method.

Both techniques yielded similar results and indicate that the surface temperatures of the slag probe at holes 1 and 2 exceeded 750 °C. On the other hand, in the case of holes 3 and 4 the surface temperatures in the upper regions of the boiler are mainly lower than 600 °C. Higher surface temperatures for holes 1 and 2 could be expected as the sampling points were in close proximity to the flame.

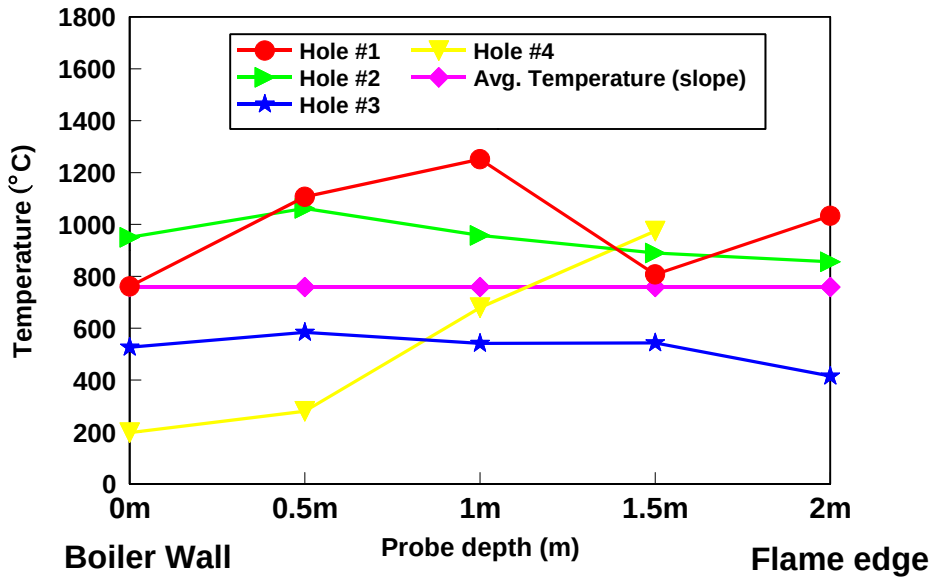

Figure 6.9: Calculated variations in slag probe surface temperature based on the slope method (Appendix D).

Apart from #4 1m and #4 1.5m, the correlation between the two methods (convection/condution and slope) for determining the surface temperature estimates is good (r=0.99) (Figure 6.10).

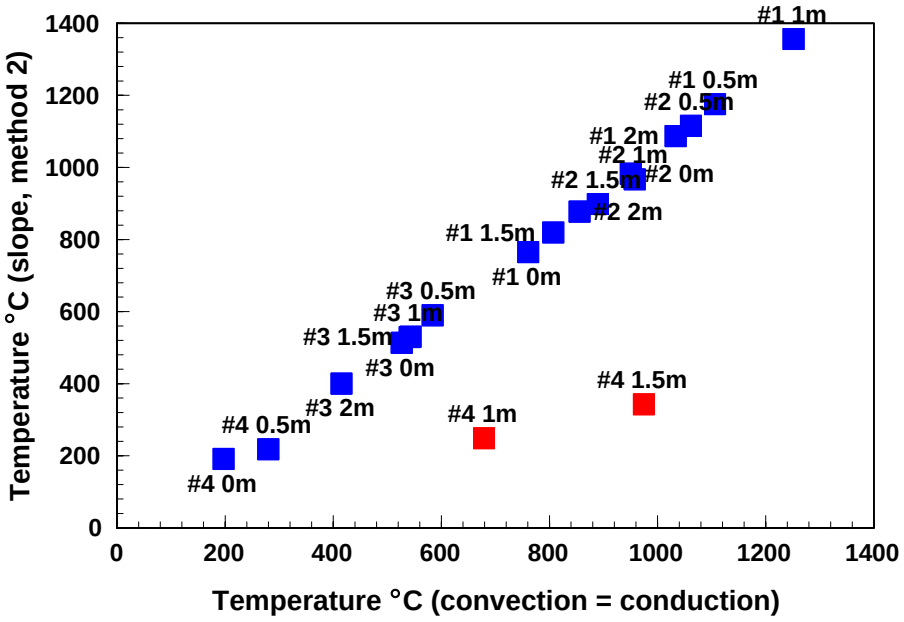

Figure 6.10: Correlation between slag probe surface temperature estimates

The surface temperature variations for hole 1 were erratic. The surface temperatures for holes 2 and 3 generally decrease from the wall to the centre, while those for hole 4 increased from the wall to the centre. The estimated surface temperatures of the slag probe at the boiler wall (simulating position of boiler tubes) are summarised in Table 6.6.

Table 6.6: Calculated surface temperatures of the slag probe at the boiler wall (0m).

	Hole #1	Hole #2	Hole #3	Hole #4
Method 1	765	983	514	192
Method 2	761	950	526	197

The expected surface temperature of the boiler tubes is between 400-570 °C, with the highest temperatures occurring in the superheater region of the boiler (560 to 570 °C). The calculated slag probe surface temperatures for holes 1 and 2, exceeded the expected surface temperatures, hole 3 were within the limits and those for hole 4 slightly low.

The high slag probe temperature for hole 1, at a depth of 1metre (>1250 ºC) could have been on account of the increase in the overall temperature of the furnace as recorded by the increase in the average furnace temperatures measured from the side and front walls (Figure 6.11).

A slag probe operating parameter was to keep the water temperature of the inner cavity at ≈100 °C. This was achieved by varying the water flow rate to the slag probe. If the water temperature of the inner cavity were a constant temperature, the calculated variation in the slag probe surface temperatures would be a manifestation of the localised fluctuating temperatures within the boiler.

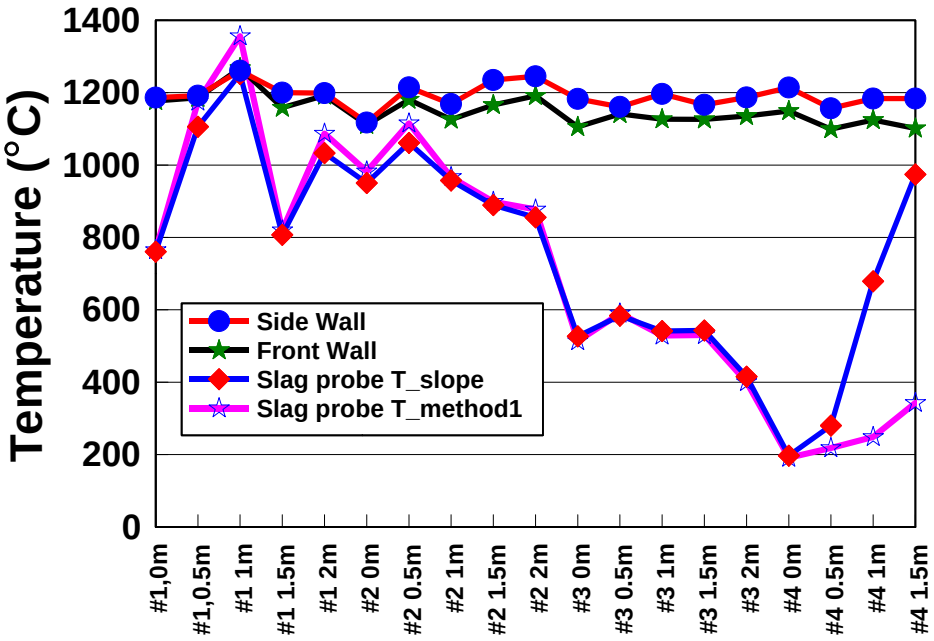

Figure 6.11: Measured furnace temperatures (thermopyle readings from side and front wall) as opposed to calculated slag probe surface temperatures.

The calculated surface slag probe temperatures for #1 0.5m, #1 1m, #1 2m, #2 0m, #2 0.5m and #2 1m are similar to the measured boiler side wall and front wall temperatures (Figure 6.11). This suggests that the slag probe cooling was marginal for these points and that the estimated surface temperatures of the slag probe is not necessarily representative of the actual boiler tube surface experienced within the boiler. The cooling of hole 3 was effective. It was perceived that the calculated slag surface temperatures simulate the surface temperatures of the boiler tubes. For hole 4, the calculated slag probe surface temperatures are probably lower than the actual boiler tube surfaces temperatures.

It has been documented that the surface temperatures of the boiler tubes influence the adhesion potential of the fly ash. The impact on the perceived discrepancy between the calculated slag probe surface temperatures and the actual surface temperatures of the boiler tube on the characteristics of the slag probe deposits will be highlighted in the following section.

6.2.2 Mineral abundance

The CCSEM method adopted for measuring the slag deposits that accumulated on the removable slag sleeves is described in section 4.6.1.3. The phase classification scheme adopted for fly ash, described in section 4.6.2 and table 4.3 is appropriate for describing the phases present in the slag deposits, the clinker samples and the bottom ash sample.

The slag deposits for holes #1 0m, #3 0.5m, #3 1.5m and #3 2m were not analysed, as it was difficult to successfully remove the slag sleeve from the slag probe. Excessive force was required to do so. On account of the extensive handling the fragile slag deposit was damaged and lost.

The detailed fly ash phase distributions for individual slag sleeve deposits are listed in Appendix P and the average slag deposit phase distribution for the respective holes is tabulated in Table 6.7. The average fly ash distribution obtained from the suction pyrometer is included in Table 6.7.

As opposed to the fly ash, the slag deposit is enriched in Fe-oxide, kaolinite(carbonate), Ca-oxide/Ca-carbonate, kaolinite(carbonate,pyrite) and kaolinite(pyrite) and depleted in kaolinite, quartz and quartz60kaol40 (Figure 6.12). Each of these enriched phases incorporates the fluxing elements, namely Ca, Mg and Fe.

Iron oxide and kaolinite (carbonate) are the major phases in the slag deposits in terms of mass (Figure 6.8 and Table 6.7).

Table 6.7: Mass percent fly ash phase distribution in slag probe slag deposit.

Phases	Hole 1	Hole 2	Hole 3	Hole 4	Average Slag Deposit	Average Fly Ash
Ca-oxide/Ca-carbonate	7.9	5.0	6.2	13.5	8.2	1.9
Fe-oxide	41.1	30.2	24.3	35.7	32.9	2.3
Kaolinite	9.0	22.3	29.0	11.8	18.0	59.2
Kaolinite(Carbonate,pyrite)	4.8	3.9	2.7	2.6	3.5	0.4
Kaolinite(Carbonate)	21.9	16.1	11.9	15.9	16.4	5.1
Kaolinite(Pyrite)	4.1	6.0	2.9	2.2	3.8	1.0
Kaolinite(Ti,K)	0.9	1.0	2.9	1.3	1.5	1.9
Orthoclase	0.2	0.3	0.2	0.3	0.2	0.3
Other	2.8	3.6	6.8	7.3	5.1	9.9
Quartz60Kaol40	0.8	1.7	2.0	0.8	1.3	3.3
Quartz80Kaol20	0.3	0.6	0.5	0.2	0.4	0.8
Quartz	6.1	9.2	10.4	8.4	8.5	13.5
Ti-oxide	0.2	0.2	0.3	0.1	0.2	0.2

Although there are differences in the composition of the slag deposits, the variation in the slag probe surface temperatures (Figures 6.8 and 6.9) seem to have had no major influence on the phase composition of the slag deposits developed on the slag sleeves.

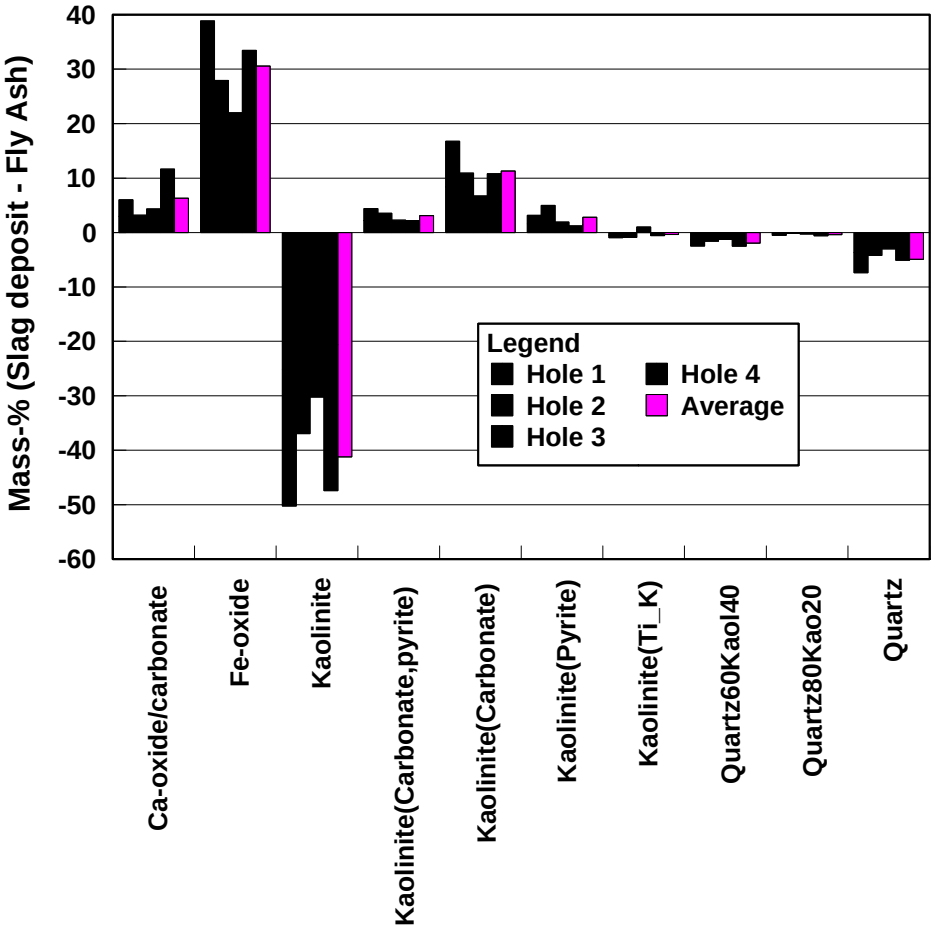

Figure 6.12: Mass% difference in proportion of slag phases in slag deposits compared to proportion in fly ash.

Clinker deposits were formed on slag sleeves #2 at depths of 2m and for hole #3 at the boiler wall (0m). These clinkers formed “eyebrows”, which adhered to and accumulated on the basal surface of the slag probe. The cooling water for the slag probe leaked from the couplings. This could have artificially stimulated the development of the hole #3 “eyebrow”/clinker. These “eyebrows/clinker” were collected and analysed on the CCSEM to determine the mass percent phase proportions.

A clinker deposit was randomly selected from the ash hopper by station personnel and analysed. To obtain a representative sample of the bottom ash is

difficult. This sample was included purely for comparative purposes. By no means is it indicative of absolute phase proportions in the ash hopper.

The mass percent phase proportions of the three slag probe clinker deposits, the randomly selected bottom ash sample and the average slag probe slag deposits (Figure 6.7). The average suction pyrometer fly ash is included in Table 6.8.

Table 6.8: Mass percent phase proportions in "eyebrow/clinker" deposits and bottom ash.

	Clinker #2,2m Section 1	Clinker #2, 2m Section 2	Clinker #3 0m	Bottom Ash	Average Slag Deposit	Average Fly Ash
CaOxide/Ca-carbonate	0.0	0.4	0.2	2.2	8.2	1.9
Fe-oxide	1.6	1.3	3.9	4.1	32.9	2.3
Kaolinite	36.2	37.6	36.0	24.6	18.0	59.2
Kaolinite(Carbonate,pyrite)	3.5	2.6	3.0	2.9	3.5	0.4
Kaolinite(Carbonate)	35.0	22.4	32.0	10.0	16.4	5.1
Kaolinite(Pyrite)	8.6	3.5	4.8	5.2	3.8	1.0
Kaolinite(Ti,K)	1.1	0.8	1.3	2.4	1.5	1.9
Orthoclase	0.1	0.3	0.2	1.5	0.2	0.3
Other	0.1	0.0	0.1	0.4	5.1	9.9
Quartz60Kaol40	6.3	4.0	3.8	3.2	1.3	3.3
Quartz80Kaol20	0.5	1.6	1.0	0.9	0.4	0.8
Quartz	6.4	12.5	11.0	42.4	8.5	13.5
Ti-oxide	0.3	0.0	0.1	0.2	0.2	0.2

There are a number of notable trends highlighted by Table 6.8 and Figure 6.13. These are:

- Fe-oxide, a dominant phase in the slag probe deposits (Figure 6.12), is a minor phase in the slag probe "eyebrows/clinker" samples.
- Kaolinite(carbonate), kaolinite, kaolinite(pyrite) and quartz are the main phases in the slag probe "eyebrows/clinker" samples.
- Ca-oxide/Ca-carbonate is a minor phase in the slag probe "eyebrow/clinker" samples
- Compared to the average fly ash distribution, kaolinite (carbonate), kaolinite(pyrite) and kaolinite(carbonate, pyrite) are enriched in the "eyebrows/clinkers" and kaolinite, quartz, Ca-oxide and Fe-oxide are depleted.
- Quartz and kaolinite and, to a lesser extent kaolinite(carbonate) are the major phases in the bottom ash. Compared to fly ash quartz and, to a

lesser extent Fe-oxide, Kaolinite(carbonate), kaolinite(carbonate,pyrite) and orthoclase are enriched in the bottom ash.

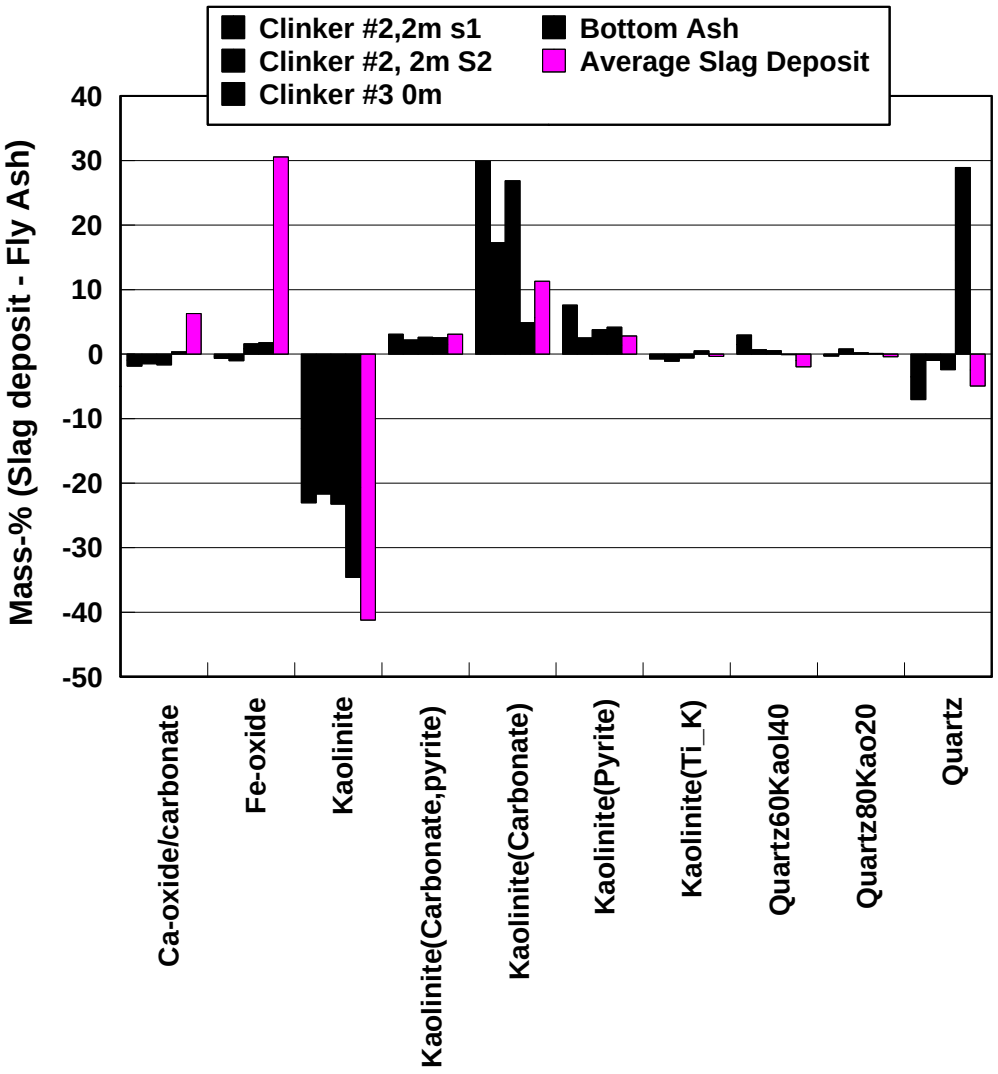

Figure 6.13: Mass% difference in the proportion of fly ash phases in the slag probe "eyebrows/clinker" deposits, bottom ash, average slag deposits compared to the average suction pyrometer fly ash distribution.

6.3 Summary

The characteristics of the fly ash acquired from within the boiler, the slag deposits accumulated on the removable slag sleeves, the developed “eyebrows/clinkers” on slag sleeves, and the bottom ash, show that a dynamic phase/mineral segregation and enrichment occurs within a boiler.

Kaolinite and quartz in original pulverised fuel sample manifests as the dominant phases in the fly ash. The fine kaolinite inclusions in the pulverised fuel are released on combustion to form fine excluded kaolinite fly ash particles. These excluded kaolinite fly ash particles are concentrated in the upper regions of the boiler and along the boiler walls.

In contrast, quartz, pyrite and carbonates are predominately excluded particles in pulverised fuel. The excluded quartz/pyrite particles are coarser than the carbonates in the pulverised fuel. These coarse excluded quartz particles remain unaffected when they are combusted and tend to gravitate towards the ash hopper and concentrate in the bottom ash. The excluded Fe-oxide (a remnant of pyrite transformation) and Ca-oxide/Ca-carbonate (the remnants of carbonate transformation) have similar liberation properties in fly ash as their counterparts in the pulverised fuel.

There is evidence that iron from pyrite, calcium from calcite/dolomite and magnesium from dolomite have reacted with kaolinite (the source of Al and Si) to form new fly ash phases kaolinite (carbonate), kaolinite(pyrite,carbonate) and kaolinite(pyrite). In contrast, there is limited interaction between quartz and kaolinite, which are strongly associated with each other in the pulverised fuel.

The slag deposits on the removable slag sleeves have an enhanced concentration of Fe-oxide and, to lesser extent kaolinite(carbonate), whereas the proportion of Fe-oxide is significantly reduced and the proportion of kaolinite(carbonate), kaolinite(carbonate,pyrite) and kaolinite(pyrite) are enriched in the thicker “eyebrows/clinkers” deposits formed on the slag sleeves. The effects of the fluxing elements, iron, calcium and magnesium, are strongly evident in the slag deposits formed.

The attributes of pulverised fuel, fly ash and slag deposits were outlined in the preceding two chapters. The next chapter will discuss the mechanism whereby minerals in pulverised fuel are transformed into fly ash and the subsequent formation of slag deposits from fly ash.

7 FLY ASH FORMATION AND SLAG DEPOSIT MODEL - RESULTS

7.1 Fly Ash Formation

The principles and methodology of the fly ash formation model are outlined in detail in section 4.8.

Simplistically, the three particle types described in the model are as follows:

- Coal rich particles with varying proportions of included minerals.
- Ash-free coal particles (no included mineral matter).
- Extraneous mineral rich particles with little of no attached or included coal.

To accommodate these particle types the fly ash formation model has three **sub-models**, namely:

- **An included mineral fly ash formation sub-model** – it is based on the principles of coalescence, partial coalescence and fragmentation (described in section 3.1, 3.2 and 3.3) of included minerals in coal (organic) rich particles,
- **An "ash free" coal particle fly ash formation sub-model** – this sub-model accounts for the ash-free coal particles, which could consist of sub-micron included mineral grains or organically bound inorganic elements,
- **An extraneous fly ash formation sub model** – fly ash formation from extraneous mineral rich particles.

The outputs of each sub-model are:

- The particle size distribution of the modelled fly ash.
- Predictions of mass% fly ash phase proportions based on the elemental signature of the modelled fly ash particle and classified on the basis of the fly ash classification scheme outlined in section 4.6.2 and summarised in Table 4.3.

The modelled predictions compared to the measured fly ash particle size distribution and mass-% phase proportions are described in this chapter.

7.1.1 Particle size distribution comparison

A comparison between the individual mineral size distributions and the corresponding transformed phases in fly ash might provide an indication of the possible fly ash formation process. In principle, if the fly ash particle size distribution is coarser than the size distributions of minerals (source of fly ash) in coal, then partial coalescence or full coalescence is assumed. Alternatively, if the fly ash particle size is finer or similar, then fragmentation must be considered.

The modelled fly ash particle size distributions and the measured fly ash particle size distributions for the major minerals, kaolinite, quartz, iron oxide and calcium oxide /carbonate, are illustrated in Figures 7.1 to 7.4 respectively.

The modelled fly ash particle size distributions are described as “coalescence”, “partial coalescence” and “fragmentation”.

“Coalescence” is the modelled fly ash particle size distribution, assuming the coalescence of all included minerals (Figure 4.16) combined with the modelled fly ash particle size distribution derived from the **“ash free“ coal particle fly ash formation sub-model** and the **extraneous fly ash formation sub model.**

“Fragmentation” is the modelled fly ash particle size distribution, assuming that all the included minerals produce a single fly ash particle (Figure 4.16) combined with the modelled fly ash particle size distribution derived from the **“ash free“ coal particle fly ash formation sub-model** and the **extraneous fly ash formation sub model.**

“Partial coalescence” is the modelled fly ash particle size distribution, assuming the partial coalescence of all included minerals (Figure 4.16) combined with the modelled fly ash particle size distribution derived from the **“ash free“ coal particle fly ash formation sub-model** and the **extraneous fly ash formation sub model.**

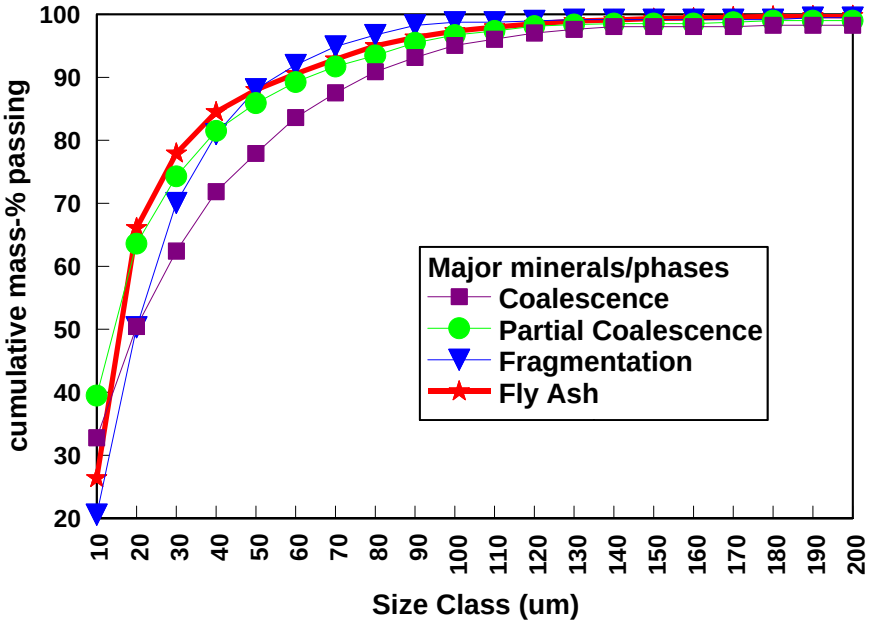

Figure 7.1: The modelled (coalescence, partial coalescence and fragmentation) and measured (fly ash) particle size distribution of kaolinite fly ash particles.

Apart from the -10 µm fraction, the partial coalescence model is a good indicator of the measured kaolinite fly ash size distribution.

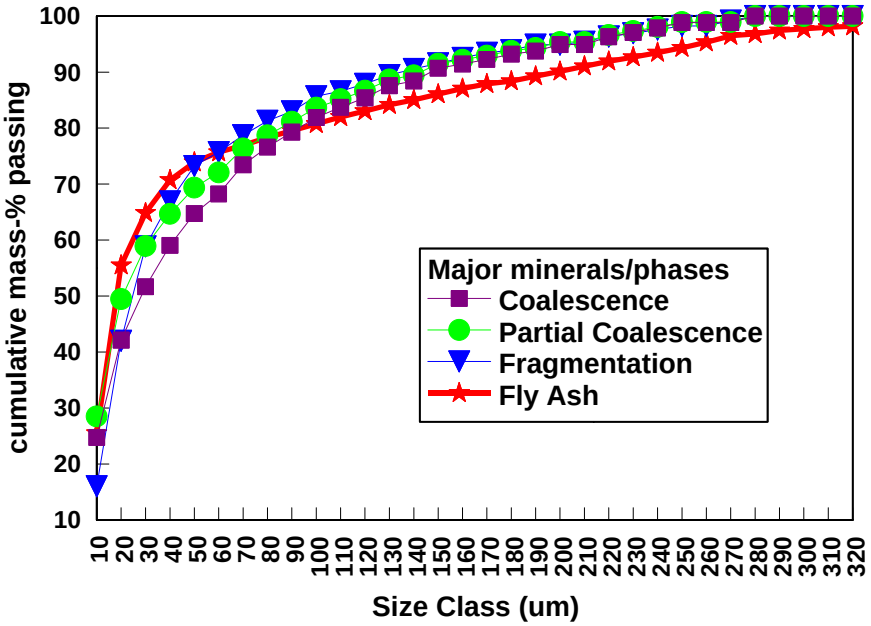

Figure 7.2: The modelled (coalescence, partial coalescence and fragmentation) and measured (fly ash) particle size distribution of quartz fly ash particles.

No fly ash formation model can adequately predict the measured quartz fly ash size distribution (Figure 7.2).

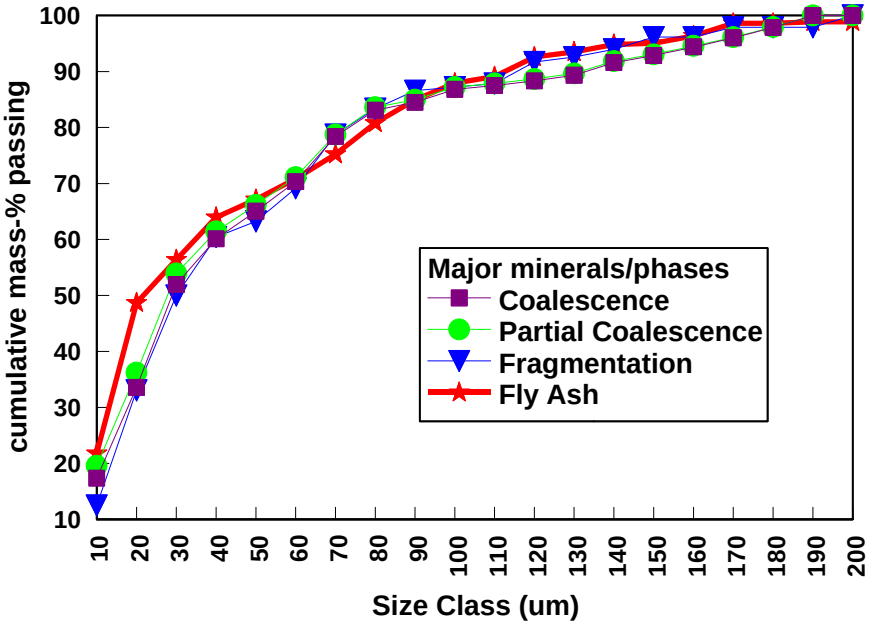

Figure 7.3: The modelled (coalescence, partial coalescence and fragmentation) and measured (fly ash) particle size distribution of iron oxide/pyrite fly ash particles.

The models significantly underestimates the proportion of Fe-oxide fly ash particles finer than 30 µm. Above 30 µm, the measured iron oxide size distribution is similar to the modelled iron oxide particle size distribution based on the fragmentation model (Figure 7.3). In interpreting the iron oxide particle size distributions trends the following points must be noted:

- the fragmentation fly ash formation model in this research assumes that one fly ash particle is produced from each mineral grain in pulverised fuel and the size of the resultant fly ash particle is the same size as the mineral grain.
- 84 mass% of pyrite in the pulverised fuel occurs as extraneous particles (Table 5.11).

The variations in the iron oxide particle size distributions suggests that extraneous pyrite finer than 30 µm is fragmenting into smaller fragments than the original extraneous pyrite particle size. Srinivasachar and Yan have noted

fragmentation of exluded pyrite. (Srinivasachar and Boni (1989) and Yan et al , 2003). Above 30 µm, extraneous pyrite transforms to iron oxide fly ash particle that are the same size as the extraneous pyrite particle

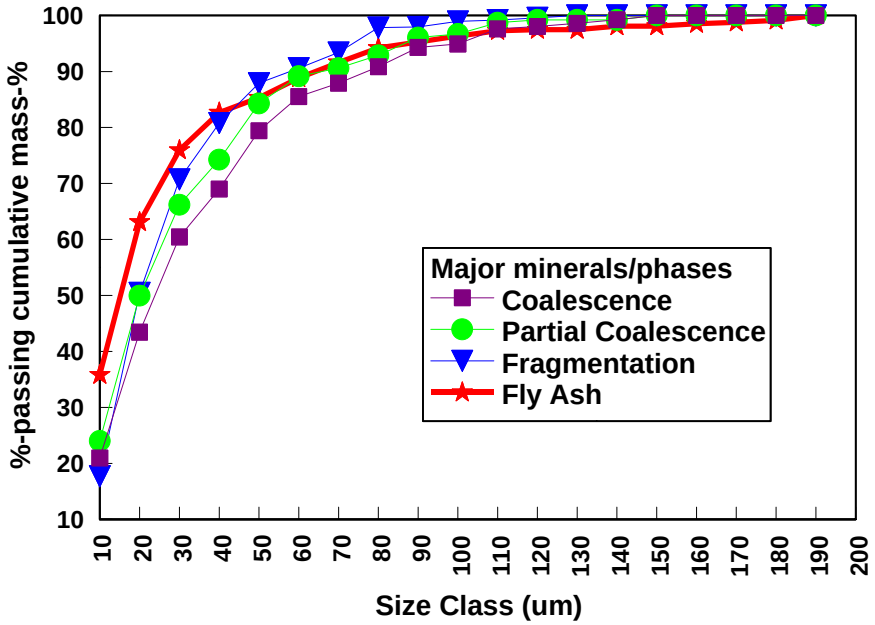

Figure 7.4: The modelled (coalescence, partial coalescence and fragmentation) and measured (fly ash) particle size distribution of Ca-oxide/carbonates fly ash particles.

The models underestimate the proportion of Ca-oxide fly ash particles finer than 30 µm. As hypothesized for pyrite, it is proposed that fine (<30 µm) extraneous carbonates fragment into smaller Ca-oxide fly ash particles. These fragments are smaller than the original particle size of the extraneous carbonates. Like quartz, the measured Ca-oxide particle size distribution has a notable inflection point at 40 to 50 µm. Above this point, there is no fly ash formation model, which can accurately predict the size distribution of Ca-oxide fly ash particles.

Instead of reporting the size distributions for the individual minerals, the minerals in the pulverised fuel can be combined and considered as a single entity. The fly ash particles size distribution can be modelled and compared to the total fly ash particle size distribution (Figure 7.5).

In Figure 7.5, “fly ash pyrometer” refers to the cumulative particle size distribution of the fly ash obtained from within the boiler and “fly ash bulk” refers to the cegrit fly ash particle size distribution.

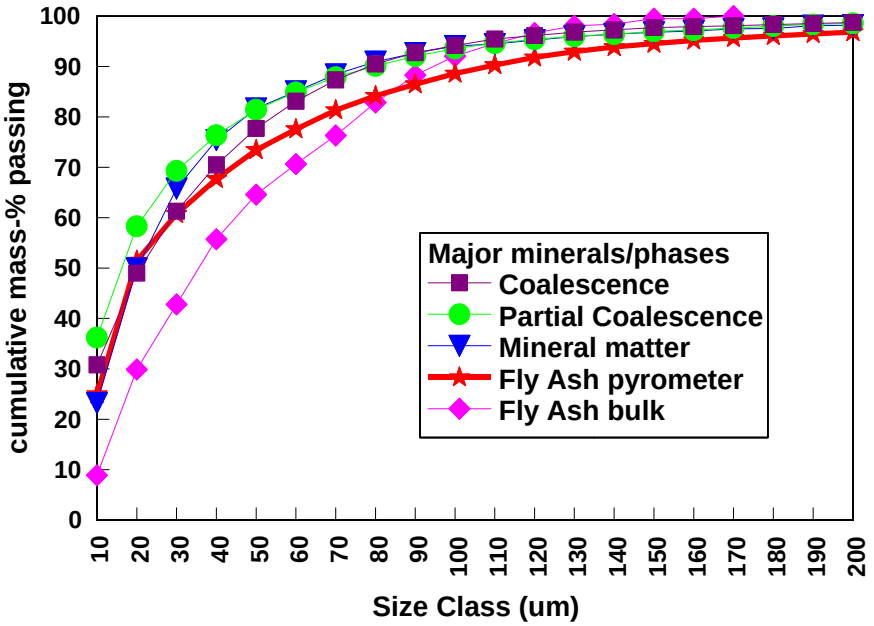

Figure 7.5: Modelled fly ash particle size distribution (coalescence, partial coalescence and fragmentation) compared to the measured suction pyrometer (fly ash pyrometer) and cegrit (fly ash bulk) fly ash.

The fly ash particle size distribution of measured fly ash below 30 µm is similar to the size distribution of the minerals in the coal (analogous to **the** fragmentation process). The measured fly ash size distribution above 30 µm is significantly coarser than the particle size distribution predict by any of the three fly ash formation models. A larger proportion of coarse fly ash particles than expected could be explained in terms of any of the following reasons (not included in the model):

1. On a localised scale, the release of volatiles (H_2O from kaolinite, CO_2 from carbonates and SO_3 from pyrite) could have produce spherical hollow cenospheres, which, by nature are coarser than the original source mineral.
2. Sootblowing dislodges coarse fragments of clinker from the internal surfaces of the boiler. These fragments form part of the fly ash sample.

The above-mentioned factors that produce coarser particles might play a more dominant role in the fly ash formation process than was originally thought. The discrepancy in predicting size distributions observed in this study and extensively reported in literature (Helble et al., 1990) (Wilemski and Srinivasachar, 1993) and described in section 3.2, suggests that there are additional or alternative mechanisms other than simple coalescence, partial coalescence and fragmentation, influencing the formation of fly ash.

7.1.2 Mass percent fly ash phase proportion comparison

It is hypothesised that the dominent fly ash formation process can be derived by comparing the elemental proportions of minerals in coal with the elemental proportions of those fly ashes formed from the minerals in coal. By definition, each coal mineral has a known and theoretically fixed elemental composition, whereas the fly ash particles can have a similar elemental composition as the source mineral or variable elemental compositions. Elemental composition of a fly ash phase is obviously dependent on the original source mineral and on the fly ash formation process.

If there is extensive interaction between minerals, either through the coalescence of included minerals or within the boiler, the inorganic elemental composition of the resultant fly ash phase will be a combination of the elements in the reacting coal minerals. If the coal mineral does not react with any other mineral, then the resultant fly ash phase will have the same relative inorganic elemental proportions as the original coal mineral. By comparing the inorganic elemental composition of the measured fly ash phases to the modelled fly ash phases, evidence of the fly ash formation process is theoretically possible. The methodology and principles of this concept is described in detail in section 4.8.

The fly ash classification scheme (Table 4.3) is based on the elemental proportions of the fly ash particles. The mass percent proportions of the fly ash phases, using this classification scheme is ideal for indirectly monitoring the variations in elemental compositions between minerals in coal and the fly ash phases. The mass% particle compositions, based on the fly ash classification scheme between the average suction pyrometer fly ash and the modelled fly ash are summarised in Table 7.1.

The proportions in Table 7.1 are normalised assuming that all the coal is combusted and no char is formed. All mass% particle compositions are based on a **particle analysis** (see section 4.8) and not on the normal **point analysis** used to describe the mineral proportions in coal (chapter 5), boiler fly ash (chapter 6) and drop tube fly ash (section 7.2). Particle analysis is analogous to scanning a whole particle, deriving the average elemental composition and using the average composition to classify the fly ash particles into fly ash mineral identification classes (defined in Table 4.3).

Table 7.1: Average fly ash particle compositions compared to measured fly ash particle compositions.

Fly ash phase	Measured Fly Ash (Particle)*	Predicted model compositions		
		Fragmentation	Partial Coalescence	Coalescence
	Mass-%	Mass-%	Mass-%	Mass-%
Ca-Oxide/Ca-carbonate	1.7	9.0	7.3	6.6
Fe-Oxide	1.4	5.3	4.9	4.2
Kaolinite	66.5	51.3	34.9	31.8
Kaolinite (carbonate,pyrite)	0.4	0.004	0.04	0.04
Kaolinite (carbonate)	5.9	0.1	1.6	2.4
Kaolinite (pyrite)	1.1	0.0	0.4	0.4
Kaolinite (illite, mica)	2.1	1.0	2.3	2.5
Orthoclase	0.4	0.9	1.7	1.5
Other	0.3	1.1	5.7	5.4
Quartz60Kaol40	3.7	0.0	12.2	18.6
Quartz80Kaol20	0.9	0.0	4.2	5.2
Quartz	15.4	31.0	24.3	20.9
Ti-Oxide	0.1	0.2	0.5	0.4
Total	100.0	100.0	100.0	100.0

*proportions are normalised, excluding char and based on particle analysis

There are a number of major trends evident from the data in Table 7.1:

- Ca-oxide/Ca-carbonate, Fe-oxide and quartz proportions in fly ash are significantly lower than the modelled proportions. It is conceivable, that a proportion of the Ca-oxide/Ca-carbonate, Fe-oxide and quartz has reported to the bottom ash and slag deposits (Table 6.8, Figure 6.13)

- Irrespective of the fly ash formation model, the proportion of kaolinite is underestimated. The fragmentation model is based on the assumption that each individual kaolinite grain in the coal is released on combustion to form an individual “kaolinite” fly ash particle. The inability of the fragmentation model to estimate the mass% proportion of kaolinite suggests that there is an alternative fly ash formation process, which will account for the concentration of “kaolinite” in the measured fly ash and cegrit fly ash (Table 6.1).
- The proportions of kaolinite(carbonate,pyrite), kaolinite(carbonate) and kaolinite(pyrite) are significantly higher in the measured fly ash than in the modelled fly ash, even assuming full coalescence. This is significant as a mineral or minerals with the same elemental proportions are not common in coal. These fly ash phases can only form in the boiler by the interaction of the specific elements or minerals. The larger proportion of kaolinite(carbonate) in the fly ash, as opposed to the coalescence model prediction, suggests that, other than the coalescence of included kaolinite with included calcite/dolomite there is an additional fly ash formation process responsible for the additional 3.5 mass% of kaolinite(carbonate) observed in the measured fly ash.
- The coalescence and partial coalescence models predicted a high proportion of quartz60kaol40 and quartz80kaol20 fly ash phases. If kaolinite and quartz can coalesce, then the predicted proportions are realistic as a high proportion of included kaolinite is associated with included quartz in pulverised fuel particles (Table 5.12). A small proportion of quartz60kaol40 and quartz80kaol20 and correspondingly large proportion of kaolinite in the measured fly ash, suggests that there is limited interaction between included quartz and included kaolinite during fly ash formation. Instead, it was found that the majority of the included kaolinite was released from the coal particle on combusting to form excluded “kaolinite” fly ash particles. This trend can be substantiated by the liberation characteristics of kaolinite in fly ash (Figure 6.6 and Table 6.3).

Incompatibilities between the measured size distributions (Figures 7.1 to 7.5) and particle composition (Table 7.1) clearly indicate that the fly ash formation process

is not simplistic and cannot be readily ascribed to any of the fly ash formation process (coalescence, partial coalescence and fragmentation) described to date.

There are strong indications, that there are alternative fly ash formation mechanisms. Alternatively, the fly ash formation model assumptions are invalid and the observed discrepancies in fly ash particle size and mass% fly ash particle proportions are due to poor modelling.

As described in section 4.9, a selected coal (20-May-1999, hole 2, 0.5m) was combusted in the drop tube furnace in order to validate the model. The comparison between the drop tube furnace (DTF) mass% fly ash phase proportions and the modelled fly ash phase phase proportions is discussed in the following section (section 7.2).

7.2 Drop Tube Furnace

The drop tube furnace is considered a single particle combustor and is analogous to the model simulating the combustion of single coal particles. Unlike the boiler, the drop tube furnace is a closed system, which means that all the ash will be recovered. A selected coal (#2 0.5m) was screened and each size fraction combusted in the DTF at different temperatures and under oxidising and reducing conditions (see section 4.9). The fly ash obtained after combusting the coal at each specified temperature was collected and analysed (Appendix R).

Combusting the coal in the drop tube furnace serves to establish the impact combustion conditions (oxidising and reducing) and temperature have on the ash forming process and also to validate the fly ash model.

7.2.1 DTF ash – influence of combustion conditions

A comparison between the mass% fly ash phase proportions (based on point analysis) of kaolinite, quartz, iron oxide and calcium oxide/carbonates in the drop tube furnace and the corresponding mass% proportions in the test coal and suction pyrometer fly ash is summarised in Figures 7.5 to 7.8. The calculated mass% proportion of the individual mineral entering the boiler is represented in these Figures. The calculated mass% mineral proportion entering the boiler is the normalised mineral proportion in the pulverised fuel (Table 5.7), excluding the proportion of coal.

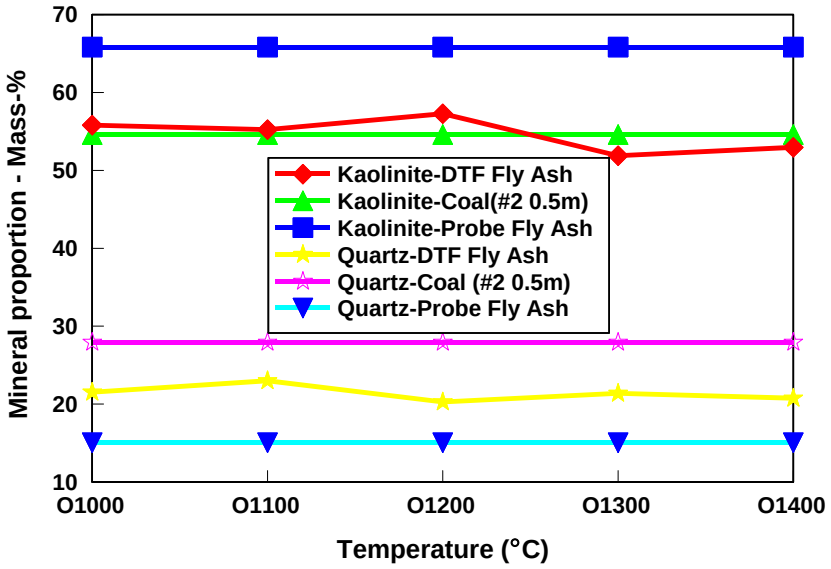

Figure 7.6: Mass% variation of kaolinite and quartz in DTF fly ash, entering the DTF (coal (#2 0.5m)) and probe fly ash for oxidising conditions.

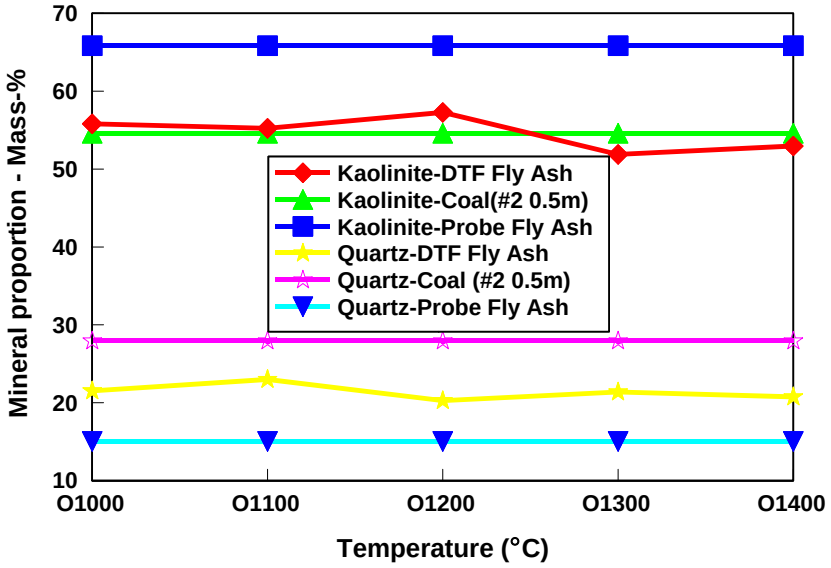

Figure 7.7: Mass-% variation of kaolinite and quartz in DTF fly ash, entering the DTF (coal (#2 0.5m)) and probe fly ash under reducing conditions.

The proportion of kaolinite in the DTF fly ash is comparable to the normalised proportion (excluding coal) of kaolinite entering the DTF for both reducing and oxidising conditions and at all temperatures (Figure 7.6). The DTF kaolinite

proportion is lower than the average proportion of kaolinite measured in the probe fly ash. Excluding reducing conditions at 1300 °C, the proportion of quartz in the DTF fly ash is slightly lower than normalised proportion of quartz in the feed coal (Figure 7.7), but higher than the proportion of quartz in the probe fly ash. Varying the temperature and combustion conditions had no appreciable impact on the mass% proportion of kaolinite and quartz in the DTF fly ash.

Comparing the variations in Ca-oxide/carbonate and pyrite/Fe-oxide is complicated by the expected mass loss of carbonates (CO_2 released) and pyrites (SO_3 released). A notable trend is the appreciably higher proportion Ca-oxide/carbonate and Fe-oxide/pyrite content in the DTF fly ash as opposed to the average probe fly ash (Figures 7.8 and 7.9). The variability of the Fe-Oxide and Ca-oxide/carbonate content in the DTF fly ash at different temperatures and under oxidising and reducing conditions is evident. It is conceivable that these higher density phases could be segregating during sample preparation and settling at the base of the polished sections. This would artificially enhance the proportion of these phases, especially the proportion of Fe-oxide for reducing at 1100 °C and oxidising at 1400 °C.

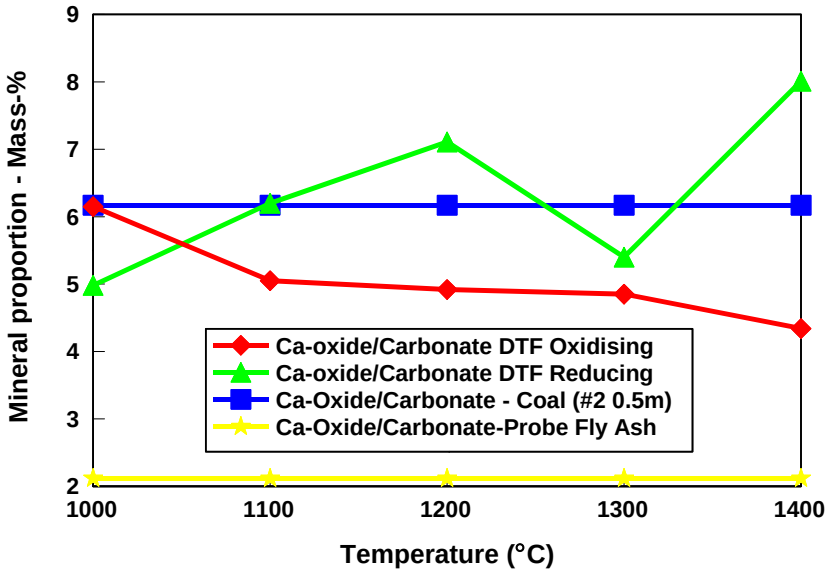

Figure 7.8: Variation of Ca-oxide/Carbonate in DTF fly ash under oxidising and reducing and conditions.

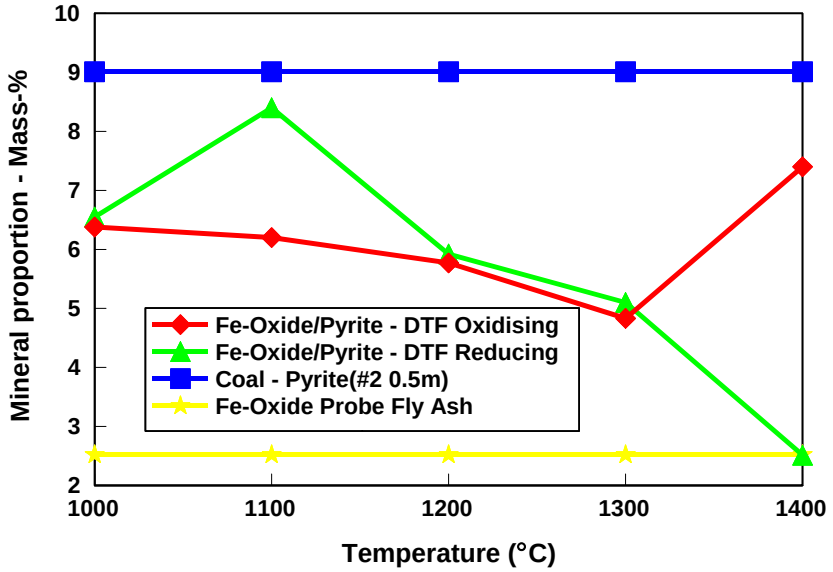

Figure 7.9: Variation of Fe-oxide/Pyrite in DTF fly ash under oxidising and reducing conditions.

Under oxidising conditions, the proportion of Ca-Oxide/Carbonate tends to decrease with an increase in temperature, whereas under reducing conditions the proportion of Ca-oxide in the DTF fly ash is similar to its proportion in the original coal. In contrast, the proportion of Fe-oxide generally decreases with an increase in temperature.

Kaolinite(carbonate), kaolinite(carbonate,pyrite) and kaolinite(pyrite) are perceived to be the reaction products between kaolinite+carbonates, kaolinite+pyrite+carbonates and kaolinite+pyrite, respectively. The increase in the proportion of kaolinite (carbonate) and to a lesser extent kaolinite (pyrite) with temperature suggests that formation of kaolinite(carbonate) and to a lesser extent kaolinite(pyrite) is promoted by an increase in temperature (Figure 7.10). The corresponding decrease in the proportion of Ca-oxide under oxidising and reducing conditions suggests that Ca from Ca-oxide is reacting with kaolinite to form kaolinite(carbonate).

The proportion of kaolinite(carbonate) is more pronounced under oxidising conditions than reducing conditions. There is no significant increase in the proportion of kaolinite (carbonate,pyrite) and kaolinite (pyrite).

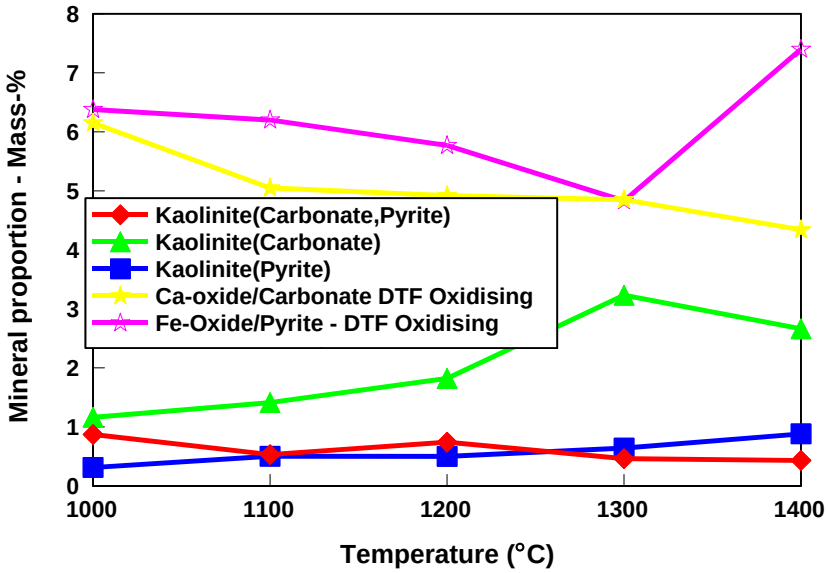

Figure 7.10: Variation of kaolinite (carbonate,pyrite), kaolinite (carbonate) and kaolinite (pyrite) under oxidising conditions.

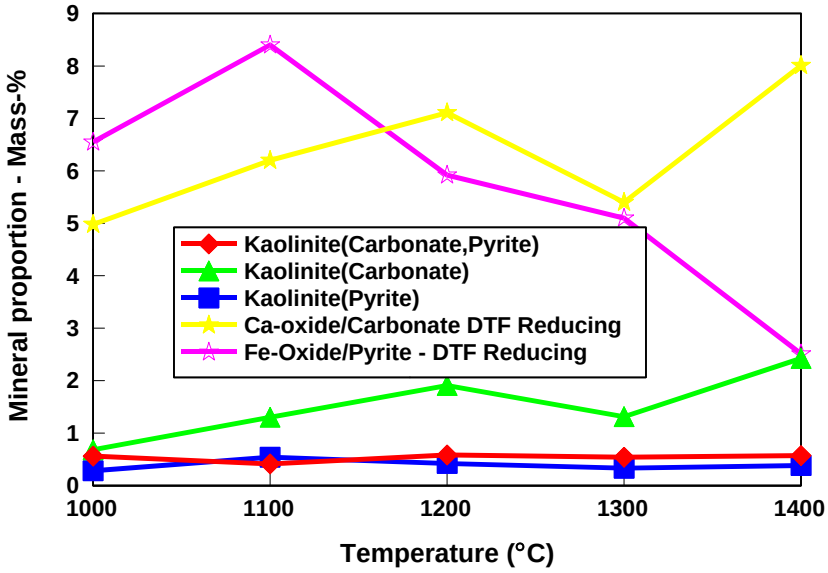

Figure 7.11: Variation of kaolinite(carbonate,pyrite), kaolinite(carbonate) and kaolinite (pyrite) under reducing conditions.

The variations in the DTF fly ash phases associated with temperature changes indicates that the formation of kaolinite(carbonate) in particular, and kaolinite(pyrite) to a lesser extent, is favoured by oxidising condition and an

increase in temperature. Considering that kaolinite(carbonate) and kaolinite(pyrite) are important clinker and slag forming phases (Table 6.8), it is contrary to common belief that reducing conditions favour the formation of slag deposits.

7.2.2 DTF ash - fly ash formation model validation

To validate the fly ash formation model, the drop tube mass% fly ash phase proportions were compared to the predicted mass% fly ash phase proportions derived from the coalescence, partial and fragmentation fly ash formation models. The absolute mass% difference between the measured and modelled, DTF fly ash phase proportions was computed. The absolute differences were totalled and could be used as an indicator of the degree of variation between the two fly ash proportions (Table 7.2). For comparative purposes, the total absolute difference between the modelled and the measured suction probe and the cegrit fly ash phase proportions are included in Table 7.2.

Ideally, if the model had accurately predicted the fly ash mass% phase proportions, the sum of the absolute difference would have been zero (Table 7.2). A large value indicates major differences between the fly ash particle compositions. The detailed mass% differences are summarised in Appendix S and the summarised differences appear in Table 7.2

Table 7.2: Total absolute mass% difference between modelled fly ash, DTF (oxidising and reducing), suction probe and cegrit fly ash.

Fly ash formation process	DTF fly ash oxidising	DTF fly ash reducing	Probe fly ash	Cegrit fly ash
Fragmentation	22.9	**19.7**	53.4	47.3
Partial Coalescence	**18.9**	20.8	66.6	58.9
Coalescence	31.3	33.2	71.4	63.7

The partial coalescence/fragmentation model proved to be a better predictor of the drop tube furnace fly ash phase compositions, but did not adequately describe the boiler-derived suction probe and cegrit fly ash.

The absolute mass% difference between the drop tube furnace and the modelled fly ash particle compositions, for each fly ash phase suggested that there is a unique fly ash formation process for the individual fly ash phases (Table 7.3 and 7.4).

Table 7.3: Average mass-% difference of each fly ash phase between modelled and DTF fly ash combusted under oxidising conditions.

Fly ash phases	Frag.	P.Coal	Coal.	Best process*
Ca-Oxide	1.9	0.6	**0.4**	Coalescence
Fe-Oxide	1.4	1.2	**0.9**	Coalescence
Kaolinite	**2.5**	-4.9	-9.6	Fragmentation
Kaolinite(Carbonate, Pyrite)	-0.6	-0.6	-0.6	Not conclusive
Kaolinite(Carbonate)	-2.0	-1.2	**-0.9**	Coalescence
Kaolinite(Pyrite)	-0.6	0.5	**0.5**	Coalescence
Kaolinite(illite,mica)	-2.2	-1.0	**-0.9**	Coalescence
Orthoclase	**-0.4**	-0.4	-0.5	Fragmentation
Quartz60Kaol40	-3.7	**3.6**	11.0	P.Coalescence
Quartz80Kaol20	**-1.2**	2.9	2.9	Fragmentation
Quartz	6.1	**-0.3**	-2.9	P. Coalescence
Ti-oxide	0.2	**0.3**	0.3	Not conclusive
Absolute total (Table 7.2)	22.9	**18.9**	31.3	P.Coalescence

Frag: Fragmentation, model P.Coal: Partical coalescence model , Coal: coalescence model

Table 7.4: Average fly ash phase mass-% difference of DTF fly ash combusted under reducing conditions.

Fly Ash phases	Frag.	P.Coal	Coal.	Best process
Ca-Oxide	1.1	**-0.7**	-0.8	P.Coalescence
Fe-Oxide	1.8	1.6	**1.2**	Coalescence
Kaolinite	**1.5**	-5.0	-9.7	Fragmentation
Kaolinite(Carbonate, Pyrite)	-0.6	-0.6	-0.6	Not conclusive
Kaolinite(Carbonate)	-1.6	-0.8	**-0.5**	Coalescence
Kaolinite(Pyrite)	-0.4	0.7	0.7	P. Coalescence Coalescence
Kaolinite(illite,mica)	-2.3	-1.1	**-0.9**	Coalescence
Orthoclase	0.3	0.5	-0.2	Not conclusive
Quartz60Kaol40	**-3.3**	4.0	11.4	Fragmentation
Quartz80Kaol20	**-1.1**	3.0	3.0	Fragmentation
Quartz	5.3	**-2.7**	-3.8	P. Coalescence
Ti-oxide	0.4	0.3	0.3	Not conclusive
Absolute total (Table 7.2)	**19.7**	20.8	33.2	Fragmentation

***Best process is the fly ash formation process with lowest difference and is marked in bold**

Frag: Fragmentation, model P.Coal: Partical coalescence model , Coal: coalescence model

It is evident from Tables 7.3 and 7.4 and the fly ash size distribution (Figures 7.1 and 7.5) that the application of a universal fly ash formation process to predict fly ash size distributions and mass% fly ash phase proportions is not necessarily feasible for the test coal. Instead, each mineral has a unique fly ash formation process as depicted Tables 7.3 and 7. The mass percent fly ash phase proportion was remodelled (Table 7.5), with this concept in mind.

Using the mass-% proportion of the individual fly ash phase (Appendix S) corresponding to the "best" fly ash process (Tables 7.3 and 7.4), the new mass% fly ash phase proportion was remodelled. The initial totals were 94.6% and 95.1% for the remodelled oxidising and reducing DTF fly ashes, respectively. The low totals could be attributed to 0 mass% concentrations for quarzt60Kaol40, quartz80kaol20 and kaolinite(carbonate,pyrite). If the partial coalescence mass% for these phases had been used instead, the totals would have exceeded 100%. To rectify, this problem, it is assumed that the mass-% proportion of quartz60kaol40 was 50% of the partial coalescence mass% and mass% proportion of quartz80kaol20 is 30% of the partial coalescence mass%. The remodelled mass% fly ash phase proportions are summarised in Table 7.5a and Table 7.5b.

Table 7.5a: Modelled fly ash distribution based on combining the best fly ash formation process for each fly ash phase. Input coal is coal sampled at hole 2, depth of 0.5m. Oxidising conditions.

Fly ash phases	Oxidising			Fly ash formation Process (Table 7.3)
	New Model	DTF Average	Difference	
Ca-oxide	4.2	4.2	0.0	Coalescence
Fe-oxide	4.4	3.8	0.6	Coalescence
Kaolinite	57.8	56.4	1.4	Fragmentation
Kaolinite(Carbonate, pyrite)	0.0	0.6	0.6	Coalescence
Kaolinite(Carbonate)	1.5	2.0	0.5	Coalescence
Kaolinite(Pyrite)	1.1	0.6	0.5	Coalescence
Kaolinite(illite, mica)	2.3	3.1	0.8	Coalescence
Orthoclase	0.9	1.2	0.3	Fragmentation
Quartz60Kaol40	3.7	3.7	0.0	50-% P.Coal.
Quartz80Kaol20	1.2	1.2	0.0	30-% Coalescence
Quartz	22.3	22.7	0.4	P.Coalescence
TiOxide	0.1	0.3	0.2	Fragmentation
Total	99.6	99.9	5.3	

Table 7.5a: Modelled fly ash distribution based on combining the best fly ash formation process for each fly ash phase. Input coal is coal sampled at hole 2, depth of 0.5m. Reducing conditions.

Fly ash phases	Reducing			Fly ash formation Process (Table 7.4)
	New Model	DTF Average	Difference	
Ca-oxide	4.7	5.0	0.3	P.Coalescence
Fe-oxide	4.4	3.3	1.1	Coalescence
Kaolinite	57.8	56.5	1.3	Fragmentation
Kaolinite(Carbonate, pyrite)	0.0	0.6	0.6	Coalescence
Kaolinite(Carbonate)	1.5	1.6	0.1	Coalescence
Kaolinite(Pyrite)	1.1	0.4	0.7	Coalescence
Kaolinite(illite, mica)	2.3	3.2	0.9	Coalescence
Orthoclase	0.9	0.9	0.0	Fragmentation
Quartz60Kaol40	3.7	3.3	0.4	50-% P.Coal.
Quartz80Kaol20	1.2	1.1	0.1	30-% Coalescence
Quartz	22.3	23.5	1.2	P.Coalescence
TiOxide	0.1	0.5	0.4	Fragmentation
Total	100.0	99.9	7.1	

The error between the predicted particle compositions using the “new” model principles and the measured drop tube furnace ashes was less than 10% for the major phases. This error is within the expected analytical and sample preparation errors for any CCSEM analysis. It could be argued that the “new” model, based on mineral associations and the unique fly ash formation process for the different minerals, can adequately predict, the fly ash phase proportions of pulverised fuel combusted in a single particle combustor (drop tube furnace).

Based on the above findings, it can be surmised that as the pulverised fuel is fed into the drop tube furnace the following mineral interactions and fly ash formation processes occurs:

- Kaolinite: Fine included kaolinite in organic rich matrix is released during combustion to form fine excluded “kaolinite” fly ash particles. If included kaolinite is in contact or associated with calcite, dolomite and/or pyrite, then kaolinite will coalesce with these phases to form kaolinite(carbonate, pyrite), kaolinite(carbonate) and kaolinite(pyrite), respectively. If the included kaolinite is in contact with included quartz, then a small proportion of kaolinite and quartz will coalesce to form quartz60kaol40 and quartz80kaol20 fly ash phases. Overall, the model predicts that the

majority of the kaolinite will be released on combustion and only a small proportion of included kaolinite will coalesce with pyrite, calcite, and dolomite and to a lesser extent with quartz.

- Quartz: Excluded quartz in pulverised fuel will remain excluded in the fly ash. The small proportion of included quartz will be released on combustion or if in contact with kaolinite can coalesce.
- Carbonates: Excluded calcite will be transformed into Ca-oxide and excluded dolomite will transform into Ca-Mg-oxide. Any included calcite or dolomite in contact with kaolinite will coalesce with kaolinite to form kaolinite(carbonate).
- Pyrite: Exluded pyrite will be transformed into Fe-oxide or Fe-O-S melt. Any included pyrite will coalesce with other minerals to form kaolinite(pyrite) and kaolinite(carbonate, pyrite).
- Orthoclase: Excluded orthoclase will remain excluded and not readily interact with other mineral phases.

7.3 Fly ash prediction – 200 MW_e boiler

It was possible to predict the fly ash phase proportions of boiler fly ash by combining the principles of the "new" model and the initial modelled results (Table 7.1). The "new" modelled fly ash phase proportions was based on the mineral attributes of the average pulverised fuel entering the boiler during the sampling period (Table 5.7). The modelled fly ash phase proportions were compared to the average fly ash phase proportions of the fly ash (Table 7.1) derived from within the boiler (Table 7.6).

Table 7.6: Modelled mass-% fly ash particle compositions compared to measured suction pyrometer fly ash particle compositions.

Fly ash distribution	Boiler fly ash			Fly ash formation Process (Table 7.4)
	Model[#]	Probe* Fly ash (Table 7.1)	Difference	
Ca-oxide	6.6	1.7	4.9	P.Coalescence
Fe-oxide	4.2	1.4	2.8	Coalescence
Kaolinite	51.3	66.5	15.2	Fragmentation
Kaolinite(Carbonate, pyrite)	0.0	0.4	0.4	Coalescence
Kaolinite(Carbonate)	2.4	5.9	3.5	Coalescence
Kaolinite(Pyrite)	0.4	1.1	0.7	Coalescence
Kaolinite(illite, mica)	2.5	2.1	0.4	Coalescence
Orthoclase	0.9	0.4	0.5	Fragmentation
Quartz60Kaol40	6.1	3.7	2.4	50-% P.Coal.
Quartz80Kaol20	1.3	0.9	0.4	30-% Coalescence
Quartz	24.3	15.4	8.9	P.Coalescence
TiOxide	0.2	0.1	0.1	Fragmentation
Total	100.2	99.7	40.1	

[#] fly ash distribution is based on average pulverised fuel entering the boiler (Table 5.7)
* average fly ash composition obtained from within the boiler.

The validated fly ash formation model is still not able to accurately predict the fly ash phase compositions of the boiler fly ash. Important differences that need highlighting are:

1. The predicted model had a higher proportion of Ca-oxide and Fe-oxide and corresponding lower proportion of kaolinite(carbonate), kaolinite(carbonate,pyrite) and kaolinite(pyrite). This suggests that calcium from the excluded Ca-oxide and iron from excluded Fe-oxide is reacting with kaolinite.
2. The model under predicted the proportion of kaolinite and over predicted the proportion of quartz.

It is proposed that the observed differences in the fly ash phase proportions described above could be attributed to an additional fly ash process that is uniquely related to combusting coal in the 200 MW_e boiler. It is proposed that this additional fly ash formation process is related to the physical size, temperature, residence times and scale difference between the drop tube furnace and the fully operational 200 MW_e boiler.

It is proposed that the fly ash formation model adequately describes the formation of ash during devolatisation, char formation and char burnout. The fly ash phase proportions formed during this stage is a function of the mineral attributes (association) in the pulverised fuel. This stage can be adequately modelled and is equivalent to combusting a pulverised fuel in the drop tube furnace. Thereafter, the size of the boiler, temperature profile, localised combustion conditions, boiler configuration, boiler design, turbulence and flow patterns, and the velocity of the flue gas have an impact on fly ash formation.

To understand these additional fly ash formation processes, the data presented to date, must be re-examined. This update is presented in the following section.

7.4 Fly ash formation in 200 MW_e boiler – additional process

The data presented in chapters 5, 6 and 7 are combined to produce the following proposed fly ash formation process for each major mineral in the 200 MW_e test boiler.

Kaolinite: The major mineral in the test coal predominantly occurs as fine inclusions in pulverised fuel particles (Figures 5.14 and 5.15). As the coal particle with included kaolinite enters the boiler, most of the included kaolinite forms fine excluded “kaolinite” fly ash particles. The flue gas is then able to convey this fine excluded kaolinite into the upper regions of the boiler. Some of the fine included kaolinite will react with calcium or iron to form the fly ash phases kaolinite(carbonate) and kaolinite(pyrite). The following substantiates this theory:

- the 15.2 mass% discrepancy between the modelled fly ash proportions and the measured probe fly ash (Table 7.6),
- the fine size distribution of kaolinite in the pulverised fuel (Figure 5.14 and Table 5.10) and the corresponding fine distribution in the fly ash (Figure 6.5)
- the increase in the proportion of excluded kaolinite (Figure 6.6 and Table 6.7) in the fly ash as opposed to kaolinite in the pulverised fuel (Figures 5.14 and 5.15).
- the relatively low proportion of kaolinite in slag probe slag deposits (Figure 6.12) and clinkers (Figure 6.13, Table 7.7) and, more importantly in the bottom ash (Figure 6.13)

Quartz: In contrast, quartz occurs predominantly as coarse excluded particles or alternatively as finer included quartz associated with kaolinite (Figures 5.14 and 5.15) in the test coal. Excluded or included quartz does not readily react with fluxing elements (Ca, Mg, and Fe) or coalesce with included kaolinite. The excluded coarse quartz remains largely unaltered and is present in fly ash as coarse excluded particles. The fine included quartz is released on combustion and forms fine excluded quartz particles in fly ash. The relatively higher proportion of quartz in the bottom ash suggests that the coarse excluded quartz in the boiler tends to gravitate towards the ash hopper. A relatively low proportion of included quartz associated with kaolinite could coalesce with the included kaolinite to form the fly ash phase's quartz60kaol40 and quartz80kaol20. The general quartz fly ash forming trends observed above are substantiated by:

- the coarse size distribution of quartz in pulverised fuel (Figure 5.14) and correspondingly in the fly ash (Figure 7.2),
- the high proportion of excluded quartz in pulverised fuel (Figure 5.15) and in the fly ash (Figure 6.7),
- the higher proportion of quartz in pulverised fuel and the even higher proportion in the bottom ash (Figure 6.13), as opposed to the proportion in the fly ash,
- the 8.9 mass% difference in the predicted and measured fly ash quartz proportion (Table 7.6). This difference can be attributed to the coarse quartz gravitating to the ash hopper, thus depleting the proportion of quartz in the fly ash.

Orthoclase follows a similar trend to quartz and is preferentially concentrated in the bottom ash.

Pyrite: Pyrite occurs predominantly as coarse excluded particles in pulverised fuel and transforms to form spherical Fe-oxide/Fe-S-oxide fly ash particles. Any included pyrite associated with included kaolinite will coalesce to form kaolinite(pyrite). If included calcite or dolomite is associated with pyrite and kaolinite the fly ash phase kaolinite(carbonate,pyrite) will form.

Calcite/dolomite: Calcite and dolomite occurs predominantly as fine excluded particles in test pulverised fuel (Figures 5.14 and 5.15) and to a lesser extent as

included calcite/dolomite in pulverised fuel. Excluded calcite/dolomite transforms to Ca-oxide/Ca-Mg-oxide and included calcite/dolomite associated with kaolinite tends to coalesce to form kaolinite(carbonate) and if pyrite is present kaolinite(carbonate,pyrite). Unlike quartz, which also occurs as predominately excluded particles, high density Ca-oxide and Fe-oxide do not preferentially report to the bottom ash (Table 7.7).

Table 7.7: Enrichment factors (relative to average probe fly ash proportions) of individual fly ash phases.

Fly ash phases	Slag probe deposit	Clinker ("eyebrows") formed on slag probe			Bottom Ash
		#2, 2m	#2,2m (round)	#3 0m	
Ca-Oxide	4.4	0.0	0.2	0.1	1.2
Fe-Oxide	14.4	0.7	0.6	1.7	1.8
Kaolinite	0.3	0.6	0.6	0.6	0.4
Kaolinite(Carbonate, pyrite)	9.3	9.3	6.9	8.0	7.8
Kaolinite(Carbonate)	3.2	6.8	4.4	6.2	2.0
Kaolinite(pyrite)	3.8	8.6	3.5	4.8	5.2
Kaolinite(illite, mica)	0.8	0.6	0.4	0.7	1.3
Orthoclase	0.7	0.2	0.8	0.5	**4.4**
Quartz60Kaol40	0.4	1.9	1.2	1.2	1.0
Quartz80Kaol20	0.5	0.6	2.0	1.3	1.1
Quartz	0.6	0.5	0.9	0.8	**3.1**
TiOxide	0.7	1.4	0.0	0.5	0.7

The lower than expected proportions of Fe-oxide and Ca-oxide and the correspondingly higher proportion of kaolinite(carbonate), kaolinite(carbonate,pyrite) and kaolinite(pyrite) in the modelled fly ash as opposed to the measured fly ash (Table 7.6) suggest that excluded pyrite and calcite/dolomite do not only form excluded Fe-oxide/Fe-S-oxide and Ca-oxide/Ca-Mg-oxide fly ash particles, but must somehow react with the fine excluded kaolinite to form kaolinite(carbonate), kaolinite(carbonate,pyrite) and kaolinite(pyrite).

It is important to recall, that minerals with the elemental assemblages of Al-Si-Ca-oxide (kaolinite(carbonate)), Al-Si-Fe-O (kaolinite(pyrite)) and Al-Si-Fe-Ca-oxide (kaolinite(carbonate,pyrite)) do not occur in any significant proportions in the

original pulverised fuel. These glass phases (kaolinite(carbonate), kaolinite(carbonate,pyrite) and kaolinite(pyrite)) can only be formed as the result of the interaction of Fe with Al-Si-O and Ca/Mg with Al-Si-O. The coalescence of included pyrite with included kaolinite and included calcite/dolomite with included kaolinite in a pulverised fuel particle is the obvious process to account for the formation of these phases. However, the fly ash formation model (Table 7.6), clearly indicates that the coalescence of included kaolinite with included pyrite and calcite/dolomite only accounts for 40% of kaolinite(carbonate), 36% of kaolinite(pyrite) and 10% of kaolinite(carbonate, pyrite). Clearly, there is an additional fly ash formation process within a boiler, which facilitates the interaction of excluded kaolinite and iron from Fe-oxide and calcium/magnesium from Ca-oxide/Ca-Mg-oxide.

The following potential processes are proposed:

- An alternative source of calcium and magensium – the inorganic elements, calcium and magnesium, associated with reactive and inert semifusinite macerals, either as sub-micron carbonates and/or organically bound elements could be reacting with the inorganic Al, Si found in macerals (Figure 5.13). Energy dispersive X-ray spectrum of “mineral-free” macerals supports the possibility of inorganically bound bound calcium, iron, aluminium and silicon (Figure 5.13). If this is the process, then the assumptions made for the “ash free” fly ash formation sub-model (section 4.8.2) needs to be reviewed.
- Vaporisation of the excluded calcium oxide and iron oxide forming calcium and iron rich cations (fume). Calcium and iron cations (fume), incorporated into the flue gas, react with excluded kaolinite. It has been reported that organically bound calcium in lignite, brown coals and sub-bituminous coals vaporise and reacts with fly ash particles (Srinivasachar et al., 1990) (Kuhnel and Eylands, 1991). It has also been reported that calcium associated with calcite or dolomite is inert to vaporisation (Srinivasachar et al., 1990). Based on current thinking outlined above, the possibility of forming calcium fume is not feasible for the test coal as the test coal is a bituminous coal (Figure J.1) and calcite and dolomite are the principal source of calcium. However, the discrepancy in model predictions, and the apparent increase in

proportion of kaolinite(carbonate) and corresponding decrease in the proportion of Ca-oxide with increase in temperature in the drop tube furnace ashes (Figures 7.8 and 7.10), suggest that there might be some merit in the proposed hypothesis that calcium and iron fume is produced from Ca-oxide and Fe-oxide.

- Alternatively, excluded Fe-oxide/Ca-oxide particles physically collide with excluded kaolinite in the combustion zone. The presence of large excluded quartz grains with surface coatings of molten particles is evidence that fly ash particles do collide in the combustion zone (Figures 7.12 and 7.13). It is unlikely, that these phases were associated in the original coal as coarse excluded quartz particles are not associated with any other minerals (Appendix O).
- Additional kaolinite(carbonate), kaolinite(carbonate, pyrite) and kaolinite(pyrite) are formed in slag deposits as a result of the coalescence of excluded kaolinite, Ca-oxide and Fe-oxide fly ash particles. Fragments of slag deposits are dislodged by natural attrition and sootblowing. These fragments form part of the fly ash sampled from within the boiler. An example of a possible slag deposit fragment in fly ash is illustrated in Figure 4.15. The relative decrease in the mass proportion of Ca-oxide and Fe-oxide and increase in the mass% proportion of kaolinite(carbonate), kaolinite(pyrite) and kaolinite(carbonate, pyrite) in the eyebrows and bottom ash samples (Table 7.7), as opposed to the slag probe deposits, suggests that calcium and iron from Ca-oxide and Fe-oxide is reacting with kaolinite in the slag deposit.
- Any combination of the processes described above.

The mechanism which controls the formation of kaolinite(carbonate), kaolinite(carbonate,pyrite) and kaolinite(pyrite) requires further research. Understanding this mechanism will go a long way to improve our understanding of the fly ash formation process in a 200 MW_e boiler.

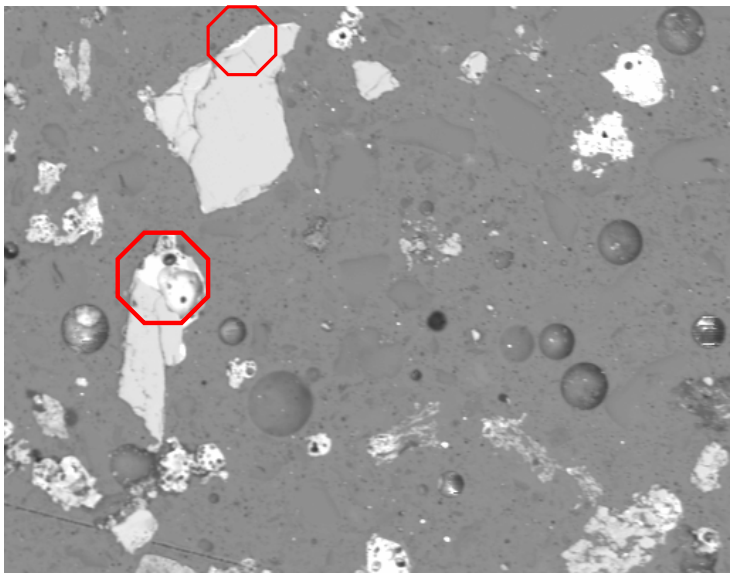

Figure 7.12: Backscattered electron image of fly ash in the +75 µm size fraction. Note the quartz grain (grey) middle left with spherical molten fly ash (white) attached onto the surface of the quartz grain (within circle).

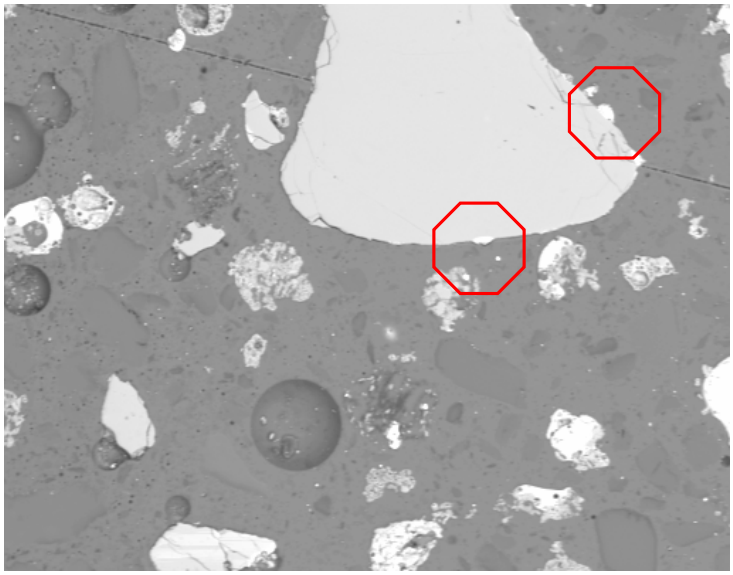

Figure 7.13: Small spherical molten fly ash droplets (white) attached to large quartz grain (grey).

7.5 Slag Deposit Formation

For this research, the slag deposits that accumulated on the removable slag sleeves were analysed. During the sampling of hole 2 (at a depth of 2m) and hole 3 (at depth of 0m), larger clinkers ("eyebrow"), which were easily removed from the initial slag deposit layer, formed. These clinker ("eyebrow") samples were carefully removed and analysed. It is assumed that the initial slag deposit layer formed on the removable slag sleeves represents the initial layer formed on clean boiler tubes, whereas the clinkers ("eyebrows") represent slag deposits formed over time and are probably similar to "eyebrows" formed on the underside of burners.

The bottom ash is regarded as a mixture of clinker or slag deposit fragments that have dislodged from within the boiler and coarse fly ash particles (quartz and orthoclase), which have naturally gravitated towards the ash hopper.

The average composition of the slag probe deposits developed on the slag sleeve is summarised in appendix P and that of the clinker ("eyebrow") in Table 6.8.

The iron and calcium in the slag probe deposits is concentrated in Fe-oxide and Ca-oxide and to a lesser extent kaolinite(pyrite) and kaolinite(carbonate). In contrast, the iron and calcium in the clinker("eyebrows") and in the bottom ash are principally concentrated in kaolinite(carbonate), kaolinite(carbonate,pyrite) and kaolinite(pyrite) fly ash phases and to a lesser extent in Fe-oxide and Ca-oxide (Table 6.8 and Table 7.7).

The variation in the iron- and calcium-bearing fly ash phases in the slag probe deposits and the clinker ("eyebrows") suggests the following:

1. Discrete Ca-oxide, Fe-oxide and kaolinite fly ash particles form the initial slag deposits. Calcium and iron react with "kaolinite" in the slag deposit to form kaolinite(carbonate), kaolinite(carbonate,pyrite) and kaolinite(pyrite) fly ash phases. These phases are concentrated in the clinker ("eyebrow") and bottom ash deposits. Solid-state diffusion of calcium and iron from Ca-oxide and Fe-oxide fly ash phases to kaolinite is proposed as the possible mechanism for formation of these alumino-silicate phases

with varying proportions of the fluxing elements (Ca and Fe). This appears to be a moderately rapid process as the time taken to develop the clinker ranged from 60 minutes for hole 2, (at depth of two metres)) and 80 minutes for hole 3 (at depth of zero metres).

2. Kaolinite(carbonate), kaolinite(carbonate,pyrite) and kaolinite(pyrite) are formed in the combustion chamber and, together with iron oxide and calcium oxide, reach the slag probe as discrete fly ash particles. (The possible formation processes of these Ca-Fe bearing alumino-silicate fly ash particles with minor fluxing elements are described in the previous section).

Figure 7.14 is a microscopic view of the initial slag deposit. A large spherical kaolinite(carbonate) particle with included Ca-Mg-oxide, (light grey) has adhered to the slag sleeve. Attached to this kaolinite(carbonate) is a large sub-angular quartz particle (dark grey), with smaller discrete Fe-oxide, Ca-oxide and kaolinite(carbonate) particles attached to the quartz grain surface. Physically entrapped between these two large fly ash particles are fine (<5 µm) kaolinite fly ash particles.

The kaolinite(carbonate) particle measures 150x308 µm and the quartz grain 110x173 µm in size. The smaller Fe-oxide, Ca-oxide and kaolinite(carbonate) particles are less than 25 µm in size. An examination of numerous slag sleeve deposits revealed that a large proportion of the discrete spherical fly ash particles are exceeding 35 microns (µm) in size.

The spatial distribution and physical characteristics of the fly ash particles in Figure 7.14, suggests that the kaolinite(carbonate)/Ca-oxide particle was “sticky” and adhered onto the slag probe. The solid quartz grain has collided with the “sticky” kaolinite(carbonate) particle and adhered to it. The molten sticky Fe-oxide particles have adhered to both the quartz and kaolinite(carbonate) grains. Small kaolinite particles have been physically entrapped between the large grains. The presence of minor proportions of Ca-oxide/Ca-Mg-oxide associated with the predominately large kaolinite(carbonate) particle suggests that either the calcium interacts with the kaolinite within the slag deposit or that the phases are formed in

the combustion zone and are transported and adhere to the removable slag sleeve.

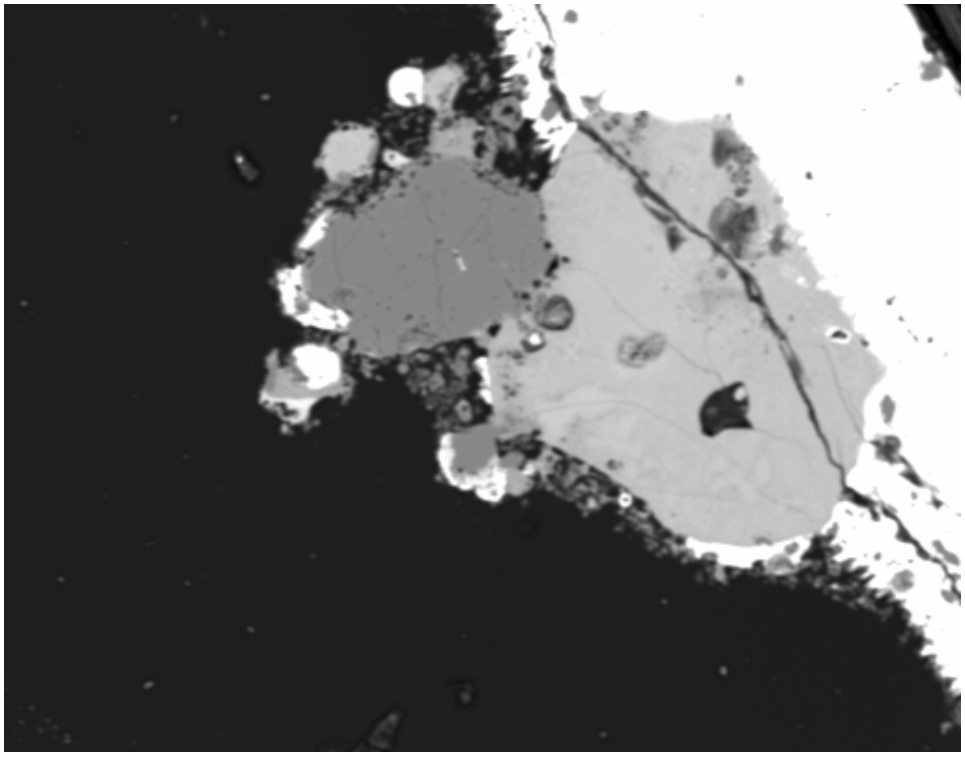

Figure 7.14 Detail of slag sleeve with kaolinite(carbonate), adhering onto slag sleeve and quartz grain attached onto the kaolinite(carbonate). (refer to figure 4.16 for phase identification, #1 0.5m, length of image is 430 µm)

Discrete solid fly ash particles are a feature of the slag probes deposits, whereas the clinker (“eyebrow”) deposits (Figure 7.15) are partially sintered spherical cenospheres or plenospheres. Occasionally, discrete quartz and “kaolinite” fly ash particles are present in the clinker (“eyebrows”) deposits. These cenospheres/plenospheres are composed principally of Al-silicates with minor to trace concentrations of calcium, magnesium and iron (analogous to the fly ash phases, kaolinite(carbonate), kaolinite(carbonate,pyrite) and kaolinite(pyrite), Table 6.8).

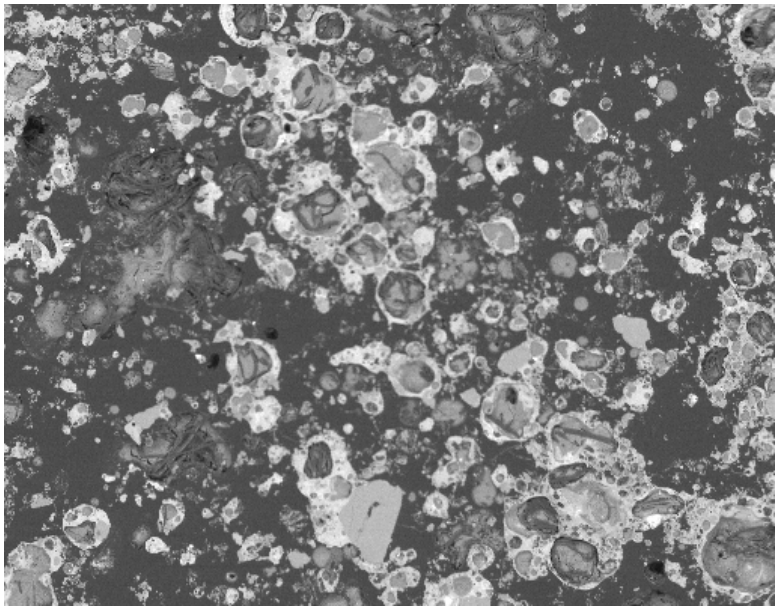

Figure 7.15: A backscattered electron image of a clinker (“eyebrow”) deposit. Note the discrete solid quartz fly ash particle (light grey) at the base of the image.

Differences in the characteristics of the slag probe deposit as opposed to the clinker (“eyebrow”) deposit point to a complex process of slag deposition and subsequent formation. Irrespective of the deposition mechanism, the common thread is the occurrence of kaolinite(carbonate), kaolinite(carbonate,pyrite) and kaolinite(pyrite). These fly ash phases are prominent constituents of the slag deposit. As stated in the previous section, understanding the fly ash formation mechanism of these alumino-silicate phases with minor concentrations of the fluxing elements (Ca, Fe and Mg) is important not only to improve our knowledge of fly ash formation process, but also our knowledge of slag deposition and formation.

7.6 Slagging Prediction Indices

A comprehensive explanation of the common slagging indices is presented in section 3.5 and Appendix B. The slag index ranges for these different indices are summarised in Table 3.5.

The traditional slagging indices are based on the bulk ash elemental analysis and in some case on ash fusion temperatures. The problem with these indices is that they are based on bulk analysis and do not take into account the impact of the size and viscosity ("stickiness") of individual fly ash particles. Since these slagging indices mask the importance of mineral associations, mineral interactions, size and "stickness", they are invariably inappropriate and do not accurately predict the slagging characteristics of the pulverised fuel.

The slagging prediction model developed from this research is based on the size and predicted viscosity of each fly ash particle.

For each measured and modelled fly ash particle, the average elemental composition is used to calculate the temperature at a viscosity of 250 (T_{250}), 2000 (T_{2000}) and 10000 (T_{10000}) poise, using the Watt and Fereday equation (table 7.8). The total Fe+Ca proportion is determined for each modelled fly ash particle and measured fly ash particle. The Fe+Ca index in Table 7.8 is the mass-% proportion of those fly ash particles with a total Fe+Ca content exceeding 12.

Table 7.8: Comparative average slagging parameters for the pulverised fuel (bulk) and fly ash (bulk).

Slagging parameter	Unit	Model – based on pulverise fuel	Measured Fly ash
T250	°C	1511.0	1537.2
T2000	°C	1342.1	1364.8
T10000	°C	1252.6	1268.7
Fe+Ca	Mass-%	9.8	5.4

The indices in Table 7.8 are based on bulk samples and do not take into account the impact of fly ash size on slag development (as depicted in Figure 7.14). The slagging prediction model accommodates the impact of size.

The particles are classified by size and in terms of the slagging limits outlined in Table 3.5 (Table 7.9).

Table 7.9 : Mass-% proportion of fly ash particles in the respective slagging parameter class and by size. Slagging parameters are T250 and Fe+Ca. (limits based on Juniper, 1995b)

T250 (°C)	+75	-75+38	-38	Total
	Mass-%	Mass-%	Mass-%	Mass-%
>1350	23.8	26.3	39.8	89.9
1200-1350	1.5	1.6	1.7	4.8
<1200	1.1	1.7	2.5	5.3
Total	26.3	29.7	44.0	100.0
Fe+Ca	**+75**	**-75+38**	**-38**	**Total**
	Mass-%	**Mass-%**	**Mass-%**	**Mass-%**
<7.0	21.0	22.4	38.1	81.4
7-12	0.9	2.8	1.9	5.6
>12	4.4	4.5	4.0	13.0
Total	26.3	29.7	44.0	100.0

Based on T250 (Table 7.9), and assuming that all particles coarser than 38 µm will be transported by flue gas to the heat transfer surfaces, it is estimated that 2.8 mass% of the fly ash particles will be sticky and adhere to the surface. Using the Fe+Ca value, it is estimated that 8.9 mass% will adhere to the surface.

This information, in conjunction with the flow rate of the coal entering the boiler, makes it possible to predict the slag deposition rate in kilograms per hour or grams per hour for different coals. With this information the comparitive slagging propensity of coals can be predicted either from the modelled fly ash phase proportions or from the measured fly ash.

7.7 Summary

A major finding emanating from the fly ash formation model developed in this research is that the simple fly ash formation models (coalescence, partial coalescence or fragmentation) described in literature cannot adequately describe the fly ash formation process in a 200 MW_e boiler. (An) additional process(es)

related to the scale of the boiler, boiler operation and boiler configuration contribute(s) to the formation of fly ash particles within the 200MW_e boiler.

The first stage of fly ash formation is controlled by the mineral attributes (association) in the pulverised fuel. This aspect can be modelled using the accepted fly ash formation processes of included minerals, coalescence, partial coalescence and fragmentation. If included calcite, dolomite and/or pyrite are/is associated with kaolinite in a pulverised fuel particle, these phases will coalesce to form important slag developing fly ash phases, kaolinite(carbonate), kaolinite(carbonate, pyrite) and kaolinite(pyrite). If quartz and kaolinite are in contact, then there is a higher probability that these phases will not coalesce and that they will be released instead after complete combustion of the pulverised fuel particle has taken place.

Fine included kaolinite in pulverised fuel will be released to form fine “kaolinite” fly ash particles. Excluded pyrite and carbonates will transform into spherical Fe-O-S/Fe-oxide, Ca-oxide and Ca-Mg-oxide particles, respectively. Excluded quartz, remains unaltered and forms fly ash particles equal in size as in the pulverised fuel. The fly ash phase proportions are expected to be analogous to those predicted by the fly ash formation model and measured in the drop tube furnace fly ash. This stage of fly ash development probably occurs during the combustion of the pulverised fuel particles and, depending on pulverised fuel particle size and maceral composition will last for one to two seconds.

After the initial stage, the impact of the boiler configuration, size and operational conditions will influence the characteristics of the fly ash. The fly ash size and phase characteristics are not homogenous within the boiler. Large excluded quartz and, to a lesser extent Fe-oxide and Ca-oxide tend to gravitate to the ash hopper, whereas the finer kaolinite fly ash particles tend to concentrate in the upper regions of the boiler. Thus the size and chemistry of the fly ash particles vary at different heights and depths within the boiler.

The fly ash formation model predicted a lower proportion of important slag deposit forming fly ash phases kaolinite(carbonate), kaolinite(carbonate, pyrite) and kaolinite(pyrite) than measured in probe fly ash, cegrit fly ash and in the

bottom ash. Since the fly ash formation model is based on the full coalescence of any included carbonates and/or pyrite associated with kaolinite within a pulverised fuel particle, the discrepancy between the modelled and measured ash phase distribution suggests that there is an alternative fly ash formation mechanism not described by the fly ash formation model processes, coalescence, partial coalescence and fragmentation.

It is proposed that the excluded kaolinite fly ash particles released after the initial fly ash formation stage have interacted with excluded Fe-oxide and Ca-oxide formed by the transformation of excluded pyrite and calcite/dolomite. What is still in dispute and requires further investigation, however, is the actual mechanism controlling the formation of the additional kaolinite(carbonate), kaolinite(carbonate,pyrite) and kaolinite(carbonate) in the combustion zone. . What needs to be considered is whether the calcium oxide and iron oxide vaporise to form fumes rich in calcium and iron which would react with the excluded kaolinite, or if there is any physical interaction (collisions) between excluded iron oxide /calcium oxide and excluded kaolinite.

It is, however, possible, that the additional kaolinite(carbonate), kaolinite(carbonate,pyrite) and kaolinite(pyrite) are actual fragments of slag deposits which have been dislodged from the heat transfer surfaces, either naturally or by sootblowing.

The inorganic elements, aluminium, silicon, calcium, magnesium and iron, which were detected in “mineral-free” coal particles, could be the alternative source of these important slagging fly ash phases. It is proposed that these elements could coalesce during particle combustion to form sub-micron to fine (<3 μm) fly ash particles.

It is important to understand the process within the boiler that results in the creation of kaolinite (carbonate), kaolinite (pyrite, carbonate) and kaolinite (pyrite) as these fly ash phases are major constituents of the slag deposits.

Because of the complicated chemistry and the intricate morphological properties of the deposits accumulating on the removable slag sleeves, the processes of slag deposition and formation are as complex as fly ash formation.

Initial slag development is characterised by large proportions of Fe-oxide and, to a lesser extent kaolinite(carbonate). Large spherical particles (>35 µm) tend to adhere to the slag sleeves. These large particles could also have smaller particles adhering to their outer surfaces. Since these particles are spherical, it implies that at some stage these particles were molten or malleable, thus enhancing the probability that these particles will stick to a surface and not rebound. Smaller excluded kaolinite fly ash particles are commonly trapped between these larger particles. Quartz, which is typically unaltered, forms part of the slag deposit if the surface of the slag deposit is “sticky” and receptive. This occurs when either Fe-oxide and/or kaolinite(carbonate) have/has reached the surface before the quartz.

With time, the chemistry and characteristics of the slag deposit change. The discrete fly ash particles evident in the initial deposit are replaced by partially sintered fly ash cenopheres forming a friable deposit. These cenospheres consist predominantly of aluminium silicates with varying concentrations of the fluxing elements, calcium, magnesium, iron and potassium. Based on the fly ash classification scheme these, slag deposit phases are described as kaolinite(carbonate), kaolinite(carbonate,pyrite) and kaolinite(pyrite). Fe-oxide and, to lesser extent, Ca-oxide, which are common phases in the initial slag deposits formed on the removable slag sleeves occur, in trace concentrations in these slag deposits which have formed over time.

It is difficult to determine whether discrete Ca-oxide, Fe-oxide and “kaolinite” fly ash phases were initially deposited onto the slag sleeve and with time, the calcium and iron has reacted with “kaolinite” to form kaolinite(carbonate), kaolinite(carbonate,pyrite) and kaolinite(pyrite) fly ash phases, or if these phases were formed in the combustion chamber and adhered onto the slag sleeve. This requires further investigation.

8 SUMMARY, CONCLUSIONS AND FUTURE RESEARCH

8.1 Summary

8.1.1 Introduction

The principle objective of this research has been to improve our understanding of fly ash formation and slag development on combusting a South African coal in a 200MW_e pulverised fuel boiler.

The minerals in coal are the principal source of fly ash in a boiler. It is hypothesised that the mineral associations and mineral grain sizes in the pulverised fuel have a direct effect on the size and chemistry of the fly ash. If we are to understand fly ash formation, the attributes of the minerals in coal have to be qualified and quantified. Association, habit and the grain size distribution of minerals in pulverised fuel are the inputs into the fly ash formation model.

The fly ash formation model simulates the combustion of single pulverised fuel particles and assumes mineral transformation and fly ash formation processes (coalescence, partially coalescence and fragmentation) to predict the size and chemistry of the fly ash particles. By comparing the modelled fly ash to measured fly ash, the accuracy of the model can be substantiated and any new fly ash formation process can be identified.

The chemistry of the slag deposits formed within a 200 MW_e boiler on removable slag sleeves is compared to the chemistry of the measured fly ash obtained from within the boiler. This comparison will identify any fly ash phases that are major constituents of slag deposits.

To achieve the said objectives outlined above, a sampling technique, an adapted CCSEM (computer controlled scanning electron microscope) analytical method was applied and a fly ash formation model was developed.

This chapter serves to summarise the new techniques developed and the contribution that this research has made to further our understanding of fly ash formation and slag development in a Southern Hemisphere coal, combusted in 200 MW_e boiler.

8.1.2 Analytical framework

The 200 MW_e, unit 9 at Hendrina power station was selected as the test boiler for undertaking these analyses. Four access holes were cut into the left hand side (view from the front of the boiler) wall of the boiler. The first hole is in line with the bottom burner row, 1.5m from the backwall of the boiler. Immediately above hole 1 and in line with the second burner row is hole 2. Hole 3 is in the centre of the boiler, approximately two to three m above the third and last burner level, while hole 4 is immediately below the superheaters.

Obtaining representative samples from within the boiler started in April 1999 and was completed in May 2000. Samples of fly ash, slag deposits were acquired using a water-cooled suction pyrometer and slag probe (section 8.2) at depth intervals of 0.5 metres, to a maximum depth of two metres. Isokinetic samples of pulverised fuel were simultaneously sampled from the pipes feeding the burners.

8.1.3 Suction pyrometer and water cooled slag probe

A six-metre water-cooled suction pyrometer with a uniquely designed slag probe attachment was ideally suited for extracting samples of fly ash and slag at different heights and depths from within the fully functional 200MW_e boiler. The suction pyrometer was able to suck fly ash from within a boiler and the temperature of the flue gas could be measured.

The removable slag probe, specifically designed for this research was attached to the upper tube of the suction pyrometer. The slag probe forms a complete unit, with thermocouples in its wall and in the centre of the water chamber. On completion of an analysis, the removable slag sleeve could be easily removed. The slag probe and slag sleeve were constructed from used sections of boiler tubing. A separate pump supplied water via 6mx8mm aluminium tubing to the slag probe. The flow rate of this water was controlled to maintain the temperature of the water in the enclosed chamber to $\pm$100 °C. The principle behind the slag probe design was to construct a unit that could simulate water/steam flowing through boiler tubes, ensure the easy removal the slag sleeve with its accumulated slag deposit and which could withstand the harsh environment of a boiler.

The slag probe and water-cooled suction pyrometer configuration allowed for the easy and controlled removal of fly ash from within the boiler. At the same time, it facilitated the accumulation of slag on the slag sleeve. This ensured that the characteristics of the fly ash, which initiates and sustains the development of slag, could be ascertained.

Algorithms based on the first principle of thermodynamics were used to predict the surface temperature of the slag sleeve. (Further research is required to refine the algorithms). The calculated temperature was the temperature taken at the interface between the slag deposit and the slag sleeve and not necessary the temperature at the surface of the slag deposit. Heat transfer coefficients through the slag deposit and the thickness of the slag deposit were not included in the calculation. The calculated temperatures for holes 1 and holes 2 were slightly higher than those that are universally expected for boiler tube surface temperatures (400-570 °C). It was hypothesized that the gap between the slag sleeve and the taper reduces the cooling from water flowing through the slag probe. It is evident from this research that the slag probe was functional, but further research is required for improving the prediction of slag deposit surface temperatures and to improve cooling of the slag probe, especially in the hotter zones of the boiler.

8.1.4 CCSEM

The Computer Controlled Scanning Electron Microscope or Coal Characterisation Scanning Electron Microscope (CCSEM) is universally accepted as an valuable new technique with the potential of resolving complex questions in coal combustion (Huggins, 2002). To achieve the said objective, the scanning electron microscope at Technology Scientific International (TSI) was reconfigured to allow for the detailed analysis of mineral associations, mass% mineral and coal proportions, mineral grain sizes and liberation characteristics in the pulverised fuel. The traditional sampling preparation techniques had to be modified, image analysis routines had to be written and a unique coal mineral and fly ash identification scheme had to be developed in order to qualify and quantify mineral and phases in the pulverised fuel, fly ash and slag deposits.

Sample preparation had to overcome the universal problem of separating coal particles from the traditionally used epoxy resin-mounting medium. Doping epoxy resin with iodoform and writing the appropriate image analysis routines successfully achieved this objective.

Rapid mineral identification was accomplished by comparing the elemental proportions derived from 100 msec X-ray spectrum to predefined mineral identification rules. Licensed software supplied from Anglo American Research Laboratories facilitated the mineral identification and the platform to design the appropriate and unique mineral and fly ash identification key files. Mineral identification is based on the principles of fuzzy logic and compares the unknown elemental proportions to the measured proportions specified in the mineral identification key files. In the context of this research, the coal mineral phase, “coal”, describes the organic carbon-rich fraction in pulverised fuel. Unfortunately, the different macerals present in the pulverised fuel cannot be distinguished.

Fly ash phase/mineral identification presented a different problem, as fly ash is a mixture of known minerals and amorphous phases with varying elemental proportions. To overcome these problems, the fly ash mineral/phase nomenclature was based on comparing the elemental proportions in the fly ash phase to the elemental composition of the known minerals in the pulverised fuel.

A common fly ash phase is “kaolinite”, which is essentially an alumino-silicate (Al-Si-O) fly ash phase that represents the transformed products of kaolinite clay found in pulverised fuel. “Kaolinite” is a generic term and collectively includes metakaolinite, mullite and silicon spinel. Another example is the fly ash phase kaolinite(carbonate), which is essentially an Al-silicate with minor to trace concentrations of Ca and Mg derived from the interaction of kaolinite with the carbonates, calcite (source of Ca) and dolomite (source of Ca and Mg).

The acceptable agreement between:

- the XRF ash elemental analysis and the elemental distribution calculated from the CCSEM analysis and,
- the CCSEM predicted ash% accounting for mineral volatile loss and the conventionally determined ash%,

indicates that CCSEM is a viable technique for quantifying and qualifying the minerals in pulverised fuel and the phases/minerals in fly ash and slag deposits.

The CCSEM consistently overestimated the proportion of iron in pulverised fuel, and underestimated the proportion of the minor elements TiO_2, K_2O and P_2O_5. The increase proportion of iron is attributed to density segregation of pyrite during sampling preparation, which consequently artificially enhancing the concentration of pyrite (Fe_2S). The underestimation of TiO_2 could be attributed to fine rutile inclusions in kaolinite and quartz and possibly organically bound Ti. Small rutile grains in kaolinite and quartz were smaller than the beam resolution of two to three microns (µm) and electron beam spacing. The underestimation of K_2O, could be attributed to fine potassium-bearing illite/mica principally associated with kaolinite.

Modifying the sample preparation technique, reduce the electron beam spacing and increasing the X-ray counting rates will resolve the problems describe above and will subsequently improve the analytical accuracy. Reducing the electron beam spacing and increasing the X-ray counting rates would improve the identification of fine titanium, potassium and phosphorus-bearing minerals in the pulverised fuel, while improvements in the sample preparation technique would reduce the density segregation of pyrite. Recent advancements in SEM technology and X-ray detectors, improvements in the software, and faster computers, will result in the required improvements in the CCSEM technique without adversely affecting the time required to analyse a sample.

With improved analytical speeds and data transfer rates, more frames can be practically scanned per section analysed. This will improve sampling statistics and reduce the analytical errors attributed to poor particle statistics (i.e. number of particles analysed). Improvements in X-ray technology and backscattered electron detectors will ultimately result in identifying the individual macerals groups by CCSEM.

The CCSEM technology, as demonstrated in this research, is a powerful technique, ideally suited to qualifying and quantifying the minerals in pulverised fuel, the minerals/phases in fly ash and in the slag deposits. Continual

advancements in SEM, the X-ray detector and backscattered detector technology will continually improve the accuracy of CCSEM.

8.1.5 CCSEM results – pulverised fuel

The bulk (72.2 mass%) of the pulverised fuel is “coal”, with kaolinite (13.2 mass%) and quartz (8.3 mass%) being the major minerals. Of the remaining 6.3 mass%, pyrite (2.5 mass%), dolomite (1.2 mass%) and calcite (1.1 mass%) are the main minerals. Trace concentrations (<1 mass%) of feldspar, illite/mica, anatase/rutile, apatite, siderite, ankerite and iron oxide (hematitite, magnetite and iron hydroxides) also occur.

Up to 50 mass-% of the test coal comprises of mineral free “coal” particles. Kaolinite predominantly (64%) occurs as fine inclusions (<10 µm) in pulverised fuel particles with varying proportions of “coal”. Inertodetrinite appears to be the major maceral associated with kaolinite. In contrast, quartz predominantly (60%) occurs as coarse to fine excluded particles with a lower proportion included quartz associated with kaolinite in inertodetrinite rich pulverised fuel particles.

Pyrite is predominantly excluded (84%), with a lesser proportion occurring as fine inclusions in predominately vitrinite-rich coal particles. Carbonates (calcite and dolomite) are also predominantly (60%) excluded particles, with lower proportions occurring in cleats and fracture fillings in inertodetrinite, vitrite and semifusinite/fusinite “coal” particles.

Simplistically, the test coal can be described as a highly volatile bituminous coal with a large proportion of mineral free “coal” particles (50 mass-%), inertodetrinite particles with fine inclusions of kaolinite (16 mass-%) and to lesser extent quartz (15.8 mass-%), excluded coarse quartz (2.9 mass-%), pyrite and carbonates, vitrite particles with fine pyrite inclusions and inertodetrinite, vitrite and semifusinite/fusinite “coal” particles with transecting carbonates-rich cleats.

Less than 23 mass% of the pulverised fuel particles are particles with more than two included minerals of which 68% (15.8 mass%) is included kaolinite and quartz in pulverised fuel. Thus the remaining 33% or 7.2 mass% of the coal particles consist of complex mineral associations of predominantly included

kaolinite/quartz associated with other minerals and other minerals included in "coal".

8.1.6 CCSEM results – fly ash

The average mass% fly ash phase proportions extracted from within the boiler (probe fly ash) and a routinely acquired cegrit fly ash sample are summarised in Table 8.1.

Table 8.1: Mass-% fly ash distribution

Single source fly ash phases			
Fly ash phase	**Probe fly ash**	**Cegrit fly ash**	**Perceived mineral source**
Kaolinite	59.2	58.3	Kaolinite – includes metakaolinite, mullite and silicon spinel
Quartz	13.5	15.1	Quartz
Iron-oxide/pyrite	2.3	3.0	Pyrite
Ca-carbonate/Ca-oxide	1.9	2.7	Carbonates (dolomite, calcite)
Kaolinite(illite, mica)	1.9	2.0	Illite and mica
Orthoclase	0.3	1.0	Feldspar
Ti-oxide	0.2	0.1	Ti-oxide (rutile, anatase)
Char	9.8	3.5	Uncombusted coal
Total	89.1	86.3	
Multi source fly ash phases			
Kaolinite(carbonate)	5.1	6.0	Kaolinite (Al.Si) + carbonate (Ca,Mg)
Quartz60Kaol40	3.3	3.7	Quartz(60%) + Kaolinite (40%)
Kaolinite(pyrite)	1.0	2.0	Kaolinite(Al.Si) + pyrite(Fe, ±S)
Quartz80Kaol20	0.8	1.3	Quartz(80%) + Kaolinite(20%)
Kaolinite(carbonate,pyrite)	0.4	0.4	Kaolinite(Al.Si)+carbonate(Ca,Mg)+pyrite(Fe)
Total	10.6	13.4	

Kaolinite the dominant mineral in pulverised fuel (59%), is the dominant fly ash phase. "Kaolinite" in fly ash predominantly occurs[8] as fine (<10 µm) excluded "kaolinite" fly ash particles. The increase in the proportion of excluded "kaolinite" fly ash particles indicate that the fine included kaolinite grains in pulverised fuel are released on combustion. The comparatively low proportion of quartz60kaol40 and quartz80kaol20 indicates that the coalescence of kaolinite associated with quartz in the inertodetrinite rich coal particles is limited.

[8] 68% of the total kaolinite proportion in the fly ash

Excluded quartz in pulverised fuel remains excluded in fly ash. Fine included quartz grains are also released on combustion to form fine excluded quartz fly ash particles.

In pulverised fuel, 84% of pyrite occurs as excluded particles, whereas in fly ash the proportion of excluded Fe-oxide (a transformation product of pyrite) is reduced to 60%. Similarly, the proportion of excluded carbonates in pulverised fuel and the corresponding transformation product, Ca-oxide/Ca-Mg-oxide has also been reduced from 60% to 56.8%. These reductions indicate that Fe-oxide and Ca-Oxide have reacted with other minerals to from alternative fly ash phases. The occurrence of the fly ash phases kaolinite(carbonate), kaolinite(carbonate, pyrite) and kaolinite(pyrite) in fly ash support this notion. Kaolinite(carbonate) principally describes a Al-Si-Ca-Mg-O fly ash particle thought to be formed as a result of the interaction of Ca/Mg from the carbonates with the Al-Si-O derived from kaolinite. Kaolinite(carbonate, pyrite) is principally a Al-Si-Ca-Mg-Fe-O fly ash particle which was formed as a result of the interaction of Fe from pyrite, Ca/Mg from carbonates and Al-Si-O from kaolinite. Kaolinite(pyrite) a Al-Si-Fe-O fly ash particle formed as a result of the interaction of Fe from pyrite and Al-Si-O from kaolinite. It is important to note that there are no minerals in the pulverised fuel of any appreciable proportions that has an elemental signature similar to that found in the kaolinite(carbonate), kaolinite(carbonate,pyrite) and kaolinite(pyrite) fly ash phases.

The dominance of single source fly ash particles over multi-mineral source fly ash particles is symptomatic of the low proportion of more than one mineral in a single pulverised fuel particle.

8.1.7 CCSEM results – slag deposits, clinkers and bottom ash

Apart from a few holes, a thin layer of ash/slag developed on the removable slag sleeves. In a few cases, a substantial thicker deposit (a clinker or “eyebrow”) will accumulate on the removable slag sleeves or will plug the bottom tube of the suction pyrometer. These particular deposits had different characteristic that could be perceived to represent the development history of slag deposits.

As opposed to the average fly ash composition (Table 8.1), the removable sleeve slag deposit had an enhanced concentration of iron oxide and to lesser extent kaolinite(carbonate). The spherical iron-oxide and kaolinite(carbonate) particles were typically >35 µm in size. In contrast, the clinker("eyebrow") deposits had an enhance concentration of kaolinite(carbonate), kaolinite(carbonate,pyrite) and kaolinite(pyrite) and a significantly lower proportion of iron oxide. Both deposits had relatively small proportions of the dominant fly ash phase's kaolinite and quartz.

The slag probe deposits were made up of a collection of discrete solid fly ash particles each with its own specific elemental composition. On the other hand, the clinker("eyebrow") deposits were principally made up of partially-sintered spherical cenospheres/plenospheres with an elemental composition analogous to the fly ash phases kaolinite(carbonate), kaolinite(carbonate,pyrite) and kaolinite(pyrite). Occasionally, discrete quartz and "kaolinite" particles were present in the clinker("eyebrow") deposit.

8.1.8 Fly ash formation model

The principal approach of the fly ash formation model is to simulate the combustion of single pulverised fuel particles. The inputs into the model are the CCSEM derived mineral associations and sizes in the pulverised fuel while the outputs are the predicted fly ash size distribution and mass% fly ash phase proportions. The model assumes that the fly ash formation processes coalescence, partial coalescence and fragmentation and the accepted mineral transformations control the characteristics of the fly ash.

Comparing the particle size distributions of individual minerals to the measured size distributions of the fly ash phases, and the mass% fly ash proportions clearly indicates that each mineral has a unique development process and that no universal fly ash formation process could adequately predict the fly ash formation process in a 200 MW_e boiler.

The discrepancy in size and mass% fly ash proportions could be valid or due to incorrect model assumptions and procedures. The fly ash formation model was

validated by combusting a pulverised fuel (hole 2 at depth of 0.5m) in a drop tube furnace (DTF). The drop tube furnace is ideal, as the drop tube furnace is a single particle combustor, which is analgous to the fly ash formation model. The modelled mass% fly ash phase proportions compared favourably to the measured drop tube furnace mass% fly ash proportions. This agreement indicates that there is some validity in the fly ash formation model.

The discrepancy between the modelled and measured fly ash results indicates that the fly ash formation process is not only influenced by the mineral attributes (mineral grain sizes and mineral association) in the pulverised fuel particle, but also by an additional process probably controlled by the boiler configuration, its size and its operating conditions.

The possible impact the boiler configuration, size and operating conditions have on fly ash formation could be derived from the differences between the modelled and measured mass% fly ash proportions. The two main influences are:

1. Flue gas carrying capacity and impact on fly ash particle distribution: For this particular pulverised fuel, fine included kaolinite is released on combustion releasing fine excluded “kaolinite” fly ash particles. These fine-excluded “kaolinite” are transported into the upper regions of the boiler. Conversely, coarse extraneous quartz and, to a lesser extent pyrite and carbonates (calcite and dolomite), transforms to form coarse excluded quartz, iron oxide and calcium oxide fly ash particles. These coarse fly ash particles tend to gravitate towards the ash hopper and concentrate in the bottom ash. The particle size segregation within the boiler, which is a function of the carrying capacity of the flue gas, size and density of the fly ash particles would explain the higher than expected kaolinite proportion and the lower than expected proportions of quartz, calcium oxide and iron oxide in the probe and cegrit fly ash compared to the modelled and drop tube furnace fly ash.
2. Chemical reactions or physical interactions within the combustion chamber -Even assuming the full coalescence of included pyrite and/or carbonates with included kaolinite, the model under predicted the proportions of the important slag forming phases kaolinite(carbonate), kaolinite(carbonate, pyrite) and kaolinite(pyrite). To account for this

shortfall, there has to be some reaction or physical interaction between the fine excluded kaolinite and excluded calcium oxide and iron oxide fly ash particles in the combustion chamber. Whatever this process/these processes might be, it appears from the drop tube furnace ashes that an increase in temperature and oxidising conditions favour the formation of these important slag development phases, kaolinite(carbonate), kaolinite(carbonate,pyrite) and kaolinite(pyrite).

The formation of the additional kaolinite(carbonate), kaolinite(carbonate,pyrite) and kaolinite(pyrite) within the combustion chamber appear to be attributed to any of the following processes:

- Inorganic calcium, magnesium, aluminium and silicon, identified by energy dispersive analysis in “mineral” free pulverised fuel particles coalesce to form sub micron aluminosilicate particles with varying proportions of fluxing elements and/or calcium-oxide and/or iron oxide particles. These sub-micron particles react with fine or coarse excluded kaolinite fly ash particles in the combustion chamber.
- The excluded calcium and iron oxide fly ash particles vaporise in the combustion chamber, releasing Ca and Fe cations into the flue gas. Calcium and iron in the flue gas reacts with the excluded kaolinite fly ash particles to produce kaolinite(carbonate), kaolinite(carbonate,pyrite) and kaolinite(pyrite) fly ash particles.
- Physical interaction (particle collisions) of excluded kaolinite with excluded calcium oxide and iron oxide fly ash particles. The fact that minor molten fly ash particles attached to the surfaces of the larger quartz fly ash particles suggest that there is a tendency for the particles to collide within the boiler.
- Alternatively, kaolinite and quartz fly ash particles vaporise to produce aluminium or silicon rich fume. Aluminium and silicon fume reacts with excluded calcium and iron oxide particles. Vaporisation of silicon and aluminium has being reported in pulverised fuel boilers combusting bituminous coals (Baxter, 1992, Canadas et al., 1990, Quann et al., 1990, Seapan and van Lo, 1990)
- The additional kaolinite(carbonate), kaolinite(carbonate, pyrite) and kaolinite(pyrite) phases are formed in slag deposits. Fragments of slag

are dislodged from the heat transfer surface through natural attrition, shedding and the impact of sootblowing. These fragments are incorporated into the fly ash.

A common thread in all the possibilities proposed above is the physical or chemical interaction of fly ash particles or elements in the combustion chamber or in the slag deposits after the initial fly ash particles have been formed as a result of the coalescence of included kaolinite with included carbonates and/or pyrite. The degree of interaction is a function of the boiler size and its operation, which cannot be simulated in the drop tube furnace. It is for this reason that the drop tube furnace ash will not reflect the additional proportion of kaolinite(carbonate), kaolinite(carbonate,pyrite) and kaolinite(pyrite) observed in the probe and cegrit fly ash.

8.1.9 Fly ash formation and slag deposition – 200MW$_e$ boiler

An important outcome from this research is an insight into the complex process of fly ash formation and ultimate slag deposition and development. Two important features of this process have emerged. Firstly, individual minerals react differently during the process of fly ash formation, and secondly, an additional fly ash formation process occurs in the combustion chamber after the initial fly ash particles have formed. This is conceivable as the combustion chamber is a dynamic, hot and turbulent environment that can produce and affect newly formed fly ash particles further.

Fly ash formation is a two-stage process. The mineral attributes (mineral proportions, grain sizes, association and liberation characteristics) in pulverised fuel (the feed) control the first stage of fly ash formation. This can be successfully modelled using the extensive data generated from a comprehensive CCSEM analysis.

Fly ash particles generated from the first stage are the inputs into the second stage. The characteristics of the fly ash after the second stage are influenced by boiler operation, size and its configuration.

Based on the model developed in this research and the CCSEM analysis of pulverised fuel, fly ash, slag deposits and bottom ash, the following fly ash forming and slag development processes are proposed for the 200MW_e boiler under study.

If included **kaolinite** in the pulverised fuel is not in contact with carbonates and/or pyrite in a pulverised fuel particle, then on combustion the kaolinite will be released to form fine excluded “kaolinite” fly ash particles. Included kaolinite in contact with carbonates and pyrite will react to form the fly ash phases kaolinite(carbonate), kaolinite(carbonate, pyrite) and kaolinite(pyrite). A large proportion of the fine kaolinite fly ash particles will be transported by flue gas into the upper region of the boiler and will exit the boiler. A smaller proportion of the fine kaolinite could be mechanically entrapped in slag deposits. Kaolinite(carbonate), kaolinite(carbonate, pyrite) and kaolinite(carbonate) form the principal phases which initiate and sustain the development of slag deposits. Depending on the turbulence, temperature and stoichiometric conditions (reducing and oxidising), a proportion of the fine kaolinite reacts with iron and calcium to form kaolinite(carbonate), kaolinite(carbonate,pyrite) and kaolinite(pyrite). This could occur as a result of particles physically colliding or as a result of fine kaolinite reacting with Ca (O?) and Fe(O?) in the flue gas. Or alternatively, Al or Si oxide/fume(?) is reacting with Ca-oxide and/or Fe-oxide. It is perceived that these reactions are promoted by higher temperatures and oxidising conditions.

Carbonates and **pyrite** in the pulverised fuel studied were predominantly excluded minerals. On entering the boiler excluded carbonates are transform to Ca-oxide, Ca-Mg-oxide. The pyrite will transform to initially Fe-O-S melt and eventually Fe-oxide (magnetite and/or hematite). A portion of Fe-oxide and Ca-oxide will react with fine excluded kaolinite in the combustion chamber to form kaolinite(carbonate), kaolinite(carbonate, pyrite) and kaolinite(pyrite), a portion will form part of the slag deposits and portion will remain in the fly ash. The included carbonates and pyrite will coalesce with included kaolinite.

Quartz in the pulverised fuel predominantly occurs as coarse excluded particles and to a lesser extent as fine inclusions commonly associated with kaolinite in

inertrodetrinite rich pulverised fuel particles. The coarse excluded quartz remains unaltered and tends to gravitate towards the bottom of the boiler. Small molten fly ash particles could physically collide with the large quartz grains. These molten fly ash particles will form a sticky surface, which will promote the inclusion of quartz grains into the slag deposits.

Orthoclase, is predominantly excluded and will behave similarly to quartz.

Slag formation, like fly ash formation, is a complex and dynamic process. Large molten spherical fly ash particles (>35 μm), predominantly Fe-oxide rich and to a lesser extent kaolinite(carbonate), adhere to the heat transfer surface to form the initial “sticky” receptive surface. Any dry kaolinite or quartz grains will adhere onto the initial receptive “sticky” surface. In addition, these large particles would also physically entrap smaller kaolinite particles, Ca-oxide or Ca-Mg-oxide particles.

With time, the chemistry and characteristics of the slag deposit change. The discrete fly ash particles evident in the initial deposit are replaced by partially sintered fly ash cenopheres/plenospheres forming a friable deposit. These cenospheres consist predominantly of aluminium silicates with varying concentrations of the fluxing elements, calcium, magnesium, iron and potassium. Based on the fly ash classification scheme, these slag deposit phases are principally kaolinite(carbonate), kaolinite(carbonate,pyrite) and kaolinite(pyrite). Fe-oxide and, to a lesser extent, Ca-oxide, are common constituents of the initial slag deposits formed on the removable slag sleeves, but are not common constuents in mature slag deposits.

8.2 Conclusion

The outcome of this research was to provide insights into the fly ash formation processes and ultimately development of slag deposits in the 200MW_e boiler. It is evident, that the characteristics of the fly ash are controlled by the mineral attributes in the pulverised fuel and by the operation and configuration of the boiler.

In summary, the major findings and conclusions from this research are:

- A slag probe with a removable sleeve attached to a water-cooled suction pyrometer is a suitable method for extracting fly ash from within a boiler while simultaneously developing slag deposits.
- CCSEM is a suitable analytical technique to quantify the proportion and characteristics of minerals in pulverised fuel, and phases/minerals in fly ash and in slag deposits. The unique fly ash identification method developed for this research is ideal for tracking elemental changes, while simultaneously leading to an understanding of the potential mineral source of the fly ash particle. Improvements in CCSEM accuracy would be achieved by reducing the beam spacing, thus increasing the number of points analysed per particle. Currently, this is hampered by the analytical time required and the shortcomings of the operating and image processing software. Improved analytical systems developed for the base metal mineral processing industry (MLA and QEM*SCAN) could be modified to include the analysis of pulverised fuel.
- Drop tube furnace is ideally suited for predicting the baseline characteristics of fly ash, but not for accurately predicting the fly ash characteristics derived from a boiler. It is for this reason that any slagging predictions based on drop tube furnace experiments and possibly small-scale combustion units should be interpreted with caution.
- The fly ash formation model, based on mineral association characteristics derived from the CCSEM data, is suitable for predicting the baseline fly ash characteristics, but not suitable for predicting the characteristics of fly ash in a fully operational boiler. Boiler configuration,

natural size segregation, boiler operation conditions and the localised environment have an impact on fly ash characteristics.

- No universal fly ash forming process (fragmentation, coalescence or partial coalescence) can adequately predict the characteristics of the fly ash formed in a 200 MW_e boiler. Each mineral in the pulverised fuel has a unique fly ash formation process.
- Fly ash formation appears to occur in two major stages. The first stage is controlled by the association and size characteristics of the minerals in the pulverised fuel and can be predicted by applying the fly ash formation model. During particle combustion, the initial fly ash particles are formed in the combustion chamber. It is in this dynamic and turbulent environment that the initial fly ash particles physically collide or react with inorganic elements concentrated in the flue gases. The boiler configuration, its size and its operation principles control the second stage. Important processes are the physical interaction (collision) of fly ash particles in the turbulent combustion zone, natural size segregation within the boiler and the chemical reactions between Ca and/or Fe in the flue gas and/or as sub-micron Ca-and/or Fe rich-particles with kaolinite fly ash particles.
- The new slagging index based on the proportion of kaolinite(carbonate), kaolinite(carbonate,pyrite) and kaolinite(pyrite) is used to predict the slagging propensity of a pulverised fuel.
- Slag deposition and formation is a complex dynamic process. It is proposed that by understanding the formation of kaolinite(carbonate), kaolinite(carbonate,pyrite) and kaolinite(pyrite) in the combustion zone even better methods of predicting slag formation and deposition would be possible.
- It is evident that fly ash formation models cannot be based purely on the attributes of minerals in pulverised fuel. The fly ash formation model needs to include the effects of boiler configuration, size and operating conditions.
- The numerous fly ash formation models, based on mineral attributes of Northern Hemisphere and Australian coals and the ash produced in small scale combustors are not necessarily valid for the South African coal studied. (Baxter, 1990, 1992) (Helbe et al., 1990) (Zygarlicke et al., 1991)

(Lui et al., 2000) (Loehden et al., 1989) (Mclennan et al., 2000) (Yan et al., 2002). It is not the integrity or the actual fly ash formation mechanisms that is questioned, but rather the experimental scale on which the model is based. These models invariably exclude the impact that the boiler has on fly ash formation and consequently slag development.

8.3 Future Research

Based upon the current research results presented in this thesis, it is recommended that future research should concentrate on the following aspects:

- This research highlighted a second stage of fly ash formation, which occurs in the combustion zone. Of particular interest is the formation of the important slagging phases, kaolinite(carbonate), kaolinite(carbonate,pyrite) and kaolinite(pyrite). A number sources and mechanisms have been proposed in this research. These include:
  - Included kaolinite/quartz coalesce with organically bound elements and/or sub-micron Ca- and Fe-bearing included minerals.
  - Ca from extraneous Ca-oxide (from extraneous carbonates) and Fe from (from extraneous pyrite) extraneous Fe-oxide chemically or physically interact with fine excluded “kaolinite” fly ash particles.
  - Organically bound Al and Si create an Al-Si rich fume, which reacts with extraneous Ca-oxide and Fe-oxide.
  - Additional Ca- and Fe-bearing alumino-silicates are actually fragments of slag and/or clinker deposits, which have been dislodged by natural attrition and/or sootblowing.

  The source or how these additional Ca- and Fe-bearing alumino-silicate are formed in the combustion zone requires further research.
- The impact of the boiler configuration and boiler operating conditions (temperature and stoichiometric) has on the formation of the important slagging fly ash phases kaolinite(carbonate), kaolinite(carbonate,pyrite) and kaolinite(pyrite). It is perceived that by varying the boiler combustion conditions the fly ash formation process and ultimately slagging can be influenced.

- Determine if there are organically bound inorganic elements (Ca, Fe, Si, Al and Ti) in South African bituminous coals. If there are organically bound cations, then the role these cations play in fly ash formation and slag development should be ascertained.
- Slag probe surface temperature predictions and algorithms require further research. Focus of research should be on the impact of the gap between the slag probe and removable slag sleeve has on heat transfer. A better system for cooling the removable slag sleeve should be considered.
- Improve the analytical accuracy of CCSEM. Research should focus on sample preparation procedures and improvements to CCSEM beam resolution.
- The average viscosity of the individual fly ash particles play an important role in initiating and sustaining slag deposits. The slagging propensity software utilises the Watt and Fereday equation to predict the viscosity of the individual fly ash particles from the average oxide composition. The suitability of using the Watt and Fereday equation requires further investigation. Developing a suitable oxide/viscosity algorithm was beyond the scope of this research.

9 REFERENCES

Abbott, M.F. and Austin, L.G. (1985), Studies on slag deposit formation in pulverized-coal combustors 6. Sticking behaviour of slag drops from three Pennsylvania steam coals, *Fuel*, vol. 64, pp. 832-838.

Abbott, M.F. and Austin, L.G. (1986), Slag deposit initiation using a drop-tube furnace, *In: Mineral Matter and Ash in Coal - Symposium of American Chemical Society August 26-31,* Vorres, K., (Ed), pp. 324-351.

Alekhnovich, A.N. and Gladkov, V.E. (1989), Formation of iron deposits during the combustion of coals with minerals containing different amounts of iron, *Teploenergetika*, vol. 36, 8, pp.4-8.

Allen, G.C. and Hallam, K.R. (1993), Small area and imaging X-Ray Photoelectron Spectroscopy of individual pulverised fuel ash particles, *In: The Impact of Ash Deposition on Coal Fired Plants,* Williamson, J. and Wigley, F. (Eds), pp. 435-444.

Barnes, D.I., Lewit, M.W. and Smith, M. (1993), The slagging behaviour of three UK power station coals in an ash deposition rig, *In: The Impact of Ash Deposition on Coal Fired Plants,* Williamson, J. and Wigley, F. (Eds), pp. 285-295.

Barta, L.E., Berr, J.M., Sarofim, A.F., Teare, J.D. and Toqan, M.A. (1993), Coal fouling tendency model, *In: The Impact of Ash Deposition on Coal Fired Plants,* Williamson, J. and Wigley, F. (Eds), pp. 177-188.

Baxter, L.L. (1990), The evolution of mineral particle size distributions during early stages of coal combustion, *Prog. Energy Combust. Sci.*, vol. 16, pp. 261-266.

Baxter, L.L. (1991), Ash composition predictions as a function of coal type, operating conditions, and boiler location, *In: Effects of coal quality on power*

plants - second international conference, Mehta, A.K. and Harding, N.S. (Eds), pp. 5-59,5-5-74.

Baxter LL (1992), Char fragmentation and fly ash formation during Pulverised-coal combustion, *Combustion and Flame*, vol. 90, pp.174-184.

Baxter, L.L. (1997), Transformations and deposition of inorganic material: the bases of a computer model approach, *In: Effects of coal quality on power plants - Fifth International conference,* Harding, N.S. and Mehta, A.K (Eds), pp. 2-17,2-34.

Baxter, L.L., Abbott, M.F. and Douglas, R.E. (1991), Dependence of elemental ash deposit composition on coal ash chemistry and combustor environment, *Inorganic Transformations and Ash Deposition During Combustion,* Benson, S.A. (Ed), pp. 679-698.

Beer, J.M., Sarofim, A.F. and Barta, L.E. (1991), From coal mineral matter properties to fly ash deposition tendencies: A modelling route, *In: Inorganic Transformation and Ash Deposition During Combustion*, Benson, S.A. (Ed), pp. 71-89.

Bellotto, M., Boni, C., Caridi, A., Cereda, E., Chemelli, C., Braga, D. Marcazzan, G.M., Parmigiani, F., Scagliotti, M. and Bellagamba, B. (1990), Analysis of coal fly ash by bulk and surface characterization techniques, *Material Research Society Symposium Proceedings*, vol. 178, pp. 45-56.

Benson, S.A., Jones, M.L. and Bryers, R.W. (1993), Practical measures to minimize ash, *In: The Impact of Ash Deposition on Coal Fired Plants,* Williamson, J. and Wigley, F. (Eds), pp. 657-677.

Bogwardt, R.H. and Bruce, K.R., (1986), Effect of specific surface area on the reactivity of CaO with SO_2, *AiChe Journal*, vol. 32, pp. 239-248.

Borio, R.W., Pease, B.R., Pohl, J.H., Radway, J.E., Wolsiffer, S. and Art, R.J. (1997), A new approach for solving ash deposits and corrosion problems, *In:*

proceedings: Effects of coal quality on power plants - Fifth International conference, Harding, N.S. and Mehta, A.K (Eds), pp. 6-1, 6-33.

Bott, T.R. (1991), The assessment of fouling and slagging propensity in combustion systems, *In: Inorganic Transformations and ash deposition during Combustion*, Benson, S.A., (Ed), pp. 499-521.

Briggs, D.L. and Lindsay, C.G. (1986), High-temperature interactions among minerals occurring in coal, *In: Mineral Matter and Ash in Coal - Symposium of American Chemical Society August 26-31,* Vorres, K., (Ed), pp. 128-137.

Bryers, R.W. (1986), Influence of segregated mineral matter in coal, *In: Mineral Matter and Ash in Coal - Symposium of American Chemical Society August 26-31,* Vorres, K., (Ed), pp 351-374.

Bryers, R.W. (1991), Fireside behaviour of mineral impurities in fuels from Marchwood 1963 to the Sheraton Palm Coast 1992, *In: Inorganic Transformation and Ash Deposition During Combustion*, Benson, S.A. (Ed), pp. 3-68.

Bryers, R.W. (1996), Fireside slagging, fouling, and high-temperature corrosion of heat transfer surface due to impurities in steam raising fuels, *Progress in Energy and Combustion Science,* Vol. 22, Issue 1, pp. 29-120.

Buhmann D (2001), A review of the mineralogical composition of the No. 4L coal seam from the Witbank and Highveld Coals, *personal communication.*

Burba, L.W. and Ward, C.R. (2000), Elemental composition of coal macerals in relation vitrinite reflectance, Gunnedah Basin, Australia, as determined by electron microprobe analysis, *International Journal of Coal Geology*, vol. 44, pp. 127-147.

Burchill, P., Richards, D.G. and Warrington, S.B. (1990), A study of the reactions of coals and coal minerals under combustion-related conditions by thermal analysis-Mass Spectrometry and other techniques, *Fuel*, vol. 69, pp. 950-956.

Canadas, L., Salvador, L. and Cortes, V. (1990), Modelling of pulverized coal combustion with respect to fly ash particle size distribution, *Fuel*, vol. 69, pp. 690-695.

Charon, O., Sarofim, A.F. and Beer, J.M. (1990), Distribution of mineral matter in pulverised coal, *Prog. Energy Combustion Science*, vol. 16, pp. 319-326.

Cohen, D.R. and Ward, C.R. (1991), SEDNORM - a program to calculate a normative mineralogy for sedimentary rocks based on chemical analyses, *Computational Geoscience*, vol. 17, 9, pp. 1235-1253.

Creelman, R.A., Holcombe, D., Gottlieb, P., Trenaman, K.J. and Juniper, L.A. (1993), Fly ash erosion measurements in utility boilers and a pilot scale facility, *In: The Impact of Ash Deposition on Coal Fired Plants,* Williamson, J. and Wigley, F. (Eds), pp. 747-758.

Creelman, R.A. and Ward, C.R. (1996), A scanning electron microscope method for automated, quantitative analysis of mineral matter in coal, *International Journal of Coal Geology*, vol. 30, pp. 249-269.

Cunningham, A.T.S., Gibb, W.H., Jones, A.R., Wigley, F. and Williamson, J. (1991), The effect of mineral doping of a coal on deposition behaviour, *In: Inorganic Transformation and Ash Deposition During Combustion,* Benson, S.A. (Ed), pp. 271-284.

Deer, W. A., Howie, R.A. and Zussman, J. (1965), An introduction to the rock forming minerals, Longman, 528pp.

Enders, M., Spiegel, M., Albrecht, J. and Putnis, A. (2000), Mineralogical problems in advanced power systems: The contributions of slag and gaseous chemical species to the fly ash, *European Journal of mineralogy*, vol. 12, issue 3, pp. 639-650.

Erickson, T.A., O'leary, E.M., Folledahl, B.C., Ramanathan, M., Zygarlicke, C.J., Steadman, E.N., Hurley, J.P. and Benson, S.A. (1991), Coal ash behaviour and

management tools, *In: The Impact of Ash Deposition on Coal Fired Plants,* Williamson, J. and Wigley, F. (Eds), pp. 271-282.

Etchepare, J., Merian, M. and Kaplan, P., (1978), Vibrational modes of SiO_2. II. Cristobalite and Tridymite, *J. Chem. Phys.*, vol. 68, 4, pp. 1531-1537.

Falcon, R.M.S. (1986), Classification of coal in Southern Africa, *Mineral deposits of Southern Africa,* Vol. 2, Anhaeusser, C.R. and Maske, S., (Eds), pp. 1899-1921.

Falcon, R.M.S. and Snyman, C.P. (1986), An introduction to coal petrogrpahy: Atlas of petrographic constituents in bituminous coals of Southern Africa. *The Geological Society of South Africa, Review Paper Number 2*. 26p.

Faraj, B.S.M. and Mackinnon, I.D.R. (1993), Micrinite in Southern Hemisphere sub-bituminous and bituminous coals: redefined as fine grained kaolinite, *Org. Geochem.* vol. 20, 6, pp. 823-841.

Field, M.A., Gill, D.W., Morgan, B.B. and Hawkesley, P.G.W. (1967), combustion of pulverised coal, *British Coal Utilisation Research Association, Leatherhead*, pp. 1-43.

Finkelman, R.B. (1988), The inorganic geochemistry of coal: A scanning electron microscopy view, *Scanning Microscopy*, vol. 2, 1, pp. 97-105.

Folkedahl, B.C., Steadman, E.N., Brekke, D.W. and Zygarlicke, C.J. (1993), Inorganic phase characterization of coal combustion products using advanced SEM techniques, *In: The Impact of Ash Deposition on Coal Fired Plants,* Williamson, J. and Wigley, F. (Eds), pp. 399-407.

Fonseca, A.G., Mai, M.C. and Harding, N.S. (1988), Coal quality and its effect on combustion, *Industrial practice of Fine coal processing*, Proceedings of the Conference at Hidden Valley, Klimpel, R.R. and Lickie, P.T (Eds), pp. 17-28.

Gaigher, G.L. (1980), Mineral matter in some South African coals, MSc, Univerisity of Pretoria, South Africa.

Galbreath, K., Zygarlicke, C., Casuccio, G., Moore, T., Gottlieb, P., Agron-Olshina, N., Huffman, G., Shah, A., Vang, N., Vleeskens, J. and Hamburg, G. (1996), Collaborative study of quantitative coal mineral analysis using Computer-Controlled Scanning Electron Microscopy, *Fuel*, vol. 75, 4, pp. 424-430.

Gentzis, T., Goodarzi, F. and Hickinbotham, A. (1995), Mineralogical composition of the Highvale mine coals and its impact on plant performance, *Energy sources*, vol. 17, 6, pp.681-702.

Gibb, W.H., Jones, A.R. and Wigley, F. (1993), The UK collaborative research programme on slagging in pulverised coal furnaces: Results of full-scale plant trials, *In: The Impact of Ash Deposition on Coal Fired Plants,* Williamson, J. and Wigley, F. (Eds), pp. 3-17.

Gibson, J.R. and Livingston, W.R. (1991), The sintering and fusion of bituminous coal ashes, *In: Inorganic Transformation and Ash Deposition During Combustion,* Benson, S.A. (Ed), pp. 425-447.

Gomesa, S., Francoisa, M., Abdelmoulab, M., Refaitb, P., Pellissier, C. and Evrarda, O. (1999), Characterization of magnetite in silico-aluminous fly ash by SEM, TEM, XRD, Magnetic Susceptibility, and Mossbauer Spectroscopy, *Cement and Concrete Research*, vol. 29, pp.1705-1711.

Gomez, C.O., Strickler, D.W. and Austin, L.G. (1984), An iodinised mounting medium for coal particles, *Journal of electron microscopy*, vol. 1, pp. 285-287.

Gottlieb, P. (2003), personal *communication*.

Gottlieb, P., Argon-Olshina, N. and Sutherland, D.N. (1991), The characterisation of mineral matter in coal and fly ash. *In: Inorganic Transformations and ash deposition during Combustion - Proceedings of the Engineering Foundation*

Conference, Benson, S.A. (Ed), pp. 135-145, The American Society of Mechanical Engineers.

Hanson, S.P. and Abbott, M.F. (1997), Pilot-Scale studies of furnace heat adsorption for four coal types, *In: proceedings: Effects of coal quality on power plants - Fifth International conference,* Harding, N.S. and Mehta, A.K (Eds), pp. 1-3, 1-19.

Helbe, J.J., Srinivasachar, S. and Boni A.A. (1990), Factors influencing the transformation of minerals during pulverised coal combustion, *Prog. Energy Combust. Sci.*, vol. 16, pp. 267-279.

Helble, J.J., Srinivasachar, S., Boni, A.A., Bool, L.E., Galagher, N.B., Peterson, T.W., Wendt, J.O.L., Huggins, F.E., Shah, N., Huffman, G.P., Graham, K.A., Sarofim, A.F. and Berr, J.M. (1991a), Mechanisms of ash evolution: A fundamental study Part II - Bituminous coals and role of iron and potassium, *Inorganic Transformation and Ash Deposition During Combustion,* Benson, S.A. (Ed), pp. 229-247.

Helble, J.J., Srinivasachar, S., Boni, A.A., Bool, L.E., Galagher, N.B., Peterson, T.W., Wendt, J.O.L., Huggins, F.E., Shah, N., Huffman, G.P., Graham, K.A., Sarofim, A.F. and Berr, J.M. (1991b), Mechanisms of ash evolution: A fundamental study Part 1 - Low rank coals and the role of calcium, *In: Inorganic Transformation and Ash Deposition During Combustion,* Benson, S.A. (Ed), pp. 209-228.

Helbe, J.J. and Kang, S.G. (1993), The effect of combustion stoichiometry on ash formation. *In: The Impact of Ash Deposition on Coal Fired Plants,* Williamson, J. and Wigley, F. (Eds), pp. 583-597.

Holman, J.P., (1997), Heat transfer. New York. McGraw & Hill, 8th Ed. 696 pp.

Hoy, H.R., Roberts, A.G. and Wilkins, D.M. (1965), Behaviour of mineral matter in slagging gasification process, *Institution of Gas Engineers, Journal*, vol. 5, 6, pp. 444-469.

Huffman, G.P., Huggins, F.E. and Dunmyre, G.R. (1981), Investigation of the high-temperature behaviour of coal ash in reducing and oxidizing atmospheres, *Fuel*, vol. 60, pp. 585-597.

Huffman, G.P., Huggins, F.E., Levasseur, A.A., Chow, O., Srinivasachar, S. and Mehta, A.K. (1989), Investigation of the transformations of pyrite in a drop-tube furnace , *Fuel*, vol. 68, pp. 485-489.

Huffman, G.P., Huggins, F.E., Shah, A., Casuccio, G. and Mershon, W.J. (1991), Development of Computer-Controlled Scanning Electron Microscopy (CCSEM) techniques for determining mineral-maceral association, *American chemical society*, vol. 36, 3, pp. 115-1163.

Huffman, G.P., Shah, A.D., Shah, N., Zhao, J., Huggins, F.E., Helbe, J.J., Srinivasachar, S., Peterson, T.W., Wendt, J.O.T., Gallagher, N.B., Bool, L.E. and Sarofim, A.F. (1993), Investigation of ash by microscopic and spectroscopic techniques, *In: The Impact of Ash Deposition on Coal Fired Plants,* Williamson, J. and Wigley, F. (Eds), pp. 409-423.

Huggins, F.E., Huffman, G. and Lee, R.J. (1982), Scanning Electron Miscroscope- based Automated Image Analysis (SEM-AlA) and Mossbauer Spectroscopy quantitative characterization of coal minerals, *ACS symposium Series*, vol. 205, pp. 239-258.

Huggins, F.E., Kosmack, D.A. and Huffman, G.P. (1981), Correlation between ash-fusion temperatures and ternary equilibrium phase diagrams, *Fuel*, vol. 60, pp. 577-583.

Huggins, F.E., Kosmack, D.A., Huffman, G.P. and Lee, F.J. (1980), Coal mineralogies by SEM Automatic Image Analysis, *Scanning Electron Microscopy*, vol. 1, pp. 531-538.

Huggins, F.E. (2002), *International Journal of Coal Geology,* vol. 50, pp. 35-45.

Hurley, J., Zygarlicke, C.J., Chow, O.K. and Hargrove, M. (1991), Physical and chemical changes in fly ash and deposits caused by coal beneficiation, I*n:*

Inorganic Transformation and Ash Deposition During Combustion, Benson, S.A., (Ed), pp. 345-365.

Hurst, H.J., Novak, F. and Patterson, J.H. (1999a), Viscosity measurements and empirical predictions for some model gasifier slags, *Fuel*, vol. 78, pp. 439-444.

Hurst, H.J., Novak, F. and Patterson, J.H. (1999b), Viscosity measurements and empirical predictions for fluxed Australian bituminous coal ashes, *Fuel*, vol. 78, pp. 1831-1840.

Jak, E., Degterov, S., Hayes, P.C. and Pelton, A.D. (1998), Thermodynamic modelling of the system Al_2O_3-SiO_2-CaO-FeO-Fe_2O_3 to predict the flux requirements for coal ash slags, *Fuel*, vol. 77, 1/2, pp. 77-84.

Joutsensaari, J., Kauppinen, E.I., Jokiniemi, J.K. and Helble, J.J. (1993), Studies on ash vaporization in power plant scale pulverized coal combustion, *In: The Impact of Ash Deposition on Coal Fired Plants,* Williamson, J. and Wigley, F. (Eds), pp. 613-624.

Juniper, L.A. (1995a), Applicability of ash slagging indices, *Combustion News*, February, pp.1-3.

Juniper, L.A. (1995b), Practical coal quality evaluation of export thermal coals, *In: Bowen Basin symposium*, pp. 1-10.

Kalmanovitch, D.P. (1991a), A practical approach to predicting ash deposition, *In: Effects of coal quality on power plants: second international conference,* Mehta, A.S. and Harding, N.S., (Eds), pp.5-93.

Kalmanovitch, D.P. (1991b), Predicting ash deposition from fly ash characteristics, *In: Inorganic Transformation and Ash Deposition During combustion,* Benson, S.A., (Ed), pp. 661-677.

Kalmanovitch, D.P. (1993), Ash deposition: A systems approach, *In: The Impact of Ash Deposition on Coal Fired Plants,* Williamson, J. and Wigley, F. (Eds), pp. 679-692.

Kalmanovitch, D.P. and Williamson J. (1986), Crystallization of coal ash melts. *In: Mineral Matter and Ash in Coal - Symposium of American Chemical Society August 26-31,* Vorres, K. (Ed), Washington. pp. 234-255.

Karr, C., (1978), Analytical methods for coal and coal products. Academic Press. 669 pp.

Kondratiev, A. and Jak, E. (2001), Predicting coal ash slag flow characteristics (Viscosity model for the Al_2O_3-CaO-FeO-SiO_2 system), *Fuel*, vol. 80, 14, pp. 1989-2000.

Koyama, S., Morimoto, T., Ueda, A. and Matsuokat, H. (1996), A microscopic study of ash deposits in a two-stage entrained-bed coal gasifier, *Fuel*, vol. 75, 4, pp.459-465.

Kuhnel, R.A. and Eylands, K. (1991), Deviations of thermal transformation in open, multicomponent systems: effects of mineralizers, *In: Inorganic Transformation and Ash Deposition During Combustion*, Benson, S.A. (Ed), pp. 449-457.

Laursen, K., Frandsen, F. and Hede Larsen, O. (1998), Ash deposition trials at three power stations in Denmark, *Energy and Fuel*, vol. 12, 2, pp.429-442.

Lee, R.J., Huggins, F.E. and Huffman, G.P. (1978), Scanning *Electron Microscopy*, vol. 1, pp. 561-571.

Levendis YA, Zhu W and Wise DL (1993), Effectiveness of calcium magnesium acetate as an SO_x sorbent in coal combustion, *AiCHe Journal*, vol. 39, 5, pp.761-773.

Liu, G., Wu, H., Gupta, R.P., Lucas, J.A., Tate, A.G. and Wall, T.F. (2000), Modelling the fragmentation of non-uniform porous char particles during pulverized coal combustion, *Fuel*, vol. 79, 6, pp. 627-633.

Livingston, W.R. and Gibb, W.H. (1993), High temperature coal ash deposition in pulverised coal-fired boilers: In-flame probing at Ratcliffe Power Station and Renfrew, *In: The Impact of Ash Deposition on Coal Fired Plants,* Williamson, J. and Wigley, F. (Eds), pp. 297-311.

Loehden, D., Walsh, P.M., Sayre, A.N., Beer, J.M. and Sarofim, A.F., (1989), Generation and deposition of fly ash in the combustion of pulverised coal, *Journal of the Institute of Energy*, pp. 119-127.

Matsuoka, K., Rosyadi, E. and Tomitam A. (2002), Mode of occurrence of calcium in various coals, *Fuel*, vol. 81, pp. 11-12.

McKie, D. and McKie, C. (1974), Crystalline Solids, *Published by Thomas Nelson and Sons,* 628p.

McLennan AR, Bryant GW, Stanmore BR and Wall TF (2000), Ash formation mechanisms during pulverised fuel combustion in reducing conditions, *Energy & Fuels*, vol. 14, pp. 150-159.

McMillan, P. (1984), Structural studies of silicate glasses and melts - Applications and limitations of Raman Spectroscopy, *American Mineralogist*, vol. 69, pp. 622-644.

Miller, F.S., and Schobert, H.H., A comparative study of ash formation during the combustion of Beulah pulverised coal and Beulah coal-water fuel. *In: Inorganic Transformations and Ash depositions during combustion.* Benson, S.A. (Ed), 1991, pp. 249-267.

Mitchell, P.S. and Gluskoter, H.J. (1976), Mineralogy of ash of some American coals; variation with temperature and source, *Fuel*, vol. 55, pp. 25-32.

Mollaha, M.Y.A., Promreukb, S., Schennachb, R., Cockeb, D.L. and Gillerc, R. (1999), Cristobalite formation from thermal treatment of Texas lignite fly ash, *Fuel*, vol. 78, pp. 1277-1282.

Moza, A.K. and Austin, L.G. (1981), Studies on slag deposit formation in pulverized coal combustors. Results on the wetting and adherence of synthetic coal ash drops on steel, *Fuel*, vol. 60, pp. 1057-1064.

Mysen, B.O., Virgo, D. and Scarfe, C. (1980), Relations between the anionic structure and the viscosity of the silicate melts - a Raman Spectroscopic Study, *American Mineralogist*, vol. 65, pp. 690-710.

Nissen, D.A. and Greulich, F.A. (1987), Automated image analysis of coal minerals, *Symposium on High temperatures materials chemistry*, pp. 494-504.

Nowok, J.W. (1996), Densification, shrinkage and strength development in selected coal ashes, *Journal of the Institute of Energy*, vol. 69, pp. 9-11.

Nowok, J.W. and Benson, S.A. (1991a), Correlation of interfacial surface tension/viscosity ratio with base/acid ratio. Nonbridging oxygen factor and compressive strength development in coal ashes, *In: Inorganic Transformations and ash deposition during Combustion*, Benson, S.A. (Ed), pp.405-423.

Nowok, J.W., Hurley, J.P. and Steadman, E.N. (1991b), A new approach to calculating coal ash viscosity, *In: The Impact of Ash Deposition on Coal Fired Plants,* Williamson, J. and Wigley, F. (Eds), pp. 527-538.

Nowok, J., Benson, S.A., Jones, M.L. and Kalmanovitch, D.P. (1990), Sintering behaviour and strength development in various coal ashes, *Fuel*, vol. 69, 8, pp. 1020-1028.

Oktay, B., (1998), Characterisation of Turkish fly ashes, *Fuel*, vol. 77, 9/10, pp.1059-1066.

Phong-anant, D., Pang, L.S.K., Vassallo, A.M. and Wilson, M.A. (1992), A comparative study of mineral matter transformation and ash deposition in the ACTC Boiler Simulation Furnace and Power Stations, *2nd Australian workshop on ash deposition,* Phong-anant, D. (Ed), pp.9-15.

Phong-anant, D., Pang, L.S.K., Vassallo, A.M. and Wilson, M.A. (1992b), Mineral matter in coal - the characterisation, transformation and effects on boiler deposit formation and boiler erosion, *2nd Australian workshop on ash deposition,* Phong-anant, D. (Ed), pp. 1-8.

Pinheiro, H.J., Pretorius, C.C., Boshoff, H.P. and Du Cann, V., (1998), Analysis of coal product samples of producing South African collieries, CSIR Bulletin 112, 43p.

Postek, M.T., Howard, K.S., Johnson, A.H. and McMichael, K.L., (1980), Scanning Electron Microscope – A students handbook, Ladd Research Industries, Inc, 305p.

Quann, R.J., Neville, M. and Sarofim, A.F. (1990), A laboratory study of the effect of coal selection on the amount and composition of combustion generated submicron particles, *Combustion Science and Technology*, vol. 74, pp. 245-265.

Raask, E., (1984), Creation, Capture and coalescence-of mineral species in coal flames, *Journal of the institute of energy*, vol. 57, pp. 231-239.

Raask, E., (1986), Flame vitrification and sintering characteristics of silicate ash. *In: Mineral Matter and Ash in Coal - Symposium of American Chemical Society August 26-31,* Vorres, K.A. (Ed), American Chemical Society, Washington. pp. 138-155.

Renton, J.J. (1986), Semi-quantitative determination of coal minerals by X-Ray diffractometry, *In: Mineral matter and Ash in Coal – Symposium of American Chemical Society August 26-31*, Vorres, K.A. (Ed), pp. 53-60.

Renton, J. (1982), Mineral matter in coal, *In: Coal structure,* Meyers, R.A., (Ed), pp. 283-327.

Richards, G.H., Harb, J.N. and Zygarlicke, C.J. (1991), The effect of variations in particle-to-particle composition on the formation of ash deposits. *In: Inorganic Transformations and ash deposition during Combustion,* Benson, S.A. (Ed), pp. 713-732.

Richet, P. (1984), Viscosity and configurational entropy of silicate melts, *Geochimica et Cosmochimica Acta*, vol. 48, pp. 471-483.

Rietveld, H.M. (1969), A profile refinement method for nuclear and magnetic structures. *Journal of Applied Crystallography*, vol. 2, pp. 65-71.

Sakorafa, V., Michailidis, K. and Burragato, F. (1996), Mineralogy, geochemistry and physical properties of fly ash From the Megalopolis lignite fields, Peloponnese, Southern Greece, *Fuel*, vol. 75, 4, pp. 419-423.

Seapan, M. and van Lo, J. (1990), A simulation model to predict slag composition in a coal-fired boiler, *High temperature Science*, vol. 26, pp.295-310.

Seggiani, M., Bardi, A. and Vitolo, S. (2000), Prediction of fly-ash size distribution: a correlation between the char transition radius and coal properties, *Fuel*, vol. 79, 8, pp. 999-1002.

Shah, N., Huffman, G.P., Huggins, F.E. and Shah, A. (1991), Graphical representation of CCSEM data for coal minerals and ash particles, *In: Inorganic Transformation and Ash Deposition During Combustion.*, Benson, S.A. (Ed), pp. 179-189.

Sharma, K.S., Simons, B. and Yoder, H.S. (1983), Raman study of Anorthite, calcium Tschermak's pyroxene, and Gehlenite in crystalline and glassy states, *American Mineralogist*, vol. 68, pp. 1113-1125.

Shirazi, A.R., Bortin, O., Eklund, L. and Lindqvist, O. (1995), The impact of mineral matter in coal on its combustion, and a new approach to the determination of the calorific value of coal. *Fuel*, vol. 74, pp. 247-251.

Shyu, H.J., Vaishnava, P.P. and Montano, P.A. (1981), In-situ study of the decomposition of pyrite in an oxygen environment, *Fuel*, vol. 60, pp. 1022-1026.

Skorupska, N.M. and Couch, G. (1993), Coal characterisation for predicting ash deposition: An international perspective, *In: The Impact of Ash Deposition on Coal Fired Plants,* Williamson, J. and Wigley, F. (Eds), pp. 137-150.

Slaghuis, J.H., Ferreira, L.C. and Judd, M.R. (1991), Volatile material in coal: effect of inherent mineral matter, *Fuel*, vol. 70, pp. 471-473.

Snyman, C.P., Van Vuuren, M.C.J. and Barnard, J.M. (1983), Chemical and physical characteristics of South African coal and a suggested classification system, *National Institute for Coal Research*, Coal 8306, pp. 1-63.

Srinivasachar, S. and Boni, A.A. (1989), A kinetic model for pyrite transformations in a combustion environment, *Fuel*, vol. 68, pp. 829-835.

Srinivasachar, S., Helble, J.J. and Boni, A.A. (1990a), Mineral behaviour during coal combustion 1. Pyrite transformations, *Progress Energy Combustion Science*, vol. 16, pp. 281-292.

Srinivasachar, S., Helble, J.J, Boni, A.A., Shah, N., Huffman, G.P. and Huggin, F.E. (1990b), Mineral behaviour during coal combustion 2. Illite transformations, *Prog. Energy Combust. Sci.*, vol. 16, pp.293-302.

Srinivasachar, S., Helble, J.J., Ham, D.O. and Domazetis, G. (1990c), A kinetic description of vapour phase alkali transformations in combustion systems, *Progress Energy Combustion Science*, vol. 16, pp. 303-309.

Stach, E., Mackowsky, M-Th., Teichmuller, M., Taylor, G.H., Chandra, D. and Teichmuller, R. (1982). Textbook of Coal Petrology. 2nd. Rev. Ed. Berlin. Gebruder Borntraeger, 535 pp.

Stanmore, B.R. and Budd, S. (1996), Measuring the viscous flow of molten coal ash, *Fuel*, vol. 75, 12, pp. 1476-1479.

Steadman, E.N., Erickson, T.A., Folkedahl, B.C. and Brekke, D.W. (1991), Coal and ash characterisation: Digital image analysis applications, *In: Inorganic Transformation and Ash Deposition During Combustion.*, Benson, S.A. (Ed), pp. 147-163.

Stewart, I., Whiteway, S.G., Cleyle, P.J. and Caley, W.F. (1986), Decomposition of pyrite in a coal matrix during the pyrolysis of coal, *In: Mineral Matter and Ash in Coal - Symposium of American Chemical Society August 26-31,* Vorres, K.A. (Ed), pp. 485-499.

Straszheim, W.E., Jounkin, K.A., Greer, R.T. and Markuszewski, R. (1988), Mounting materials for automated image analysis of coal using Backscattered Electron Imaging, *Scanning Electron Microscopy*, vol. 2, 3, pp. 1257-1264.

Straszheim, W.E. and Markuszewski, R. (1990), Automated Image Analysis of minerals and their association with organic components in bituminous coals, *Energy and Fuels*, vol. 4, pp. 748-754.

Straszheim, W.E. and Markuszewski, R. (1991), Characterisation of mineral matter in coal for prediction of ash composition and particle size, *In: Inorganic Transformation and Ash Deposition During Combustion.*, Benson, S.A. (Ed), pp. 165-177.

Straszheim, W.E. and Markuszewski, R. (1992), SEM-AIA measurement of the association of mineral matter with the organic coal matrix for predicting fine coal cleanability, *Coal Preparation*, vol. 10, pp. 59-75.

Taylor, J.C. (1991), Computer programs for standard less quantitative analysis of minerals using full powder diffraction profile. *Powder Diffractions*, vol. 6, pp. 2-9.
Ten Brink, H.M. (1990), Mineral matter transformations in pulverised coal combustion, *Netherlands Research Institute*, August, pp.1-30.

Ten Brink, H.M., Eenkhoorn, S. and Hamburg, G. (1991), Transformation and deposition of pyrite in a burner simulation study, *In: Inorganic Transformation and Ash Deposition During Combustion*, Benson, S.A. (Ed), pp. 367-374.

Ten Brink, H.M., Eenkhoorn, S. and Weeda, M. (1993), Flame transformations of coal-siderite, *In: The Impact of Ash Deposition on Coal Fired Plants,* Williamson, J. and Wigley, F. (Eds), pp. 373-383.

Unsworth, J.F., Barratt, D.J., Park, D. and Titchener, K.J. (1988), Ash formation during pulverized coal combustion 2. The significance of crystalline anorthite in boiler deposits, *Fuel*, vol. 67, pp.632-641.

Unsworth, J., Cunliffe, F., Graham, S.C. and Morgan, P.A. (1987), Ash formation during pulverised coal combustion 1: Aerodynamic influences, *Fuel*, vol. 66, pp. 1672-1679.

Urbain, G., Bottinga, Y. and Richet, P. (1982), Viscosity of liquid silica, silicates and alumino-silicates, *Geochimica et Cosmochimica Acta*, vol. 46, pp. 1061-1072.

Van Alphen, C. and Falcon, L. (2000), Application of CCSEM to coal processing, *In: Coal - The Future, 12th International conference on Coal Research, South African Institute of Mining and Metallurgy*, pp. 197-201.

Varshneya, A.K., (1994), Fundamentals of inorganic glasses. Boston: Academic Press, 570p.

Vorres, K.S. (1984), Chemistry of mineral matter and ash in coal: An overview, *In: Mineral Matter and Ash in Coal, Symposium of American Chemical Society August 26-31*, Vorres, K.S. (Ed), pp. 1-8.

Vorres, K.S., Greenberg, S. and Poeppel, R. (1984), Viscosity of synthetic coal ash slags , *In: Mineral Matter and Ash in Coal - Symposium of American Chemical Society August 26-31*, Vorres, K.S. (Ed), pp. 156-169.

Wagoner, C.L. and Yan, X.-X. (1991), Deposit initiation via thermophoresis: Part 1 - Insight on deceleration and retention of inertially transported particles , I*n:*

Inorganic Transformation and Ash Deposition During Combustion., Benson, S.A. (Ed), pp. 607-623.

Wagoner, C.L. and Yan, X.-X. (1993), How ash impaction changes shape of a superheater deposit with time , *In: The Impact of Ash Deposition on Coal Fueled Plants,* Williamson, J. and Wigley, F. (Eds), pp. 625-636.

Wain, S.E., Livingston, W.R., Sanyal, A. and Williamson, J. (1991), Thermal and mechanical properties of boiler slags of relevance to soot blowing, *In: Inorganic Transformation and Ash Deposition During Combustion,* Benson, S.A. (Ed), pp. 459-470.

Wall, T.F., Gupta, S.K., Gupta, R.P., Sanders, R.H., Creelman, R.A. and Bryant, G.W. (1999), False deformation temperatures for ash fusibility associated with the conditions for ash preparation, *Fuel*, vol. 78, pp. 1057-1063.

Walsh, P.M., Sayre, A.N., Loehden, D.O., Monroe, L.S., Beer, J.M. and Sarofim, A.F. (1990), Deposition of bituminous coal ash on an isolated heat exchanger tube: effects of coal properties on deposit growth. *Prog. Energy Combust. Sci.*, vol. 16, pp.327-346.

Ward, C.R., Bocking, M. and Raun, C. (2001), Mineralogical analysis of coal as an aid to seam correlation in the Gloucester Basin, New South Wales, Australia, *International Journal of Coal Geology*, vol. 47, pp. 31-49.

Ward, C.R. and Taylor, J.C. (1996), Quantitative mineralogical analysis of coals from the Callide Basin, Queensland, Australia Using X -Ray diffractometry and normative interpretation, *International Journal of Coal Geology*, vol. 30, pp. 211-229.

Ward, C.R., Taylor, J.C., Matulis, C.E. and Dale, L.S. (2001), Quantification of mineral matter in the Argonne Premium Coals using the interactive Rietveld-based X-Ray Diffraction, *International Journal of Coal Geology*, vol. 46, pp. 67-82.

Watt, J.D. and Fereday, F. (1969), The flow properties of slags formed from the ashes of British coals: Part 1. Viscosity of homogeneous liquid slags in relation to slag composition, *Journal of the Institute of Fuel*, vol. 42, 338, pp. 99-103.

Weisbecker, T., Zygarlicke, C.J. and Jones, M.L. (1991), Correlation of inorganics in Powder River Basin coals in full-Scale combustion, *In: Inorganic Transformation and Ash Deposition During Combustion,* Benson, S.A. (Ed), pp. 699-711.

Wigley, F. and Williamson, J. (1991), The characterisation of fly ash samples and their relationship to the coals and deposits from UK boiler Trials, *In: The Impact of Ash Deposition on Coal Fired Plants,* Williamson, J. and Wigley, F. (Eds), pp. 385-397.

Wigley, F., Williamson, J. and Gibb, W.H. (1997), The distribution of mineral matter in pulverised coal particles in relation to burnout behaviour, *Fuel*, vol. 76, 13, 1283-1288.

Wibberley, L.J. and Wall, T.F. (1982), Alkali-ash reactions and deposit formation in pulverised coal-fired Boilers: Experimental aspects of sodium silicate fomation and the formation of deposits, *Fuel*, vol. 61, pp. 93-99.

Wilemski, J.G. and Srinivasachar, S., (1993), Prediction of ash formation in pulverized coal combustion with mineral distribution and char fragmentation models, *In: The Impact of Ash Deposition on Coal Fired Plants,* Williamson, J., and Wigley, Y F. (Eds), pp. 151-164.

Wilemski, J.G., Srinivasachar, S and Sarofim, A.F. (1992), Modelling of mineral matter redistribution and ash formation in pulverised coal combustion, *In: Inorganic Transformations and ash deposition during Combustion*, Benson, S.A. (Ed), pp. 545-564.

Xie, K.-C., Li, W.-Y. and Zhu, S.-Y. (1994), Pyrolysis studies on coal macerals using DTA-GC,13C-NMR and SEM Techniques. *Fuel Science and Technology* , vol. 12, pp. 1159-1168.

Yan, L., Gupta, R.P. and Wall, T.F. (2001), The implication of mineral coalescence behaviour on ash formation and ash deposition during pulverised coal combustion, *Fuel*, vol. 80, 9, pp. 1333-1340.

Yan, L., Gupta, R.P. and Wall, T.F. (2002), A mathematical model of ash formation during pulverized coal combustion, *Fuel*, vol. 81, 3, pp. 337-344.

Yan, L., Gupta, R.A. and Wall, T.F. (2003). Fragmentation behaviour of pyrite and calcite during hgh-temperature processing and mathematical simulation, *Fuel and Energy,* vol. 15, Issue 2, pp. 389-394.

Yang, N.Y.C. and Baxter, L.L. (1991), Instrument and sample preparation for Computer Controlled Scanning Electron Microscopy (CCSEM), *In: Inorganic Transformation and Ash Deposition During Combustion.*, Benson, S.A. (Ed), pp. 191-206.

Yu, H., Marchek, J.E., Adair, N.L. and Harb, J.N. (1993), Characterization of minerals and coal/mineral associations in pulverized coal, *In: The Impact of Ash Deposition on Coal Fired Plants,* Williamson, J., and Wigley, Y F. (Eds), pp. 361-371.

Zygarlicke, C.J., Ramanathan, M. and Erickson, T.A. (1991), Fly ash particle size Ddstribution and composition: Experimental and phenomenological approach. *In: Inorganic Transformations and ash deposition during Combustion - Proceedings of the Engineering Foundation Conference,* Benson, S.A. (Ed), pp. 525-544.

Zygarlicke, C.J., Steadman, E.N. and Benson, S.A. (1990a), Studies of transformations of inorganic constituents in Texas lignite during combustion, *Prog. Energy Combust. Sci.*, vol. 16, pp. 195-204.

Zygarlicke, C.J., Toman, L.D. and Benson, S.A. (1990b), Trends in the evolution of fly ash size during combustion, *Am. Chem. Soc. Div. Fuel Chem,* vol. 35, 3, pp. 621-636.

APPENDIX A: INTERNATIONAL WORKING GROUPS

Table A1: United States of America working groups (circa 1996)

Country	Organisation	Research Focus	Equipment
U.S.A Massachusetts	PSI Technology Centre	Mineral Transformations Ash Formations, Deposition	PSIT Reactor
U.S.A Kentucky	University of Kentucky Centre of Fossil Fuel Liquefaction Science	Mineral Transformations Instrumentation Combustion Modelling	CCSEM
U.S.A	University of North Dakota Energy and Environment Research Centre	Instrumentation Fly Ash Formation Ash Deposition	CCSEM
USA California	Electric Power Research Institute	Ash Deposition	Coal Quality Impact Model
U.S.A California	Sandia National Laboratories Combustion Research Facility	Mineral Transformation Instrumentation	CCSEM
USA Pittsburgh	Dept. of Energy Pittsburgh Energy Technology Centre	Pilot Scale Combustion Rig	DTF PSCR
U.S.A Iowa	Iowa State University Ames Laboratory	Image Analysis	CCSEM
U.S.A Massachusetts	Dept. Chemical Engineering, Massachusetts Institute of Technology	Mineral Transformations Fouling Models	CCSEM
USA	Riley Stocker Corporation	Phase Diagrams Ash Formation	
USA	Foster Wheeler Corporation		
USA	Brigham Young University	Mineral Characterisations Modelling	CCSEM

Table A2: European Working Groups (circa 1996)

Country	Organisation	Research Focus	Equipment
UK	PowerGen Power Technology Center	Slagging –Plant Scale	Utility
UK	Imperial College	Analytical Instrumentation	DTF CCSEM
UK	National Power	Combustion Ash Depositions	
U.K. Nottinngham	University of Nottingham Coal Technology Research Group	Automatic Image Analysis (AIA)	
Netherlands	Netherlands Energy Research Center	Instrumentation Mineral Matter Transformations	CCSEM

Table A3: Australian Working Groups (circa 1996)

Country	Organisation	Research Focus	Equipment
Australia	Cooperative Research Centre for Black Coal Utilisation. University of Newcastle Dept. Chemical Engineering	Combustion Fly ash formation models Mineral matter transformation Slag development models	CCSEM
Australia	CSIRO*	Instrumentation	QEMSCAN laser microreactor
Australia	ACIRL, Ltd	Erosion Mineral Matter Transformations	

*Intellection markets and distributes QEMSCAN

Table A4: CCSEM configurations (circa 1996)

Institution	SEM/EPMA[a]	X-Ray Analyser	Automatic Image Analyser	Specialised Software	Ref.
EERC	JEOL 35U EPMA	TN-5600	TN-8500	PRC-Partchar[b]	19
EERC	ADEM[c]	Integrated System		PBSEM[d]	19
AMES	JEOL 840 SEM	Kevex Delta	LeMont Scientific	Line Scan Analysis	20
MIT	JEOL 733 EPMA	TN5500	TN5500	PRC[e]	21
UNDEERC[f]	JEOL Jxa-35 SEM				22
Sandia National Labrorories	JEOL 35C SEM	TN 5600	TN5600	PRC	24
University Kentucky	ISI 100	TN5500	TN5500	CMA[g]	25
R.J. Lee Group	JEOL 733 EPMA	TN5502	TN5502	CMA	25
ECN[h]	JEOL JSM-840	TN5500	TN5500		25
Brigham Young University	JEOL 840a SEM	Oxford eXL	eXL Image Analysis Liberation Software	QMA[i] AMCA[j]	26
CSIRO	ISI SX-30	Integrated System		QEM*SEM[k]	25
Imperial College	JEOL 6400 SEM	Voyager	Voyager		23
TSI, South Africa	Camscan	Oxford ISIS	Imquant	ASCAN	27 This research

Notes to accompany Table A4.

[a] SEM – scanning electron microscope, EPMA – electron probe microanalyser
[b] Particle Characterisation, developed by EERC
[c] Automatic digital electron microscope
[d] Particle by Particle Scanning Electron Microscopy program
[e] Particle Recognition and Characterisation
[f] University of North Dakota Energy and Environmental Research Centre
[g] Coal Mineral Analysis
[h] Netherlands Energy Research Foundation
i Quantitative Mineral Analysis
[j] Analysis of Mineral and Coal Associations
[k] Quantitative evaluation of minerals using scanning electron microscope

Reference

19 : Steadman, et al.,1991
20 : Straszheim and Markuzewski, 1991
21 : Beer et al.. 1991
22 : Miller and Schobert, 1991
23 : Wigley and Williamson, 1991
24 : Yang and Baxter, 1991
25 : Galbreath, et al., 1996
26 : Yu et al., 1993
27 : Van Alphen and Falcon, 2000

APPENDIX B: SLAGGING INDICES

Slagging indices used to predict the slagging propensity of a coal are generally based on ash elemental analysis (oxide-%) and ash fusion temperatures. Examples include:

- **Silica Ratio (S_r)**

$$S_r = \frac{\%SiO_2}{\%SiO_2 + \%Fe_2O + \%CaO + \%MgO_3} x100 \qquad \textbf{B.1}$$

- **Base/Acid Ratio (B/A)**

$$B/A = \left(\frac{Fe_2O_3 + Na_2O + K_2O + CaO + MgO}{SiO_2 + Al_2O_3 + TiO_2} \right) \qquad \textbf{B.2}$$

- **Calculated Viscosity, $CV_{1426\,°C}$**

$$CV_{1426oC} = 10^Z$$
$$Z = 0.05784 x S_r - 1.8452 \qquad \textbf{B.3}$$

- **Slagging Factor (R_s)**

$$R_s = B/A * \%TS$$
$$\%TS = \text{total sulphur} \qquad \textbf{B.4}$$

- **Iron Index (Fi)**

$$F_i = \%Fe_2O_3 * B/A \qquad \textbf{B.5}$$

- **Iron + Calcium**

$$Fe + Ca = \%Fe_2O_3 + CaO \qquad \textbf{B.6}$$

- **Multi-Viscosity Index (MV_i)**

$$MV_i = \left(\frac{T_{250} - T_{10,000}}{97.5 x F_s} \right)$$
$$T_{250} = Temperature\ at\ 250\ poise$$
$$T_{10,000} = Temperature\ at\ 10000\ poise \qquad \textbf{B.7}$$
$$F_s = 10^{0.00186 XT_{2000}} - 1.933$$

- **Slagging Temperature (St)**

$$S_T = \left(\frac{IDT + 4 * HDT}{5} \right) \qquad \textbf{B.8}$$

APPENDIX C: SUCTION PYROMETER AND SLAG PROBE

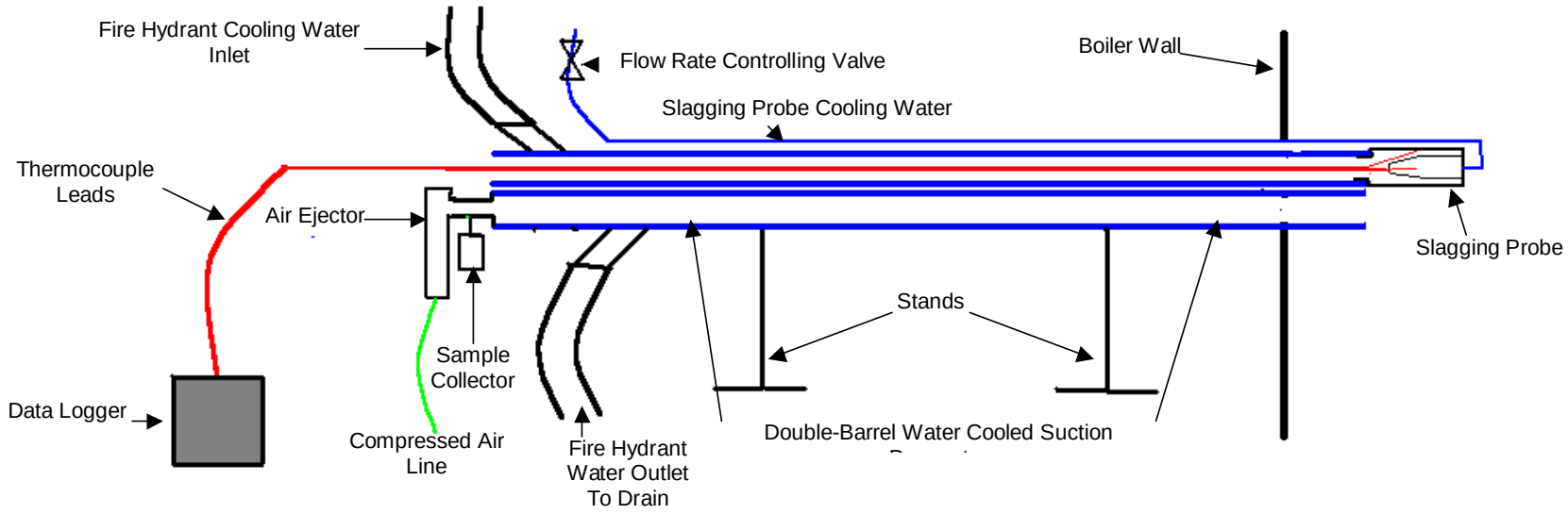

Figure C.1. Water-cooled suction pyrometer and slag probe.

Fire Hydrant Water is used to cool the double-barrel suction pyrometer. The removable slag probe is placed in the top tube, whereas fly ash and flue gases are sucked from the boiler via the bottom tube. Passing compressed air through the air-ejector creates a vacuum. Thermocouple leads are threaded along the centre of the top suction pyrometer tube and connected to a data logger. A manually operated valve is used to control the water flow rate to the slag probe. Water is introduced to the slag probe via a 8mm diameter aluminium tube, which is secured to the outside of the suction pyrometer.

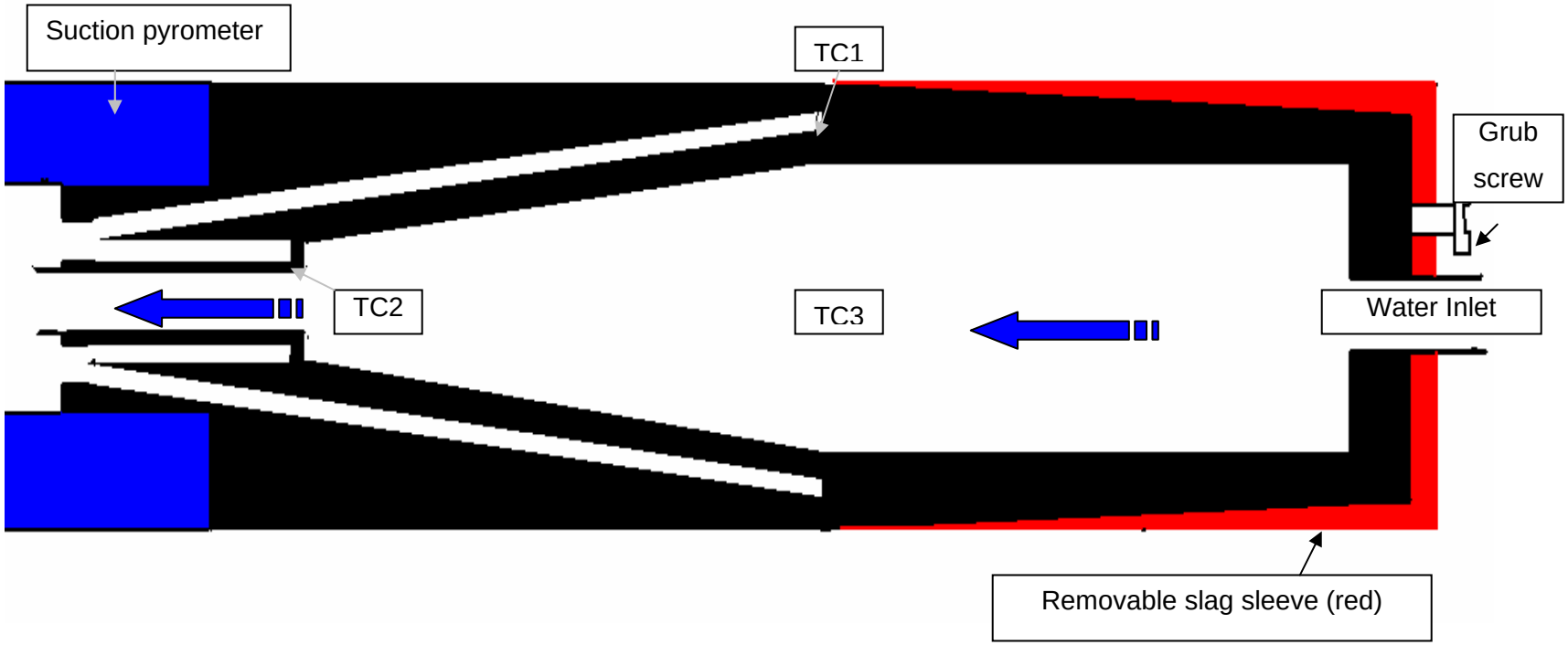

Figure C.2.: Slag probe.

The slag probe dimensions are 230 mm long, with a 60mm diameter radius. The probe wall is 10mm thick. A grub Screw is used to remove the slag sleeve once analysis is complete. The drawing is not to scale. TC = Thermocouple. TC1 – thermocouple 1, positioned 5mm from probe surface, TC2, position against the inner wall. A thermocouple (TC3) is positioned in the water cavity of the slag probe. Blue arrows indicated the expected flow direction of water.

Figure C.3. Suction pyrometer at hole 4.

The fire hydrant holes are attached and the thermocouple data logger is in the background. The water tank is water supply for cooling the slag probe. The sample holder attached to the suction pyrometer with black air ejector is in the foreground.

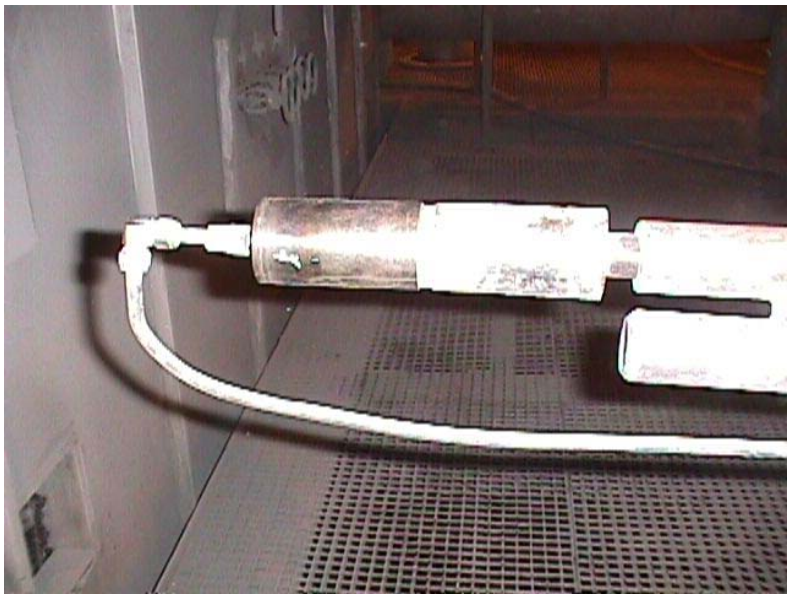

Figure C.4: Slag probe attached to top of the suction pyrometer. Cooling water is supplied to the front end of slag probe. Boiler wall is on the left of the photograph.

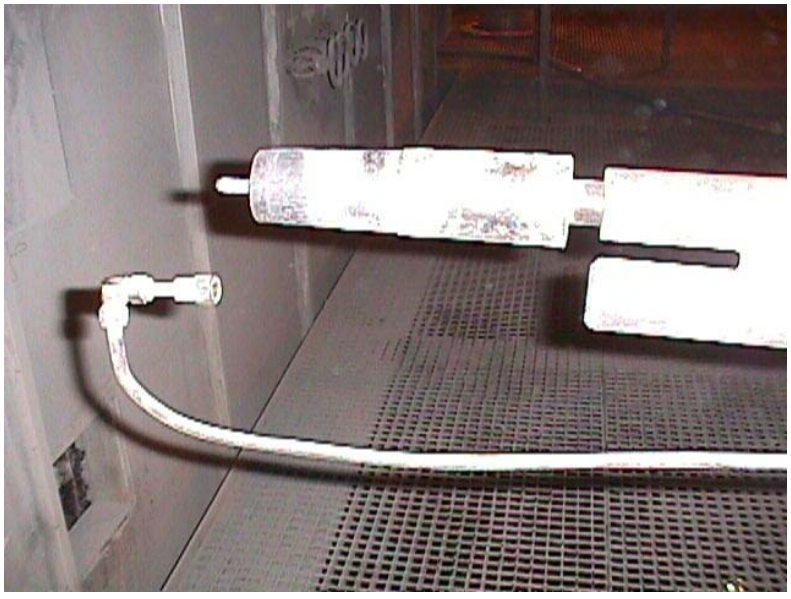

Figure C.5: The slag probe without the removable slag sleeve. The tapered front end is evident. The aluminium tube supplying cooling water to the slag probe is in the foreground. The boiler wall is on the lefthand side.

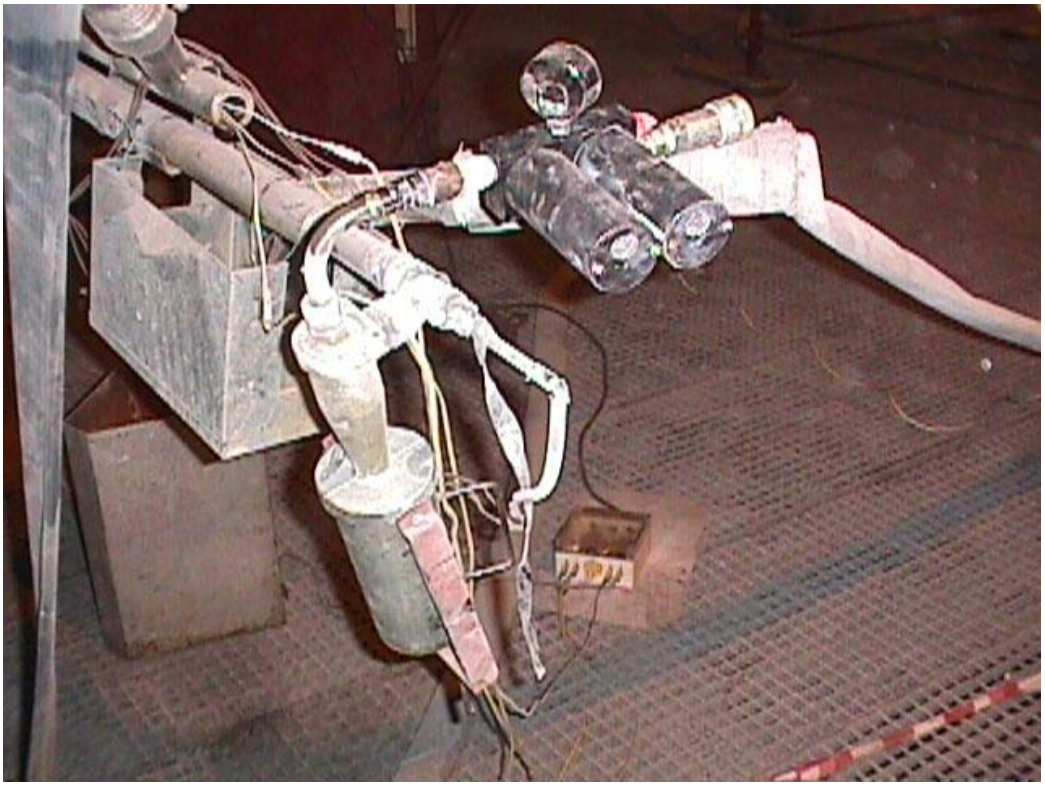

Figure C.6: The backend of the suction pyrometer illustrating the air-ejector (black) attached to the fly ash sample receiver.

Compressed air (high pressure brass attachment) is passed through the air-ejector creating a vacuum. Fly ash is sucked along the length of the bottom tube of the suction pyrometer into the sample receiver. Cooling water from the slag probe drains into the square galvinised steel “bucket”. Thermocouple leads from the slag probe extend out the top tube of the suction pyrometer and connect to the signal box situated on the floor.

Figure C.7: Computer screen showing the temperatures at the start of a run. The high negative temperature is indicative of a faulty thermocouple.

APPENDIX D: DERIVING SLAG PROBE SURFACE TEMPERATURE

Two methods are used to estimate the surface temperature of the slag probe. For a detailed review of heat transfer refer to Holman (1997).

Method 1:

To calculate the surface temperatures (Ts) of the slag probe the following assumptions are made:

1. The conducted heat flux (heat transfer per unit area) through the slag probe is equal to the convection heat flux required to heat the flowing water in the slag cavity to ≈100 °C (T∞).

$$\frac{Q}{A}conduction = \frac{Q}{A}convection \qquad \textbf{D.1}$$

2. There is minimal loss of heat between the removable slag sleeve and slag probe.
3. Water in the slag cavity is turbulent and the temperature reading of thermocouple TC3 (in slag probe cavity) is the bulk temperature of the water in the slag probe cavity (T∞).

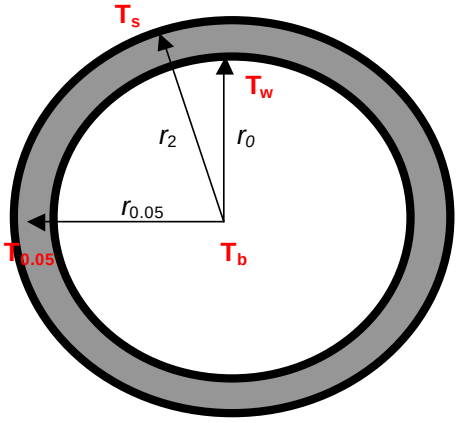

T_s : Probe surface temperature
T_w : Temperature of inner wall (measured, TC2)
$T_{0.05}$: Temperature middle of slag probe 5mm from surface. (measured, TC1)

r_2 : Raduis of slag probe (0.03m)
r_0 : Raduis to inner wall (0.02m)
$r_{0.05}$: Raduis to center of thermocouple (TC1) at 0.05mm from surface (0.025m)

Figure D.1.: Cross section through slag probe illustrating the different radius and temperature readings required for calculating the surface temperature of the probe (Ts). (Not drawn to scale)

Based on these assumptions the following equation is derived:

$$\frac{Q}{A} = \lambda \left[\frac{T_{0.05} - Tw}{\ln\left(\frac{r0.05}{r_{00}}\right)} \right] = h(Tw - Tb) \qquad \textbf{D.2}$$

Rearranging equation D1 the surface temperature (Ts) of slag probe can be calculated:

$$Ts = \left[Q \big/ A \right] \left[\frac{\ln(r2/ro)}{\lambda} \right] + Tw \qquad \textbf{D.3}$$

Calculating the heat transfer coefficient in equation D1 is function of Reynold number and Nusselt number. The equations used are as follows:

Reynold number (*Re*):

$$\mathrm{Re} = \left(\frac{\rho U d}{\eta} \right) \qquad \textbf{D.4}$$

Nusselt number (*Nud*): (after Dittus and Boeler)

$$Nud = 0.023\,\mathrm{Re}^{0.8}\,\mathrm{Pr}^{0.4} \qquad \textbf{D.5}$$

Prandl Number (Pr):

$$\mathrm{Pr} = \nu / \kappa$$

$$\nu = \eta / \rho \qquad \textbf{D.6}$$

$$\kappa = k / \rho Cp$$

Heat transfer coefficient (*h*):

$$h = \left(\frac{\lambda_{H20} * Nud}{2r_0} \right) \qquad \textbf{D.6}$$

Variations in the physical parameter of water (density, dynamic viscosity and Prandl number) with temperature are taken into account. The basic data is obtained from published tables.

Method 2:

A second method of calculating the surface temperature is based on the assumption that the heat transfer through the slag probe wall is linear. The surface temperature can be calculated by extrapolating the curve (Figure D.2). (The measured $T_{0.05}$ and Tw temperatures are used.)

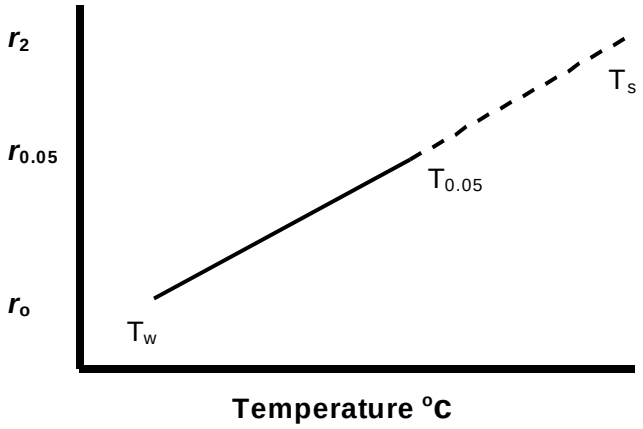

Figure D.2.: Estimate the surface temperature of the probe by assuming linear heat transfer through the slag probe.

APPENDIX E: MACERAL, MICROLITHOTYPES AND MINERAL

The maceral, microlithotype and mineral classification used in this study is based on the comprehensive definitions in Falcon and Snyman (1986), Stach (1982), Falcon Research Laboratory in-house classifications and the ISO standard ISO 7404-4 1988(E). The origin of macerals is comprehensively discussed in chapter two of this study.

The maceral groups and microlithotypes used in this study are summarised in Table E.1 and E.2, respectively.

Table E.1. Maceral classifications (*bold, italics*) used in this study.

Maceral Group	Maceral	Origin
Vitrinite	Telinite Collinite Vitrodetrinite	Wood, bark, fleshy stems and resin. Formed under anaerobic conditions
Liptinite (formally exinite)	Sporinite Cutinite Resinite Alginite Liptodetrinite	Cuticles, spores, resin bodies and algae in sub-aquatic conditions
Inertinite	***Fusinite*** ***Semifusinite*** Sclerotinite ***Micrinite*** ***Inertodetrinite***	Similar to vitrinite but formed in aerobic oxidising conditions

The names of the macerals used in this study are in ***bold italics*** in Table E.1.

Table E.2: Microlithotypes classifications used in this study.

Microlithotype Group	Definition
Vitrite	>95% Vitrinite, MM<20%, balance inertinite, liptinite
Intermediate	>5% Vitrinite, MM<20%, inertinite the balance
Semi-Fusinite/Fusinite	Total fusinite+semi-fusinite >95%, MM<20%, balance vitrinite, liptinite
Inertodetrite	>95% Inertodetrinite, MM<20%, balance vitrinite, inertinite, liptinite
Clarite (CE)	>20% exinite in vitrinite (<80%), MM<20%
Trimacerite (TE)	>20% exinite in intermediate (<80%), MM<20%
Durite (DE)	>20% exinite in inertinite (<80%), MM<20%
Carbargillite	Maceral + 20-60 vol-% clay minerals
Carbosilicate	Maceral + 20-60 vol-% quartz
Carbopyrite	Maceral + 5-20 vol-% sulphides
Carboankerite	Maceral + 20-60 vol-% carbonates
Carbopolyminerite	Maceral + 20-60 vol-% mineral matter
Minerite (Free)	MM >60%

MM – mineral matter

A further adaptation to the microlithotype classification is a unique particle classification for carbominerite (20-60 vol-% MM) and minerite particles (>60 vol-% mineral matter). This classification describes the characteristics of the mineral matter and associated organic component. To classify the organic fraction, the nomenclature of the microlithotypes containing <20 vol-% MM (5 vol-% for pyrite) is used (as described in Table E.2.). The table template designed for this analysis is summarised in Table E.3.

Table E.3. Template - carbominerite and minerite classification scheme

		Organic Component				
		Vitrite	**Inter.**	**Semifusite Fusite**	**Inerto.**	**Minerite (Free)**
Mineral Matter Component	**CarboArgillite**					
	Carbosilicate					
	Carboankerite					
	Carbopyrite					
	Carbopolyminerite					

Inter. : Intermediate

Inerto. : Inertodetrite

If the predominant (>95 vol% of total maceral composition) maceral in a carboargillite particle is vitrinite and the total kaolinite proportion of the particle is between 20-60 volume-% then the particle was classified as carboargillite/vitrite particle. If the proportion of a kaolinite in a carboargillite particle exceeds 60 volume-% then the particle was classified as carboargillite/free.

APPENDIX F: CHEMICAL ANALYSES

Proximate Analysis

Proximate analysis is widely used as an international standard for coal comparison. Proximate analysis measures the total moisture (surface and inherent moisture), ash proportion, volatile matter and fixed carbon by difference. ISO and ASTM standards are available for each component analysed. Proximate analysis is typically undertaken on an “on air dried basis”. The following is a brief description of each component in proximate analyses. For details refer to Karr (1978)

Inherent Moisture (IM) – Water is either held on the surface of coal particles (surface moisture) or occurs trapped in surface cracks and between particles. Hygroscopic water (found in the capillaries of the coal structure) is included as inherent moisture. Inherent moisture is defined % mass-loss after heating one gram of sample to a constant mass at 105 °C. The water associated with minerals (especially clays) and forming part of the organic compounds is not released at these temperatures and will not be included as inherent moisture.

Volatile Matter (VM) – Volatile matter are the constituents (excluding moisture) driven off upon heating the coal in an inert atmosphere (no air). Volatiles might be derived from the organic components or from mineral impurities. Volatile matter is determined by heating one gram of coal for a predefined time in an inert atmosphere to 950°C. The percentage mass-loss, less the mass-loss attributed to inherent moisture (described above) is percent volatile matter.

Ash (A) – Ash is the mass% proportion of non-combustible inorganic residue (ash) remaining after slowly heating one gram of coal in a muffled furnace to 750°C. The coal is completely burnt. The ash-percentage is always less than the absolute proportion of mineral matter in coal. The ash% does not include the proportion of volatile matter released from minerals. Ash% does not include water derived from clay minerals, CO_2 derived from the decomposition of carbonates (calcite, dolomite and ankerite) and SO_2 from sulphides (pyrite). The well-known

Parr formula (Parr, 1932) computes the mineral matter (MM) content from ash-% and total sulphur (S_t):

$$MM = 1.08Ash + 0.55S_t \quad \textbf{F.1.}$$

The Parr formula has being extensively modified to accommodate a variety of coals. The King-Maries-Crossley formula (KMC) includes the includes influence of carbonates (CO_2), sulphur from pyrite (S_p), sulphur from sulphates (S_{ash}), inherent S (S_{SO4}) in the organic fraction and chlorine (Parr, 1932):

$$MM = 1.13Ash + 0.8CO_2 + 0.5Sp + -2.8(S_{ash} – S_{SO4}) + 0.5Cl \quad \textbf{F.2.}$$

Snyman et al. (1983) derived a South African equivalent to the Parr formula as:

$$MM = 1.10Ash + 0.55CO_2 \quad \textbf{F.3.}$$

Gaigher (1980) estimated the mineral matter factor of South African coals to be in the order of 1.08 to 1.25. If the coal had high concentrations of illite and quartz, then the factor is 1.08, whereas if the coals were enriched in carbonates, the mineral matter factor will be closer to 1.25.

To negate the volatile released from minerals upon heating, the organic fraction can be destroyed by electronically-excited oxygen plasma at 120 °C. The method is known as Low Temperature Ashing (LTA). It is not commonly used as it can take several days to complete.

Fixed Carbon (FC) – Fixed carbon refers to the carbon that remains after the volatiles and surface and inherent moisture have been removed. Carbon is burnt off and the ash-% is measured. Fixed carbon is then calculated by difference. It is normally calculated as:

$$FC = 100\% - (\%IM + \%Ash + \%VM_{inorganic} + \%VM_{organic}) \quad \textbf{F.4.}$$

Ultimate Analysis

Ultimate Analysis is the measurement for the elemental compounds of the coal and includes the proportion of carbon, hydrogen, nitrogen, oxygen and sulphur. Excluding nitrogen, these elements are the predominant components of macerals and are found in minerals.

***Carbon and hydrogen* –** Carbon and hydrogen occur as complex hydrocarbons and on heating are released by the reactions:

$$C + O = CO_2 + \text{heat} + \text{other gasses}$$
$$2H + O = H_2O + \text{heat} + \text{other gasses}$$

The measured carbon and hydrogen also includes carbon (from carbonates (CO_2)) and hydrogen (H_2O from clays) derived from minerals.

***Nitrogen* –** For all practical purpose N is only associated with the organic fraction and not with minerals. Coal is digested in H_2SO_4 and nitrogen reacts with the acid to form ammonium sulphate.

***Sulphur* –** Sulphur in coal can occur associated with sulphides (pyrite) and is organically bound to the complex organic hydrocarbons.

***Oxygen* –** Oxygen is normally calculated by difference.

Carbonate (as CO_2) - Measuring the CO_2 concentration evolved from dissolving pulverised fuel in hydrochloric acid (HCl) is indicative of the proportion of carbonates (calcite, dolomite and ankerite).

Calorific Value

Calorific value (CV) is the heating value of the coal. Coal is heated in oxygen in a pressurised bomb calorimeter immersed in water. The change in water temperature is indicative of the heating value (MJ/kg) of the coal. The heat is either recorded as gross calorific value or as net calorific value. The gross calorific value includes the heat of water vapours and other components that

escape to the atmosphere, whereas net calorific value excludes the heat associated with these vapours. The gross calorific value is used in this study.

Ash elemental analysis

A fixed quantity of coal is slowly combusted to 750°C to produce ash (non-combustible residue). The non-organic elements are quantified either by X-ray fluorescence analysis (XRF) or by wet chemistry techniques. The elements determined are SiO_2, Al_2O_3, Fe_2O_3, SO_3, CaO, MgO, Na_2O, K_2O, P_2O_5 and MnO. SO_3 proportion in ash can be misleading as it is commonly accepted that a moderately high proportion of the evolved S reacts with Ca-oxide in the ash to form Ca-sulphates (anhydrite or gypsum).

APPENDIX G: CCSEM MEASUREMENT PARAMETERS

Any automated mineral analytical system utilising the first law of stereology to compute area%, volume% and sizes of mineral components in a sample are based on a number of measurable parameters. With reference to Figure G.1 the terms and parameters required are explained.

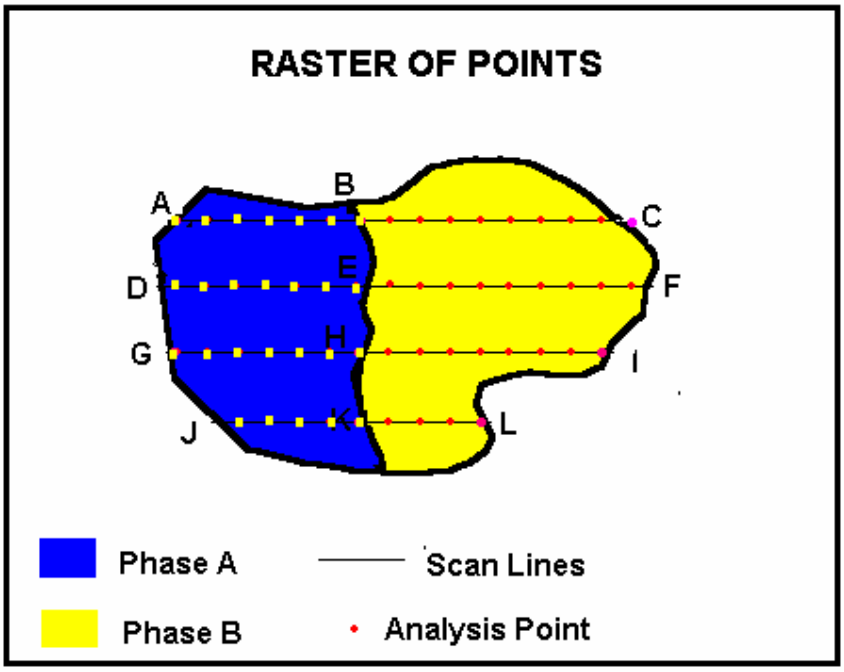

Figure G.1: Terms and concepts used in automated mineral analysis.

Particles and mineral grains:

A particle is defined as a separated entity comprising of either single mineral grains or a multitude of mineral grains. The particle consists of the mineral grains, “phase A” and “phase B” (Figure G.1). In context of this study, phase A or phase B could be any mineral, organic fraction (macerals or char) or any phase in pulverised fuel and fly ash (glass).

Volume-% mineral distribution (point analysis):

Based on the first law of stereology:

$$P_p=L_L=A_a=V_v \qquad \textbf{G.1.}$$

Where: P_p = Proportion of points

L_L = Proportion of linear intercepts

A_a = Area proportion

V_v = Volume proportion

The first three terms of this law can be measured, whereas the volume percent is assumed based on the law.

With reference to Figure G.1:

Volume-%: Number of points

$$volume\text{-}\%\ A=\left(\frac{\sum\ points}{\sum\bullet\ \ points}\right)x\ 100.0 \qquad \textbf{G.2.}$$

$$volume-\%B=\left(\frac{\sum\bullet\ points}{\sum\bullet\ \ points}\right)\text{x}\ 100.0 \qquad \textbf{G.3.}$$

Volume-%: Intercepts proportion

$$volume-\%A=\left(\frac{\sum I_{AB}+I_{DE}+I_{GH}+I_{JK}}{\sum I_{AC}+I_{DF}+I_{GI}+I_{JL}}\right)x100.0 \qquad \textbf{G.4}.$$

$$volume-\%B=\left(\frac{\sum I_{BC}+I_{EF}+I_{HI}+I_{KL}}{\sum I_{AC}+I_{DF}+I_{GI}+I_{JL}}\right) \qquad \textbf{G.5.}$$

Mass-% mineral distribution

The mass-% mineral distribution is based on:

$$mass-\%_j = \frac{(volume-\%_j * density_j)}{\sum_o^{all} volume-\% \ * density} * 100.0 \qquad \textbf{G.6.}$$

For minerals in coal, the density is obtained from literature (Deer et al. 1965), whereas for fly ashes the density is calculated using the Huggins and Sun method (Appendix H).

Particle Size and Grain Size:

Depending on the magnification setting the point spacing is known (Table G.1).

Table G.1. Typical fields of view dimensions, analytical point spacings and field of view area for different magnification settings.

Magnification	Field of view dimensions		Point Spacing (μm)	Field of view area (μm^2)
	X (μm)	Y (μm)		
100	1077	842	16.52	905412
150	718	561	11.21	402406
200	538	421	8.41	226353
250	431	336	6.72	144866
300	359	280	5.61	100601
350	308	240	4.81	73911
400	269	210	4.21	56588
450	239	187	3.74	44711
500	215	168	3.36	36216

The length of the intercept (μm) can be calculated on the basis of this point spacing and depending on the number of points in an intercept. The size of a mineral grain or of a particle can be expressed as the average intercept length, the equivalent area diameter and the maximum intercept length.

Elemental composition

Elemental composition in pulverised fuel is calculated from mass% mineral distribution and using either standard mineral composition derived from literature or analysed directly using quantitative energy dispersive X-ray analysis. The formula used is:

$$mass - \%E_i = \sum M_m * Ep_i \qquad \textbf{G.7.}$$

Determining the elemental proportions in fly ash and slag deposits is requires an alternative approach. The principal problem is the high proportion of glasses in fly ash that do not have a fixed elemental composition. To overcome this problem, the X-ray spectrum of minerals with known elemental compositions was obtained. This 50s (acquisition time) spectrum were broken down randomly into 100msec X-ray spectrum and the elemental counts were computed. The linear algorithm describing the quantitative elemental proportion compared to the CCSEM derived elemental counts was determined (Table G.2).

Table G.2: Linear algorithms used to estimate elemental proportions from CCSEM elemental count proportions. Equation is in the form y=mx+c, where y is mass-% proportion of element and x the normalised CCSEM elemental counts

Element	Slope (m)	Intercept (c)	Correlation coefficient
Al	56.78	0.128	0.99
Si	60.46	0.17	0.98
Fe	94.93	2.78	0.98
Ca	79.18	-0.43	0.98
Mg	73.87	0.11	0.98
K	88.05	-0.03	0.99
S	27.04	0.069	0.88
Ti	88.39	0.074	0.89

Based on these algorithms, the CCSEM elemental counts can be used to estimate the actual elemental proportions. The relationship for aluminium, silicon,calcium and iron are illustrated in Figures G.2, G.3, G.4 and G.5.

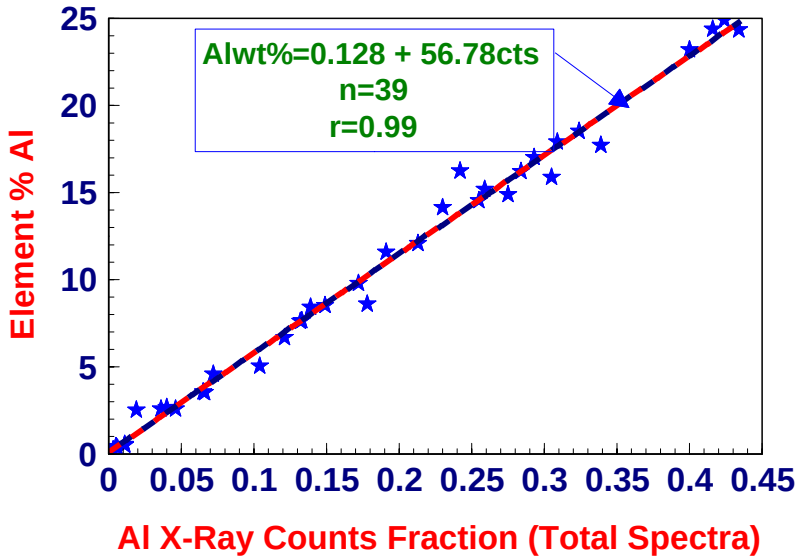

Figure G.2: Aluminium X-ray counts and elemental percent

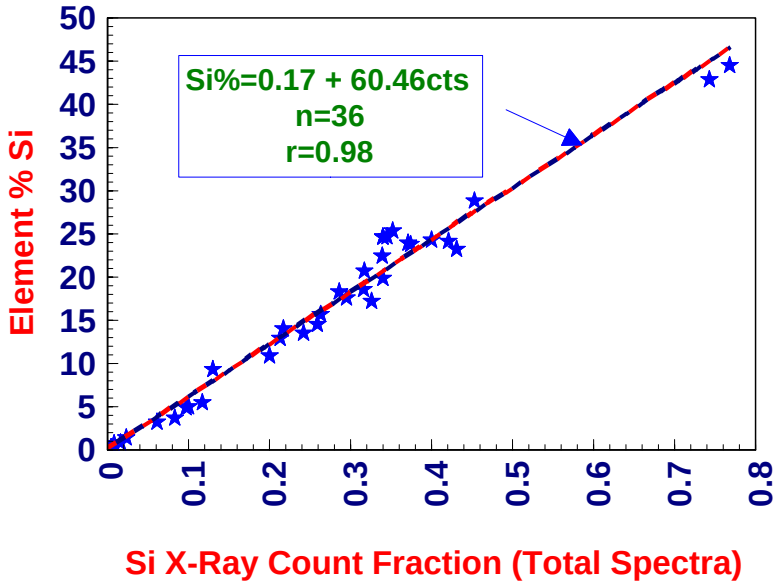

Figure G.3: Silicon X-ray counts and elemental percent

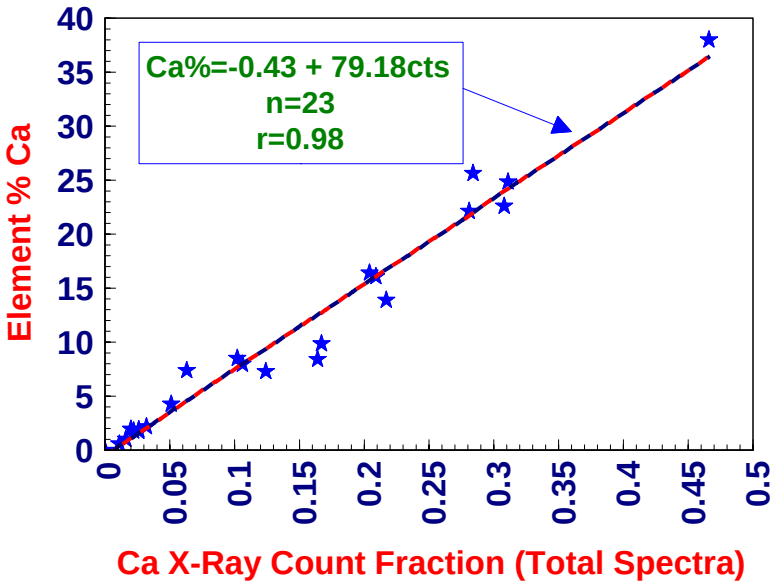

Figure G.4: Calcium X-ray counts and elemental percent

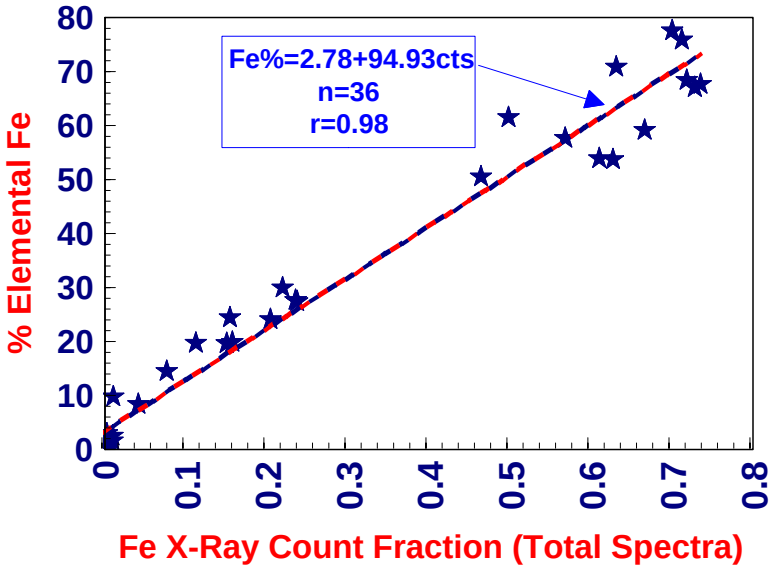

Figure G.5: Iron X-ray counts and elemental percent

Association

Analysed pulverised fuel and fly ash particles are classified into association classes. The definition of an association class is governed by the minerals/phases present in each particle analysed. The total particle area for each association class is computed and the area percent distribution is determined.

Association describes the minerals/phases present for each particle and classifies each particle accordingly. Liberation, described below, is also based on a particle level describes the area-% proportion of a reference mineral in each particle.

The principal focus of this study is to predict the formation of fly ash particles. One approach is to use the elements as tracers and to compare mineral associations in pulverised fuel to that in the fly ash. If the particle is described as kaolinite + coal (common association class) in pulverised fuel, the resultant fly ash could consist of Al-Si-O in similar proportions to Al-Si-O in kaolinite. Alternatively, if the particle is kaolinite+pyrite+coal, then the resultant fly ash composition should be different proportions of Al-Si-Fe-O. Obviously the proportions of Al-Si-Fe-O in the resultant fly ash particle are dependent on the mineral proportions in the original kaolinite+pyrite+coal pulverised fuel particle. The nomenclature used to describe association characteristics of fly ash particles is based on same principles as those used for pulverised fuel, except that the typical fly ash phases are used instead. An example could be quartz+kaolinite. This describes a particle with a remnant quartz grain associated with Al-Si-O (kaolinite) phase.

Describing mineral/phase association is an appropriate method for modelling and predicting fly ash formation processes.

Liberation

The liberation characteristics of an individual mineral are quantified by computing the area-% of the reference mineral in each particle analysed. Depending on the area% of the reference mineral, the particles are classified into eleven classes. These classes are grouped into intervals of 10 area-%, with the first interval

starting at 0 to 10 area% and the last being 100 area%. The defined classes are thus:
0-10, 10-20, 20-30, 30-40, 40-50, 50-60, 60-70, 70-80, 80-90,90-100 and finally 100 area-%.

The microlithotype classification (Table E2), is based on volume-% mineral matter in the particle and not on the area%. The defined classification ranges are <20 volume%, 20 to 60 volume% and >60 volume%. Vitrite, intermediate, semi-fusinite/fusinite and inertodetrinite have <20 volume% mineral matter (MM), arbargillite, carbosilicate, carboankerite and carbopolyminerite have between 20 to 60 volume% MM and minerite >60 volume-% MM. Relative to the liberation classes, included minerals will be classified in the <20 area% classes and excluded/adventitious or free in the >60 area% classes.

The cumulative liberation yield (CLY) is the numerical method of expressing liberation characteristics. As the name states, the CLY is the cumulative mass% distribution for the respective liberation classes, described above. The mass% proportion for each liberation class is computed by using the total area (in μm^2) for that class multiplied by the density of the reference mineral. An example of CLY liberation plot is described in Figure G.6.

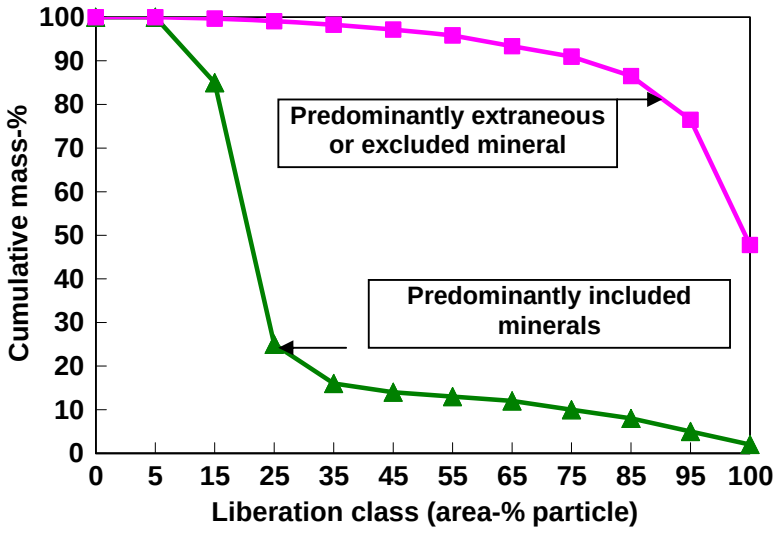

Figure G.6: Example of a cumulative liberation plot for individual minerals

APPENDIX H: GLASS DENSITY CALCULATION

Huggins and Sun (In: Varshneya, 1994) developed a method to calculate the density of glass based on the oxide components in the glass. This method is adopted to calculate the density of fly ash particles using the ASCAN oxide-% proportion (as calculated using the algorithms described in appendix G). For a detailed description of the method refer to Fundamentals of Inorganic glass. (Varshneya, 1994)

The Huggins and Sun method:

f_m is the weight fraction of each oxide component in the fly ash. The first step is to obtain the $\sum s_m f_m$ where s_m is the ratio of the number of oxygen atoms in the molar formula to the total formula weight of the oxide component. These values for the typical oxides found in fly ash are summarised in Table H.1

Table H.1: Factors for calculation of Density (after Huggins and Sun), adapted from Fundamentals of Inorganic Glass (Varshneya, 1994).

		Specific Volume (1g) v_m			***v^i_m***
		A	**B**	**C**	**D**
Component	**S_mx10^2**	**N_{si}=0.27-0.345**	**N_{si}=0.345-0.40**	**N_{si}=0.40-0.435**	**N_{si}=0.435-0.50**
Na_2O	1.6131	0.373	0.349	0.324	0.281
K_2O	1.0617	0.390	0.374	0.357	0.329
MgO	2.48	0.397	0.360	0.322	0.256
CaO	1.7832	0.285	0.259	0.231	0.184
Al_2O_3	2.9429	0.462	0.418	0.373	0.294
Fe_2O_3	1.878	0.282	0.255	0.225	0.176
SiO_2	3.330	0.4063	0.4281	0.4409	0.4542
TiO_2	2.5032	0.319	0.282	0.243	0.176

Calculate the number of gram atoms of silicon per gram atom of oxygen (N_{si}) in the glass:

$$N_{Si} = \left(\frac{f_{si}}{60.06 * \sum Smfm} \right) \qquad \textbf{H.1.}$$

Compare the computed Nsi to Table E.1 and determine the specific volume (v_m) of 1.0g of the component oxide. The total specific volume of the glass (v) is obtained by:

$$v = \sum v_m f_m \qquad \textbf{H.2.}$$

And the density (ρ, g/cm^3) of the glass is the reciprocal of total specific volume:

$$\rho = \frac{1}{v} \qquad \textbf{H.3.}$$

The formula is applied to determine the density of glasses and not necessarily the density of known minerals that occur in fly ash. Such minerals are quartz, mullite, hematite, anorthoclase and magnetite. These densities are derived from literature (Deer et al., 1965).

APPENDIX I: PARTICLE SIZE DISTRIBUTION

Pulverised Fuel

The particle size distribution of probe pulverised fuel and April 2000 bulk sample taken are summarised in Table I.1

Table I.1: Particle size distribution of pulverised fuel

Date	Hole	Depth (m)	+75µm	-75+38µm	-38µm	%-75 µm
06-Apr-99	1	0	26.86	15.14	58.00	73.14
07-Apr-99	1	0.5	30.85	22.94	46.20	69.15
08-Apr-99	1	1	31.40	14.60	53.90	68.60
20-Apr-99	1	1.5	38.13	14.09	47.77	61.87
09-Apr-99	1	2	39.46	24.32	36.22	60.54
18-May-99	2	0	33.22	20.96	45.82	66.78
20-May-99	2	0.5	30.79	21.65	47.57	69.21
27-May-99	2	1	23.01	19.15	57.84	76.99
27-May-99	2	1.5	24.72	19.95	55.32	75.28
01-Jun-99	2	2	34.08	22.32	43.58	65.92
24-Sep-99	3	0	37.84	24.81	37.35	62.16
19-Aug	3	0.5	28.69	23.70	47.61	71.31
03-Feb-00	3	1	28.32	23.75	47.93	71.68
17-Feb-00	3	1.5	32.60	26.60	40.80	67.40
17-Feb-00	3	2	32.60	26.60	40.80	67.40
18-Apr-00	4	0	33.75	23.80	42.45	66.25
20-Apr-00	4	0.5	27.21	27.77	45.02	72.79
20-Apr-00	4	1	27.21	27.77	45.02	72.79
02-May-00	4	1.5	27.77	27.10	45.13	72.23
Average			**30.97**	**22.47**	**46.54**	**69.03**
April 2000			**37.34**	**22.44**	**39.82**	**62.26**

Fly ash

The particle size distribution of the fly ash sampled by water-cooled suction pyrometer and April 2000 bulk cegrit sample are summarised in Table I.2.

Table I.2: Particle size distribution of fly ash

Date	Hole	Depth	+75µm	-75+38µm	-38µm	%-75 µm
06-Apr-99	1	0	13.44	32.08	54.48	86.56
07-Apr-99	1	0.5	26.21	28.80	44.99	73.79
08-Apr-99	1	1	23.04	21.94	55.02	76.96
20-Apr-99	1	1.5	23.55	39.09	37.36	76.45
09-Apr-99	1	2	35.82	18.64	45.54	64.18
18-May-99	2	0	18.23	26.54	55.23	81.77
20-May-99	2	0.5	37.71	25.76	36.53	62.29
27-May-99	2	1	23.38	23.65	52.97	76.62
27-May-99	2	1.5	30.10	17.82	52.08	69.90
01-Jun-99	2	2	26.26	39.07	34.66	73.74
24-Sep-99	3	0	14.87	14.28	70.85	85.13
19-Aug	3	0.5	10.99	9.97	79.04	89.01
03-Feb-00	3	1	16.88	9.55	73.58	83.12
17-Feb-00	3	1.5	23.45	8.04	68.51	76.55
17-Feb-00	3	2	26.35	7.74	65.91	73.65
18-Apr-00	4	0	4.39	7.76	87.85	95.61
20-Apr-00	4	0.5	1.42	1.67	96.91	98.58
20-Apr-00	4	1	13.59	8.27	78.14	86.41
02-May-00	4	1.5	23.57	3.80	72.64	76.43
Average (Fly)			20.70	18.13	61.17	79.30
Cegrit Sample – April 2000			26.31	29.66	44.03	73.69

APPENDIX J: PETROGRAPHIC RESULTS

Maceral Analysis

The volume% maceral distribution of the +75 and the -75+38 µm size fraction are summarised in Table J.1 and J.2, respectively. For a detailed description of maceral definitions and characteristics refer to Table E.1.

Table J.1: Volume-% maceral distribution of the +75 µm sized fraction

Hole	Depth	Vitrinite	Liptinite	Inertinite Maceral Group						TOTAL REACTIVE
				RSF	ISF	FUS	MIC	RINT	IINT	
1	0	37	6.8	4.6	18.2	3	0.4	16	14	64.4
1	0.5	36	6.4	5.4	19.6	2.6	0.2	17.8	12	65.6
1	1	36.8	7	8.8	22.8	0.8	0.2	15.6	8	68.2
1	1.5	37.6	7.4	8.2	21	3.4	0.4	13.2	8.8	66.4
1	2	37.4	6.2	7.8	21	1.4	0.4	17	8.8	68.4
2	0	32.2	8.4	8.8	20.2	1.8	1.2	17.2	10.2	66.6
2	0.5	34.8	9.4	7.6	19.2	0.6	0.2	18.8	9.4	70.6
2	1	37	10	9	20.4	0.8	0.2	14.2	8.4	70.2
2	1.5	35.8	11.4	7.2	19	1.6	0.2	14.8	10	69.2
2	2	37.8	6.4	8.6	21.4	0	0.4	17	8.4	69.8
3	0	36	8	8	22.4	2	0.6	14.2	8.8	66.2
3	0.5	31.4	6.4	11	17.4	3	0.6	20.8	9.4	69.6
3	1	38.8	7.2	8.4	21.6	0	0.6	18	5.4	72.4
3	1.5	39	8	5.2	17.8	2.8	0.4	18.2	8.6	70.4
4	0	40	7.6	11.8	20.2	1.6	0.4	11.4	7	70.8
4	0.5/1	38	8.4	10	22.8	1	0.4	12.6	6.8	69.0
4	1.5	38.2	7.4	10.6	22.0	2.2	0.6	14.4	4.6	70.6
Average		**36.7**	**7.8**	**8.3**	**20.4**	**1.7**	**0.4**	**15.9**	**8.7**	**68.7**

Table J.2: Volume-% maceral distribution in the -75+38 µm sized fraction.

Hole	Depth	Vitrinite	Liptinite	Inertinite Maceral Group						TOTAL REACTIVE
				RSF	ISF	FUS	MIC	RINT	IINT	
1	0	33	4.8	9	23.6	0.8	1	18.4	9.4	65.2
1	0.5	32.2	6.8	9.2	23.8	0.4	0.4	18.8	8.4	67.0
1	1	34.2	4.4	9.2	24.2	1.2	0	17.8	9	65.6
1	1.5	35.4	5.6	9.4	24.4	0.4	0.2	18.6	6	69
1	2	27.4	4	10	26.2	0.2	0.2	22	10	63.4
2	0	34.8	6.4	9	23.8	0.6	0.2	17.2	8	67.4
2	0.5	33	5.8	10	25.8	0.4	0.4	16	8.6	64.8
2	1	33.8	8.4	10	25.8	0.4	0.4	15.4	5.8	67.6
2	1.5	33.2	7.2	13.8	25.6	0.6	0	14.4	5.2	68.6
2	2	36	6.6	8.6	26	1.4	0.2	12	6.4	63.2
3	0	31	5.8	10.4	27	0.6	0.4	16.6	8.2	63.8
3	0.5	31	5.8	11	20.2	2.6	0.4	21	8	68.8
3	1	35.2	6.6	9.2	24	0.4	0	16.8	7.8	67.8
3	1.5	31.8	7.6	8.8	23	0.6	0.6	21.4	6.2	69.6
4	0	41.8	5.2	7.2	24.8	1.2	0.2	14.4	5.2	68.6
4	0.5/1	33.6	6.4	8.8	22.8	1.4	0.8	18	8.2	66.8
4	1.5	39.2	7.2	6.2	24	2	0.4	16.6	4.4	69.2
Average		**33.9**	**6.2**	**9.4**	**24.4**	**0.9**	**0.3**	**17.4**	**7.3**	**66.9**

RSF: Reactive semi-fusinite, **ISF:** Inert semi-fusinite, **FUS:** Fusinite,

MIC: Micrinite, **RINT:** Reactive inertodetrinite, **IINT:** Inert inertodetrinite

Total Reactive : Sum of vitrinite+liptinite+RSF+RINT

Microlithotype Analysis

The volume% microlithotype distribution for the +75 and the -75+38 µm sized fractions are summarised in Tables J.3 and J.4, respectively. For a detailed description of the microlithotype definitions and characteristics refer to Table E.2.

Table J.3: Volume-% microlithotype distribution of the +75 µm sized fraction

Hole	Depth	Vitrite	Intermedia	Sem/Fus	Inertod	CE	TE	DE	Liptinite	Carbominerite
1	0	20.4	18.2	18.8	20.6	1	0.4	2	0	18.6
1	0.5	20	20.4	17.6	22.2	0.4	1	2	0	16.4
1	1	21.8	20.6	21	20.2	0.8	0.6	2.2	0.4	12.4
1	1.5	23.2	18.4	21.2	22	1.2	0.6	1.4	0	12
1	2	16.2	17.8	18.2	24.6	0.6	1.2	1	0.4	20
2	0	16	23	18.4	19.2	0.8	0.6	2.6	0.2	19.2
2	0.5	19	23.4	20.4	16.8	0.8	1.6	1.6	0.4	16
2	1	19.6	26.2	19	16.4	0.4	0.4	3.4	0	14.6
2	1.5	19.2	23.6	17.6	23.4	0.2	0.8	3.2	0.4	11.6
2	2	21.8	21.4	24.4	17.2	0.2	0.6	1.6	0.4	12.4
3	0	20	23.4	18.4	19.4	0.2	0.4	1.6	0	16.6
3	0.5	15.2	19.6	21	22.8	0.4	0.4	2.4	0	18.2
3	1	19.2	26	21.4	14.4	1.4	1.6	2	0	14
3	1.5	23.2	18.2	21	19.4	1	0.6	2.2	0.4	14
4	0	23.4	20.4	28	14	0.4	0.6	1.6	0	11.6
4	0.5/1	20.8	22.4	18.8	19.2	0.4	0.2	2.2	0.2	15.8
4	1.5	24.4	18.6	18.8	19.4	1.2	0.4	2.2	0	15
Average		20.2	21.27	20.24	19.48	0.67	0.71	2.07	0.16	15.20

Table J.4: Volume-% microlithotypes distribution of the –75+38 µm sized fractions

Hole	Depth	Vitrite	Intermedia	Sem/Fus	Inertod	CE	TE	DE	Liptinite	Carbominerite
1	0	22.4	9.8	29.2	20.2	0.4	0.2	1.6	0	15.8
1	0.5	21.2	9.4	22.4	27.6	0.8	0.4	2.2	0	16
1	1	26.8	8.2	26.2	22.8	0.2	0	2	0	14
1	1.5	24.4	10	30.6	18.8	0.2	0.2	2.8	0	13
1	2	20.2	6.8	33.2	21.8	0.6	0.8	3	0.2	13.6
2	0	26.2	6.6	33.2	17.8	0.2	0	3.6	0	12.4
2	0.5	22.4	12.6	33	17.2	0.2	0.2	2.2	0.2	11.8
2	1	21.8	13.6	35.6	11.4	0.6	0.2	3.8	0.4	12.6
2	1.5	24.2	13	42.6	8.4	1.2	0.4	2.6	0.8	6.8
2	2	24	12.8	38.4	13.6	0.4	0	2.4	0.4	8.6
3	0	19.2	16.4	29.4	15.6	0.2	0.2	3.8	0.2	15
3	0.5	16.6	13.2	43	10.8	0	0.2	1.8	0.2	14.4
3	1	19	18.6	37.2	7.8	1.2	0.4	1	0.2	14.6
3	1.5	20.4	14.2	29	18.4	0.6	0.6	2.8	0.6	13.4
4	0	30.4	11	33.6	12.2	0	0.4	1.6	0	10.6
4	0.5/1	23.6	15.6	36.6	10	1.2	0.2	2.2	0.6	10
4	1.5	26	14.2	35.2	9.2	0.4	0.2	1.8	0.2	12.8
Average		22.87	12.12	33.44	15.51	0.49	0.27	2.42	0.24	12.67

Intermedia: Intermediate, **Sem/Fus**: SemiFusinite/Fusinite, **Inertod**: Interdodetrinite

CE : Clarite, **TE**: Trimacerite, **DE**: Durite

Petrographic mineral matter classification

The percent distribution of the carbominerite/microlithotype particle types for the +75 µm and -75+38 µm sized fractions are summarised in Table J.5 and J.6, respectively. For a full explanation of the classification used refer to Table E3.

Table J.5: Percent carbominerite/microlithotype particle type distribution in the +75 µm sized fraction. (Vit: vitrite, Int: Intermediate, SF: semifusinite/fusinite, IN:inertodetrinite, Free:minerite (>60% mineral matter).

Hole	Depth	Carboargiilite					Carbosilicate					Carbopyrite					Carboankerite					Carbopolyminerite				
		Vit	Int	SF	IN	Free	Vit	Int	SF	IN	Free	Vit	Int	SF	IN	Free	Vit	Int	SF	IN	Free	Vit	Int	SF	IN	Free
1.0	0.0	6.5	4.3	0.0	41.9	3.2	0.0	2.2	0.0	1.1	20.4	5.4	0.0	0.0	0.0	6.5	1.1	0.0	0.0	1.1	4.3	0.0	0.0	0.0	2.2	0.0
1.0	0.5	6.3	2.5	1.3	46.3	5.0	0.0	0.0	0.0	0.0	17.5	2.5	0.0	0.0	0.0	2.5	0.0	1.3	1.3	3.8	7.5	1.3	1.3	0.0	0.0	0.0
1.0	1.0	4.2	5.6	1.4	56.9	11.1	0.0	0.0	0.0	0.0	9.7	5.6	0.0	0.0	0.0	1.4	0.0	0.0	1.4	1.4	1.4	0.0	0.0	0.0	0.0	0.0
1.0	1.5	3.3	5.0	1.7	51.7	1.7	0.0	0.0	0.0	1.7	15.0	3.3	0.0	0.0	0.0	5.0	0.0	0.0	0.0	3.3	5.0	1.7	0.0	0.0	1.7	0.0
1.0	2.0	6.9	2.3	5.7	54.0	2.3	0.0	0.0	0.0	1.1	6.9	5.7	0.0	0.0	0.0	1.1	0.0	0.0	2.3	1.1	3.4	0.0	2.3	1.1	3.4	0.0
2.0	0.0	2.7	3.6	0.9	45.0	5.4	0.0	0.0	0.0	0.0	15.3	1.8	0.9	0.0	0.0	5.4	0.0	0.0	0.9	0.9	10.8	0.9	0.0	0.0	3.6	1.8
2.0	0.5	3.9	10.4	1.3	57.1	3.9	0.0	0.0	0.0	0.0	7.8	1.3	0.0	0.0	0.0	1.3	0.0	0.0	1.3	1.3	6.5	1.3	2.6	0.0	0.0	0.0
2.0	1.0	5.5	8.2	1.4	60.3	2.7	0.0	0.0	0.0	0.0	8.2	2.7	0.0	0.0	0.0	1.4	0.0	0.0	0.0	2.7	5.5	0.0	0.0	0.0	0.0	1.4
2.0	1.5	3.8	5.8	0.0	38.5	1.9	0.0	0.0	0.0	0.0	19.2	1.9	0.0	0.0	0.0	5.8	0.0	0.0	5.8	3.8	5.8	1.9	0.0	3.8	0.0	1.9
2.0	2.0	8.1	6.5	0.0	54.8	1.6	0.0	0.0	0.0	0.0	9.7	3.2	0.0	0.0	0.0	6.5	0.0	0.0	0.0	1.6	6.5	0.0	0.0	0.0	1.6	0.0
3.0	0.0	9.6	4.8	0.0	43.4	7.2	0.0	0.0	1.2	0.0	10.8	1.2	0.0	0.0	0.0	13.3	1.2	1.2	0.0	0.0	4.8	0.0	1.2	0.0	0.0	0.0
3.0	0.5	6.6	4.4	0.0	44.0	4.4	0.0	0.0	0.0	0.0	11.0	2.2	0.0	0.0	0.0	4.4	0.0	0.0	3.3	4.4	13.2	0.0	0.0	0.0	1.1	1.1
3.0	1.0	14.5	7.2	4.3	43.5	5.8	0.0	0.0	0.0	0.0	0.0	1.4	0.0	1.4	0.0	5.8	0.0	0.0	2.9	1.4	7.2	0.0	0.0	0.0	1.4	2.9
3.0	1.5	5.1	1.3	1.3	50.6	7.6	0.0	0.0	0.0	0.0	8.9	2.5	0.0	0.0	0.0	5.1	0.0	1.3	0.0	6.3	10.1	0.0	0.0	0.0	0.0	0.0
4.0	0.0	3.4	3.4	1.7	50.0	12.1	0.0	0.0	0.0	0.0	13.8	5.2	0.0	0.0	0.0	1.7	0.0	0.0	1.7	1.7	5.2	0.0	0.0	0.0	0.0	0.0
4.0	0.5/1	1.1	5.3	0.0	37.9	9.5	0.0	0.0	0.0	0.0	23.2	1.1	0.0	0.0	0.0	8.4	1.1	1.1	2.1	5.3	4.2	0.0	0.0	0.0	0.0	0.0
4.0	1.5	7.4	3.7	3.7	35.8	8.6	0.0	0.0	0.0	0.0	21.0	3.7	0.0	0.0	0.0	3.7	0.0	0.0	0.0	6.2	6.2	0.0	0.0	0.0	0.0	0.0
Average		5.8	5.0	1.5	47.7	5.5	0.0	0.1	0.1	0.2	12.8	3.0	0.1	0.1	0.0	4.7	0.2	0.3	1.3	2.7	6.3	0.4	0.4	0.3	0.9	0.5

Table J.6: Percent carbominerite/microlithotype particle type distribution in the -75+38 µm sized fraction. (Vit: vitrite, Int: Intermediate, SF: semifusinite/fusinite, IN:inertodetrinite, Free:minerite (>60% mineral matter).

Hole	Depth	Carboargiilite					Carbosilicate					Carbopyrite					Carboankerite					Carbopolyminerite				
		Vit	Int	SF	IN	Free	Vit	Int	SF	IN	Free	Vit	Int	SF	IN	Free	Vit	Int	SF	IN	Free	Vit	Int	SF	IN	Free
1.0	0.0	2.5	2.5	6.3	31.6	13.9	0.0	0.0	0.0	0.0	10.1	2.5	0.0	0.0	0.0	10.1	0.0	2.5	1.3	2.5	11.4	0.0	0.0	0.0	0.0	2.5
1.0	0.5	7.5	7.5	1.3	40.0	2.5	0.0	0.0	1.3	1.3	15.0	2.5	0.0	0.0	0.0	7.5	0.0	3.8	1.3	8.8	0.0	0.0	0.0	0.0	0.0	0.0
1.0	1.0	2.9	0.0	4.3	51.4	1.4	0.0	0.0	0.0	0.0	11.4	4.3	0.0	0.0	0.0	4.3	0.0	0.0	5.7	1.4	12.9	0.0	0.0	0.0	0.0	0.0
1.0	1.5	6.2	4.6	1.5	33.8	4.6	0.0	0.0	0.0	1.5	15.4	3.1	0.0	0.0	0.0	7.7	3.1	0.0	4.6	0.0	12.3	1.5	0.0	0.0	0.0	0.0
1.0	2.0	7.4	1.5	2.9	48.5	2.9	0.0	0.0	0.0	1.5	5.9	2.9	0.0	0.0	0.0	4.4	1.5	0.0	1.5	0.0	11.8	0.0	0.0	0.0	1.5	5.9
2.0	0.0	4.8	0.0	1.6	48.4	6.5	0.0	0.0	0.0	0.0	9.7	3.2	0.0	0.0	0.0	9.7	0.0	0.0	0.0	1.6	14.5	0.0	0.0	0.0	0.0	0.0
2.0	0.5	3.4	3.4	0.0	44.1	8.5	0.0	0.0	0.0	1.7	13.6	1.7	0.0	0.0	0.0	5.1	1.7	0.0	1.7	5.1	8.5	0.0	0.0	0.0	0.0	1.7
2.0	1.0	3.2	1.6	0.0	39.7	3.2	0.0	0.0	0.0	0.0	9.5	4.8	0.0	0.0	0.0	15.9	0.0	0.0	1.6	1.6	14.3	0.0	0.0	0.0	0.0	4.8
2.0	1.5	0.0	0.0	5.9	47.1	0.0	0.0	0.0	0.0	0.0	2.9	5.9	0.0	0.0	0.0	11.8	0.0	0.0	5.9	2.9	17.6	0.0	0.0	0.0	0.0	0.0
2.0	2.0	7.1	0.0	1.8	46.4	5.4	0.0	0.0	0.0	1.8	0.0	1.8	0.0	0.0	0.0	19.6	0.0	0.0	1.8	1.8	12.5	0.0	0.0	0.0	0.0	0.0
3.0	0.0	5.0	2.5	0.0	51.3	10.0	0.0	0.0	0.0	0.0	6.3	2.5	0.0	0.0	0.0	11.3	0.0	0.0	1.3	1.3	8.8	0.0	0.0	0.0	0.0	0.0
3d.0	0.5	2.8	1.4	0.0	58.3	12.5	0.0	0.0	0.0	0.0	5.6	2.8	0.0	0.0	0.0	4.2	0.0	0.0	0.0	5.6	5.6	0.0	0.0	0.0	0.0	1.4
3.0	1.0	10.8	10.8	6.8	44.6	6.8	0.0	0.0	0.0	0.0	4.1	2.7	0.0	0.0	0.0	5.4	0.0	1.4	0.0	1.4	5.4	0.0	0.0	0.0	0.0	0.0
3.0	1.5	6.0	3.0	0.0	59.7	7.5	0.0	0.0	0.0	1.5	1.5	4.5	0.0	0.0	0.0	7.5	1.5	0.0	3.0	3.0	1.5	0.0	0.0	0.0	0.0	0.0
4.0	0.0	1.9	0.0	0.0	45.3	13.2	0.0	0.0	0.0	0.0	5.7	3.8	0.0	0.0	0.0	5.7	0.0	1.9	1.9	3.8	17.0	0.0	0.0	0.0	0.0	0.0
4.0	0.5/1	2.0	0.0	3.9	56.9	15.7	0.0	0.0	0.0	0.0	2.0	3.9	0.0	0.0	0.0	2.0	0.0	0.0	0.0	7.8	5.9	0.0	0.0	0.0	0.0	0.0
4.0	1.5	6.3	1.6	6.3	57.8	15.6	0.0	0.0	0.0	0.0	0.0	4.7	0.0	0.0	0.0	0.0	0.0	0.0	0.0	3.1	4.7	0.0	0.0	0.0	0.0	0.0
Average		4.7	2.4	2.5	47.3	7.7	0.0	0.0	0.1	0.5	7.0	3.4	0.0	0.0	0.0	7.8	0.5	0.6	1.8	3.0	9.7	0.1	0.0	0.0	0.1	1.0

Rank Determination

The +75 µm size fraction of the hole#1 0m, hole#3 0.5m and hole#4 0m were randomly selected for determining the rank of the pulverised fuel. Rank determination is based on the average vitrinite reflectance (RoV% random) from randomly selected vitrinite grains. The +75 µm size fraction was selected to ensure that coarse vitrinite grains could be selected and analysed. For each sample, 100 readings were taken. The vitrinite reflectance distribution is illustrated in Figure J.1.

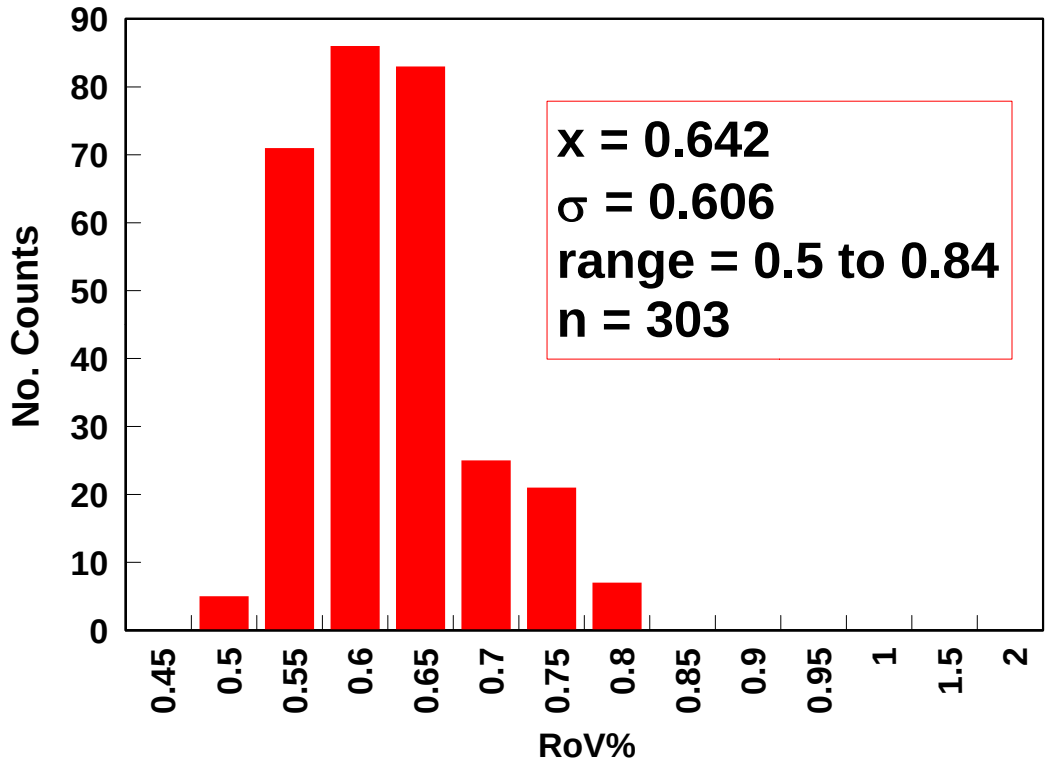

Figure J.1: Vitrinite reflectance variation

Based on the USA classification the coal is classified as high volatile bituminous (after Falcon, (Falcon, 1986)) and based on the International Classification of In-Seam Coals of the Economic Commission for Europe – United Nations the coal is classified as a Medium - Rank C coal (after Pinheiro et al., 2000)

APPENDIX K: PROXIMATE, ULTIMATE AND ASH ELEMENTAL

The ultimate and proximate analysis for the pulverised fuel samples and respective ash elemental analysis are summarised in Tables K.1 and K.2, respectively. The analysis is based on air dried (AR) samples.

Table K.1: Ultimate and proximate analysis

Hole# Depth (m)	Inherent Moisture	Ash	Volatile Matter	Fixed Carbon	Carbon	Hydrogen	Nitrogen	Total_Sulphur	Carbonate	Oxygen	CV
#1 0m	2.6	25.7	23.4	48.3	58.14	2.9	1.27	0.75	1.03	7.61	22.6
#1 0.5	2.9	25.5	23.3	48.3	58.19	2.75	1.27	0.78	0.88	7.73	22.68
#1 1m	2.8	24.4	23.8	49	58.68	2.89	1.31	0.81	1.75	7.36	22.92
#1 1.5	2.8	24.1	23.8	49.3	59.4	2.85	1.3	0.72	1.03	7.8	23.37
#1 2	3.1	24.8	23.4	48.7	58.47	2.69	1.26	0.65	1.04	7.99	22.68
#2 0m	3	25.4	23.1	48.53	58.17	2.81	1.27	0.73	0.65	7.97	22.63
#2 0.5m	2.7	24.2	23.7	49.4	59.13	2.86	1.31	0.84	0.77	8.19	23.22
#2 1m	2.8	24.6	23.8	48.8	58.86	2.93	1.27	0.68	0.87	7.99	23
#2 1.5m	3	24.9	23.9	48.2	58.51	2.83	1.26	0.64	0.57	8.29	22.87
#2 2	2.7	24.2	23.7	49.5	59.43	2.92	1.3	0.87	0.73	7.85	23.24
#3 0.5m	2.9	26.2	22.4	48.5	57.44	2.74	1.25	0.73	0.87	7.87	22.28
#3 1m	2.1	23.8	24.7	49.4	60.4	3.1	1.33	0.85	1.07	7.35	23.9
#3 1.5/2m	3	24.4	23.3	49.3	58.84	2.81	1.3	0.86	0.97	7.82	23.17
#4 0m	2.1	24.2	24.8	48.9	60.48	3.06	1.35	0.92	1.05	6.84	23.77
#4 0.5/1m	2.4	24.6	24.1	48.9	59.54	2.82	1.31	0.75	1.04	7.54	23.39
#4 1.5m	1.7	27.5	23.4	47.4	57.78	2.85	1.26	0.81	0.83	7.27	22.66
Average	**2.66**	**24.91**	**23.66**	**48.78**	**58.84**	**2.86**	**1.29**	**0.77**	**0.95**	**7.72**	**23.02**
Min	**1.70**	**23.80**	**22.40**	**47.40**	**57.44**	**2.69**	**1.25**	**0.64**	**0.57**	**6.84**	**22.28**
Max	**3.10**	**27.50**	**24.80**	**49.50**	**60.48**	**3.10**	**1.35**	**0.92**	**1.75**	**8.29**	**23.90**
Std. Dev.	**0.39**	**0.96**	**0.58**	**0.56**	**0.86**	**0.11**	**0.03**	**0.08**	**0.26**	**0.37**	**0.45**

Table K.2: XRF Ash elemental analysis

Hole# Depth(m)	SiO_2	Al_2O_3	Fe_2O_3	TiO_2	P_2O_5	CaO	MgO	Na_2O	K_2O	SO_3
#1 0m	61.3	23.8	3.42	1.5	0.66	3.85	0.83	0.23	0.74	2.25
#1 0.5m	59.2	24.9	3.63	1.52	0.9	4.08	1.11	0.15	0.77	2.53
#1 1m	60.5	22.7	3.94	1.27	0.76	4.4	1.07	0.17	0.52	3.01
#1 1.5m	60.3	24.9	3.45	1.64	0.53	3.89	1.05	0.27	0.56	2.65
#1 2m	62.3	23.6	3.15	1.3	1.09	4.2	0.99	0.18	0.57	2.54
#2 0m	60.8	25.2	3.27	1.51	1.17	3.45	0.68	0.28	0.51	2.29
#2 0.5m	57.6	27.2	3.84	1.4	0.76	3.85	1.02	0.13	0.5	2.53
#2 1m	60.8	24.9	3	1.86	0.53	4.06	1.1	0.22	0.49	2.81
#2 1.5m	63.3	22.3	3.12	1.51	0.42	3.87	1.12	0.23	0.59	2.69
#2 2m	59.8	25.2	3.99	1.74	0.56	3.12	0.71	0.19	0.51	2.36
#3 0.5m	59.9	26.1	3.21	1.51	0.51	3.54	1.1	0.14	0.64	2.04
#3 1m	60.2	25	3.31	1.71	0.4	3.75	0.78	0.19	0.63	2.51
#3 1.5/2m	60	24.9	3.76	1.06	0.51	3.91	1.01	0.16	0.62	2.33
#4 0m	59.7	24.7	4.83	1.63	0.54	4.02	1.01	0.19	0.82	2.25
#4 0.5/1m	60.5	25	3.38	1.37	0.44	4.18	1.29	0.23	0.62	2.23
#4 1.5m	64	24.4	3.43	1.54	0.31	2.87	0.83	0.15	0.7	1.72
Average	**60.64**	**24.68**	**3.55**	**1.50**	**0.63**	**3.82**	**0.98**	**0.19**	**0.61**	**2.42**
Min	**57.60**	**22.30**	**3.00**	**1.06**	**0.31**	**2.87**	**0.68**	**0.13**	**0.49**	**1.72**
Max	**64.00**	**27.20**	**4.83**	**1.86**	**1.17**	**4.40**	**1.29**	**0.28**	**0.82**	**3.01**
Std. Dev.	**1.55**	**1.18**	**0.45**	**0.20**	**0.25**	**0.40**	**0.17**	**0.05**	**0.10**	**0.31**

APPENDIX L: PULVERISED FUEL CONSTITUENTS

The CCSEM derived mass-% mineral and coal distribution for each hole sampled and each size fraction are summarised in Tables L.1, L.2, L.3. and L.4.

The detailed description of the minerals identifications used in tables L.1 to L.4 are described in the table below:

Table L.1: Description of mineral groups

Table reference	Description
Pyrite	Pyrite is the major mineral. Can include the sulphide minerals pyrrhotite, sphalerite and chalcopyrite
Quartz	Quartz only
Feldspar	Microcline/Orthoclase is the major feldspar. Trace concentrationsof Na-feldspar (albite?) can occur
Illite/Mica	Includes illite and muscovite (mica)
Kaolinite	Kaolinite is the major mineral. Mixed clays and smectite clays could be included
Fe-oxide	Includes hematite or magnetite and tramp metal (derived from mills and processing equipment)
Calcite	Calcite only
Dolomite	Dolomite only
Other carbonates	Includes siderite, ankerite and magnesite
Ti-oxide	Could be rutile or anatse
Other	Any mineral not positively identified
Coal	Organic component of sample. Includes predominately C-bearing phases which can have trace concentrations of the inorganic elements S, Al, Si, Ca, Mg and Ti

Table L.2: Calculate mass% mineral and coal distribution of the total pulverised fuel samples analysed. (The calculation is the individual size fractions mass% distributions weighted by the mass% screened size distribution)

Hole (#) Depth (m)	Pyrite	Quartz	Feldspar	Illite/Mica	Kaolinite	Fe-oxide	Calcite	Dolomite	Other Carbonates	Apatite	Ti-oxide	Other	Coal	Total
#1 0m	1.5	9.0	0.4	0.3	15.6	0.7	1.8	1.2	0.2	0.2	0.1	0.2	68.9	100.0
#1 0.5m	2.9	8.8	0.2	0.5	14.7	0.3	1.1	1.3	0.2	0.1	0.1	0.0	69.8	100.0
#1 1m	3.1	9.6	0.3	0.3	14.7	0.5	1.7	2.4	0.4	0.2	0.1	0.5	66.3	100.0
#1 1.5	0.8	5.9	0.2	0.2	9.6	0.2	0.5	0.5	0.1	0.1	0.1	0.0	81.9	100.0
#1 2m	1.8	10.0	0.2	0.1	11.1	0.4	1.2	1.6	0.3	0.1	0.2	0.4	72.5	100.0
#2 0m	2.7	8.7	0.2	0.3	13.2	0.3	1.0	0.7	0.1	0.1	0.1	0.0	72.6	100.0
#2 0.5m	2.4	8.8	0.3	0.3	17.3	0.4	0.8	1.0	0.2	0.1	0.1	0.1	68.4	100.0
#2 1m	2.5	5.9	0.1	0.1	10.7	0.1	0.8	1.0	0.1	0.0	0.1	0.1	78.5	100.0
#2 1.5m	1.8	10.0	0.2	0.3	16.1	0.6	1.9	1.6	0.2	0.0	0.1	0.1	67.0	100.0
#2 2m	3.5	8.7	0.2	0.2	14.8	0.4	1.2	0.9	0.3	0.1	0.2	0.2	69.3	100.0
#3 0m	3.6	5.8	0.2	0.2	12.4	0.2	0.6	1.1	0.2	0.3	0.0	0.1	75.3	100.0
#3 0.5m	1.0	6.7	0.4	0.3	14.9	0.3	0.8	1.2	0.1	0.1	0.1	0.8	73.3	100.0
#3 1m	2.6	5.6	0.2	0.2	11.4	0.1	1.3	1.2	0.1	0.1	0.3	0.2	76.8	100.0
#3 1.5/2m	3.1	9.6	0.2	0.2	12.8	0.1	1.5	1.5	0.1	0.1	0.1	0.1	70.7	100.0
#4 0m	2.9	8.3	0.7	0.4	11.5	0.6	1.6	1.3	0.3	0.1	0.1	0.0	72.1	100.0
#4 0.5/1m	3.3	9.9	0.1	0.3	9.9	1.1	1.2	1.7	0.3	0.1	0.0	0.0	72.0	100.0
#4 1.5m	1.8	9.6	0.5	0.4	14.8	0.7	0.7	1.6	0.2	0.0	0.0	0.0	69.6	100.0
Average	**2.4**	**8.3**	**0.3**	**0.3**	**13.3**	**0.4**	**1.2**	**1.3**	**0.2**	**0.1**	**0.1**	**0.2**	**72.1**	
Min	**0.8**	**5.6**	**0.1**	**0.1**	**9.6**	**0.1**	**0.5**	**0.5**	**0.1**	**0.0**	**0.0**	**0.0**	**66.3**	
Max	**3.6**	**10.0**	**0.7**	**0.5**	**17.3**	**1.1**	**1.9**	**2.4**	**0.4**	**0.3**	**0.3**	**0.8**	**81.9**	
Std. Dev	**0.8**	**1.6**	**0.2**	**0.1**	**2.3**	**0.3**	**0.4**	**0.4**	**0.1**	**0.1**	**0.1**	**0.2**	**4.1**	

Table L.3: Mass-% mineral and coal distribution in the +75 µm sized fraction of pulverised fuel.

Hole (#) Depth (m)	Pyrite	Quartz	Feldspar	Illite/Mica	Kaolinite	Fe-oxide	Calcite	Dolomite	Other Carbonates	Apatite	Ti-oxide	Other	Coal	Total
#1 0m	1.5	15.2	0.8	0.3	20.1	0.0	2.6	0.9	0.0	0.3	0.2	0.0	57.9	100.0
#1 0.5m	3.0	10.2	0.3	0.4	15.8	0.1	0.6	0.9	0.0	0.0	0.2	0.0	68.4	100.0
#1 1m	1.3	6.3	0.2	0.2	11.3	0.1	0.2	1.2	0.1	0.2	0.0	0.8	78.0	100.0
#1 1.5	0.7	7.1	0.2	0.2	10.9	0.1	0.7	0.5	0.2	0.1	0.0	0.0	79.3	100.0
#1 2m	1.9	11.2	0.2	0.2	12.1	1.1	1.7	1.6	0.5	0.2	0.0	0.0	69.4	100.0
#2 0m	4.1	15.3	0.3	0.3	17.1	1.0	0.0	0.0	0.2	0.7	0.0	0.4	60.6	100.0
#2 0.5m	3.5	10.3	0.4	0.3	16.7	0.1	0.8	0.8	0.2	0.1	0.1	0.1	66.6	100.0
#2 1m	5.4	7.0	0.2	0.1	13.6	0.0	1.0	1.0	0.1	0.1	0.0	0.0	71.4	100.0
#2 1.5m	1.8	10.9	0.3	0.2	13.7	0.2	1.4	1.4	0.1	0.0	0.2	0.5	69.4	100.0
#2 2m	3.8	12.3	0.3	0.2	14.7	0.3	1.6	0.6	0.3	0.2	0.3	0.0	65.3	100.0
#3 0m	1.3	5.0	0.4	0.2	11.0	0.0	0.6	0.7	0.0	0.1	0.0	0.0	80.7	100.0
#3 0.5m	0.5	5.6	0.4	0.2	15.9	0.0	0.3	0.8	0.0	0.2	0.0	0.0	76.0	100.0
#3 1m	3.8	5.6	0.0	0.2	10.4	0.0	0.5	0.6	0.0	0.0	0.2	0.0	78.7	100.0
#3 1.5/2m	5.6	12.3	0.0	0.1	11.2	0.0	0.4	0.5	0.0	0.2	0.0	0.0	69.7	100.0
#4 0m	3.3	7.8	0.6	0.1	9.1	0.3	1.4	1.2	0.1	0.0	0.2	0.0	75.8	100.0
#4 0.5/1m	2.6	9.0	0.1	0.3	10.0	2.3	0.8	1.0	0.2	0.0	0.1	0.0	73.5	100.0
#4 1.5m	1.9	12.2	1.0	0.5	13.9	1.4	0.4	0.5	0.0	0.0	0.0	0.0	68.2	100.0
Average	**2.7**	**9.6**	**0.3**	**0.2**	**13.4**	**0.4**	**0.9**	**0.8**	**0.1**	**0.1**	**0.1**	**0.1**	**71.1**	
Min	**0.5**	**5.0**	**0.0**	**0.1**	**9.1**	**0.0**	**0.0**	**0.0**	**0.0**	**0.0**	**0.0**	**0.0**	**57.9**	
Max	**5.6**	**15.3**	**1.0**	**0.5**	**20.1**	**2.3**	**2.6**	**1.6**	**0.5**	**0.7**	**0.3**	**0.8**	**80.7**	
Std. Dev	**1.5**	**3.3**	**0.3**	**0.1**	**3.0**	**0.7**	**0.7**	**0.4**	**0.1**	**0.2**	**0.1**	**0.2**	**6.5**	

Table L.4: Mass-% mineral and coal distribution in the -75 + 38 µm sized fraction of pulverised fuel.

Hole (#) Depth (m)	Pyrite	Quartz	Feldspar	Illite/Mica	Kaolinite	Fe-oxide	Calcite	Dolomite	Other Carbonates	Apatite	Ti-oxide	Other	Coal	Total
#1 0m	2.2	6.2	0.0	0.2	15.5	0.1	2.5	0.9	0.6	0.2	0.0	0.1	71.6	100.0
#1 0.5m	2.5	8.5	0.2	0.6	17.8	0.0	1.3	0.8	0.0	0.2	0.1	0.4	67.6	100.0
#1 1m	3.1	6.9	0.4	0.1	10.5	0.9	1.4	2.1	0.2	0.5	0.1	0.0	73.7	100.0
#1 1.5	1.3	6.8	0.2	0.3	11.6	0.1	0.5	0.8	0.1	0.1	0.1	0.0	78.0	100.0
#1 2m	0.8	5.5	0.0	0.0	10.0	0.0	0.4	1.7	0.2	0.0	0.0	0.2	81.0	100.0
#2 0m	1.5	4.9	0.1	0.1	11.0	0.0	0.9	0.6	0.0	0.0	0.0	0.2	80.7	100.0
#2 0.5m	2.3	4.9	0.3	0.3	14.7	0.5	1.0	0.8	0.2	0.0	0.0	0.1	74.8	100.0
#2 1m	2.6	6.5	0.1	0.2	13.9	0.1	0.9	1.2	0.1	0.0	0.1	0.2	74.3	100.0
#2 1.5m	2.7	7.5	0.1	0.2	12.8	1.0	1.6	1.8	0.3	0.0	0.1	0.0	71.9	100.0
#2 2m	3.1	4.6	0.0	0.2	12.2	0.1	0.9	1.0	0.2	0.0	0.0	0.1	77.6	100.0
#3 0m	3.5	6.1	0.2	0.2	15.3	0.5	1.2	0.9	0.5	0.0	0.0	0.0	71.5	100.0
#3 0.5m	0.1	7.5	0.5	0.1	14.8	0.0	0.4	1.1	0.0	0.0	0.0	0.1	75.4	100.0
#3 1m	1.8	5.7	0.0	0.2	14.0	0.1	1.9	1.7	0.1	0.0	0.4	0.1	73.8	100.0
#3 1.5/2m	2.0	9.8	0.1	0.2	14.5	0.1	3.1	1.9	0.2	0.0	0.1	0.0	68.2	100.0
#4 0m	5.0	9.5	1.6	0.6	10.9	0.3	1.5	1.2	0.3	0.2	0.1	0.7	68.2	100.0
#4 0.5/1m	2.3	8.4	0.0	0.3	8.9	0.3	0.6	2.2	0.1	0.0	0.0	0.9	76.1	100.0
#4 1.5m	1.5	8.7	0.4	0.5	17.7	0.0	0.7	2.2	0.3	0.0	0.0	0.7	67.2	100.0
Average	2.3	6.9	0.2	0.3	13.3	0.2	1.2	1.4	0.2	0.1	0.1	0.3	73.6	
Min	0.1	4.6	0.0	0.0	8.9	0.0	0.4	0.6	0.0	0.0	0.0	0.0	67.2	
Max	5.0	9.8	1.6	0.6	17.8	1.0	3.1	2.2	0.6	0.5	0.4	0.9	81.0	
Std. Dev	1.1	1.6	0.4	0.2	2.6	0.3	0.7	0.6	0.2	0.1	0.1	0.3	4.3	

Table L.5: Mass-% mineral and coal distribution in the -38 µm sized fraction of pulverised fuel.

Hole (#) Depth (m)	Pyrite	Quartz	Feldspar	Illite/Mica	Kaolinite	Fe-oxide	Calcite	Dolomite	Other Carbonates	Apatite	Ti-oxide	Other	Coal	Total
#1 0m	1.3	6.9	0.2	0.3	13.6	1.2	1.2	1.3	0.1	0.1	0.0	0.0	73.7	100.0
#1 0.5m	3.0	8.1	0.2	0.3	12.3	0.6	1.3	1.8	0.3	0.1	0.1	0.0	71.8	100.0
#1 1m	4.1	12.3	0.3	0.3	17.8	0.6	2.6	3.3	0.5	0.1	0.2	0.2	57.6	100.0
#1 1.5	0.7	4.5	0.1	0.2	8.1	0.3	0.3	0.4	0.1	0.0	0.1	0.1	85.1	100.0
#1 2m	2.3	11.9	0.3	0.2	10.8	0.0	1.3	1.5	0.1	0.1	0.4	1.0	70.2	100.0
#2 0m	2.2	5.8	0.2	0.3	11.3	0.4	1.0	0.8	0.2	0.1	0.0	0.0	77.7	100.0
#2 0.5m	1.8	9.7	0.2	0.2	18.8	0.6	0.7	1.1	0.1	0.1	0.1	0.0	66.6	100.0
#2 1m	1.4	5.2	0.1	0.1	8.4	0.2	0.7	1.0	0.1	0.0	0.1	0.0	82.7	100.0
#2 1.5m	1.5	10.5	0.2	0.4	18.4	0.7	2.2	1.5	0.2	0.0	0.1	0.0	64.2	100.0
#2 2m	3.5	7.9	0.1	0.2	16.2	0.7	1.1	1.2	0.2	0.1	0.1	0.4	68.3	100.0
#3 0m	6.0	6.3	0.0	0.3	11.9	0.2	0.3	1.6	0.1	0.7	0.0	0.3	72.3	100.0
#3 0.5m	1.9	7.0	0.3	0.5	14.4	0.6	1.2	1.5	0.2	0.1	0.2	0.6	70.7	100.0
#3 1m	2.4	5.6	0.5	0.2	10.8	0.1	1.5	1.2	0.1	0.1	0.3	0.3	77.1	100.0
#3 1.5/2m	1.8	7.4	0.3	0.3	12.9	0.1	1.5	1.9	0.1	0.1	0.1	0.2	73.2	100.0
#4 0m	1.4	8.0	0.4	0.3	13.8	0.8	1.8	1.4	0.4	0.0	0.1	0.0	71.4	100.0
#4 0.5/1m	4.3	11.5	0.1	0.3	10.5	0.4	1.9	1.7	0.4	0.3	0.0	0.1	68.6	100.0
#4 1.5m	2.4	8.3	0.2	0.3	10.3	0.1	0.8	0.9	0.2	0.0	0.0	0.0	76.5	100.0
Average	2.5	8.1	0.2	0.3	13.0	0.5	1.3	1.4	0.2	0.1	0.1	0.2	72.2	100.0
Min	0.7	4.5	0.0	0.1	8.1	0.0	0.3	0.4	0.1	0.0	0.0	0.0	57.6	
Max	6.0	12.3	0.5	0.5	18.8	1.2	2.6	3.3	0.5	0.7	0.4	1.0	85.1	
Std. Dev	1.3	2.4	0.1	0.1	3.3	0.3	0.6	0.6	0.1	0.2	0.1	0.3	6.6	

APPENDIX M: MINERAL LIBERATION – PULVERISED FUEL

The Cumulative Liberation Yield (CLY) plots for the individual minerals and corresponding data is summarised. For the individual minerals, the data is the CLY plots for the individual size fractions. This data represent the average liberation characteristic for all the holes sampled. The “total” CLY curve in these plots represents the weighted average of the size fractions using the particle size distribution as the weighting factor (refer to Figure 5.3).

The liberation categories, which depicted in the CLY plots, are based on the microlithotype classification. These classes are:

- Included : Mineral of interest accounts for <20 area% in the particle and the remaining 80 to 100 area% is predominately “coal” (organic component) and other minerals. The microlithotype classes, which are comparable to the this liberation class, are vitrite, intermediate, semi-fusinite/fusinite, intermediate and inertodetrinite
- Middling : The mineral of interest accounts for between 20 to 60 area% and the remaining 40 to 80 area-% is predominately “coal” (organic component) and other minerals. The middling class is analogous to the carbominerite microlithotype.
- Excluded/Free : The mineral of interest accounts for >60 area% in the particle and the remaining particle is predominately “coal” (organic component). Minerite microlithotype comparable to the excluded/free liberation class

Table M.1: Kaolinite mass-% liberation, cumulative liberation yield and cumulative liberation class by size fraction and weighted "total" across all size fractions.

Liberation Data - Mass-%

Lib. Class	+75	-75+38	-38	Total
0	0.0	0.0	0.0	0.0
5	18.8	17.8	7.0	13.1
15	18.5	15.3	8.1	12.9
25	16.4	13.3	7.7	11.6
35	10.7	12.1	8.0	9.8
45	8.6	8.9	5.5	7.2
55	8.1	8.0	11.4	9.6
65	7.1	7.9	11.7	9.4
75	4.8	7.3	10.9	8.2
85	3.2	6.9	14.5	9.3
95	3.8	2.5	4.4	3.8
100	0.0	0.0	10.9	5.1
Total	100.0	100.0	100.0	100.0
CLY				
Lib. Class	+75	-75+38	-38	Total
0	100.0	100.0	100.0	100.0
5	100.0	100.0	100.0	100.0
15	81.2	82.2	93.0	86.9
25	62.7	66.9	85.0	74.0
35	46.3	53.6	77.3	62.4
45	35.6	41.5	69.3	52.6
55	27.0	32.6	63.8	45.4
65	18.9	24.6	52.4	35.8
75	11.8	16.7	40.7	26.4
85	7.0	9.4	29.9	18.2
95	3.8	2.5	15.3	8.9
100	0.0	0.0	10.9	5.1

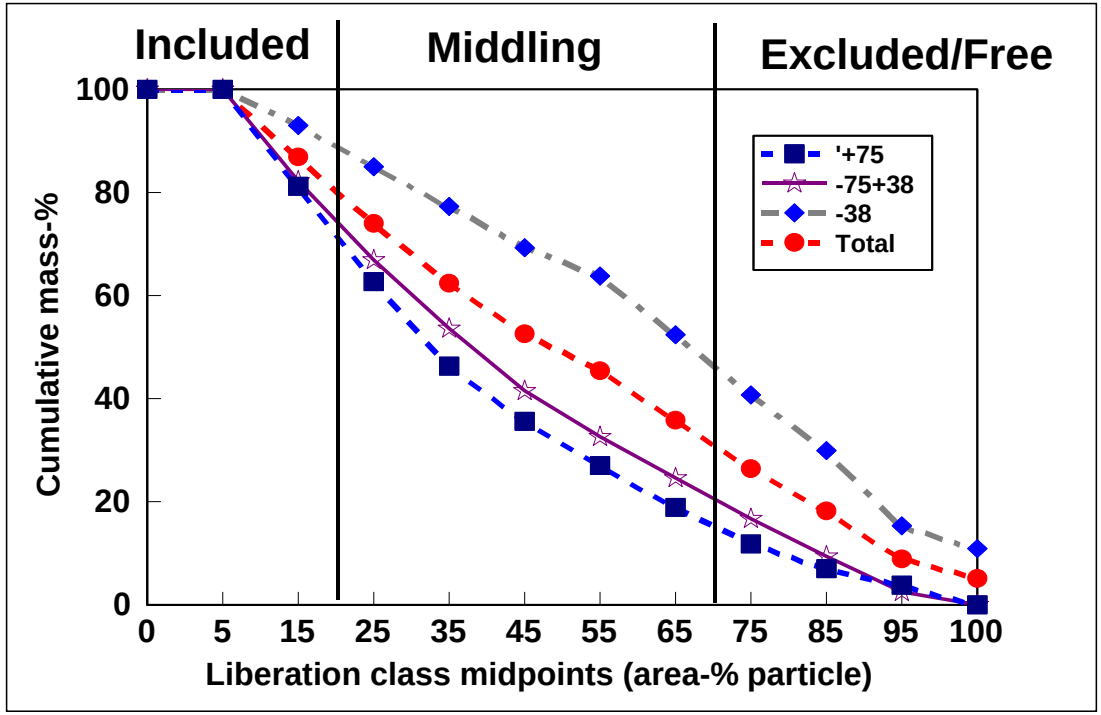

Table M.2: Quartz mass-% liberation, cumulative liberation yield and cumulative liberation class by size fraction and weighted "total" across all size fractions.

Liberation Data - Mass-%

Lib. Class	+75	-75+38	-38	Total
0	0.0	0.0	0.0	0.0
5	17.7	17.5	5.3	11.9
15	7.2	10.2	4.6	6.7
25	4.4	8.0	4.4	5.2
35	3.0	5.7	6.3	5.2
45	1.7	5.1	3.2	3.2
55	4.1	6.0	10.6	7.5
65	4.0	5.3	10.2	7.2
75	6.2	10.2	17.8	12.5
85	11.9	12.8	16.3	14.1
95	38.9	17.0	7.6	19.4
100	1.0	2.0	13.7	7.1
Total	100.0	100.0	100.0	100.0
CLY				
Lib. Class	+75	-75+38	-38	Total
0	100.0	100.0	100.0	100.0
5	100.0	100.0	100.0	100.0
15	82.3	82.5	94.7	88.1
25	75.2	72.2	90.1	81.5
35	70.8	64.2	85.7	76.3
45	67.8	58.5	79.4	71.1
55	66.1	53.4	76.2	67.9
65	62.0	47.4	65.6	60.4
75	58.0	42.0	55.4	53.2
85	51.7	31.8	37.6	40.7
95	39.9	19.0	21.3	26.6
100	1.0	2.0	13.7	7.1

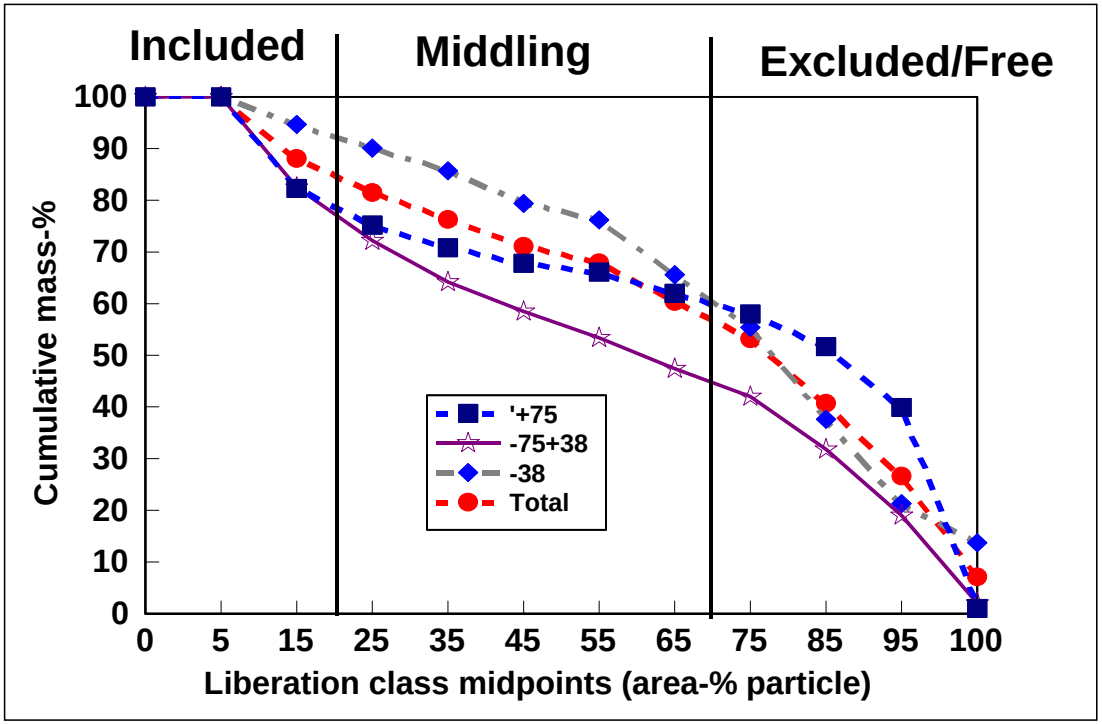

Table M.3: Carbonate mass-% liberation, cumulative liberation yield and cumulative liberation class by size fraction and weighted "total" across all size fractions.

Liberation Data

Lib. Class	+75	-75+38	-38	Total
0	0.0	0.0	0.0	0.0
5	17.5	8.9	3.1	8.8
15	10.7	8.0	3.6	6.8
25	11.5	2.3	4.3	6.1
35	7.9	7.9	3.8	6.0
45	4.9	2.2	4.7	4.2
55	6.8	7.9	8.6	7.9
65	7.3	7.4	12.5	9.7
75	5.8	8.6	10.4	8.6
85	6.3	13.9	24.1	16.3
95	20.3	29.3	16.6	20.6
100	1.0	3.6	8.4	5.1
Total	100.0	100.0	100.0	100.0
CLY				
Lib. Class	+75	-75+38	-38	Total
0	100.0	100.0	100.0	100.0
5	100.0	100.0	100.0	100.0
15	82.5	91.1	96.9	91.2
25	71.8	83.1	93.4	84.4
35	60.4	80.9	89.0	78.3
45	52.5	73.0	85.2	72.3
55	47.5	70.8	80.6	68.1
65	40.7	62.9	72.0	60.3
75	33.4	55.5	59.5	50.5
85	27.6	46.9	49.1	42.0
95	21.3	33.0	25.0	25.6
100	1.0	3.6	8.4	5.1

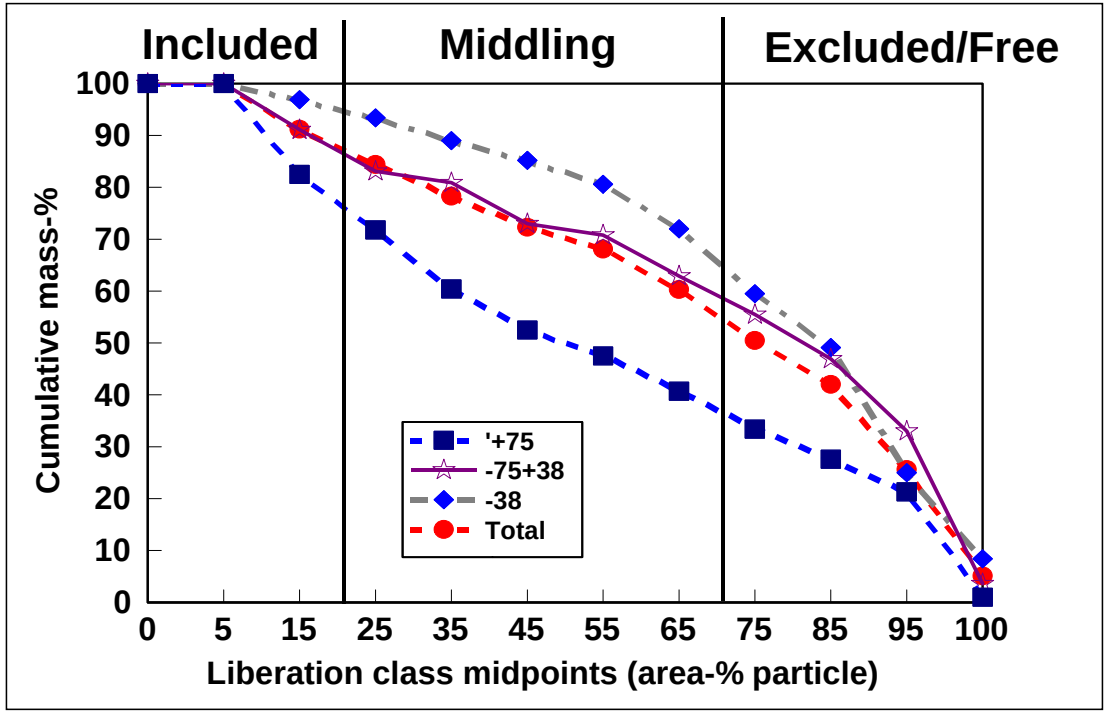

Table M.4: Pyrite mass-% liberation, cumulative liberation yield and cumulative liberation class by size fraction and weighted "total" across all size fractions.

Liberation Data

Lib. Class	+75	-75+38	-38	Total
0.0	0.0	0.0	0.0	0.0
5.0	3.0	3.0	2.7	2.8
15.0	1.5	2.0	1.1	1.4
25.0	1.2	2.8	2.6	2.2
35.0	1.9	2.2	2.5	2.3
45.0	0.0	3.9	2.1	1.8
55.0	3.8	5.2	6.5	5.4
65.0	13.1	7.0	6.5	8.7
75.0	15.4	18.3	20.9	18.6
85.0	26.9	15.8	28.3	25.1
95.0	31.6	38.5	17.6	26.6
100.0	1.7	1.3	9.2	5.1
Total	100.0	100.0	100.0	100.0
CLY				
Lib. Class	+75	-75+38	-38	Total
0.0	100.0	100.0	100.0	100.0
5.0	100.0	100.0	100.0	100.0
15.0	97.0	97.0	97.3	97.2
25.0	95.5	95.0	96.2	95.7
35.0	94.3	92.2	93.6	93.5
45.0	92.4	90.0	91.1	91.3
55.0	92.4	86.1	89.0	89.4
65.0	88.6	80.9	82.5	84.0
75.0	75.5	73.9	76.0	75.4
85.0	60.1	55.6	55.1	56.8
95.0	33.3	39.8	26.8	31.7
100.0	1.7	1.3	9.2	5.1

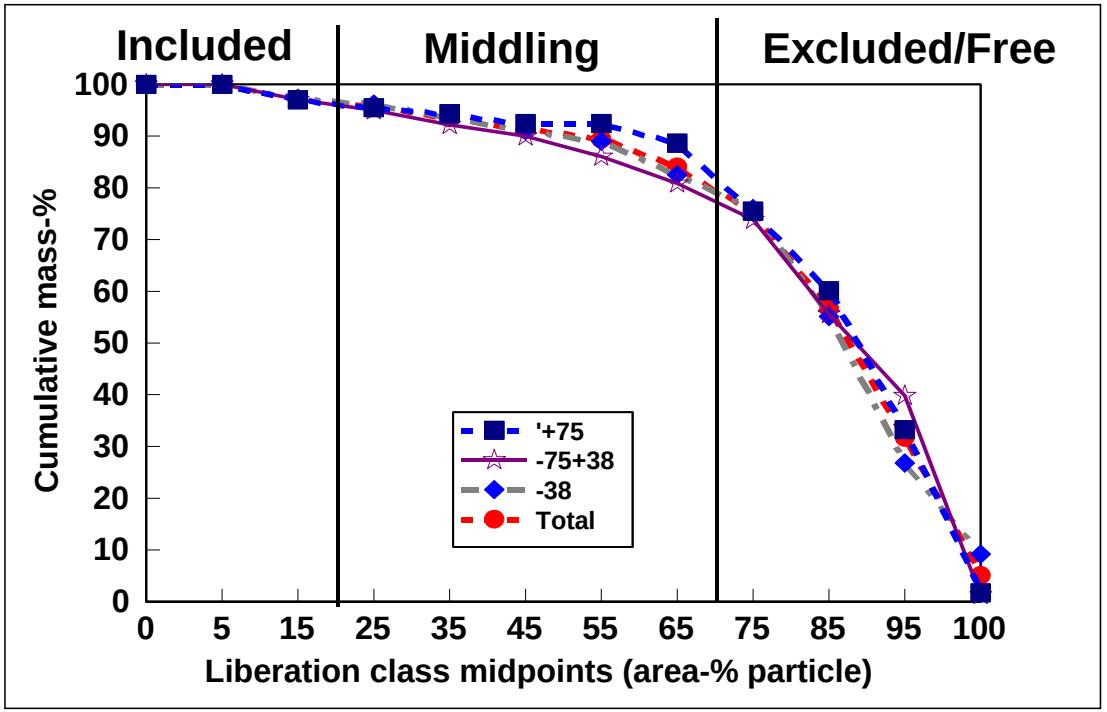

Table M.5: Coal mass-% liberation, cumulative liberation yield and cumulative liberation class by size fraction and weighted "total" across all size fractions.

Liberation Data

Lib. Class	+75	-75+38	-38	Total
0	0.0	0.0	0.0	0.0
5	0.3	0.2	0.2	0.2
15	0.5	0.4	0.7	0.6
25	0.4	0.7	1.0	0.8
35	0.6	0.5	1.1	0.8
45	0.9	0.9	0.8	0.8
55	1.7	1.8	1.8	1.8
65	3.2	2.6	1.8	2.4
75	5.8	4.3	2.3	3.8
85	14.2	10.9	5.3	9.3
95	44.6	38.0	15.6	29.6
100	27.8	39.5	69.4	49.8
Total	100.0	100.0	100.0	100.0
CLY				
Lib. Class	+75	-75+38	-38	Total
0	100.0	100.0	100.0	100.0
5	100.0	100.0	100.0	100.0
15	99.7	99.8	99.8	99.8
25	99.3	99.4	99.1	99.2
35	98.8	98.7	98.1	98.4
45	98.2	98.1	97.0	97.6
55	97.3	97.2	96.2	96.8
65	95.7	95.4	94.4	95.0
75	92.5	92.9	92.6	92.6
85	86.6	88.5	90.3	88.7
95	72.4	77.6	85.0	79.4
100	27.8	39.5	69.4	49.8

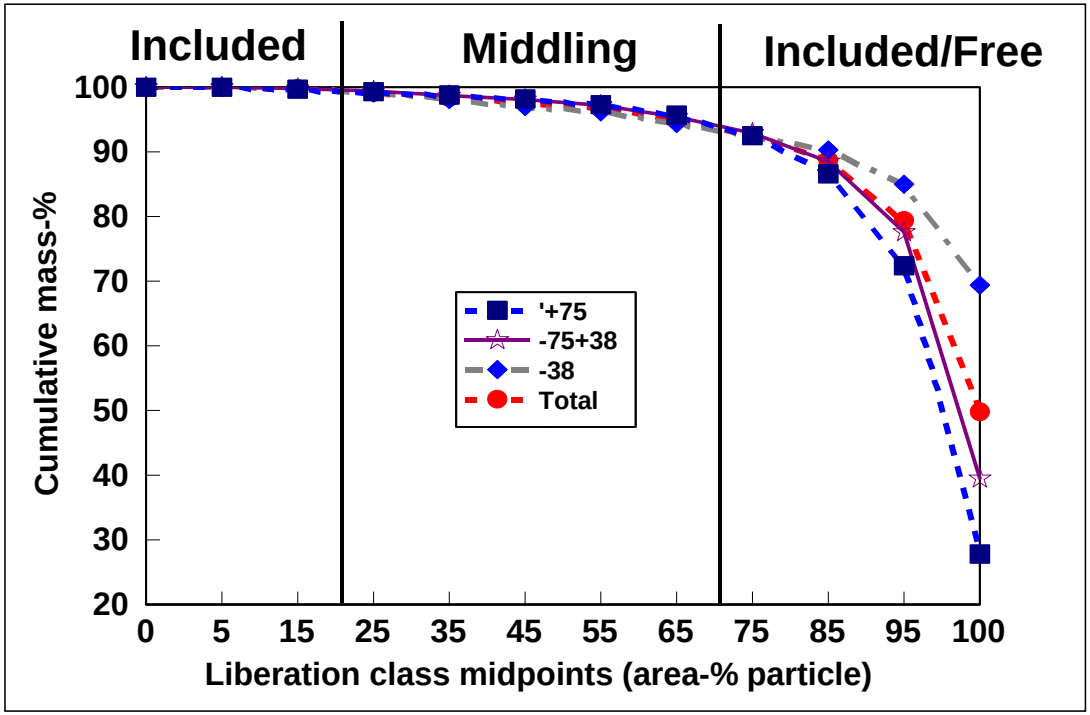

APPENDIX N: FLY ASH MASS-% PROPORTION

The CCSEM derived mass% mineral and coal distribution for each hole sampled and each size fraction are summarised in Tables N.2, N.3, N.3 and N.4, respectively.

The detailed description of the minerals identifications used in tables N.1 to N.4 are described in the table below:

Table N.1 : Fly ash phase description

Fly Ash Phase`	Elemental Composition	Original source
Carbonate	Ca-oxide, Ca-Mg-oxide and Mg-oxide with minor C	Incomplete transformation of calcite and dolomite
Ca/Mg-oxide	Ca-oxide, Ca-Mg-oxide, Mg-oxide	Reaction products of calcite and dolomite transformation
Kaolinite	Al-Si-O with variable Al/Si compositions	Transformation products of kaolinite (metakaolinite, mullite and silicon spinel)
Kaolinite(pyrite, carbonate)	Al-Si-Fe-Ca-Mg-O, Al-Si-Fe-Ca-O, Al-Si-Fe-Mg-O	Interaction of pyrite, carbonate and kaolinite
Kaolinite(carbonate)	Al-Si-Ca-Mg-O, Al-Si-Ca-O, Al-Si-Mg-O	Interaction between calcite/dolomite and kaolinite
Kaolinite (pyrite)	Al-Si-Fe-O	Interaction between kaolinite and pyrite/Fe-oxide
Kaolinite (K,Ti)	Al-Si-Ti-K-O	Interaction between kaolinite, illite/mica and or feldspar
Orthoclase	Al-Si-K-O (Al, Si and K proportions similar to orthoclase	Orthoclase (feldspar)
Quartz60Kaol40	Si-Al-O	Similar to kaolinite, but elevated Si (assume mixture of ±60% quartz and 40% kaolinite)
Quartz80Kaol20	Si-Al-O	Similar to kaolinite, but elevated Si (assume mixture of ±80% quartz and 20% kaolinite)
Quartz	Si-O (trace Al)	Quartz
Iron-oxide/pyrite	Fe-S-O, Fe-oxide	Transformation of pyrite
Ti-oxide	Ti-oxide	Transformation of rutile/anatase
Char	C	Unburnt carbon
Unmatched	Complex elemental composition	Variety of sources.

Table N.2: Calculate Mass-% mineral of the total fly ash samples analysed. (Calculation is the individual size fractions mass-% distributions weighted by the mass-% screened size distribution)

Hole (#) Depth (m)	Carbonate	Ca/Mgoxide	Kaolinite	Kaolinite (pyrite, carbonate)	Kaolinite carbonate	Kaolinite (pyrite)	Kaolinite (K,Ti)	Orthoclase	Quartz60 Kaol40	Quartz80 Kaol20	Quartz	Iron_Oxide pyrite	Ti-oxide	Char	Unmatch	Total
#1 0m	1.4	1.4	59.7	0.4	5.9	1.3	2.0	0.7	3.2	0.8	13.9	2.3	0.1	6.6	0.2	100.0
#1 0.5m	0.7	0.9	58.2	0.3	4.4	0.7	2.0	0.4	2.9	0.7	11.2	1.4	0.2	15.9	0.0	100.0
#1 1m	1.3	1.7	54.6	0.3	3.7	0.8	1.5	0.2	2.8	0.7	11.1	1.9	0.3	19.3	0.0	100.0
#1 1.5	0.8	1.2	47.7	0.3	2.8	0.5	1.5	0.4	2.6	0.6	12.0	1.1	0.3	28.1	0.0	100.0
#1 2m	2.2	1.9	42.6	0.3	2.8	0.7	1.2	0.3	2.6	0.9	25.6	4.4	0.2	14.3	0.1	100.0
#2 0m	0.7	0.8	60.6	0.3	5.1	0.9	1.9	0.1	3.1	0.8	11.9	1.4	0.4	12.0	0.1	100.0
#2 0.5m	0.2	0.2	67.2	0.3	3.7	0.7	1.8	0.2	2.6	0.7	8.3	0.7	0.5	12.6	0.0	99.7
#2 1m	0.5	0.7	64.4	0.3	4.5	1.2	2.0	0.2	3.1	0.6	12.0	2.1	0.2	8.3	0.0	100.0
#2 1.5m	0.6	0.7	62.7	0.4	4.8	1.0	2.1	0.1	2.9	0.7	11.7	2.9	0.3	9.0	0.1	100.0
#2 2m	0.3	0.5	53.1	0.3	3.7	1.3	1.6	0.6	2.7	0.7	16.3	3.2	0.3	15.4	0.0	100.0
#3 0m	1.3	0.9	64.5	0.4	4.8	1.1	1.8	0.4	3.3	0.8	11.3	1.8	0.1	6.8	0.1	99.4
#3 0.5m	0.9	1.1	65.6	0.4	5.4	1.1	1.8	0.2	3.6	0.8	11.5	1.6	0.2	5.0	0.1	99.3
#3 1m	0.9	0.7	63.0	0.5	7.3	1.0	1.9	0.3	4.1	1.2	13.6	2.2	0.1	2.7	0.1	99.5
#3 1.5m	0.6	1.2	58.2	0.7	7.9	1.2	2.3	0.5	3.3	0.7	14.3	2.0	0.3	5.9	0.2	99.2
#3 2m	0.7	1.0	57.9	0.5	6.3	1.3	1.7	0.5	3.6	1.0	14.9	2.4	0.2	7.3	0.1	99.5
#4 0m	1.3	0.8	60.4	0.3	5.7	1.5	2.5	0.6	4.7	0.9	14.5	3.6	0.2	2.3	0.1	99.3
#4 0.5m	1.4	1.3	61.7	0.4	4.5	0.8	2.1	0.1	3.7	0.8	14.2	2.2	0.1	6.1	0.0	99.4
#4 1m	0.9	0.8	60.3	0.4	8.9	0.9	1.9	0.2	3.9	0.8	14.2	2.2	0.1	3.9	0.2	99.3
#4 1.5m	0.7	0.6	63.0	0.4	5.5	1.2	1.7	0.2	3.7	0.6	13.3	4.0	0.3	4.2	0.2	99.5
Average	0.9	1.0	59.2	0.4	5.1	1.0	1.9	0.3	3.3	0.8	13.5	2.3	0.2	9.8	0.1	99.7
Min	0.2	0.2	42.6	0.3	2.8	0.5	1.2	0.1	2.6	0.6	8.3	0.7	0.1	2.3	0.0	99.2
Max	2.2	1.9	67.2	0.7	8.9	1.5	2.5	0.7	4.7	1.2	25.6	4.4	0.5	28.1	0.2	100.0
Std.Dev	0.5	0.4	6.2	0.1	1.6	0.3	0.3	0.2	0.6	0.2	3.5	1.0	0.1	6.6	0.1	0.3

Table N.3: Calculate Mass-% mineral distribution in the +75 µm sized fraction of the fly ash samples analysed.

Hole (#) Depth (m)	Carbonate	Ca/Mgoxide	Kaolinite	Kaolinite (pyrite, carbonate)	Kaolinite carbonate	Kaolinite (pyrite)	Kaolinite (K,Ti)	Orthoclase	Quartz60 Kaol40	Quartz80 Kaol20	Quartz	Iron_Oxide pyrite	Ti-oxide	Char	Unmatch	Total
#1 0m	1.9	2.4	31.7	1.0	8.0	1.8	1.2	1.5	2.8	1.1	30.4	3.1	0.2	12.7	0.1	100.0
#1 0.5m	0.9	1.2	48.7	0.6	4.8	0.7	2.0	0.5	2.2	0.6	12.0	1.8	0.2	23.8	0.1	100.0
#1 1m	0.6	1.3	38.3	0.4	2.5	0.5	0.9	0.3	1.8	0.5	8.7	0.6	0.3	43.2	0.0	100.0
#1 1.5	1.2	1.8	39.6	0.3	4.0	0.5	0.9	0.6	2.2	0.8	11.1	0.7	0.4	35.6	0.0	99.8
#1 2m	2.4	1.3	19.7	0.3	1.2	0.9	0.4	0.5	2.3	1.6	47.1	7.5	0.1	14.6	0.1	100.0
#2 0m	1.1	0.7	43.8	0.3	4.8	0.9	0.9	0.2	2.2	0.5	8.4	1.9	0.3	34.1	0.0	100.0
#2 0.5m	0.3	0.1	65.1	0.2	2.8	0.6	1.1	0.2	2.2	0.8	5.2	0.6	0.8	19.3	0.0	99.3
#2 1m	0.2	0.8	62.8	0.3	4.5	1.1	1.4	0.2	2.9	0.7	7.0	0.6	0.1	17.4	0.1	100.0
#2 1.5m	0.2	0.4	55.4	0.4	4.1	1.5	1.3	0.2	2.6	0.8	14.0	6.9	0.3	11.9	0.1	100.0
#2 2m	0.8	0.5	35.7	0.4	2.7	2.2	0.8	0.9	2.4	0.6	26.2	5.5	0.3	21.0	0.1	100.0
#3 0m	1.1	1.2	49.4	0.7	7.5	1.8	1.2	0.6	3.4	1.0	15.5	3.0	0.3	12.7	0.0	99.4
#3 0.5m	1.4	0.4	35.7	0.6	9.8	1.9	1.2	1.6	3.6	1.2	30.9	3.8	0.3	7.1	0.1	99.6
#3 1m	0.9	0.5	34.4	1.1	15.9	2.0	0.9	0.3	3.8	1.3	30.9	3.4	0.3	3.5	0.0	99.3
#3 1.5m	1.6	1.5	36.4	1.0	18.5	1.7	1.3	0.9	3.3	0.9	19.5	3.1	0.3	9.3	0.2	99.4
#3 2m	0.8	0.5	35.6	0.7	11.0	1.9	1.0	0.9	2.9	1.0	25.6	3.0	0.5	14.0	0.1	99.5
#4 0m	0.6	0.2	16.8	1.0	5.1	2.0	0.5	1.1	1.7	0.6	53.2	14.3	0.2	2.0	0.0	99.3
#4 0.5m	0.9	0.3	18.4	0.8	5.7	1.7	0.8	0.9	2.1	0.7	51.0	13.9	0.1	1.5	0.1	99.0
#4 1m	1.2	0.4	35.5	1.4	24.8	2.4	1.6	0.2	3.3	0.7	17.2	6.9	0.0	3.1	0.4	99.1
#4 1.5m	1.0	0.3	52.3	0.8	12.2	2.4	2.0	0.4	3.6	0.5	11.3	9.7	0.0	2.6	0.4	99.3
Average	1.0	0.8	39.8	0.6	7.9	1.5	1.1	0.6	2.7	0.8	22.4	4.8	0.3	15.2	0.1	99.6
Min	0.2	0.1	16.8	0.2	1.2	0.5	0.4	0.2	1.7	0.5	5.2	0.6	0.0	1.5	0.0	99.0
Max	2.4	2.4	65.1	1.4	24.8	2.4	2.0	1.6	3.8	1.6	53.2	14.3	0.8	43.2	0.4	100.0
Std.Dev	0.6	0.6	13.6	0.3	6.2	0.6	0.4	0.4	0.6	0.3	15.0	4.2	0.2	12.1	0.1	0.4

Table N.4: Calculate Mass-% mineral distribution in the –75+38 µm sized fraction of the fly ash samples analysed.

Hole (#) Depth (m)	Carbonate	Ca/Mgoxide	Kaolinite	Kaolinite (pyrite, carbonate)	Kaolinite carbonate	Kaolinite (pyrite)	Kaolinite (K,Ti)	Orthoclase	Quartz60 Kaol40	Quartz80 Kaol20	Quartz	Iron_Oxide pyrite	Ti-oxide	Char	Unmatch	Total
#1 0m	2.1	1.3	52.4	0.4	7.8	1.7	1.9	1.0	3.9	1.3	13.7	3.4	0.1	8.9	0.1	100.0
#1 0.5m	0.9	1.4	51.3	0.3	4.0	0.9	1.4	0.4	2.7	0.8	8.6	0.6	0.1	26.4	0.0	100.0
#1 1m	1.9	2.4	43.0	0.2	3.8	0.9	1.3	0.2	2.3	0.6	10.0	1.6	0.2	31.6	0.0	100.0
#1 1.5	0.6	0.9	40.0	0.3	1.8	0.5	1.4	0.5	2.2	0.6	11.0	0.2	0.4	39.6	0.0	100.0
#1 2m	3.3	2.5	36.4	0.4	3.6	0.6	1.1	0.4	2.0	0.6	11.1	3.8	0.3	33.9	0.0	100.0
#2 0m	0.8	0.3	57.7	0.4	6.6	1.3	1.8	0.0	3.1	1.0	11.4	1.4	0.5	13.6	0.1	100.0
#2 0.5m	0.0	0.1	63.5	0.3	4.6	0.9	2.0	0.2	2.7	0.9	9.8	0.9	0.2	13.8	0.0	100.0
#2 1m	0.5	0.4	58.6	0.4	5.6	1.3	1.3	0.3	3.0	0.4	12.6	2.3	0.3	13.1	0.0	100.0
#2 1.5m	1.1	0.8	57.8	0.3	6.1	0.9	2.0	0.4	2.8	0.6	8.6	0.6	0.1	17.6	0.0	100.0
#2 2m	0.1	0.2	53.9	0.3	4.4	1.0	1.9	0.6	2.9	0.9	11.9	2.2	0.2	19.5	0.0	100.0
#3 0m	1.8	1.3	60.9	0.6	6.6	1.3	1.5	1.6	4.3	1.3	13.7	0.9	0.0	3.7	0.0	99.5
#3 0.5m	2.2	1.2	60.6	0.5	9.0	2.7	1.2	0.0	4.1	1.2	7.9	2.0	0.1	6.6	0.2	99.5
#3 1m	1.6	1.4	57.2	0.6	10.1	1.5	2.0	1.0	4.4	1.5	11.2	2.6	0.1	4.2	0.1	99.5
#3 1.5m	0.8	1.4	54.9	1.0	11.8	2.1	2.0	0.4	3.4	0.8	10.5	3.7	0.2	5.7	0.4	99.0
#3 2m	0.7	1.0	60.4	0.8	11.8	1.9	2.1	0.7	3.7	0.9	10.9	1.9	0.1	2.3	0.5	99.5
#4 0m	2.7	1.8	41.5	0.7	9.4	3.2	2.3	2.4	3.9	1.2	16.6	6.7	0.0	6.2	0.5	99.1
#4 0.5m	1.8	0.6	44.6	0.4	10.4	2.7	2.2	1.0	5.0	1.6	19.2	4.5	0.0	5.3	0.2	99.4
#4 1m	1.5	0.7	44.6	0.6	20.1	1.3	1.6	0.8	4.8	1.4	16.3	3.0	0.0	2.7	0.1	99.3
#4 1.5m	1.0	0.5	40.3	0.5	12.1	2.6	1.6	0.3	4.1	1.2	18.2	13.5	0.1	2.9	0.4	99.3
Average	1.3	1.1	51.6	0.5	7.9	1.5	1.7	0.6	3.4	1.0	12.3	2.9	0.2	13.6	0.1	99.7
Min	0.0	0.1	36.4	0.2	1.8	0.5	1.1	0.0	2.0	0.4	7.9	0.2	0.0	2.3	0.0	99.0
Max	3.3	2.5	63.5	1.0	20.1	3.2	2.3	2.4	5.0	1.6	19.2	13.5	0.5	39.6	0.5	100.0
Std.Dev	0.9	0.7	8.6	0.2	4.3	0.8	0.4	0.6	0.9	0.3	3.2	3.0	0.1	11.6	0.2	0.4

Table N.5: Calculate Mass-% mineral distribution in the –38 µm sized fraction of the fly ash samples analysed.

Hole (#) Depth (m)	Carbonate	Ca/Mgoxide	Kaolinite	Kaolinite (pyrite, carbonate)	Kaolinite carbonate	Kaolinite (pyrite)	Kaolinite (K,Ti)	Orthoclase	Quartz60 Kaol40	Quartz80 Kaol20	Quartz	Iron_Oxide pyrite	Ti-oxide	Char	Unmatch	Total
#1 0m	0.8	1.1	71.0	0.3	4.3	0.8	2.3	0.3	2.9	0.5	9.9	1.5	0.1	3.6	0.4	100.0
#1 0.5m	0.6	0.5	68.2	0.2	4.4	0.7	2.4	0.3	3.5	0.7	12.3	1.7	0.2	4.5	0.0	100.0
#1 1m	1.4	1.5	66.1	0.3	4.1	0.8	1.8	0.2	3.3	0.7	12.5	2.5	0.4	4.4	0.0	100.0
#1 1.5	0.8	1.1	60.7	0.2	3.0	0.6	2.0	0.2	3.3	0.6	13.8	2.2	0.2	11.2	0.0	100.0
#1 2m	1.6	2.1	63.1	0.2	3.8	0.6	1.9	0.1	3.0	0.5	14.6	2.2	0.1	6.0	0.1	100.0
#2 0m	0.5	1.0	67.6	0.2	4.5	0.6	2.2	0.2	3.4	0.7	13.3	1.3	0.3	4.0	0.1	100.0
#2 0.5m	0.2	0.3	71.9	0.5	3.9	0.7	2.3	0.2	3.0	0.6	10.5	0.8	0.3	4.7	0.0	100.0
#2 1m	0.6	0.7	67.7	0.3	4.0	1.2	2.5	0.2	3.2	0.6	13.9	2.8	0.3	2.1	0.0	100.0
#2 1.5m	2.0	0.3	68.5	0.3	4.7	0.7	2.6	0.1	3.1	0.7	11.5	0.0	0.0	4.2	0.4	99.1
#2 2m	0.2	0.8	65.5	0.2	3.6	0.9	2.0	0.2	2.7	0.6	13.8	2.5	0.5	6.5	0.1	100.0
#3 0m	1.2	0.8	68.4	0.4	3.9	0.9	2.0	0.2	3.1	0.7	10.0	1.7	0.1	6.1	0.1	99.4
#3 0.5m	0.7	1.2	70.4	0.4	4.3	0.7	1.9	0.1	3.5	0.7	9.3	1.3	0.2	4.5	0.1	99.3
#3 1m	0.8	0.6	70.3	0.3	5.0	0.7	2.1	0.2	4.2	1.2	9.9	1.9	0.1	2.4	0.1	99.5
#3 1.5m	0.2	1.1	66.1	0.6	3.8	0.9	2.6	0.3	3.4	0.6	13.0	1.4	0.3	4.8	0.2	99.2
#3 2m	0.6	1.3	66.6	0.4	3.7	1.0	2.0	0.3	3.9	1.1	11.1	2.3	0.2	5.2	0.1	99.5
#4 0m	1.2	0.7	64.3	0.2	5.4	1.3	2.6	0.4	4.9	0.9	12.4	2.8	0.2	2.0	0.1	99.3
#4 0.5m	1.4	1.3	62.7	0.4	4.4	0.8	2.1	0.1	3.7	0.7	13.5	2.0	0.1	6.2	0.0	99.4
#4 1m	0.7	0.9	66.2	0.2	4.9	0.6	2.0	0.1	3.9	0.8	13.4	1.3	0.1	4.2	0.2	99.3
#4 1.5m	0.5	0.7	67.6	0.2	3.0	0.8	1.7	0.2	3.7	0.5	13.6	1.6	0.4	4.8	0.1	99.5
Average	0.8	0.9	67.0	0.3	4.1	0.8	2.2	0.2	3.5	0.7	12.2	1.8	0.2	4.8	0.1	99.7
Min	0.2	0.3	60.7	0.2	3.0	0.6	1.7	0.1	2.7	0.5	9.3	0.0	0.0	2.0	0.0	99.1
Max	2.0	2.1	71.9	0.6	5.4	1.3	2.6	0.4	4.9	1.2	14.6	2.8	0.5	11.2	0.4	100.0
Std.Dev	0.5	0.4	2.9	0.1	0.6	0.2	0.3	0.1	0.5	0.2	1.7	0.7	0.1	2.0	0.1	0.3

APPENDIX O: LIBERATION CHARACTERISTICS – FLY ASH

The Cumulative Liberation Yield (CLY) plots for the individual minerals/phases in fly ash and corresponding data is summarised. For the individual minerals, the data is the CLY plots for the individual size fractions. This data is the average liberation characteristic for all the holes sampled. The “total” CLY curve in these plots represented the weighted average of the size fractions using the particle size distribution as the weighting factor (refer to Figure 5.3).

The liberation categories based on microlithotype classification (Appendix M) for pulverised fuel is still used for fly ash. Fly ash liberation class definitions are:

- Included : The fly ash phase of interest (reference phase) is locked in a complex association with other fly ash phases or a single fly ash phase. Discrete fly ash phase is less than 20 area% of the total particle.
- Middling : The fly ash phase of interest (reference phase) accounts for between 20 to 60 area% and the remaining 40 to 80 area% other fly ash phases.
- Excluded/Free : The fly ash phase of interest (reference phase) for >60 area% in the particle and the remaining 40 area% of the particle comprises other fly ash phases.

The cumulative liberation yield (CLY) distributions for the major reference fly ash phases, kaolinite, Ca-oxide, Fe-oxide, kaolinite(carbonate), quartz and char.

Table O.1: Ca-oxide/Ca-carbonate cumulative liberation yield and cumulative liberation class by size fraction and weighted "total" across all size fractions.

Liberation Data				
Lib. Class	+75	-75+38	-38	Total
0	0.0	0.0	0.0	0.0
5	14.4	10.7	3.6	8.5
15	8.3	8.3	4.9	6.7
25	6.7	4.1	4.5	5.1
35	6.6	5.2	5.5	5.8
45	9.4	14.7	5.2	8.6
55	8.3	4.7	10.5	8.5
65	5.7	4.4	9.9	7.4
75	7.0	15.8	12.8	11.7
85	16.1	15.4	12.2	14.1
95	15.5	14.7	5.4	10.6
100	2.1	1.9	25.7	13.0
Total	100.0	100.0	100.0	100.0
CLY				
Lib. Class	+75	-75+38	-38	Total
0	100.0	100.0	100.0	100.0
5	100.0	100.0	100.0	100.0
15	85.6	89.3	96.4	91.5
25	77.4	81.0	91.5	84.8
35	70.7	76.9	87.1	79.7
45	64.1	71.7	81.6	73.9
55	54.7	56.9	76.4	65.3
65	46.4	52.2	65.9	56.8
75	40.7	47.8	56.0	49.4
85	33.7	32.0	43.3	37.7
95	17.6	16.5	31.1	23.6
100	2.1	1.9	25.7	13.0

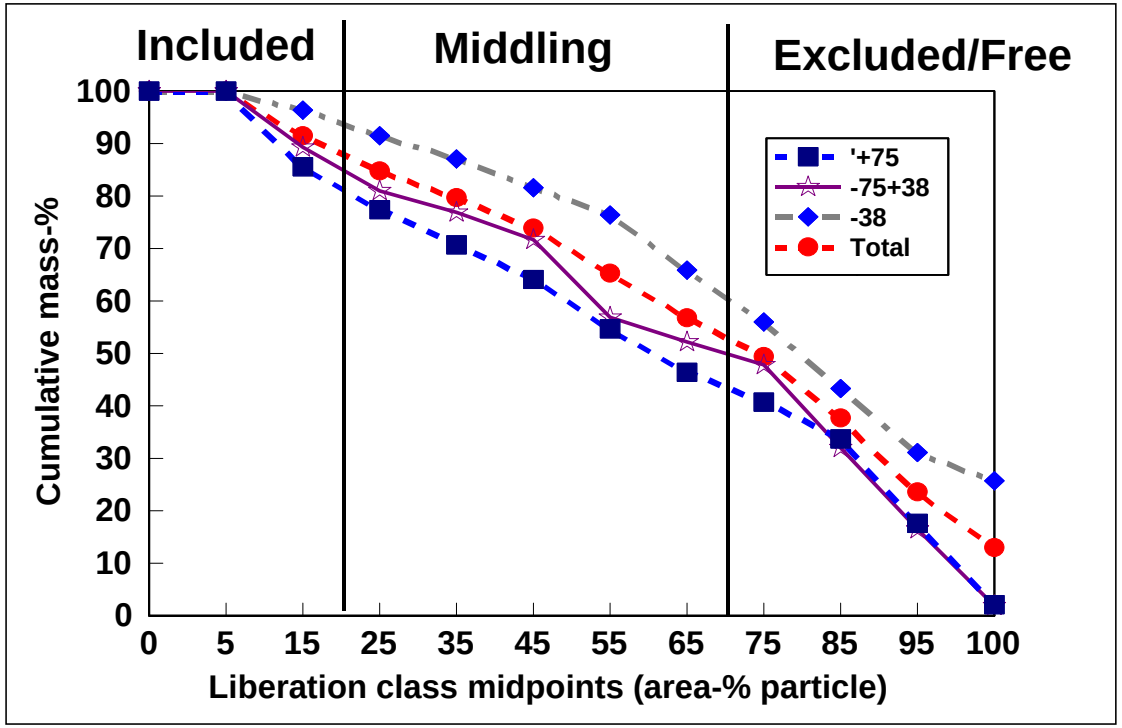

Table O.2: Kaolinite cumulative liberation yield and cumulative liberation class by size fraction and weighted "total" across all size fractions.

Liberation Data				
Lib. Class	+75	-75+38	-38	Total
0	0.0	0.0	0.0	0.0
5	2.8	1.7	0.3	1.4
15	5.2	3.9	0.8	2.8
25	7.8	7.1	1.6	4.7
35	9.6	10.0	1.8	6.1
45	11.7	13.7	2.2	7.8
55	12.6	13.6	5.2	9.4
65	13.7	9.4	7.2	9.7
75	16.4	12.9	7.8	11.6
85	12.4	14.2	13.1	13.1
95	6.2	11.1	9.8	9.0
100	1.6	2.3	50.3	24.4
Total	100.0	100.0	100.0	100.0
CLY				
Lib. Class	+75	-75+38	-38	Total
0	100.0	100.0	100.0	100.0
5	100.0	100.0	100.0	100.0
15	97.2	98.3	99.7	98.6
25	92.0	94.4	98.9	95.8
35	84.2	87.3	97.4	91.0
45	74.6	77.3	95.6	85.0
55	62.9	63.6	93.4	77.2
65	50.3	49.9	88.1	67.8
75	36.6	40.5	81.0	58.1
85	20.2	27.6	73.1	46.5
95	7.7	13.4	60.1	33.4
100	1.6	2.3	50.3	24.4

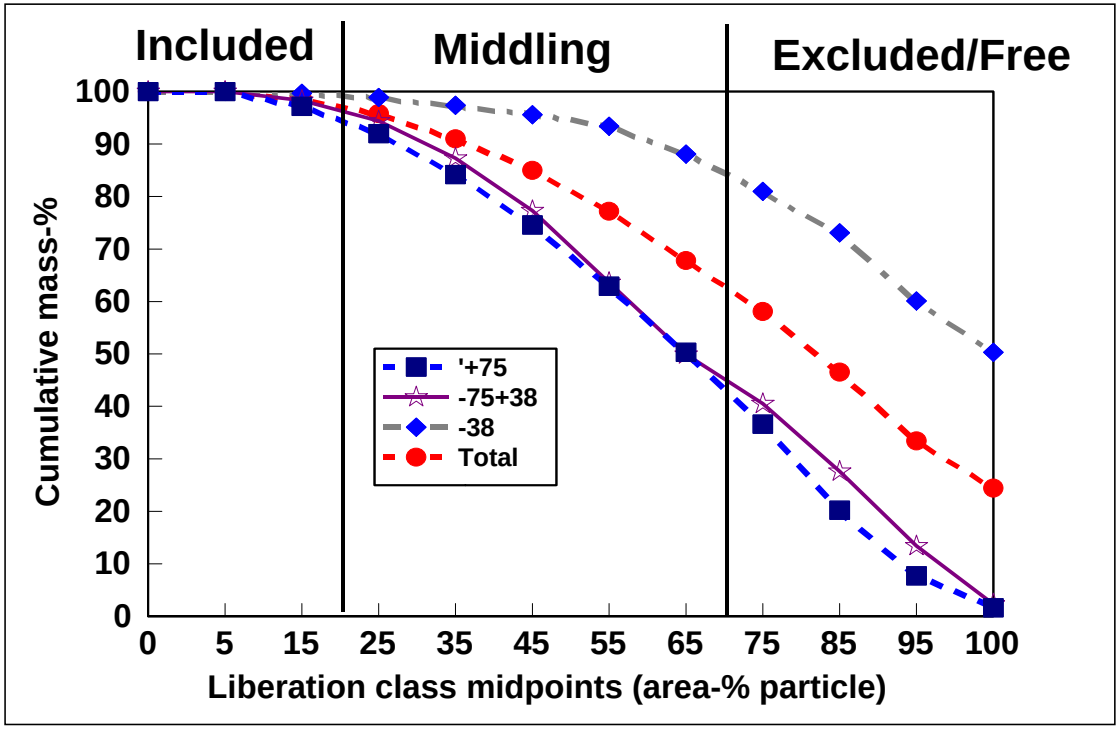

Table O.3: Kaolinite(carbonate) cumulative liberation yield and cumulative liberation class by size fraction and weighted "total" across all size fractions.

Liberation Data				
Lib. Class	+75	-75+38	-38	Total
0	0.0	0.0	0.0	0.0
5	13.5	7.3	7.2	9.2
15	15.5	9.6	11.9	12.5
25	17.6	17.5	11.7	14.8
35	15.2	19.5	12.3	14.8
45	11.9	17.9	7.6	11.2
55	9.2	14.3	10.7	11.1
65	9.1	7.2	9.9	9.1
75	3.7	2.4	7.1	5.0
85	2.6	2.6	7.4	4.8
95	1.4	1.5	2.8	2.1
100	0.3	0.0	11.4	5.4
Total	100.0	100.0	100.0	100.0
CLY				
Lib. Class	+75	-75+38	-38	Total
0	100.0	100.0	100.0	100.0
5	100.0	100.0	100.0	100.0
15	86.5	92.7	92.8	90.8
25	71.0	83.1	80.9	78.3
35	53.4	65.5	69.2	63.5
45	38.2	46.0	56.9	48.6
55	26.3	28.1	49.3	37.4
65	17.1	13.8	38.6	26.3
75	7.9	6.5	28.7	17.3
85	4.3	4.1	21.6	12.3
95	1.6	1.5	14.2	7.5
100	0.3	0.0	11.4	5.4

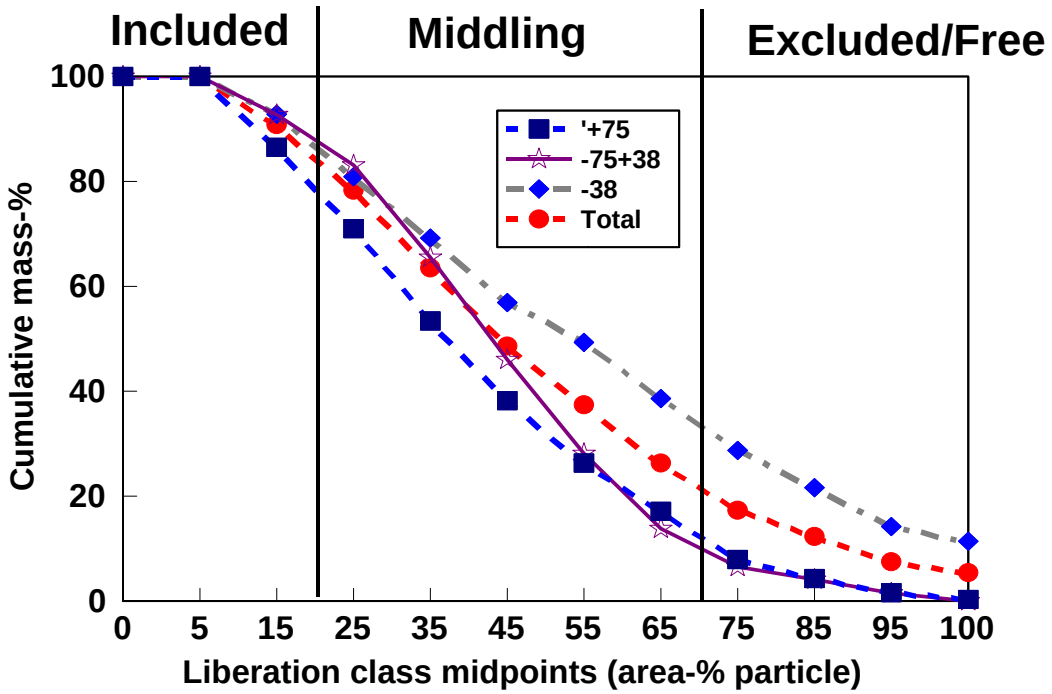

Table O.4: Fe-oxide/pyrite cumulative liberation yield and cumulative liberation class by size fraction and weighted "total" across all size fractions.

Liberation Data				
Lib. Class	+75	-75+38	-38	Total
0	0.0	0.0	0.0	0.0
5	6.5	13.7	2.4	6.2
15	4.9	7.3	1.8	4.0
25	5.5	6.4	5.2	5.6
35	8.5	12.3	2.2	6.4
45	6.1	11.3	7.3	7.8
55	14.6	8.3	7.3	9.8
65	7.9	3.4	10.1	7.9
75	12.6	7.1	17.5	13.7
85	16.0	16.7	10.9	13.8
95	14.5	8.8	6.9	9.7
100	2.6	4.7	28.4	15.1
Total	100.0	100.0	100.0	100.0
CLY				
Lib. Class	+75	-75+38	-38	Total
0	100.0	100.0	100.0	100.0
5	100.0	100.0	100.0	100.0
15	93.5	86.3	97.6	93.8
25	88.6	79.1	95.8	89.8
35	83.1	72.6	90.6	84.2
45	74.5	60.4	88.5	77.8
55	68.4	49.1	81.1	70.0
65	53.8	40.8	73.8	60.2
75	45.9	37.4	63.7	52.3
85	33.2	30.3	46.2	38.6
95	17.2	13.6	35.3	24.8
100	2.6	4.7	28.4	15.1

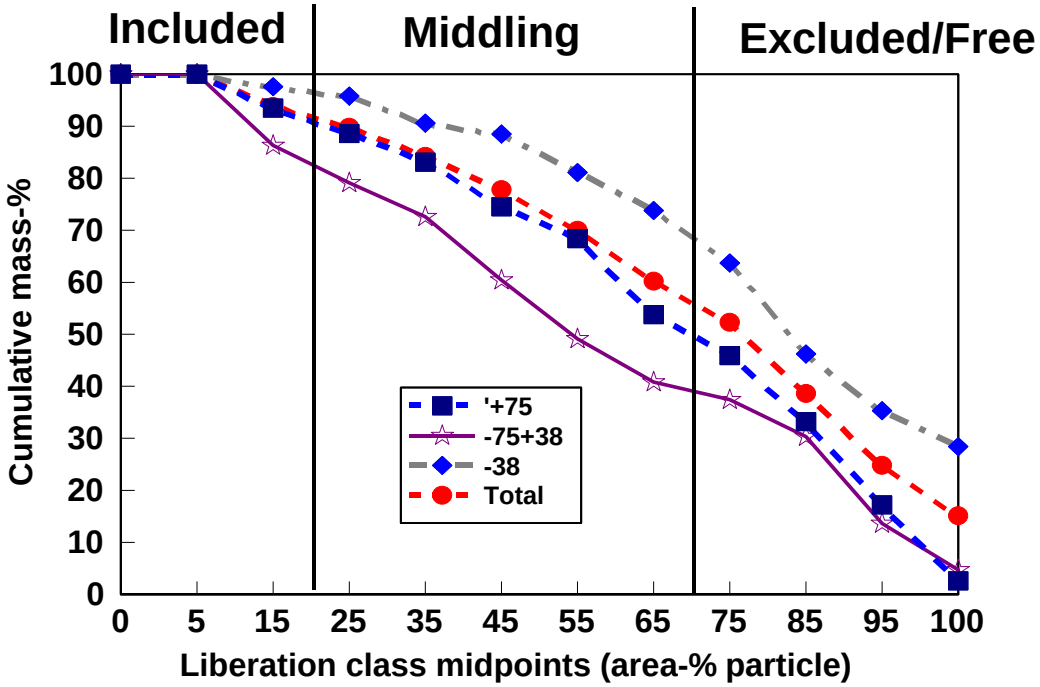

Table O.5: Quartz cumulative liberation yield and cumulative liberation class by size fraction and weighted "total" across all size fractions.

Liberation Data				
Lib. Class	+75	-75+38	-38	Total
0	0.0	0.0	0.0	0.0
5	52.2	56.0	14.8	35.6
15	25.5	28.7	25.8	26.4
25	9.9	11.4	23.2	16.4
35	8.3	3.4	11.1	8.5
45	1.6	0.5	4.4	2.7
55	2.2	0.1	11.1	5.9
65	0.0	0.0	2.6	1.2
75	0.3	0.0	1.0	0.5
85	0.0	0.0	0.2	0.1
95	0.0	0.0	0.0	0.0
100	0.0	0.0	5.7	2.6
Total	100.0	100.0	100.0	100.0
CLY				
Lib. Class	+75	-75+38	-38	Total
0	100.0	100.0	100.0	100.0
5	100.0	100.0	100.0	100.0
15	47.8	44.0	85.2	64.4
25	22.3	15.4	59.4	38.0
35	12.5	4.0	36.2	21.6
45	4.1	0.6	25.1	13.1
55	2.6	0.1	20.7	10.4
65	0.3	0.0	9.5	4.5
75	0.3	0.0	6.9	3.3
85	0.0	0.0	5.9	2.7
95	0.0	0.0	5.7	2.6
100	0.0	0.0	5.7	2.6

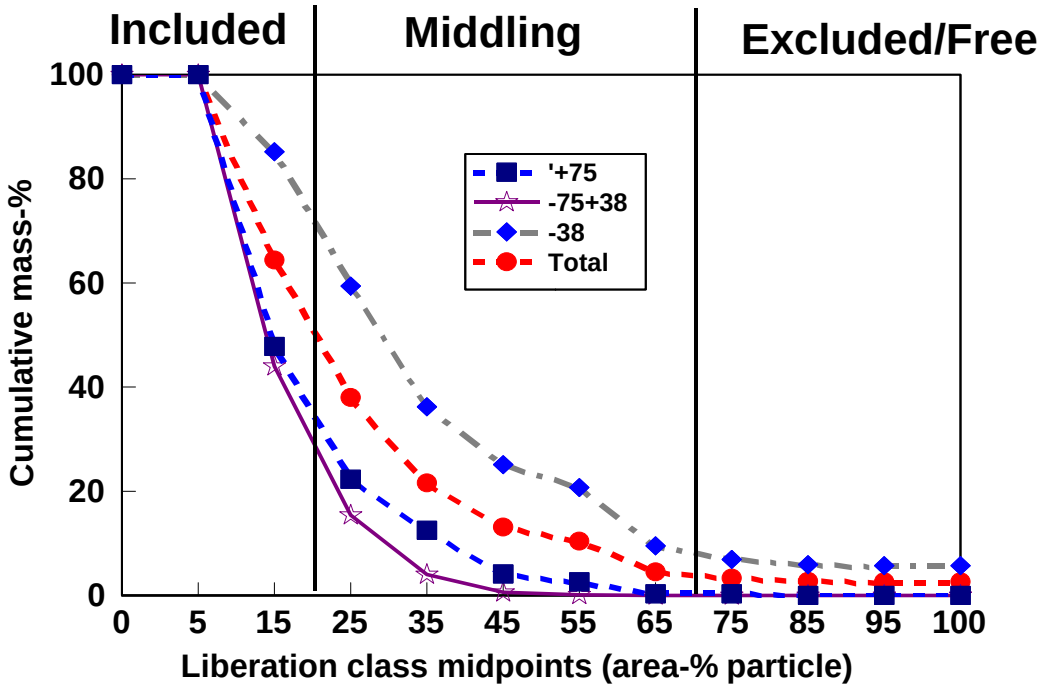

Table O.6: Quartz>kaolinite mix cumulative liberation yield and cumulative liberation class by size fraction and weighted "total" across all size fractions.

Liberation Data				
Lib. Class	+75	-75+38	-38	Total
0	0.0	0.0	0.0	0.0
5	52.2	56.0	14.8	35.6
15	25.5	28.7	25.8	26.4
25	9.9	11.4	23.2	16.4
35	8.3	3.4	11.1	8.5
45	1.6	0.5	4.4	2.7
55	2.2	0.1	11.1	5.9
65	0.0	0.0	2.6	1.2
75	0.3	0.0	1.0	0.5
85	0.0	0.0	0.2	0.1
95	0.0	0.0	0.0	0.0
100	0.0	0.0	5.7	2.6
Total	100.0	100.0	100.0	100.0
CLY				
Lib. Class	+75	-75+38	-38	Total
0	100.0	100.0	100.0	100.0
5	100.0	100.0	100.0	100.0
15	47.8	44.0	85.2	64.4
25	22.3	15.4	59.4	38.0
35	12.5	4.0	36.2	21.6
45	4.1	0.6	25.1	13.1
55	2.6	0.1	20.7	10.4
65	0.3	0.0	9.5	4.5
75	0.3	0.0	6.9	3.3
85	0.0	0.0	5.9	2.7
95	0.0	0.0	5.7	2.6
100	0.0	0.0	5.7	2.6

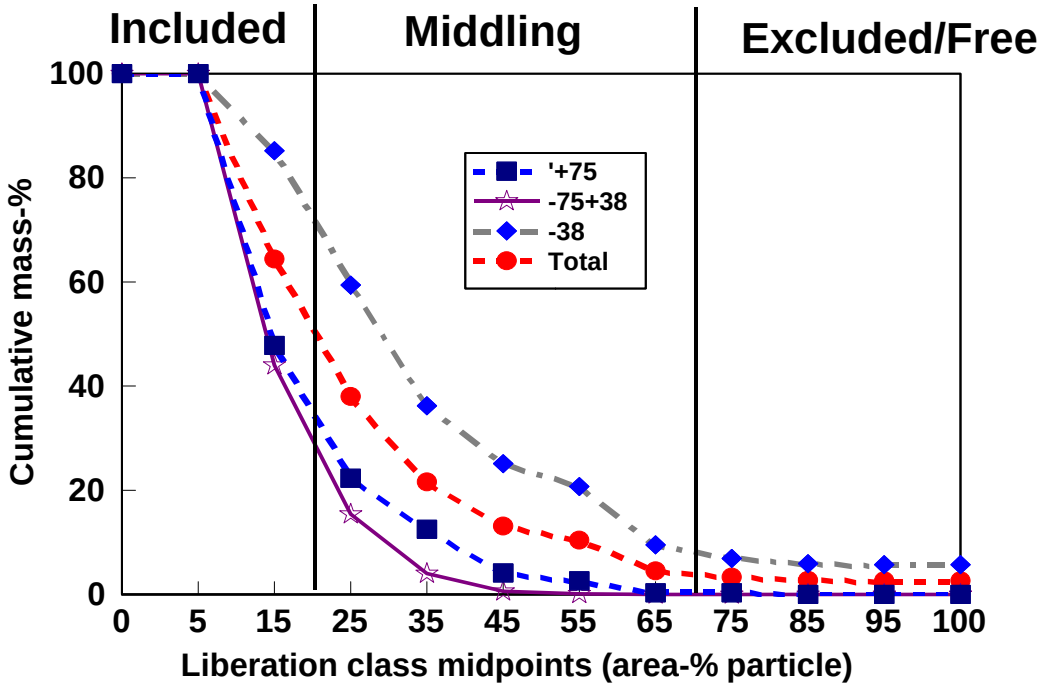

Table O.7: Kaolinite(pyrite) cumulative liberation yield and cumulative liberation class by size fraction and weighted "total" across all size fractions.

Liberation Data				
Lib. Class	+75	-75+38	-38	Total
0	0.0	0.0	0.0	0.0
5	32.7	40.4	10.0	23.9
15	21.2	15.3	11.8	15.5
25	15.9	13.8	16.1	15.5
35	13.4	9.3	11.0	11.3
45	7.1	9.3	7.7	7.9
55	5.0	2.9	11.6	7.6
65	3.7	5.6	8.0	6.1
75	0.4	2.1	5.4	3.1
85	0.2	1.2	8.0	4.1
95	0.0	0.0	1.2	0.5
100	0.4	0.0	9.2	4.4
Total	100.0	100.0	100.0	100.0
CLY				
Lib. Class	+75	-75+38	-38	Total
0	100.0	100.0	100.0	100.0
5	100.0	100.0	100.0	100.0
15	67.3	59.6	90.0	76.1
25	46.1	44.2	78.2	60.6
35	30.2	30.4	62.1	45.1
45	16.8	21.1	51.1	33.7
55	9.6	11.9	43.4	25.9
65	4.7	9.0	31.8	18.3
75	0.9	3.4	23.8	12.1
85	0.5	1.2	18.4	9.0
95	0.4	0.0	10.4	5.0
100	0.4	0.0	9.2	4.4

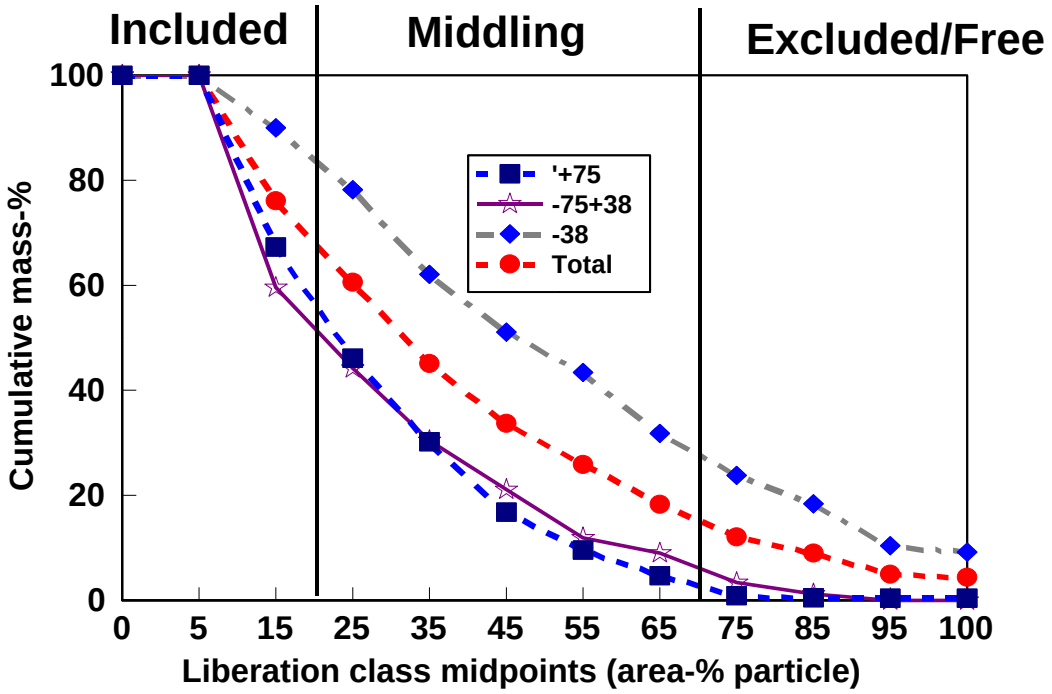

Table O.8: Char cumulative liberation yield and cumulative liberation class by size fraction and weighted "total" across all size fractions.

Liberation Data				
Lib. Class	+75	-75+38	-38	Total
0.0	0.0	0.0	0.0	0.0
5.0	5.9	8.0	6.2	6.5
15.0	7.4	8.3	10.0	8.8
25.0	6.2	5.4	9.3	7.5
35.0	5.9	5.1	5.5	5.5
45.0	6.4	4.4	3.4	4.6
55.0	9.7	6.5	9.5	8.9
65.0	11.7	9.9	4.0	7.7
75.0	13.4	15.1	4.6	9.7
85.0	14.9	16.2	5.6	10.9
95.0	11.8	14.2	3.5	8.4
100.0	6.8	7.0	38.5	21.6
Total	100.0	100.0	100.0	100.0
CLY				
Lib. Class	+75	-75+38	-38	Total
0.0	100.0	100.0	100.0	100.0
5.0	100.0	100.0	100.0	100.0
15.0	94.1	92.0	93.8	93.5
25.0	86.8	83.7	83.8	84.7
35.0	80.6	78.3	74.5	77.2
45.0	74.7	73.2	69.0	71.7
55.0	68.3	68.8	65.6	67.1
65.0	58.6	62.3	56.1	58.3
75.0	46.8	52.4	52.1	50.5
85.0	33.4	37.4	47.5	40.9
95.0	18.5	21.1	41.9	30.0
100.0	6.8	7.0	38.5	21.6

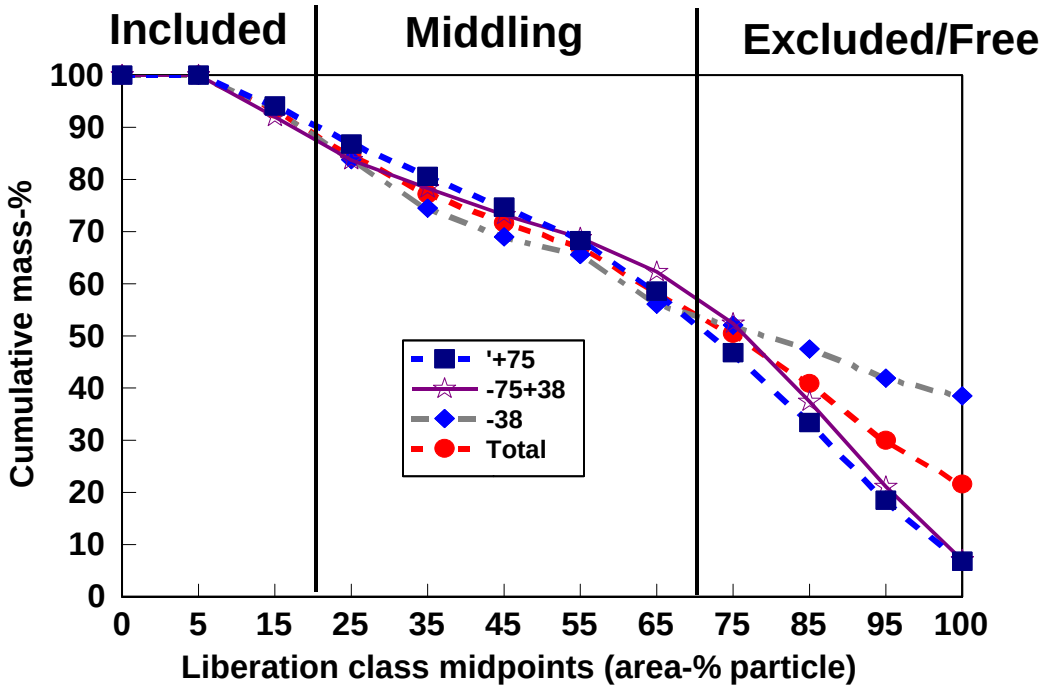

APPENDIX P: MINERAL ASSOCIATION

Table P.1: Comparative association characteristics between pulverised fuel and fly ash.

Original coal associations	Coal	Total Coal	Total Fly	Fly	Equivalent Fly ash Asscoaition
Kaolinite+Quartz	35.1	37.8		6.9	Quartz>Kaolinite Mix+Kaolinite+Quartz
Mica_Illite+Kaolinite+Quartz	2.6			5.1	Quartz+Kaolinite
			16.4	2.4	Quartz>Kaolinite Mix+Kaolinite
				1.1	Quartz>Kaolinite Mix
				0.9	Quartz>Kaolinite Mix+Quartz
Kaolinite	32.5	34.4	44.8	44.8	Kaolinite
Mica_illite+Kaolinite	1.9				
Quartz	5.8	5.8	5.8	5.8	Quartz
Pyrite	3.3	3.3	0.7	0.6	Fe-Oxide
Carbonate	7.2	7.2	0.8	0.8	Ca-Oxide
Kaolinit+Quartz+Carbonate	1.9	1.9	10.2	6.7	Quartz>Kaolinite Mix+Kaolinite+Kaolinite(Ca)+Quartz
				1.8	Kaolinite+Quartz+Kaolinite(Ca)
				1.3	Quartz>Kaolinite Mix+Kaolinite+Kaolinite(Ca)
				0.5	Quartz+Kaolinite(Ca)+Kaolinite+Ca-Oxide
Kaolinite+Carbonate	1.6	1.6	5.9	3.0	Kaolinite+Kaolinite(Ca)
				1.5	Kaolinite(Ca)
				0.5	Kaolinite+Ca-Oxide
				0.8	Kaolinite(Ca)+Kaolinite+Ca-Oxide
Kaolinite+Quartz+Pyrite	0.2	0.2	1.0	1.0	Quartz>Kaolinite Mix+Quartz+Kaolinite(Fe)+Kaolinite
Kaolinite+Pyrite	0.2	0.2	0.7	0.4	Kaolinite(Fe)
				0.3	Kaolinite+Kaolinite(Fe)
Gypsum+Kaolinite+Quartz+Carbonate	0.3	0.3	1.0	1.0	Quart>Kaolinite Mix+Quartz+Kaolinite(Ca)+Kaolinite+ Ca-Oxide
Quartz+Kaolinite+Carbonate+pyrite	0.0	0.0	6.2	2.5	Quartz>Kaolinite Mix+Kaolinite+Quartz+Kaolinite(Fe)+Kaolinite(Ca)
				1.0	Quartz>Kaolinite Mix+Quartz+Kaolinite(Ca)+Kaolinite(Fe)+Kaolinite+Fe-Oxide+Ca-
				0.5	Quartz+Kaolinite(Ca)+Kaolinite(Fe)+Kaolinite+Fe-Oxide
				0.5	Quartz>Kaolinite Mix + Quartz + Kaolinite(Ca) + Kaolinite(Fe) + Fe-Oxide
				0.5	Quartz>Kaolinite Mix+Kaolinite(Ca)+Kaolinite(Fe)Kaolinite
				0.5	Quartz>Kaolinite Mix+Quartz+Kaolinite(Ca)+Kaolinite(Fe)+Fe-Oxide
				0.3	Quartz+Kaolinite(Ca)+Kaolinite(Fe)+Kaolinite
				0.5	Kaolinite(Ca)+Kaolinite(Fe)+Kaolinite
Orthoclase+Kaolinite+Quartz	0.3	0.3	0.3	0.3	Quartz>Kaolinite Mix+Quartz+Orthoclase+Kaolinite
Mica_Illite+Kaolinite+Quartz+Carbonate	0.2	0.2	0.3	0.3	Quartz>Kaolinite Mix+Quartz+Orthoclase+Kaolinite+Ca-Oxide
Quartz+Pyrite	1.6	1.6	0.1	0.1	Quartz+Fe_oxide
Other	5.2	5.2	5.9	5.9	Other
Total	100.0	100.0	100.0	100.0	Total

APPENDIX Q: PHASE PROPORTIONS – SLAG DEPOSITS

Table Q.1: Mass-% phase distribution in the slag deposits for holes 1 and 2

HOLE 1						
Phases	**0m**	**0.5m**	**1m**	**1.5m**	**2m**	**Average**
CaOxide/Ca-carbonate		7.8	10.4	8.7	4.5	7.9
Fe-oxide		41.6	42.6	42.4	38.1	41.1
Kaolinite		3.9	11.0	3.9	17.1	9.0
Kaolinite(Carbonate,pyrite)		5.9	1.9	5.7	5.6	4.8
Kaolinite(Carbonate)		27.0	14.5	26.5	19.6	21.9
Kaolinite(Pyrite)		5.6	2.9	4.6	3.6	4.1
Kaolinite(Illite)		0.5	2.1	0.4	0.6	0.9
Orthoclase		0.1	0.1	0.0	0.6	0.2
Other		1.3	6.1	2.8	1.1	2.8
Quartz60Kaol40		0.5	0.8	0.2	1.7	0.8
Quartz80Kaol20		0.2	0.3	0.1	0.5	0.3
Quartz		5.7	7.4	4.6	6.5	6.1
Ti-oxide		0.1	0.0	0.0	0.5	0.2
HOLE 2						
Phases	**0m**	**0.5m**	**1m**	**1.5m**	**2m**	**Average**
CaOxide/Ca-carbonate	7.5	7.1	4.8	2.9	3.0	5.0
Fe-oxide	59.9	18.1	27.4	27.5	18.3	30.2
Kaolinite	3.4	22.4	28.0	36.8	20.8	22.3
Kaolinite(Carbonate,pyrite)	3.6	4.3	3.0	3.0	5.7	3.9
Kaolinite(Carbonate)	10.6	25.1	21.8	8.2	14.6	16.1
Kaolinite(Pyrite)	6.3	6.4	2.6	9.3	5.4	6.0
Kaolinite(K.Ti)	0.3	1.1	0.6	1.0	1.9	1.0
Orthoclase	0.1	0.4	0.1	0.0	0.6	0.3
Other	4.4	1.0	1.4	1.9	9.1	3.6
Quartz60Kaol40	0.3	2.3	2.1	2.0	1.8	1.7
Quartz80Kaol20	0.1	1.5	0.3	0.4	0.8	0.6
Quartz	3.4	10.2	7.9	7.0	17.6	9.2
Ti-oxide	0.2	0.1	0.0	0.0	0.4	0.2

Table Q.2: Mass-% phase abundance in the slag deposits for holes 3 and 4

HOLE 3						
Phases	**0m**	**0.5m**	**1m**	**1.5m**	**2m**	**Average**
CaOxide/Ca-carbonate	6.0		6.4			6.2
Fe-oxide	20.8		27.8			24.3
Kaolinite	40.1		17.9			29.0
Kaolinite(Carbonate,pyrite)	1.7		3.6			2.7
Kaolinite(Carbonate)	9.0		14.8			11.9
Kaolinite(Pyrite)	1.8		4.0			2.9
Kaolinite(K.Ti)	3.3		2.4			2.9
Orthoclase	0.3		0.2			0.2
Other	4.7		8.8			6.8
Quartz60Kaol40	2.8		1.2			2.0
Quartz80Kaol20	0.7		0.3			0.5
Quartz	8.3		12.6			10.4
Ti-oxide	0.4		0.2			0.3
HOLE 4						
Phases	**0m**	**0.5m**	**1m**	**1.5m**	**2m**	**Average**
CaOxide/Ca-carbonate	15.0	17.7	11.7	9.7		13.5
Fe-oxide	33.3	56.8	40.9	11.9		35.7
Kaolinite	7.7	1.7	8.1	29.7		11.8
Kaolinite(Carbonate,pyrite)	3.8	1.4	3.2	1.8		2.6
Kaolinite(Carbonate)	22.9	9.7	17.0	14.2		15.9
Kaolinite(Pyrite)	2.4	2.0	3.1	1.3		2.2
Kaolinite(K.Ti)	1.4	0.4	0.7	2.6		1.3
Orthoclase	0.3	0.4	0.0	0.5		0.3
Other	6.5	6.7	8.3	7.6		7.3
Quartz60Kaol40	0.5	0.0	0.5	2.1		0.8
Quartz80Kaol20	0.0	0.0	0.0	0.7		0.2
Quartz	6.2	3.1	6.4	17.8		8.4
Ti-oxide	0.0	0.1	0.0	0.1		0.1

APPENDIX R: DTF FLY ASH PHASE PROPORTIONS

Table R.1: Mass-% fly ash distribution – reducing conditions

	Temperature °C					
Fly Ash Phase	**1000**	**1100**	**1200**	**1300**	**1400**	**Average**
Ca-Oxide/Carbonate	5.0	6.2	7.1	5.4	8.0	6.3
Fe-Oxide/Pyrite	6.5	8.4	5.9	5.1	2.5	5.7
Kaolinite	54.4	54.6	52.5	52.4	54.3	53.7
Kaolinite(Carbonate,Pyrite)	0.6	0.4	0.6	0.5	0.6	0.5
Kaolinite(Carbonate)	0.7	1.3	1.9	1.3	2.4	1.5
Kaolinite(Pyrite)	0.3	0.5	0.4	0.3	0.4	0.4
Kaolinite(Ti_K)	2.5	2.6	3.6	2.5	3.8	3.0
Orthoclase	0.5	0.7	1.0	0.6	1.8	0.9
Other	0.1	0.1	0.2	0.1	0.1	0.1
Quartz60Kaol40	2.9	3.5	3.4	2.8	2.8	3.1
Quartz80Kaol20	1.3	1.0	1.1	0.9	1.1	1.1
Quartz	24.1	20.3	21.9	27.7	18.5	22.5
TiOxide	1.0	0.3	0.4	0.3	3.7	1.1
Total	100.0	100.0	100.0	100.0	100.0	100.0

Table R.2: Mass-% fly ash distribution – oxidising conditions

	Temperature °C					
Fly Ash phases	**1000**	**1100**	**1200**	**1300**	**1400**	**Average**
Ca-Oxide/Carbonate	6.2	5.0	4.9	4.9	4.3	5.2
Fe-Oxide/Pyrite	6.4	6.2	5.8	4.8	7.4	5.8
Kaolinite	55.8	55.2	57.3	51.9	53.0	55.0
Kaolinite(Carbonate,Pyrite)	0.9	0.5	0.7	0.5	0.4	0.7
Kaolinite(Carbonate)	1.2	1.4	1.8	3.2	2.7	1.9
Kaolinite(Pyrite)	0.3	0.5	0.5	0.6	0.9	0.5
Kaolinite(Ti_K)	2.7	2.5	3.3	3.6	3.2	3.0
Orthoclase	0.6	0.7	0.7	2.0	1.4	1.0
Other	0.2	0.1	0.1	0.2	0.1	0.1
Quartz60Kaol40	3.0	3.3	3.4	4.0	3.9	3.4
Quartz80Kaol20	1.1	1.0	1.0	1.1	1.4	1.1
Quartz	21.5	23.0	20.3	21.4	20.8	21.5
TiOxide	0.2	0.4	0.2	1.9	0.5	0.7
Total	100.0	100.0	100.0	100.0	100.0	100.0

APPENDIX S: MODEL PREDICTION AND DTF FLY ASH

The absolute difference in the mass% proportion of the individual fly ash phases between the modelled fly ash (based on #2 0.5m pulverised fuel) and drop tube furnace fly ash for the different combustion conditions and varying temperatures is summarised in Tables S.1, S.2 and S.3. The absolute mass% difference of individual fly ash phases between the modelled fly ash (based on all pulverised samples collected) and the average fly ash obtained from within the boiler (slag probe) and the individual cegrit fly ash sample collected is summarised in Table S.4.

Ideally, if the fly ash formation model accurately predicts the fly ash distribution the total difference should be zero. The magnitude of the difference is directly related to accuracy of the model to predict the mass% fly ash phase proportions.

To recall, the fly ash formation model is based on association characteristics of minerals in the pulverised fuel and assumes the three principal fly ash formation processes, coalescence, partial coalescence and fragmentation as described in chapter 3 and in detail in section 4.8.

The mass% fly ash phase proportions in appendix R are based on a point analysis (see Appendix G), whereas the mass% fly ash phase proportions in Tables S1 to S4 are based on scanning the whole particle (particle analysis) and computing the average elemental composition of the whole particle. The difference in analytical technique would account for the difference in mass% fly ash phase proportions in Appendix R and in this appendix.

Table S.1: Absolute mass-% difference between fragmentation model prediction and DTF fly ash.

Fly ash phase	Fragmentation (#2 0.5m)	Avg. Oxid	Avg. Red	Oxidising (°C)					Reducing (°C)				
				1000	1100	1200	1300	1400	1000	1100	1200	1300	1400
Ca-Oxide	6.1	4.2	5.0	5	4.5	3.8	4.1	3.7	4.1	5.2	6.1	4.2	5.4
Fe-Oxide	5.1	3.7	3.3	3.4	4.9	3.8	2.6	4	4	4.6	3.2	2.8	1.8
Kaolinite	57.8	56.4	56.5	58.3	53.9	59.9	54.2	55.6	57	57.8	54.9	54.5	58.2
Kaolinite(Carbonate,pyrite)	0	0.6	0.6	0.9	0.5	0.8	0.5	0.4	0.6	0.4	0.6	0.6	0.9
Kaolinite(Carbonate)	0	2.0	1.6	1.2	0.9	1.9	3.3	2.8	0.7	1.4	2	1.4	2.5
Kaolinite(Pyrite)	0	0.6	0.4	0.3	0.5	0.5	0.7	0.9	0.3	0.6	0.4	0.4	0.5
Kaolinite(illite,mica)	0.9	3.1	3.2	2.8	2.1	3.6	3.7	3.4	2.6	2.8	3.8	2.6	4.1
Orthoclase	0.9	1.2	0.9	0.6	1	0.9	2.1	1.5	0.6	0.8	1	0.7	1.5
Quartz60Kaol40	0	3.7	3.3	3.1	3.3	3.8	4.2	4.1	3.2	3.7	3.5	2.9	3
Quartz80Kaol20	0	1.2	1.1	1.2	1	1.1	1.2	1.5	1.4	1	1.1	0.9	1.1
Quartz	28.8	22.7	23.5	22.5	27.1	19.7	22.3	21.7	24.8	21.5	23	28.8	19.5
TiOxide	0.1	0.3	0.5	0.1	0.1	0.1	1.1	0.3	0.6	0.2	0.2	0.2	1.4
Total	100	100.0	100.0	100	100	100	100	100	100	100	100	100	100
Fly ash phase	**Fragmentation (#2 0.5m)**	**Absolute difference (Mass-% coalescence – DTF mass-% fly ash)**											
		Avg. Oxid	**Avg. Red**	**Oxidising (°C)**					**Reducing (°C)**				
				1000	**1100**	**1200**	**1300**	**1400**	**1000**	**1100**	**1200**	**1300**	**1400**
Ca-Oxide	0.0	1.9	1.1	1.1	1.6	2.3	2	2.4	2	0.9	0	1.9	0.7
Fe-Oxide	0.0	1.4	1.8	1.7	0.2	1.3	2.5	1.1	1.1	0.5	1.9	2.3	3.3
Kaolinite	0.0	2.5	1.5	0.5	3.9	2.1	3.6	2.2	0.8	0	2.9	3.3	0.4
Kaolinite(Carbonate,pyrite)	0.0	0.6	0.6	0.9	0.5	0.8	0.5	0.4	0.6	0.4	0.6	0.6	0.9
Kaolinite(Carbonate)	0.0	2.0	1.6	1.2	0.9	1.9	3.3	2.8	0.7	1.4	2	1.4	2.5
Kaolinite(Pyrite)	0.0	0.6	0.4	0.3	0.5	0.5	0.7	0.9	0.3	0.6	0.4	0.4	0.5
Kaolinite(illite,mica)	0.0	2.2	2.3	1.9	1.2	2.7	2.8	2.5	1.7	1.9	2.9	1.7	3.2
Orthoclase	0.0	0.4	0.3	0.3	0.1	0	1.2	0.6	0.3	0.1	0.1	0.2	0.6
Quartz60Kaol40	0.0	3.7	3.3	3.1	3.3	3.8	4.2	4.1	3.2	3.7	3.5	2.9	3
Quartz80Kaol20	0.0	1.2	1.1	1.2	1	1.1	1.2	1.5	1.4	1	1.1	0.9	1.1
Quartz	0.0	6.1	5.3	6.3	1.7	9.1	6.5	7.1	4	7.3	5.8	0	9.3
TiOxide	0.0	0.2	0.4	0	0	0	1	0.2	0.5	0.1	0.1	0.1	1.3
Total	0.0	22.9	19.7	18.5	14.9	25.6	29.5	25.8	16.6	17.9	21.3	15.7	26.8

Table S.2: Absolute mass-% difference between partial coalescence model prediction and DTF fly ash.

Fly ash phase	P.Coalescence (#2 0.5m)	Avg. Oxid	Avg. Red	Oxidising (°C)					Reducing (°C)				
				1000	1100	1200	1300	1400	1000	1100	1200	1300	1400
Ca-Oxide	4.7	4.2	5.0	5	4.5	3.8	4.1	3.7	4.1	5.2	6.1	4.2	5.4
Fe-Oxide	4.9	3.7	3.3	3.4	4.9	3.8	2.6	4	4	4.6	3.2	2.8	1.8
Kaolinite	51.5	56.4	56.5	58.3	53.9	59.9	54.2	55.6	57	57.8	54.9	54.5	58.2
Kaolinite(Carbonate,pyrite)	0	0.6	0.6	0.9	0.5	0.8	0.5	0.4	0.6	0.4	0.6	0.6	0.9
Kaolinite(Carbonate)	0.8	2.0	1.6	1.2	0.9	1.9	3.3	2.8	0.7	1.4	2	1.4	2.5
Kaolinite(Pyrite)	1.1	0.6	0.4	0.3	0.5	0.5	0.7	0.9	0.3	0.6	0.4	0.4	0.5
Kaolinite(illite,mica)	2.1	3.1	3.2	2.8	2.1	3.6	3.7	3.4	2.6	2.8	3.8	2.6	4.1
Orthoclase	0.9	1.2	0.9	0.6	1	0.9	2.1	1.5	0.6	0.8	1	0.7	1.5
Quartz60Kaol40	7.3	3.7	3.3	3.1	3.3	3.8	4.2	4.1	3.2	3.7	3.5	2.9	3
Quartz80Kaol20	4.1	1.2	1.1	1.2	1	1.1	1.2	1.5	1.4	1	1.1	0.9	1.1
Quartz	22.3	22.7	23.5	22.5	27.1	19.7	22.3	21.7	24.8	21.5	23	28.8	19.5
TiOxide	0.2	0.3	0.5	0.1	0.1	0.1	1.1	0.3	0.6	0.2	0.2	0.2	1.4
Total	100	100.0	100.0	100.02	100.04	100	100.02	100.01	100	100	100	100	100
Fly ash phase	**P.Coalescence (#2 0.5m)**	**Absolute difference (Mass-% coalescence – DTF mass-% fly ash)**											
		Avg. Oxid	**Avg. Red**	**Oxidising (°C)**					**Reducing (°C)**				
				1000	**1100**	**1200**	**1300**	**1400**	**1000**	**1100**	**1200**	**1300**	**1400**
Ca-Oxide	0.0	0.6	0.7	0.3	0.2	0.9	0.6	1	0.6	0.5	1.4	0.5	0.7
Fe-Oxide	0.0	1.2	1.6	1.5	0	1.1	2.3	0.9	0.9	0.3	1.7	2.1	3.1
Kaolinite	0.0	4.9	5.0	6.8	2.4	8.4	2.7	4.1	5.5	6.3	3.4	3	6.7
Kaolinite(Carbonate,pyrite)	0.0	0.6	0.6	0.9	0.5	0.8	0.5	0.4	0.6	0.4	0.6	0.6	0.9
Kaolinite(Carbonate)	0.0	1.2	0.8	0.4	0.1	1.1	2.5	2	0.1	0.6	1.2	0.6	1.7
Kaolinite(Pyrite)	0.0	0.5	0.7	0.8	0.6	0.6	0.4	0.2	0.8	0.5	0.7	0.7	0.6
Kaolinite(illite,mica)	0.0	1.0	1.1	0.7	0	1.5	1.6	1.3	0.5	0.7	1.7	0.5	2
Orthoclase	0.0	0.4	0.3	0.3	0.1	0	1.2	0.6	0.3	0.1	0.1	0.2	0.6
Quartz60Kaol40	0.0	3.6	4.0	4.2	4	3.5	3.1	3.2	4.1	3.6	3.8	4.4	4.3
Quartz80Kaol20	0.0	2.9	3.0	2.9	3.1	3	2.9	2.6	2.7	3.1	3	3.2	3
Quartz	0.0	1.6	2.7	0.2	4.8	2.6	0	0.6	2.5	0.8	0.7	6.5	2.8
TiOxide	0.0	0.3	0.3	0.1	0.1	0.1	0.9	0.1	0.4	0	0	0	1.2
Total	0.0	18.9	20.8	19.1	15.9	23.6	18.7	17	19	16.9	18.3	22.3	27.6

Table S.3: Absolute mass-% difference between coalescence model prediction and DTF fly ash.

Fly ash phase	Coalescence (#2 0.5m)	Avg. Oxid	Avg. Red	Oxidising (°C)					Reducing (°C)				
				1000	1100	1200	1300	1400	1000	1100	1200	1300	1400
Ca-Oxide	4.2	4.2	5.0	5.0	4.5	3.8	4.1	3.7	4.1	5.2	6.1	4.2	5.4
Fe-Oxide	4.4	3.7	3.3	3.4	4.9	3.8	2.6	4.0	4.0	4.6	3.2	2.8	1.8
Kaolinite	46.8	56.4	56.5	58.3	53.9	59.9	54.2	55.6	57.0	57.8	54.9	54.5	58.2
Kaolinite(Carbonate,pyrite)	0.0	0.6	0.6	0.9	0.5	0.8	0.5	0.4	0.6	0.4	0.6	0.6	0.9
Kaolinite(Carbonate)	1.5	2.0	1.6	1.2	0.9	1.9	3.3	2.8	0.7	1.4	2.0	1.4	2.5
Kaolinite(Pyrite)	1.1	0.6	0.4	0.3	0.5	0.5	0.7	0.9	0.3	0.6	0.4	0.4	0.5
Kaolinite(illite,mica)	2.3	3.1	3.2	2.8	2.1	3.6	3.7	3.4	2.6	2.8	3.8	2.6	4.1
Orthoclase	0.8	1.2	0.9	0.6	1.0	0.9	2.1	1.5	0.6	0.8	1.0	0.7	1.5
Quartz60Kaol40	14.7	3.7	3.3	3.1	3.3	3.8	4.2	4.1	3.2	3.7	3.5	2.9	3.0
Quartz80Kaol20	4.1	1.2	1.1	1.2	1.0	1.1	1.2	1.5	1.4	1.0	1.1	0.9	1.1
Quartz	19.8	22.7	23.5	22.5	27.1	19.7	22.3	21.7	24.8	21.5	23.0	28.8	19.5
TiOxide	0.2	0.3	0.5	0.1	0.1	0.1	1.1	0.3	0.6	0.2	0.2	0.2	1.4
Total	100.0	100.0	100.0	100.0	100.0	100.0	100.0	100.0	100.0	100.0	100.0	100.0	100.0
Fly ash phase	**Coalescence (#2 0.5m)**	**Absolute difference (Mass-% coalescence – DTF mass-% fly ash)**											
		Avg. Oxid	**Avg. Red**	**Oxidising (°C)**					**Reducing (°C)**				
				1000	**1100**	**1200**	**1300**	**1400**	**1000**	**1100**	**1200**	**1300**	**1400**
Ca-Oxide	0.0	0.4	0.8	0.8	0.3	0.4	0.1	0.5	0.1	1	1.9	0	1.2
Fe-Oxide	0.0	0.9	1.2	1	0.5	0.6	1.8	0.4	0.4	0.2	1.2	1.6	2.6
Kaolinite	0.0	9.6	9.7	11.5	7.1	13.1	7.4	8.8	10.2	11	8.1	7.7	11.4
Kaolinite(Carbonate,pyrite)	0.0	0.6	0.6	0.9	0.5	0.8	0.5	0.4	0.6	0.4	0.6	0.6	0.9
Kaolinite(Carbonate)	0.0	0.9	0.5	0.3	0.6	0.4	1.8	1.3	0.8	0.1	0.5	0.1	1
Kaolinite(Pyrite)	0.0	0.5	0.7	0.8	0.6	0.6	0.4	0.2	0.8	0.5	0.7	0.7	0.6
Kaolinite(illite,mica)	0.0	0.9	0.9	0.5	0.2	1.3	1.4	1.1	0.3	0.5	1.5	0.3	1.8
Orthoclase	0.0	0.5	0.2	0.2	0.2	0.1	1.3	0.7	0.2	0	0.2	0.1	0.7
Quartz60Kaol40	0.0	11.0	11.4	11.6	11.4	10.9	10.5	10.6	11.5	11	11.2	11.8	11.7
Quartz80Kaol20	0.0	2.9	3.0	2.9	3.1	3	2.9	2.6	2.7	3.1	3	3.2	3
Quartz	0.0	2.9	3.8	2.7	7.3	0.1	2.5	1.9	5	1.7	3.2	9	0.3
TiOxide	0.0	0.3	0.3	0.1	0.1	0.1	0.9	0.1	0.4	0	0	0	1.2
Total	0.0	31.3	33.2	33.3	31.9	31.4	31.5	28.6	33	29.5	32.1	35.1	36.4

Table S.4: Absolute mass-% difference between model fly ash distribution, probe and cegrit fly ash

	Mass-%					
Fly ash phases	Coal (Fragmentation)	Partial Coalescence	Coalescence	Probe Fly ash	Cegrit Fly ash	
Ca-Oxide	9.0	7.3	6.6	2.1	2.8	
Fe-Oxide	5.3	4.9	4.2	2.5	3.1	
Kaolinite	51.3	34.9	31.8	65.8	60.4	
Kaolinite(Carbonate,pyrite)	0.0	0.0	0.0	0.4	0.5	
Kaolinite(Carbonate)	0.1	1.6	2.4	5.7	6.2	
Kaolinite(Pyrite)	0.0	0.4	0.4	1.1	2.1	
Kaolinite(illite,mica)	1.0	2.3	2.5	2.1	2.1	
Orthoclase	0.9	1.7	1.5	0.4	1.0	
Quartz60Kaol40	0.0	12.2	18.6	3.7	3.9	
Quartz80Kaol20	0.0	4.2	5.2	0.9	1.4	
Quartz	31.0	24.3	20.9	15.0	16.3	
TiOxide	0.2	0.5	0.4	0.2	0.1	
Total	100.0	100.0	100.0	99.9	100.0	
	Absolute mass-% difference (Fly ash model – probe or cegrit fly ash)					
	Fragmentation		Partial Coalescence		Coalescence	
Fly ash phases	Probe fly ash	Cegrit fly ash	Probe fly ash	Cegrit fly ash	Probe fly ash	Cegrit fly ash
Ca-Oxide	6.9	6.1	5.2	4.4	4.5	3.7
Fe-Oxide	2.8	2.2	2.4	1.8	1.7	1.1
Kaolinite	14.6	9.2	30.9	25.5	34.1	28.7
Kaolinite(Carbonate,pyrite)	0.4	0.5	0.4	0.4	0.4	0.4
Kaolinite(Carbonate)	5.6	6.1	4.1	4.6	3.2	3.7
Kaolinite(Pyrite)	1.1	2.1	0.7	1.7	0.7	1.7
Kaolinite(illite,mica)	1.0	1.1	0.2	0.2	0.4	0.4
Orthoclase	0.6	0.1	1.4	0.7	1.1	0.5
Quartz60Kaol40	3.6	3.8	8.5	8.3	14.9	14.7
Quartz80Kaol20	0.9	1.4	3.3	2.8	4.3	3.8
Quartz	16.0	14.7	9.3	8.0	5.9	4.6
TiOxide	0.0	0.1	0.3	0.4	0.2	0.3
Total	53.4	47.3	66.6	58.9	71.4	63.7